

# **Study on control and simulation of H&V shield behavior**

**H&Vシールド機挙動の制御とシミュレーションに関する研究**

A dissertation submitted in partial fulfillment of the requirements for the Degree  
of Doctor of Engineering

by

**HUYNH NGOC THI**

Academic advisor: **Prof. Mitsutaka Sugimoto**

Department of Civil Engineering  
Nagaoka University of Technology  
Niigata, JAPAN

March, 2017

## **ACKNOWLEDGEMENTS**

The author would like to express gratitude, great appreciation and indebtedness to his advisor Professor Mitsutaka Sugimoto, who introduced him to shield tunneling field, for his encouragement, invaluable guidance, support and apportion the knowledge throughout the research. Without his guidance, providing a spur to the author confidence, the final works would have never been reached.

A special gratitude is offered to his beloved wife Phan Thi Anh Thu for her emotional support, patience and many sacrifices throughout the study period. She is always behind me and encourages me. Her constant affection and forbearance have been a source of strength.

Acknowledgements are also extended to Professor Satoru Ohtsuka, Associate Professor Hirofumi Toyota and Professor Osamu Takahashi for their insight, helpful discussions and reviewing thesis manuscripts.

The author thanks to Dr. Chen Jian for invaluable help in various ways for academic, and private matters throughout the research. Additionally, the author appreciates to the students of Geotechnical laboratory, who contributed to the work of the research project, and provide an enjoyable atmosphere.

The author deeply thanks to the faculties and other staff of Civil Engineering Department. He will remain grateful to them for their cooperation during the study. He would also like to thanks the members of Vietnamese Student Association for making his stay in Japan more enjoyable.

## *Acknowledgements*

Author wishes to thankful for financial supported by Monbusho Scholarship Program, provided by the Ministry of Education, Culture, Sports, Science and Technology of Japan.

A special sincere appreciation extends to Associate Professor Le Van Nam and Dr. Dang Dang Tung for their continuing supports and good wishes. Sincere appreciation goes to all those who help in numerous ways in successfully completing this piece of research work.

Finally, the author dedicates this little piece of work to his father and mother for their strong encouragement, tremendous sacrifices given to him.

Huynh Ngoc Thi

Nagaoka University of Technology, Japan

## **ABSTRACT**

Due to limited underground space in the urban area and for saving construction cost, multi-circular face shield (MF shield) had been innovated to construct a twin tunnel at once. Furthermore, according to the more severe restriction of underground space use, horizontal and vertical variation shield method (H&V shield) was innovated, so that the cross section of an MF shield tunnel is changed from horizontal multi-circular shape to vertical one or vice versa. The H&V shield is manufactured by connecting two articulated shields at their rear bodies and is steered by articulation mechanism and copy cutter, which can be operated individually at each body. These steering options can generate rotating force around the shield axis, which can realize the construction of a spiral tunnel.

The characteristics of H&V shield method, compared with other type shields, are as follows:

1) Tunnel shape and alignment: H&V shield can construct a separate tunnel and a spiral tunnel. In the case of a separate tunnel, H&V shield forms a tunnel with a multi-circular cross section at first, and two ordinary tunnels with a circular cross section after a specified point along the tunnel alignment by separating the H&V shield to two ordinary shields. On the other hand, in the case of a spiral tunnel, H&V shield constructs a tunnel with a multi-circular cross section, which is changed continuously from horizontal multi-circular shape to vertical one, or vice versa; 2) Construction period: H&V shield can shorten a construction period because H&V shield can omit an intermediate vertical shaft to separate the body in the case of a separate tunnel, and can construct multiple tunnels at once in the case of a spiral tunnel; and 3) Construction cost: H&V

shield can save a construction cost because H&V shield body can separate without an intermediate vertical shaft and a ground improvement in the case of a separate tunnel, and can reduce the adjacent distance between two circular tunnels in the case of a spiral tunnel.

Shield is operated for excavation, steering shield, filling up in the tail void, and segment installation mainly. As for steering shield, the shield is controlled by jack, copy cutter and articulation mechanism in practice. The jack generates thrust and horizontal and vertical moment, which can be determined by jack pattern and shield jack pressure. The copy cutter can carry out overcutting with a specified depth and a specified range along the circumference of cutter face. The overcutting by copy cutter defines excavation area and reduces ground reaction force at the overcutting range, which makes the shield rotate toward the overcutting range easier. The articulation mechanism for articulated shield can crease shield with a specified direction and a specified angle. The crease of the shield can reduce ground reaction force at curves by fitting the shield for its excavation area, which makes the shield rotate easily.

H&V shield for a spiral tunnel can be controlled by spiral jacks, copy cutter and articulation system. The shield jack system including spiral jacks, causes the eccentric forces to generate torque to twist an H&V shield around its axis. The copy cutter can reduce the ground reaction force at a specified area by overcutting the ground, and the articulation system also can reduce the ground reaction force by articulating the front body from the rear body of each shield. Using these functions, H&V shield can rotate around its axis and can advance, thus, H&V shield can construct a spiral tunnel.

Recently, a construction project has been planned using H&V shield method. Because of the limitation of land use, such as, narrow river and existing structures over the planned route of the tunnel, only the spiral excavation mode of this method can construct the tunnel, of which the cross section enables the required amount to be discharged. However, this is the first application

in practice except for the test execution. Therefore, this study aims to examine the H&V shield control method before the construction.

At first, the shield steering parameters, such as, copy cutter operation (length and range) and articulation operation (direction and angle), were determined, based on the geometric conditions for both bodies of H&V shield independently. After that the jack operation (jack thrust force, horizontal moment and vertical moment) were determined, using the kinematic shield model for H&V shield. Next, the H&V shield behavior was simulated using the kinematic shield model for H&V shield, which has been developed from the one for the single circular shield to simulate H&V shield behavior during excavation theoretically based on equilibrium conditions. In the simulation process, the ground displacement around the shield was taken into account, and the shield operational parameters obtained from the above were also used. In this process in order to validate the model performance, the calculated shield behavior was examined from the viewpoint of theory, and the H&V shield control method was confirmed by comparing the calculated shield behavior with the plan data. Besides, the force acting at the connection point between the left body and the right body was calculated for shield design. This paper describes the H&V shield behavior at the a curve.

As a result, the followings were found: 1) The calculated H&V shield behavior is reasonable from the viewpoint of the theory and site experience. 2) The calculated shield behavior has an overall good agreement with the planned one; 3) The ground displacement is a predominant factor affecting shield behavior; and 4) The proposed model can simulate the H&V shield behavior reasonably.

## TABLE OF CONTENTS

ACKNOWLEDGEMENTS .....	i
ABSTRACT .....	iii
TABLE OF CONTENTS.....	vi
LIST OF TABLES .....	xi
LIST OF FIGURES .....	xii
CHAPTER 1: INTRODUCTION.....	1
<b>1.1 Background .....</b>	<b>1</b>
<b>1.2 Mechanized Shield Tunneling Work .....</b>	<b>3</b>
1.2.1 Shield Tunneling Works .....	3
1.2.1.1 General Aspect of Shield Tunneling Method .....	3
1.2.1.2 Shield Tunneling Machine Types .....	3
1.2.1.3 Ground Responses Caused by Shield Tunneling.....	5
1.2.2 Shield Tunneling Control.....	7
1.2.2.1 Face Stabilization .....	8
1.2.2.2 Muck Volume .....	12
1.2.2.3 Back filling.....	12
1.2.2.4 Tail Seal.....	13
1.2.2.5 Shield Direction.....	14
1.2.3 Horizontal and Vertical Variation Shield Method .....	14
1.2.3.1 Concept.....	14
1.2.3.2 Characteristics .....	14
1.2.3.3 Mechanism of Tunnel Driving .....	15

<b>1.3 Literature Review .....</b>	<b>16</b>
1.3.1 Shield behavior .....	16
1.3.2 Ground movement.....	18
<b>1.4 Simulation Method of Shield Behavior.....</b>	<b>20</b>
1.4.1 Kinematic shield model .....	20
1.4.2 Simulation method of single circular shield .....	21
1.4.3 Simulation Method of Articulated Shield .....	23
<b>1.5 Objective of This Study .....</b>	<b>24</b>
<b>CHAPTER 2: METHODOLOGY .....</b>	<b>25</b>
<b>2.1 Calculation Method Of Steering Parameters.....</b>	<b>25</b>
2.1.1 Calculation conditions.....	25
2.1.2 Coordinate System .....	26
2.1.2.1 Definition.....	26
2.1.2.2 Coordinate Transformation.....	26
2.1.3 Tunnel Alignment Description .....	27
2.1.3.1 Spatial Curve .....	27
2.1.3.2 Discretization and Interpolation .....	29
2.1.4 Articulation Angle .....	31
2.1.5 Machine Type.....	34
2.1.6 Excavation Stage.....	34
2.1.6.1 Operation Rules at Curve .....	35
2.1.6.2 Operation Rules around BC .....	35
2.1.6.3 Operation Rules around EC.....	35
2.1.7 Calculation Method for Articulation Angle .....	36
2.1.7.1 Type 1 .....	36

2.1.7.2 Type 2 .....	38
2.1.7.3 Type 3 .....	40
2.1.8 Calculation Method for Copy Cutter Length .....	40
<b>2.2 Simulation Method of H&amp;V Shield Behavior.....</b>	<b>45</b>
2.2.1 Types of Forces .....	45
2.2.1.1 Self-weight of the Shield $f_1$ .....	47
2.2.1.2 Forces on the Shield Tail $f_2$ .....	47
2.2.1.3 Jack Force $f_3$ .....	52
2.2.1.4 Force at the Face $f_4$ .....	53
2.2.1.5 Earth Pressure Acting on the Shield Periphery $f_5$ .....	59
2.2.2. Summations of Forces, Moments, and Cutter Torque.....	61
<b>2.3 Simulation Algorithms.....</b>	<b>62</b>
2.3.1 General .....	62
2.3.2 Simulation Techniques .....	63
2.3.3 Indexes of Shield Tunneling Behavior .....	65
2.3.3.1 Curvature on the Vertical Plane .....	66
2.3.3.2 Tilt Angle on the Vertical Plane .....	66
2.3.3.3 Curvature on the Horizontal Plane .....	67
2.3.3.4 Tilt Angle on the Horizontal Plane .....	68
CHAPTER 3: SENSITIVITY ANALYSES .....	69
<b>3.1 Introduction .....</b>	<b>69</b>
3.1.1 Analysis Data .....	69
3.1.2 Analysis Parameters .....	69
<b>3.2 Parameter 1: Copy Cutter Length.....</b>	<b>70</b>
3.2.1 Shield Behavior .....	70

3.2.2 Trace .....	71
3.2.3 Force .....	71
3.2.4 Gap Around Shield Periphery.....	72
3.2.5 Effective Normal Earth Pressure.....	73
3.2.6 Summary .....	73
<b>3.3 Parameter 2: Crease Angle <math>\theta_{CV}</math> and Pitching Angle <math>\phi_{pRR}</math> .....</b>	<b>74</b>
3.3.1 Shield Behavior .....	74
3.3.2 Trace .....	76
3.3.3 Force .....	76
3.3.4 Gap Around Shield Periphery.....	76
3.3.5 Effective Normal Earth Pressure.....	77
3.5.6 Summary .....	77
<b>3.4 Parameter 3: Share of Jack Force For Both Bodies.....</b>	<b>78</b>
3.4.1 Shield Behavior .....	79
3.4.2 Trace .....	79
3.4.3 Force .....	80
3.4.4 Gap Around Shield Periphery.....	80
3.4.5 Effective Normal Earth Pressure.....	81
3.4.6 Summary .....	81
<b>3.5 Parameter 4: Ground Stiffness .....</b>	<b>82</b>
3.5.1 Shield Behavior .....	82
3.5.2 Trace .....	82
3.5.3 Force .....	82
3.5.4 Gap Around Shield Periphery.....	82
3.5.5 Effective Normal Earth Pressure.....	83

3.5.6 Summary .....	83
CHAPTER 4: APPLICATION .....	84
<b>4.1 Site Description .....</b>	<b>84</b>
<b>4.2 Simulation of H&amp;V Shield at a Sharp Curve .....</b>	<b>84</b>
4.2.1 Operation Data .....	85
4.2.2 Simulation Results .....	86
4.2.2.1 H&V Shield Behavior .....	86
4.2.2.2 Ground-shield Interaction.....	87
4.2.2.3 Forces and Moments Acting on the Shield.....	89
<b>4.3 Simulation of H&amp;V Shield at the Spiral Section .....</b>	<b>90</b>
4.3.1 Operation data .....	90
4.3.2 Simulation Results .....	91
4.3.2.1 H&V Shield Behavior .....	91
4.3.2.2 Ground-shield Interaction.....	92
4.3.2.3 Forces and Moments Acting on the Shield.....	94
CHAPTER 5: CONCLUSIONS.....	95
REFERENCES .....	98
APPENDIX	
TABLES	
FIGURES	

## LIST OF TABLES

- Table 1.1 Selection of shield (*JSCE, 1986*).
- Table 1.2 Summary of changes of earth pressure during shield tunneling operation with passing of time (*Revised from JSSMFE, 1993*).
- Table 1.3 Proportion of settlement by settlement type (*Makata, 1981 and Yamada et al., 1988*).
- Table 2.1 Parameters at  $\beta=0, 1/2, 1$ .
- Table 2.2 Operational sign.
- Table 2.3 Machine types
- Table 2.4 Operation rule at curve.
- Table 2.5 Judging conditions of Type 1 for shield position.
- Table 2.6 Judging conditions of Type 2 for shield position
- Table 2.7 Judging conditions of Type 3 for shield position.
- Table 2.8 Position vector  $\mathbf{r}_*$  and unit normal direction vector  $\mathbf{k}_*$  in analysis
- Table 2.9 Relationship between applications of shield model and affecting factors.
- Table 3.1 Shield data used in the analysis
- Table 3.2 Ground parameters
- Table 3.3 Analysis case
- Table 4.1 Ground properties
- Table 4.2 Dimensions of tunnel and shield
- Table 4.3 Force and moment acting on shield (at distance 4.345m)
- Table 4.4 Force and moment acting on shield (at distance 22.574m)
- Table 4.5 Force and moment acting on shield (at distance 125.5m)

## LIST OF FIGURES

- Figure 1.1 Mechanism of shield movement (Shimizu and Suzuki, 1992).
- Figure 1.2 Construction sequences of shield tunneling works (*Fujita, 1989*).
- Figure 1.3 Illustration of ground movement caused by shield tunneling work (*JSSMFE, 1993*).
- Figure 1.4 Relationships between ground displacement and affecting factors (*Makata, 1980*).
- Figure 1.5 Ground surface settlement in longitudinal direction (*JGS, 1996*).
- Figure 1.6 Ground surface settlement in transverse direction (*JGS, 1996*).
- Figure 1.7 Three dimensional displacement of ground around the cutter face for clayey soil (*JGS, 1996*).
- Figure 1.8 Three dimensional displacement of ground around the cutter face for sandy soil (*JGS, 1996*).
- Figure 1.9 Illustration of pressure acting on cutter face (*Kanayasu et al., 1995*).
- Figure 1.10 Relationship between earth pressure and deformation (*Sugimoto et al., 1992*).
- Figure 1.11 An example of control system for face stabilization and excavated soil volume of slurry shield.
- Figure 1.12 An example of automatic back filling control system.
- Figure 1.13 Installation of wire brush seal on the inside shield tail.
- Figure 1.14 An example of automatic shield direction control system.
- Figure 1.15 H&V shield. (STA 2011b)
- Figure 1.16 Utilization of H&V shield. (STA 2011b)
- Figure 1.17 Spiral jack. (STA 2011b)
- Figure 1.18 Copy cutter and articulated mechanism in excavation. (STA 2011b)
- Figure 1.19 Model to analyze taking tail void and segment rigidity into consideration

*(Yamada et al., 1979).*

Figure 1.20 Model of loads acting on shield (*Sugimoto and Sramoon 2002*).

Figure 1.21 Ground reaction curve.

Figure 1.22 Definition of displacement of excavated surface for stiff ground

Figure 1.23 Model of load acting on both of right and left body of H&V shield.

Figure 2.1 Flowchart of numerical procedure for articulation angle and copy cutter length.

Figure 2.2 Coordinate systems.

Figure 2.3 Fundamental unit vectors of a spatial curve.

Figure 2.4 Relation between articulation angle and direction vectors.

Figure 2.5 Dimension of articulated shield.

Figure 2.6 Crease Type 1.

Figure 2.7 Crease Type 2 and Type 3.

Figure 2.8 Operation rules at BC section for all types.

Figure 2.9 (a) Operation rules at EC section for Type1.

Figure 2.9 (b) Operation rules at EC section for Type2.

Figure 2.9 (c) Operation rules at EC section for Type3.

Figure 2.10 Contact condition of Type 1 at curve section.

Figure 2.11 Contact condition of Type 2 at curve section.

Figure 2.12 Contact condition of Type 3 at curve section.

Figure 2.13 Concept to calculate copy cutter length.

Figure 2.14 Calculation points for Procedure A.

Figure 2.15 Calculation points for Procedure B.

Figure 2.16: Model of load acting on both front body and rear body of H&V shield

Figure 2.17 Coordinate systems.

Figure 2.18 Definition of jack position measurement.

Figure 2.19 Definition of division on front face.

Figure 2.20 Pressure on cutter face.

Figure 2.21 Definition of length measured on shield.

Figure 2.22 Definition of calculation point on cutter face periphery.

Figure 2. 23 Factors affecting shield model.

Figure 2.24 Description of  $R_v$  and  $\theta_{vT}$

Figure 2.25 Description of  $R_h$  and  $\theta_{xT}$

Figure 3.1 Shield behavior (Parameter 1: CCL)

Figure 3.2 Shield behavior (curvatures and tilt angles on the horizontal and vertical planes)  
(Parameter 1: CCL)

Figure 3.3 Trace of shield on the vertical and horizontal plan (Parameter 1: CCL)

Figure 3.4 Forces and Moments against distance (Parameter 1: CCL)

Figure 3.5 Gap around the shield periphery (Parameter 1: CCL)

Figure 3.6 Effective normal earth pressure on the shield periphery (Parameter 1: CCL)

Figure 3.7 Shield Behavior (Parameter 2: Crease Angle and Pitching Angle,  $\phi_{pRR} = -0.5\theta_{CV}$ )  
Condition 1)

Figure 3.8 Shield Behavior (Parameter 2: Crease Angle and Pitching Angle,  $\phi_{pRR} = -\theta_{CV}$ )

Figure 3.9 Trace of shield on the vertical and horizontal plane (Parameter 2: Crease Angle and  
Pitching Angle,  $\phi_{pRR} = -0.5\theta_{CV}$ )

Figure 3.10 Trace of shield on the vertical and horizontal plane (Parameter 2: Crease Angle and  
Pitching Angle,  $\phi_{pRR} = -\theta_{CV}$ )

Figure 3.11 Forces and Moments against distance (Parameter 2: Crease Angle and Pitching  
Angle,  $\phi_{pRR} = -0.5\theta_{CV}$ )

Figure 3.12 Forces and Moments against distance (Parameter 2: Crease Angle and Pitching

Angle,  $\phi_{\text{pRR}} = -\theta_{\text{CV}}$  )

Figure 3.13 Gap around the shield periphery (Parameter 2: Crease Angle and Pitching Angle,

$\phi_{\text{pRR}} = -0.5\theta_{\text{CV}}$  )

Figure 3.14 Gap around the shield periphery (Parameter 2: Crease Angle and Pitching Angle,

$\phi_{\text{pRR}} = -\theta_{\text{CV}}$  )

Figure 3.15 Normal effective earth pressure on the shield periphery (Parameter 2: Crease Angle and Pitching Angle,  $\phi_{\text{pRR}} = -0.5\theta_{\text{CV}}$  )

Figure 3.16 Normal effective earth pressure on the shield periphery (Parameter 2: Crease Angle and Pitching Angle,  $\phi_{\text{pRR}} = -\theta_{\text{CV}}$  )

Figure 3.17 Shield Behavior (Parameter 3: Share of jack force for both bodies)

Figure 3.18 Trace of shield on the vertical and horizontal plane (Parameter 3: Share of jack force for both bodies)

Figure 3.19 Forces and moments against distance (Parameter 3: Share of jack force for both bodies)

Figure 3.20 Gap around the shield periphery (Parameter 3: Share of jack force for both bodies)

Figure 3.21 Normal effective earth pressure on the shield periphery (Parameter 3: Share of jack force for both bodies)

Figure 3.22 Shield behavior (Parameter 4: Ground stiffness)

Figure 3.23 Trace of shield on the vertical and horizontal plane (Parameter 4: Ground stiffness)

Figure 3.24 Forces and moments against distance (Parameter 4: Ground stiffness)

Figure 3.25 Gap around shield periphery (Parameter 4: Ground stiffness)

Figure 3.26 Normal effective earth pressure on the shield periphery (Parameter 4: Ground stiffness)

Figure 4.1 Site location and geological profile

Figure 4.2 Ground reaction curve of the soil layers at the construction.

Figure 4.3 Dimension of H&V shield machine.

Figure 4.4 Shield tunneling input data at sharp curve

Figure 4.5 Calculated and planned shield traces at sharp curve

Figure 4.6 Calculated and planned shield behavior.at sharp curve

Figure 4.7  $U_n$  around shield on the straight line at 4.345 m.

Figure 4.8  $\sigma_n'$  around shield on the straight line at 4.345m.

Figure 4.9  $U_n$  around shield on the sharp curve at 22.574m.

Figure 4.10  $\sigma_n'$  around shield on the sharp curve at 22.574m.

Figure 4.11 Shield tunnelling input data at spiral section

Figure 4.12 Calculated and planned shield traces at spiral section

Figure 4.13 Calculated and planned shield behavior at spiral section

Figure 4.14  $U_n$  around shield on the spiral section at 125.5m.

Figure 4.15  $\sigma_n'$  around shield on the spiral section at 125.5m.

## **CHAPTER 1: INTRODUCTION**

### **1.1 Background**

The main construction method of tunnels under groundwater level in soft ground of urban areas is shield tunneling method. Shield tunneling method is developed to minimize the disturbance of the surrounding ground and also to install the ground support under the protection of the shield.

Shield tunneling method is defined as any method in which a solid cylinder, or shield, is driven through the ground. The tunnel lining is constructed inside the shield to prevent the ground from collapsing. At the beginning, the shield tunneling used a manual type with an open face. The slurry shield and the earth pressure balanced (EPB) shield were developed around 1970. The machines are classified based on the face support method and the cutting technique. The slurry shield and the EPB shield are classified together as the closed-type shield, which were popular tunneling methods in the soft ground tunneling during the past decade.

The planned alignment of shield tunneling method should be designed as simple as possible. A straight line or a gradual curve with a large radius on 2-D horizontal plane is generally desired. However, due to completeness of infrastructures in urban areas, underground space at shallow depth is congested constantly. To construct new tunnel projects, deep-depth space starts to be used, which increases the opportunities on the use of vertical alignments. This fact involves the using of 3-D compound alignments. Furthermore, due to shield adjacent construction near existing structures, the precise control of shield is being placed on the agenda. Taking a wide view of present technologies on precise control of shield, they have not yet been developed well under complex conditions.

As for shield control, too many control parameters reflect as the following aspects: (1) Excavation area, which involves copy cutter range, length, and articulation angle; (2) Forces (including thrust, horizontal, and vertical moments), which are determined by jack pattern and shield jack pressure; and (3) Stability of excavation face, which involves face pressure, advancing speed, and mucking rate.

Excavation area is the predominant factor to influence shield behavior, which can be determined by geometrical relations under certain conditions. However, it is not enough to ensure excavation area only. Conditions of force equilibrium should be considered at the same time. Jack force and jack moment give small influences to shield behavior, compared with the influences of excavation area. To consider the force equilibrium, it is necessary to ensure stability of excavation face. Stability of excavation face is also an important factor to control the settlement of ground surface. At present, technologies on stability control of excavation face have been developed very well.

As for the first step to develop a precise control system of shield, the kinematic shield model had been developed. Based on the operation data including copy cutter length, range, and articulation angle, the kinematic shield model was verified by in-situ data. Secondly, a numerical method to calculate copy cutter length and range and articulation angle on 3-D compound alignments had been developed by considering discrete shield trace. At present, similar calculation methods by shield manufacturers just can consider 2-D circular alignments. This numerical method can consider straight, circular, and clothoid curves on the horizontal plane and straight, circular, and parabolic curves on the vertical plane. But it is a problem that this method cannot be applied to the special alignments which do not follow the above alignment.

The direction control systems of shield machine based on empirical relationships were developed. These systems cannot take into account the excavation area around the shield, which is considered to be the predominant factor affecting the shield behavior.

## **1.2 Mechanized Shield Tunneling Work**

### **1.2.1 Shield Tunneling Works**

#### **1.2.1.1 General Aspect of Shield Tunneling Method**

The shield tunneling method was invented by M.T. Brunel in the United Kingdom in 1818, and it was used first in 1825 for constructing a tunnel under the Thames River. The shield is usually a cylindrical steel shell to prevent the ground from collapsing and to provide the space for the excavation and the lining as well. The shell is supported by ribs and ring girders and is moved by built-in hydraulic jacks. Figure 1.2 shows the construction sequences of shield tunneling with simplified longitudinal sections of a conventional type of shield (Fujita 1989). Various pieces of equipment and other devices are installed in the shield to make the operation easier. The shield is assembled in the launching shaft, and the construction sequences of the shield tunneling can be described as follows:

- (1) Excavate ahead for a distance equivalent to the length of one segmental lining. Support the face if necessary by the jacks, the sheeting, and/or the face supporting pressure.
- (2) Advance the shield one-ring length forward by applying the jack thrust against the lining, which is already built.
- (3) Install the segments of one-ring length in the shield tail after retracting the jacks.
- (4) Fill the tail void, which is developed between the lining and the opening ground, by grouting.

#### **1.2.1.2 Shield Tunneling Machine Types**

Various types of shields have been developed to increase the advanced rate of excavation to save the construction costs and to maintain the face stability under various ground conditions. The shields have been classified into three categories: the open face type, the partial open face type, and the closed face type, according to the interaction at the tunnel face (JSCE 1986).

In the open-face-type shield or the open-type shield, either the full face or part of the face is opened for excavation. It can be used for self-stabilized ground. This type includes the hand-mining shield, the excavator shield and the mechanical shield. The partial open face type shield is the blind shield. The collapse of the face is prevented by a bulkhead for a blind shield. It is meant that the muck through the slits on the rotary cutting head, is free from any pressure immediately.

It is possible to classify the balanced face type shield or the closed type shield into the slurry shield and the earth pressure balanced (EPB) shield. The EPB shield intends to secure the stability of the face by applying a constant pressure to chamber. It is composed of an excavation mechanism to excavate the ground, a mixing mechanism to agitate the excavated soil, a discharge mechanism to discharge the excavated soil, and a control mechanism to give a certain degree of binding strength to the excavated soil. In some cases, the EPB shield tunneling method uses soil additives to lubricate the soil. In comparison, the slurry shield circulates the pressurized slurry to stabilize the face while transporting the excavated soil in fluid form. The slurry shield is composed of an excavation mechanism to excavate the ground, an agitated mechanism to mix the excavated soil with slurry, a slurry feed mechanism to circulate the slurry, a slurry processing mechanism to process the slurry transport after initial excavation, and a slurry adjustment mechanism to feed the face with predetermined properties of slurry.

The difference between the EPB shield and the slurry shield is the face pressure, which is given to the excavated soil in the chamber to balance or to cope with the overburden pressure and the groundwater pressure acting on the face. Consequently, the use of the slurry shield or the EPB shield produces a good result in minimizing the ground movement or settlement.

In selecting the shield type used for tunneling, it is important to maintain the ground surface settlement or the ground movement to a minimum to achieve safety and economical operation. The main factors in selecting the type of shield includes the construction period, the ground

conditions, the tunnel length, the tunnel depth, the cross-sectional area, the minimum radius of the tunnel curvature, and the nature of the surrounding ground conditions. Fujita (1989) defined the ground conditions affecting the selection of the shield type as follows:

- (1) Ground-water level;
- (2) Physical properties of soil;
- (3) Composition of strata;
- (4) Size and amount of gravel and boulders;
- (5) Existence of obstacles;
- (6) Existence of explosive gas or deoxidizing materials;
- (7) Amount of inflow water.

JSCE (1986) proposed the applicable shield type for the various ground conditions as shown in Table 1.1.

### **1.2.1.3 Ground Responses Caused by Shield Tunneling**

The earth pressure acting on the shield or the lining changes in accordance with the ground deformation around the tunnel during construction. When the ground deformation around the tunnel occurs inward to the tunnel, the earth pressure decreases in proportion to the degree of deformation, that is, active earth pressure. In contrast, when the ground deformation around the tunnel appears outward from the tunnel, the earth pressure becomes passive. The earth pressure acting on the tunnel is governed not only by the tunnel shape and the characteristics of the ground, but also by many other factors, such as the excavation method, the control of shield, the stiffness and the erection timing of the lining, the grouting method, and the groundwater conditions.

JSSMFE (1993) proposed the imaginative ground movement, where the tunnel is excavated by a shield, as illustrated in Figure 1.3. The earth pressure acting on the shield or the lining, which

includes the subgrade reaction, changes in accordance with the difference stages of the ground movements along the tunnel wall as defined in Table 1.2 and can be explained as follows.

The first step is where the shield face has not reached an observed point in the ground, nevertheless, the ground movement appears even at this stage. In case of the open type shield tunneling work, the ground at the face deforms toward inside of the tunnel. In contrast, with the closed-type shield tunneling method, the ground would be deformed outward away from the tunnel face, provided that the total face pressure, which is composed of slurry pressure or mud pressure and support pressure by cutter face should be slightly greater than the earth pressure at rest at the face.

The second step is located at the actual digging of the ground by the cutter bit of the shield or by hand. If the fluid pressure can adequately support the face and the ground around the face, there would be little ground movement. In case of the open-type shield tunneling, even the compressed air is simultaneously applied, the ground movement would be deformed toward the tunnel.

The third step is where the shield actually passes the ground at the consideration point. At this step, the ground movement depends on deviation and rotation of the shield and local collapse of the ground around the shield since the ground is supported by the shield periphery. It is believed that it is impossible to create the fluid pressure strong enough to prevent the ground movement, even in case of the closed-type shield tunneling work.

The fourth step is considered that the shield has completely passed an observed point in the ground, and the segment lining assembled inside the shield tail is detached from the shield tail. At this moment, the tail void is created between the lining and the excavation surface. Any delay in backfilling or delay in hardening of the back-filling materials leads to the ground deformation toward to this tail void.

The fifth step is considered when consolidation settlement or creep deformation of the ground and back-filling materials gradually appear with diminishment of the three dimensional supporting effect by further advancement of the shield upon completion of the backfilling. At this stage, the soft cohesive soil begins to consolidate as its soil structure collapses, whereas the creep deformation is appeared in cohesionless soil.

While the ground movement finally comes to an end after the above processes, the earth pressure acting on the shield or tunnel lining largely depends on the degree of the ground deformation.

Figure 1.4 shows the relationship between the affecting factors and causes of the ground movement (Makata 1980). JGS (1996) proposed the typical shape of the ground displacement caused by the shield tunneling which takes into account the type of ground for longitudinal and transverse directions as shown in Figures 1.5 and 1.6 respectively and for three-dimensional ground movements as shown in Figures 1.7 and 1.8 for clayey soil and sandy soil respectively.

Table 1.3 shows proportion of the settlement, which was explained in Figure 1.3 and Table 1.2, for the two types of soils, alluvial cohesive and alluvial sandy soils. For both types of soils, proportion of the settlement caused by the tail void is fairly large. In case of the cohesive soil, the following settlement is as much as 45%–50% of the total settlement. In contrast, in case of the sandy soil, proportion of the following settlement is quite smaller than the settlement during passing of the shield, and the settlement caused by the tail void is predominant factor of the settlement (Makata 1981; Yamada et al. 1988).

### **1.2.2 Shield Tunneling Control**

Closed-type shield tunneling methods have been recently developed together with the computer aided automatic control systems, the tunneling operations, and the new grouting techniques for the tail void to minimize the ground surface settlement (Kurihara 1998). Control systems are used for the face stabilization, computation amount of the excavated soil volume, the

backfilling, the tail sealed control, and the shield directional control. The above control systems are developed based on empirical formulae and engineering practices. Shield tunneling control systems, which utilize the computer technology, are described as follows.

### 1.2.2.1 Face Stabilization

The general custom of the face stability is to divide the ground into cohesive and cohesionless soil types. In cohesive soil, cohesion leads to a low permeability, therefore, the pressure of water and soil is calculated together, which is known as *total stress analysis*. The total initial earth pressure in the horizontal direction,  $\sigma_{ho}$ , is calculated by the total initial earth pressure in the vertical direction,  $\sigma_{vo}$ , multiplied by the total earth pressure coefficient,  $K_T$ , and can be written as

$$\sigma_{ho} = K_T \sigma_{vo} \quad (1.1)$$

For cohesionless soil, the pressures of soil and water are calculated separately, which is known as *effective stress analysis*. Therefore, the effective initial earth pressure in the horizontal direction,  $\sigma'_{ho}$ , is calculated by the effective initial earth pressure in the vertical direction,  $\sigma'_{vo}$ , multiplied by the coefficient of earth pressure at rest,  $K_o$ , as

$$\sigma'_{ho} = K_o \sigma'_{vo} \quad (1.2)$$

where

$$\sigma'_{vo} = \sigma_{vo} - P_w \quad (1.3)$$

and  $P_w$  is the water pressure.

The face stabilization mechanism of the closed-type shield tunneling methods depend on the pressurized material in the chamber, the pressurizing technique, and the soil discharging method

in accordance with either EPB or slurry shield tunneling works. JSSMFE (1993) explained the face stabilization mechanism of the EPB shield as follows:

- (1) The plastic fluid soil excavated out by the cutters is filled into the chamber to support the face;
- (2) The soil discharging rate is controlled by speed of the screw conveyor and the soil discharge adjustment apparatus to encounter a balance of the generating counter-pressure by the soil inside the chamber against both the earth pressure and the water pressure at the face;
- (3) The excavated soil, which is filled and compacted inside the chamber and the screw conveyor, is expected to prevent the water seepage.

In contrast, the face stabilization mechanism of the slurry shield can be described as follows:

- (1) The pressurized slurry counteracts against the earth and water pressures at the face to stabilize the face;
- (2) A hardly permeable slurry layer is created at the face for the effective utilization of slurry pressure;
- (3) The slurry penetrates into the ground to a certain depth through the face to give the cohesion around the face.

Face stability in case of the closed-type shield tunneling method is ensured through the interaction as described above. Under such circumstances as the shield stops, the cutter face temporarily sustains face stability. The face pressure to prevent the collapse and to maintain the face stability is the mud pressure in case of the EPB shield tunneling method and the slurry pressure in case of the slurry shield tunneling method. The methods to determine the level of pressure and to maintain the setting pressure level is crucial factor in the face stability. The face pressure is generally expressed by the equation:

$$\text{Face Pressure} = \text{Ground Pressure} + \text{Reserve Pressure} \quad (1.4)$$

and can be illustrated in Figure 1.9.

For the practical application of Eq. (1.4), the water pressure is treated as part of the earth pressure to calculate the ground pressure in case of the impermeable ground. The water and the earth pressures are calculated separately in case of the permeable ground. This indicates that the earth pressure and the water pressure at the face are increasingly mutually independent from the mechanical behavior, but they depend on permeability of the ground to be excavated; therefore, the excavation should be necessary handled carefully.

The ground pressure will be discussed in terms of the water pressure and the earth pressure. The water pressure is part of the ground pressure, and is particularly observed in case of the permeable ground, such as sandy soil. In general, the actual value of the water pressure can be determined with a fairly accurate extent by a preliminary soil survey or other investigations. Nevertheless, a careful attention should be paid to possible existence of the confined water or substantial seasonal fluctuations of the groundwater level, which depends on the topographical and geological conditions. For the earth pressure, it is currently unclear in principle to evaluate it at the face for the closed-type shield tunneling work. Application of earth pressure in the shield tunneling work is usually assumed that the earth pressure becomes active when the ground deforms toward the front of the face by using the state of earth pressure at rest as the reference level, and it becomes passive when the ground is compressed at the face as shown in Figure 1.10 (Sugimoto et al. 1992). Kanayasu et al. (1995) proposed the supported pressure,  $P_s$ , as shown in the equation

$$P_s = \sigma'_a + P_w + 10 \sim 20 \quad (\text{kN/m}^2) \quad (1.5)$$

where  $\sigma'_a$  is the effective active earth pressure.

The pressure released by cutting at the face is usually considered to be equivalent to the earth pressure at rest. For closed-type shield tunneling, use of the static earth pressure as the face pressure is theoretically optimum from the viewpoint of minimizing the face deformation and maintaining the face stability. Unfortunately, however, it is generally difficult to determine the coefficient of earth pressure at rest.

One aspect is that the face stability can be maintained as long as the face deformation remained within the elastic range. The active earth pressure is sometimes employed as the face pressure. Since the face deformation is accepted in theory, the careful control of the ground deformation accompanying the progress of shield tunneling work is necessary. In most cases, the active earth pressure is used as the lowest permissible level of the face pressure and often employed as such in the closed-type shield tunneling work for alluvial soft cohesive soil. The rational way in actual tunneling to determine the optimal earth pressure at the face is to establish a trial section at the commencement of excavation to measure the surface and subterranean deformations due to the excavation. Degree of the face stabilization effected by the face pressure in the closed-type shield tunneling is determined by the soil properties filled in the chamber in case of the EPB shield tunneling method and the pressurized slurry properties in case of the slurry shield tunneling method.

As mentioned above, in case of the closed type shield, the tunnel face is stabilized by pressurizing the slurry or the excavated soil in the chamber in order to resist the water pressure and the earth pressure on the excavated surface. For this purpose, control of the supported pressure in the chamber is the most important. This control is done by the pressure indicator regulators installed inside the chamber for both slurry and EPB shields. An example of the face stabilized control system for slurry shield is illustrated in Figure 1.11.

### 1.2.2.2 Muck Volume

For a perfect pressure balanced at the face, the volume of discharged soil is equal to the soil volume occupied by the shield as its advancement. Therefore, the shield is controlled to satisfy the excavated volume ratio,  $R_v$ , as

$$R_v = \frac{V_E}{A_{CF}v_s} = 1 \quad (1.6)$$

where  $V_E$  is the removal of excavated soil volume per unit time,  $A_{CF}$  is the cross section area of cutter face, and  $v_s$  is the excavation speed.

Control of this operation is crucial for proper performance of the shield. If the excavated soil is discharged excessively, the void can be developed in the chamber, leading to possible running or flowing soil conditions into the chamber. The status of the soil volume in the chamber is empirically correlated with the readings of the earth pressure cell installed inside the bulkhead. The removed soil volume is basically slightly lower than that of the excavated soil volume (i.e.,  $R_v \approx 0.98\sim 0.99$ ). This practice is designed initially to heave the soil outward from the shield to some degrees and to compensate for the subsequent inward movements caused by the tail void closure.

Since the face cannot be directly observed in the closed type shield, it is necessary to measure the excavated soil volume accurately. In the slurry shield, the excavated soil volume is calculated and controlled by measured value of the flow meter and the densitometer. This control is employed while the excavated soil is extruded out in case of the EPB shield. Figure 1.11 also shows the excavated soil volume control system for slurry shield.

### 1.2.2.3 Back filling

Generally, the backfilling materials of the shield is poured at the same time while the shield is excavating the ground because this enables to control the setting time of the grouting material.

The backfilling pressure is usually adjusted within the initial earth pressure at the crown, which should be the net pressure after the pressure loss from the pump to spew out had already been deducted. Amount of the grouting is controlled based on the concept that the large expansion caused by the grouting does not appear (Kishio et al. 1995).

The backfilling pressure and the shield jack speed are registered in the backfilling control system, and afterward pressure and volume of the backfilling are controlled automatically. An example of the automatic backfilling control system is illustrated in Figure 1.12.

#### **1.2.2.4 Tail Seal**

Tail skin seal is an important component of the shields. Since it is used to protect the rear end of the shield from the groundwater, the surrounding ground, the supported fluid, and the grouting material.

In comparison between the wire brush (developed in Japan) and the rubber (developed in Germany) seals, the advantage of wire brush seal is that the water and the ground do not infiltrate into the annular gap in case of the decrease of backfilling pressure because the pressurized grease will enter the annular gap (Mair et al. 1995). Special attention has to be paid to the environmental acceptability of the grease used, and bedding of the segment rings is impaired by infiltration of the grease. The wire brush seal is more advantageous in case of the crossing joints since the gaps of the joints can be reliably sealed by means of this type of seal.

The wire brush seal is firmly mounted on the inside tail skin. For safety purposes, up to five rows are installed. Grease is injected into the chambers between individual rows of the wire brushes and maintains at a certain pressure (i.e., two bars above the grouting pressure) (Mair et al. 1995). The grease pressure is increasingly applied to prevent the water, the ground, or the grouting infiltration from the sealing area (see Figure 1.13).

### 1.2.2.5 Shield Direction

For detecting the position and the rotation of shield, automatic survey systems are employed to observe in real time during construction. Automatic survey systems consist of a gyrocompass, an inclinometer, a water level, a jack stroke counter, and a total station. The direction of shield is controlled automatically by manipulating the shield jacks according to the shield position attained from the above systems. Figure 1.14 illustrates an example of automatic shield directional control system.

## 1.2.3 Horizontal and Vertical Variation Shield Method

### 1.2.3.1 Concept

Due to limited underground space in urban area and for saving construction cost, multi circular face shield (MF shield) (STA 2011a) had been innovated to construct a twin tunnel at once. Furthermore, according to the more severe restriction of underground space use, horizontal and vertical variation shield method (H&V shield) (Sonoda et al. 1992; STA 2011b) was innovated so that the cross section of an MF shield tunnel is changed from horizontal multi-circular shape to vertical one, or vice versa. The H&V shield is manufactured by connecting two articulated shields (Maidl et al. 2012) at their rear bodies and is steered by articulation mechanism and copy cutter, which can be operated individually at each body. These steering options can generate rotating force around the shield axis, which can realize the construction of a spiral tunnel. As an example, the H&V shield for a railway station is shown in Figure 1.15.

### 1.2.3.2 Characteristics

The characteristics of H&V shield method, compared with other type shields, are as follows:

*Tunnel shape and alignment.* H&V shield can construct a separate tunnel and a spiral tunnel as shown in Figure 1.16. In the case of a separate tunnel, H&V shield constructs a tunnel with a multi-circular cross section at first, and two ordinary tunnels with a circular cross section after a specified point along the tunnel alignment by separating the H&V shield to two ordinary shields.

On the other hand, in the case of a spiral tunnel, H&V shield constructs a tunnel with a multi-circular cross section, which is changed continuously from horizontal multi-circular shape to vertical one, or vice versa;

*Construction period.* H&V shield can shorten a construction period because it can omit an intermediate vertical shaft to separate the body in the case of a separate tunnel and can construct a multiple tunnel at once in the case of a spiral tunnel;

*Construction cost.* H&V shield can save construction cost because its body can be separated without an intermediate vertical shaft and a ground-improving work in the case of a separate tunnel and can reduce the adjacent distance between two circular tunnels in the case of a spiral tunnel.

### **1.2.3.3 Mechanism of Tunnel Driving**

Shield is operated for excavation, steering shield, filling up in the tail void, and segment installation mainly. As for steering shield, the shield is controlled by jack, copy cutter, and articulation mechanism in practice. The jack generates thrust and horizontal and vertical moments, which can be determined by jack pattern and shield jack pressure. The copy cutter can carry out overcutting with a specified depth and a specified range along the circumference of cutter face. The overcutting by copy cutter defines excavation area and reduces ground reaction force at the overcutting range, which makes the shield rotate toward the overcutting range easily. The articulation mechanism of articulated shield can crease shield with a specified direction and a specified angle. The crease of the shield can reduce ground reaction force at curves by fitting the shield for its excavation area, which makes the shield rotate easily.

The H&V shield for a spiral tunnel can be controlled by spiral jacks, copy cutter, and articulation system. The shield jack system including spiral jacks, as shown in Figure 1.17, causes the eccentric forces to generate torque to twist an H&V shield around its axis. The copy cutter can reduce the ground reaction force at a specified area by overcutting the ground, and the

articulation system can also reduce the ground reaction force by articulating the front body from the rear body of each shield, as shown in Figure 1.18. Using these functions, the H&V shield can rotate around its axis and can advance. Thus, the H&V shield can construct a spiral tunnel.

### **1.3 Literature Review**

#### **1.3.1 Shield behavior**

Shield behavior has been studied by both statistical and theoretical methods. The former is used to predict and control the shield behavior (the deviation and rotation of the shield) by statistically obtaining the unascertained parameters on the correlation between the change of shield attitude and the jack moment, whereas the theoretical method is able to predict and control the shield behavior based on the equilibrium conditions of force and moment acting on the shield. Since the empirical method controls a shield so as to move it back to the planned alignment, it is difficult to control the shield in complicated geological formations. Therefore, to reduce shield's snake-like motions a theoretical approach is necessary.

The direction control systems of shield machine based on empirical relationships were developed. These systems cannot take into account the excavation area around the shield, which is considered to be the predominant factor affecting the shield behavior.

Sakai et al. (1987, 1993) applied the Kalman filtering theory to recursively predict and control shield tunneling behavior. In their study, horizontal and vertical movement of shield machine were treated as time series records in autoregressive equations. Linear regression equations were utilized between the rate of direction change and biased moment. Parameters in these equations were sequentially identified in state equations of the Kalman filter. As the results of correlation analysis between the identified parameters and ground conditions, the shield behavior has been certified to be highly related to the stiffness, such as  $N$ -value and elastic modulus of ground characters.

Kuwahara et al. (1988) designed a fuzzy controller for pressure regulation of the shield chamber and direction control of the shield machine. This controller is based on a few control rules founded on the know-how which skilled operators have obtained through their experiences. The root mean square of the operation deviation between the skilled operators and the fuzzy controller is defined as the performance index. The optimum controller can be obtained when the performance index is minimized.

Shimizu and Suzuki (1992) proposed the mechanisms of shield movement as the process of the angle change and the forward movement, which is shown in Figure 1.1. A model experiment was conducted to develop a mathematical model of shield movement in soil. In this model, the characteristics of the movement were expressed as two state equations. One is the linear function of rotation moment and the tilt angle change of the shield machine; the other is the linear function of the tilt angle and position deviation of the shield machine. Based on these two state equations, the one-input-two-outputs state feedback control system was designed using the pole assignment method. After that, fitting analysis from operation data at real construction projects (Shimizu and Furukawa et al. 1992), simplified estimate (Shimizu et al. 1996) and FEM analysis (Shimizu et al. 1997) were conducted to estimate the coefficients in the proposed model.

On the other hands, the theoretical approaches were carried as follows

Szechy (1966) did the first attempt at a theoretical approach to study the loads acting on shield and presented the approximate formulae to calculate the jacking thrust,

MHI (1988) proposed the method to estimate the equipped capacities of the shield, which are the jack thrust and the cutter torque,

Sugimoto et al. (1991) proposed the theoretical approach for the acting loads on the shield. They indicated that it was necessary to consider the ground displacement due to the shield tunneling behavior in order to satisfy the equilibrium conditions, since the jack moment could not be explained by using this model.

Yoshida and Yamada (1992) simplified the model proposed by Sugimoto et al. (1991) to obtain the ground properties. In this model, only the axial force was considered, which composed of the earth pressure at the cutter face and the frictional resistance between the shield and the surrounding ground. Based on the assumption that the earth pressure acting at the face was equal to the earth pressure at rest, the frictional coefficient between the shield skin plate and the ground was obtained by reverse analysis, based on in-situ data during excavation.

Sugimoto and Tamamura (1992) developed a model of the loads acting on the shield in which the shield tunneling behavior and the ground displacement around the shield periphery are taken into consideration. They investigated the validity of the model by using in-situ data. This study showed that the consideration of the ground displacement was necessary to satisfy the equilibrium conditions. They also pointed out that the ground properties could be obtained by the reverse analysis, based on measured data.

Sugimoto and Luong (1996) modified the above model with applied  $f_4$  as the function of the shield velocity and the rotating speed of the cutter face.

The detail of the kinematic shield model is shown in “ 1.4 Simulation method of shield behavior”.

### **1.3.2 Ground movement**

The ground movements induced by shield tunneling and its effect on structures are always a great concern for tunnel engineering, and are caused by ground stress turbulence due to several factors such as the face stability, the lowering of the groundwater level and the release of stress at the face. The face stability during excavation gets influence from the shear strength of ground, the stress-strain characteristics of the ground, the overcharge pressure, the face pressure, and the construction procedures. Mair (1987) pointed out that the face pressure should be as close to the overburden pressure as possible to minimize the ground movements. Paying attention to the

position of the shield and its rotation during excavation is essential to predict the ground movement. With this, the real time observation and the actual construction procedures are taken into consideration.

Making a tunnel inexorably causes ground movements, which induce local deflections and introduce additional stresses within the existing underground and in the surface structures. The excessive stresses and the deflections may lead to the failure of the structures or the leakage of fluids from buried ducts, such as gas and water. The problem of ground behavior due to tunneling is one of the typical soil-structure interaction problems. Consequently, the size, the depth, and the materials of structures are important for the design consideration.

Two design approaches are commonly adopted:

- (1) Empirical method;
- (2) Numerical methods.

As for the empirical method, Peck (1969) contributed a concept related with the settlement trough in the ground surface due to the construction of a tunnel by conventional mining method, employing the hand mining or the open type shield with or without air pressure. Fujita (1982) proposed the prediction of maximum ground surface settlement caused by shield tunneling method taking account of the types of shield and the soil types.

In the numerical methods, we can find the finite element method (FEM), the boundary element method (BEM), etc. Among them, FEM simulation has become increasingly accepted for simulating very complex construction sequences. Kawamoto et al. (1972) proposed the analytical method where the settlement caused by loosening was added to the elastic settlement based on the FE analysis to achieve the better correspondence between the actual measurement and the theoretical settlement. They also explained that the correspondence could be improved by taking the nonlinear characteristics of the ground into consideration. Yamada et al. (1979) suggested a model, shown in Figure 1.19, to explain the release of stress by taking the tail void's

size and the segment rigidity into consideration. This model constrained the ground displacement to the size of the tail void in FE analysis of an unsupported tunnel. The final displacement was achieved as the sum of the above ground displacement and the displacement due to the segment deformation.

Although the proper finite element modeling has been made, the analysis of shield tunneling construction has some shortcomings because the finite element (FE) analysis cannot take account of the important factors affecting the shield tunneling behavior, such as the initial space between the shield periphery and the surrounding ground, the dynamic condition, the direction of the cutter face rotation, and the loosening earth pressure. In addition, it is almost impossible to simulate the shield behavior in the curve alignment because the FEM cannot generate the mesh for an arbitrary movement of the shield. Furthermore, 3-D FE analysis has a restriction due to the time consuming and the high cost in the analysis of the shield tunneling process.

## **1.4 Simulation Method of Shield Behavior**

### **1.4.1 Kinematic shield model**

To develop the model of the loads acting on the shield during excavation, kinematic loads model is appropriate. By applying the model, the shield behavior can be obtained based on the balance of the forces  $F$  and the moment  $M$  acting on the shield.

Some of the characteristics of shield behavior and the known factors affecting it based on past shield tunneling engineering practices are as follows:

1. The earth pressure acting on the skin plate is assumed to mainly depend on the ground displacement around the shield. This displacement or the gap between the shield and the excavated area is considered to be the predominant factor of the shield behavior since the ground displacement determines the earth pressure acting on the shield.
2. The forces on the shield tail (which is composed of the contact force between the shield and the segment ring, the force due to the deformation of wire brush at the shield tail,

and the grease pressure between the wire brush acting on the shield tail) also affect the shield behavior.

3. When the jack thrust increases, the jack speed and the cutter torque also increases. The shield behavior is in this manner a dynamic problem.
4. The rotation direction of the cutter face (CT) influences the shield behavior, especially the yawning of the shield.
5. At a sharp curve, the shield axis in a horizontal plane does not coincide with the tunnel alignment, and both are independent each other.
6. Over excavation especially in sandy ground causes loosening of the ground around the shield crown and large ground surface settlement. These also cause the release of earth pressure acting on the shield.

By comparing the calculated shield behaviors with the observed one, the model was validated, and are inspected by the sensitivity analyses of the model parameters to confirm the performance of the model.

The jack thrust mentioned in the third point is the summation of the resistant force against the movement of the shield in the shield axis direction. The cutter torque is the summation of the resistant torque against the rotation of the cutter face, which rotates around the shield axis.

#### **1.4.2 Simulation method of single circular shield**

The model of the loads acting on the shield were developed, taking into account shield tunnel engineering practices (i.e., the excavated area, the tail clearance, the rotation direction of the cutter disc, sliding of the shield, ground loosening at the shield crown, and the dynamic equilibrium condition) (Sugimoto et al. 2002). The model is composed of five forces: force due to self-weight of machine  $f_1$ , force on the shield tail  $f_2$ , force due to jack thrust  $f_3$ , force on the cutter disc  $f_4$ , and force on the shield periphery  $f_5$ , as shown in Figure 1.20. The shield behavior

is represented by the movement of the shield in  $x$ ,  $y$ , and  $z$  directions ( $\Delta x$ ,  $\Delta y$ , and  $\Delta z$ ), and the shield postures (yawing angle  $\phi_y$ , pitching angle  $\phi_p$ , and rolling angle  $\phi_r$ ). Since the change of  $\phi_r$  is limited in practice, the factor of shearing resistance against the cutter torque  $\alpha$  was adopted as the parameter instead of  $\phi_r$ . By applying the model, the shield behavior can be obtained based on balance of the forces  $\mathbf{F}$  and the moments  $\mathbf{M}$  acting on the shield.

$$\begin{bmatrix} \sum_{i=1}^5 \mathbf{F}_i \\ \sum_{i=1}^5 \mathbf{M}_i \end{bmatrix} = 0 \quad (1.7)$$

The force on the shield periphery is composed of the ground reaction force and the dynamic frictional force on the shield skin plate, which are due to the earth pressure acting on the shield skin plate. Since earth pressure is relied on the ground deformation and the excavated cross section area is usually a little bit larger than the shield cross section area, the ground reaction force from the ground to the shield can be obtained by considering the coefficient of earth pressure  $K$ , which is given by a function of the distance between the original excavated surface and the shield skin plate  $U_n$ , as shown in Figure 1.21. In Figure 1.21,  $K$  at  $U_n=0$  means the coefficient of earth pressure at rest and the gradient of  $K$  at  $U_n=0$  represents the coefficient of subgrade reaction  $k$ . Here, note that the subscripts  $h$  and  $v$  are the horizontal and vertical directions, respectively; the subscripts  $min$ ,  $o$ , and  $max$  define minimum, initial, and maximum, respectively; and  $\sigma_{vo}$  is the overburden pressure.  $K$  in any direction can be calculated by interpolation between  $K_h$  and  $K_v$ .

The displacement of the excavated surface normal to the shield skin plate  $d_n$  is shown in Figure 1.22, which is defined as follows:

When the shield skin plate is outside the original excavated surface, the earth pressure is in compression state since the shield pushes the ground. Therefore,  $d_n$  is equal to  $U_n$ .

When the shield skin plate is inside the original excavated surface and on the excavated surface after deformation, the earth pressure is in extension state. Since the excavated surface after deformation contacts the shield skin plate,  $d_n$  is the same as  $U_n$ .

When the shield skin plate is inside of the excavated surface after deformation, the original excavated surface moves freely until its deformation stops and there is a gap between the excavated surface and the shield skin plate. In this case, there is no earth pressure acting on the shield skin plate. Thus,  $d_n$  is defined as the distance from the original excavated surface to the excavated surface after deformation. In this case,  $d_n$  is defined as  $U_n$  when  $K_n$  reaches minimum in Figure 1.21. This phenomenon is due to self-stabilization of the ground especially in the case of stiff ground. It should be noted here that the position of the original excavated surface and the shield skin plate can be determined by the observed shield position and rotation or by the simulated shield position and rotation based on the shield tunneling operation. Considering the displacement of the excavated surface is similar to a contact problem in FEM.

### 1.4.3 Simulation Method of Articulated Shield

Applying the kinematic shield model for single circular shield (Sugimoto et al. 2002) to the front and rear sections of articulated shield individually, the articulated shield model has been developed (Komuro et al. 2003). The model is composed of five forces: force due to self-weight of machine  $f_1$ , force on shield tail  $f_2$ , force due to jack thrust  $f_3$ , force on cutter disc  $f_4$ , and force on shield periphery  $f_5$ , as shown in Figure 1.23. The force due to self-weight of machine  $f_1$  and the force on shield periphery  $f_5$  act on the both sections of shield. The force at shield tail  $f_2$  acts only on the rear section, whereas the force at face  $f_4$  is loaded on cutter disc of the front section. The force on jack thrust  $f_3$  is composed of the forces due to shield jack and articulated jack.

The shield behavior during excavation can be obtained by solving the equilibrium conditions of forces and moments acting on the shield as follows:

$$\begin{bmatrix} \sum_{i=1}^5 (\mathbf{F}_{F_i}^M + \mathbf{F}_{R_i}^M) \\ \sum_{i=1}^5 (\mathbf{M}_{F_i}^M + \mathbf{M}_{R_i}^M) \end{bmatrix} = 0 \quad (1.8)$$

where  $\mathbf{F}$  and  $\mathbf{M}$  are the force and moment vectors respectively, the subscripts  $F$  and  $R$  denote the front and rear sections of shield respectively, and the superscript  $M$  indicates the machine coordinate system. It is noted that the force due to articulated jack  $\mathbf{f}_{32}$  is not necessary to calculate since the summation of the force due to  $\mathbf{f}_{32}$  is always zero.

### 1.5 Objective of This Study

The purpose of this study is to develop the method to control and simulate the H&V shield. Then the following procedures are taken:

(1) A numerical method is developed to determine copy cutter length and articulation angles for horizontal and vertical variation shield method (H&V shield). It considers the rolling angles  $\phi_r$  in the spiral condition of shield.

(2) Sensitive analyses are carried out to examine the influence of the shield machine operation on H&V shield behavior and the above-proposed method in steering the H&V shield is validated from the viewpoint of the theory.

(3) Applying the developed model to an actual site, the steering method of the H&V shield is discussed to realize a spiral twin tunnel.

## CHAPTER 2: METHODOLOGY

### 2.1 Calculation Method Of Steering Parameters

For excavation of a tunnel with sharp curves, the articulated shield machine is adopted usually. To ensure reliable construction, the attitude of articulated shield machine should be controlled precisely. However, many parameters, such as ground conditions, jack forces and moments, articulation angle, copy cutter length and range, etc., will affect actual shield attitude. Since these parameters have collinearity, multiple solutions exist. To overcome the above problems, some conditions to determine the articulation angle and copy cutter length and range are set from the view of geometrical relations. At present, some shield manufacturers developed their own procedures to determine the articulation angle and copy cutter length and range on 2-D plane.

In this section, a numerical method to determine articulation angle and copy cutter length on 3-D compound alignments was proposed based on geometrical relations of tunnel alignment and shield dimension. The total flowchart is shown in Figure 2.1.

#### 2.1.1 Calculation conditions

The numerical method is based on the following conditions:

1. The center point of erector plane  $P_{CSE}$  follows the planed tunnel alignment;
2. The axis direction of rear body  $r_2$  is the tangential direction of the planed tunnel alignment at  $P_{CSE}$ ;
3. According to the different dimensions of the front body and the rear body, articulation angle is determined so that overcutting space by cutter face and copy cutter on opposite major normal direction of curve are minimized. This means that the (1) cutter face touches the trace of rear body on opposite major normal direction of curve, or (2) front body touches the trace of rear body on major normal direction of curve;

4. Copy cutter length and range are determined so that shield bodies do not push the ground (i.e., shield bodies exist inside the excavated space).

## 2.1.2 Coordinate System

### 2.1.2.1 Definition

The coordinate systems :  $C^T$ ,  $C^{T'}$ ,  $C^{M1}$ ,  $C^{M2}$ ,  $C^{MR1}$ ,  $C^{MR2}$  are shown in Figure

2.2, which are defined as following:

$C^T$  :  $x, y, z$ , the global reference coordinate system. The direction of  $x$  axis is vertical downward.

$C^{T'}$  :  $x', y', z'$ , the local reference coordinate system, of which the origin is set at origin of curve and  $z'$ -axis follows the axial direction of straight line;

$C^{M1}$  :  $p_1, q_1, r_1$ , attached to the front body of shield, of which the origin is located at the crease center. The direction of  $p$  axis is vertical downward without rotation of shield and the direction of  $r$  axis is the shield axis direction to cutter face.

$C^{M2}$  :  $p_2, q_2, r_2$ , attached to the rear body of shield, of which the origin is located at the crease center. The direction of  $p$  axis is vertical downward without rotation of shield and the direction of  $r$  axis is the shield axis direction to cutter face.

$C^{MR1}$  :  $p_{R1}, q_{R1}, r_{R1}$ , rotate  $C^{M1}$  by rotation angle  $\theta_z$  around  $r$ -axis

$C^{MR2}$  :  $p_{R2}, q_{R2}, r_{R2}$ , rotate  $C^{M2}$  by rotation angle  $\theta_z$  around  $r$ -axis

### 2.1.2.2 Coordinate Transformation

$C^T - C^{T'}$  :

$$\mathbf{r}^{T'} = \mathbf{T}_x(\theta_0)(\mathbf{r}^T - \mathbf{r}_{OR}^T) \quad (2.1)$$

$C^T - C^{M1}$  :

$$\mathbf{r}^{M1} = \mathbf{T}_z(\theta_{z1})\mathbf{T}_y(\theta_{y1})\mathbf{T}_x(\theta_{x1})(\mathbf{r}^T - \mathbf{r}_O^T) = \mathbf{T}_1(\mathbf{r}^T - \mathbf{r}_O^T) \quad (2.2)$$

$$C^T - C^{M2} :$$

$$\mathbf{r}^{M2} = \mathbf{T}_z(\theta_{z2})\mathbf{T}_y(\theta_{y2})\mathbf{T}_x(\theta_{x2})(\mathbf{r}^T - \mathbf{r}_O^T) = \mathbf{T}_2(\mathbf{r}^T - \mathbf{r}_O^T) \quad (2.3)$$

$$C^{M1} - C^{MR1} :$$

$$\mathbf{r}^{MR1} = \mathbf{T}_z(\theta_z)\mathbf{r}^{M1} = \mathbf{T}_z(\theta_z)\mathbf{T}_1(\mathbf{r}^T - \mathbf{r}_O^T) = \mathbf{T}_{n1}(\mathbf{r}^T - \mathbf{r}_O^T) \quad (2.4)$$

$$C^{M2} - C^{MR2} :$$

$$\mathbf{r}^{MR2} = \mathbf{T}_z(\theta_z)\mathbf{r}^{M2} = \mathbf{T}_z(\theta_z)\mathbf{T}_2(\mathbf{r}^T - \mathbf{r}_O^T) = \mathbf{T}_{n2}(\mathbf{r}^T - \mathbf{r}_O^T) \quad (2.5)$$

in which,

$\theta_0$ : Direction angle of  $z'$ - axis.

$\theta_x$ : Rotation angle around  $x$ - axis.

$\theta_y$ : Rotation angle around  $y$ - axis.

$\theta_z$ : Rotation angle around  $z$ - axis (here =0), as shown in Figure 2.2.

$\mathbf{r}_{QR}$ : Origin of curve.

$\mathbf{r}_O$ : Origin of  $C^{M1}$ ,  $C^{M2}$ , which is at crease center  $\mathbf{r}_C$ .

$\mathbf{T}_x$ : Transformation matrix around  $x$ - axis.

$\mathbf{T}_y$ : Transformation matrix around  $y$ - axis.

$\mathbf{T}_z$ : Transformation matrix around  $z$ - axis. (Refer to Appendix C)

## 2.1.3 Tunnel Alignment Description

### 2.1.3.1 Spatial Curve

A 3-D tunnel alignment is treated as a spatial curve in a Euclidean space, which can be represented by the locus of the end point of the position vector given by

$$\mathbf{r}(t) = x(t)\mathbf{i} + y(t)\mathbf{j} + z(t)\mathbf{k} \quad (2.6)$$

where  $t$  is a parameter ranging over a set of values  $t_0 \leq t \leq t_1$ .  $x(t)$ ,  $y(t)$ , and  $z(t)$  are assumed that they have continuous derivatives of all orders and can be expanded in a Taylor series in the neighborhood of any point of the curve.

The unit tangent vector to the curve  $\mathbf{t}$  is defined as  $\mathbf{t} = \frac{d\mathbf{r}}{ds}$ . Moreover, the derivative  $\frac{d\mathbf{t}}{ds}$  is perpendicular to  $\mathbf{t}$ , and  $\left| \frac{d\mathbf{t}}{ds} \right|$  represents how fast the unit tangent vector  $\mathbf{t}$  is changing direction as the position vector  $\mathbf{r}$  moves along the curve. The principal normal vector to the curve is consequently defined by the equation

$$\frac{d\mathbf{t}}{ds} = \kappa \mathbf{n} \quad (2.7)$$

where  $\kappa$  is the length of  $\frac{d\mathbf{t}}{ds}$  and is called the curvature.  $\rho = \frac{1}{\kappa}$  is called the radius of curvature. It is important to note that (2.7) defines both  $\kappa$  and  $\mathbf{n}$ , where  $\mathbf{n}$  is the unit vector parallel to  $\frac{d\mathbf{t}}{ds}$ , which is called the unit principal normal vector. At any point  $P$  of a spatial curve, there are two vectors  $\mathbf{t}$  and  $\mathbf{n}$ . A local right hand coordinate system at the point  $P$  can set up a third vector  $\mathbf{b}$ , which is shown in Figure 2.3. The vector  $\mathbf{b}$  is called as the unit binormal vector, which is defined as  $\mathbf{b} = \mathbf{t} \times \mathbf{n}$ . All vectors associated with the curve at the point  $P$  can be written as a linear combination of the three fundamental vectors  $\mathbf{t}$ ,  $\mathbf{n}$ ,  $\mathbf{b}$ .

Since derivative of  $\mathbf{b}$  is perpendicular to  $\mathbf{b}$  and so lies in the plane of  $\mathbf{t}$  and  $\mathbf{n}$ , the next can be obtained.

$$\frac{d\mathbf{b}}{ds} = \frac{d}{ds}(\mathbf{t} \times \mathbf{n}) = \frac{d\mathbf{t}}{ds} \times \mathbf{n} + \mathbf{t} \times \frac{d\mathbf{n}}{ds} = \kappa \mathbf{n} \times \mathbf{n} + \mathbf{t} \times \frac{d\mathbf{n}}{ds} = \mathbf{t} \times \frac{d\mathbf{n}}{ds} \quad (2.8)$$

Hence  $\frac{d\mathbf{b}}{ds}$  is also perpendicular to  $\mathbf{t}$  so that  $\frac{d\mathbf{b}}{ds}$  must be parallel to  $\mathbf{n}$ . Consequently, set

$\frac{d\mathbf{b}}{ds} = -\tau\mathbf{n}$ , where  $\tau$  by definition is the magnitude of  $\frac{d\mathbf{b}}{ds}$ .  $\tau$  is called the torsion of the

curve.

Finally,  $\frac{d\mathbf{n}}{ds}$  can be obtained, using  $\mathbf{n} = \mathbf{b} \times \mathbf{t}$

$$\frac{d\mathbf{n}}{ds} = \mathbf{b} \times \frac{d\mathbf{t}}{ds} + \frac{d\mathbf{b}}{ds} \times \mathbf{t} = \mathbf{b} \times \kappa\mathbf{n} - \tau\mathbf{n} \times \mathbf{t} = -\kappa\mathbf{t} + \tau\mathbf{b} \quad (2.9)$$

Then, the Frenet-Serret formulas are derived

$$\begin{aligned} \frac{d\mathbf{t}}{ds} &= \kappa\mathbf{n} \\ \frac{d\mathbf{n}}{ds} &= -\kappa\mathbf{t} + \tau\mathbf{b} \\ \frac{d\mathbf{b}}{ds} &= -\tau\mathbf{n} \end{aligned} \quad (2.10)$$

### 2.1.3.2 Discretization and Interpolation

For numerical analysis, the discretization for the tunnel alignment is carried out on each calculation point of position with a certain interval. The intermediate points are determined by linear interpolation between the discretization points. Each parameter at the discretization points and interpolation points are shown in Table 2.1.

To calculate each parameter, the following procedures were adopted:

1.  $\mathbf{r}_{i(2)}$ ,  $\mathbf{k}_{i(2)}$ ,  $i = \dots, k-2, k-1, k$ , (discretization values) are obtained directly from the planned alignment (refer to Appendix A).

2.  $\mathbf{r}_{i(1)}$ ,  $\mathbf{t}_{i(1)}$ ,  $\mathbf{n}_{i(1)}$ ,  $\mathbf{b}_{i(1)}$ ,  $i = \dots, k-1, k$ , are interpolation values at intermediate points of  $\beta = 1/2$ .

$$\mathbf{r}_{i(1)} = \frac{\mathbf{r}_{i-1(2)} + \mathbf{r}_{i(2)}}{2} \quad (2.11)$$

$$\mathbf{t}_{i(1)} = \frac{\mathbf{k}_{i-1(2)} + \mathbf{k}_{i(2)}}{|\mathbf{k}_{i-1(2)} + \mathbf{k}_{i(2)}|} \quad (2.12)$$

$$\mathbf{n}_{i(1)} = \frac{1}{k} \frac{\mathbf{k}_{i(2)} - \mathbf{k}_{i-1(2)}}{|\mathbf{r}_{i(2)} - \mathbf{r}_{i-1(2)}|} = \frac{|\mathbf{r}_{i(2)} - \mathbf{r}_{i-1(2)}|}{|\mathbf{k}_{i(2)} - \mathbf{k}_{i-1(2)}|} \frac{\mathbf{k}_{i(2)} - \mathbf{k}_{i-1(2)}}{|\mathbf{r}_{i(2)} - \mathbf{r}_{i-1(2)}|} = \frac{\mathbf{k}_{i(2)} - \mathbf{k}_{i-1(2)}}{|\mathbf{k}_{i(2)} - \mathbf{k}_{i-1(2)}|} \quad (2.13)$$

$$\mathbf{b}_{i(1)} = \mathbf{t}_{i(1)} \times \mathbf{n}_{i(1)} = \frac{\mathbf{k}_{i-1(2)} \times \mathbf{k}_{i(2)}}{|\mathbf{k}_{i-1(2)} \times \mathbf{k}_{i(2)}|} \quad (2.14)$$

For any interpolation point at  $\beta$ ,

$$\mathbf{r}_\beta = \mathbf{r}_{i-1(2)} + \beta(\mathbf{r}_{i(2)} - \mathbf{r}_{i-1(2)}) \quad (2.15)$$

$$\mathbf{t}_\beta = \frac{\mathbf{k}_{i-1(2)} + \beta(\mathbf{k}_{i(2)} - \mathbf{k}_{i-1(2)})}{|\mathbf{k}_{i-1(2)} + \beta(\mathbf{k}_{i(2)} - \mathbf{k}_{i-1(2)})|} \quad (2.16)$$

where, 
$$\beta = \frac{\mathbf{r} - \mathbf{r}_{i-1(2)}}{|\mathbf{r}_{i(2)} - \mathbf{r}_{i-1(2)}|} \quad (0 \leq \beta < 1)$$

3. According to  $\mathbf{t}_{i(1)}$ ,  $i = \dots, k-1, k$ , solve  $\theta_{xi(1)}$  and  $\theta_{yi(1)}$ ,  $i = \dots, k-1, k$ ,

$$\begin{aligned} \theta_{xi(1)} &= \arctan \left[ \frac{-(\mathbf{t}_{i(1)})_y}{(\mathbf{t}_{i(1)})_z} \right] \\ \theta_{yi(1)} &= \arcsin \left[ (\mathbf{t}_{i(1)})_x \right] \end{aligned} \quad (2.17)$$

where,

$\theta_x$ : Yawing angle ( $0 \leq \theta_x < 2\pi$ )

$\theta_y$ : Pitching angle ( $|\theta_y| < \frac{\pi}{2}$ )

Substituting the obtained  $\mathbf{n}_{i(1)}$  to the Eqs.(2.2), then  $\mathbf{n}_i^M = \mathbf{T}_y^{-1}(\theta_y) \mathbf{T}_x^{-1}(\theta_x) \mathbf{n}_i^T$ , and

$\mathbf{p}_i^M = [1 \ 0 \ 0]^T$ ,  $\theta_{zi(1)}$  can be obtained as:

$$\theta_{zi(1)} = \arctan \left( \frac{(\mathbf{p}_i^M \times \mathbf{n}_{i(1)}^M)_r}{\mathbf{p}_i^M \cdot \mathbf{n}_{i(1)}^M} \right) \quad (2.18)$$

To ensure the continuity of  $\theta_{zi}$  at any point, the following interpolation equation is used:

$$\theta_{z_R} = \theta_{z_R^{k-1}(1)} + \alpha(\theta_{z_R^k(1)} - \theta_{z_R^{k-1}(1)}) \quad (2.19)$$

where,

$\theta_{z_R}$ : Rotation angle from  $p$ -axis to  $\mathbf{n}$  ( $0 \leq \theta_z < 2\pi$ )

$\theta_{z_R^{k-1}(1)}$ :  $\theta_z$  at  $\frac{1}{2}(\mathbf{r}_{k-1(2)} + \mathbf{r}_{k-2(2)})$

$\theta_{z_R^k(1)}$ :  $\theta_z$  at  $\frac{1}{2}(\mathbf{r}_{k(2)} + \mathbf{r}_{k-1(2)})$

$$\alpha = \frac{\left| \mathbf{r} - \frac{1}{2}(\mathbf{r}_{k-1(2)} + \mathbf{r}_{k-2(2)}) \right|}{\left| \frac{1}{2}(\mathbf{r}_{k(2)} + \mathbf{r}_{k-1(2)}) - \frac{1}{2}(\mathbf{r}_{k-1(2)} + \mathbf{r}_{k-2(2)}) \right|} = \frac{\left| \mathbf{r} - \frac{1}{2}(\mathbf{r}_{k-1(2)} + \mathbf{r}_{k-2(2)}) \right|}{\frac{1}{2} \left| \mathbf{r}_{k(2)} - \mathbf{r}_{k-2(2)} \right|}, \quad (0 \leq \alpha < 1)$$

And  $\theta_x, \theta_y$  at any point can be written

$$\theta_x = \arctan \left( \frac{-(\mathbf{t}_\beta)_y}{(\mathbf{t}_\beta)_z} \right)$$

$$\theta_y = \arcsin \left( (\mathbf{t}_\beta)_x \right)$$

Then, the unit principal normal vector  $\mathbf{n}^T$  and the unit bi-normal vector  $\mathbf{b}^T$  at any point can be expressed as

$$\mathbf{n}^T = \mathbf{T}_x^{-1}(\theta_x) \mathbf{T}_y^{-1}(\theta_y) \mathbf{T}_z^{-1}(\theta_{z_R}) \mathbf{p}^{MR} = \mathbf{T}_n^{-1} \mathbf{p}^{MR} \quad (2.20)$$

$$\mathbf{b}^T = \mathbf{T}_n^{-1} \mathbf{q}^{MR} = \mathbf{t}^T \times \mathbf{n}^T \quad (2.21)$$

where  $\mathbf{p}^{MR} = [1 \ 0 \ 0]^T$ ,  $\mathbf{q}^{MR} = [0 \ 1 \ 0]^T$

#### 2.1.4 Articulation Angle

The articulation angle in horizontal direction  $\theta_{CH}$  and the articulation angle in vertical direction  $\theta_{CV}$  are defined as the rotation angle of the  $r$ -axis from front body to rear body around

$p$ -axis and  $q$ -axis in Figure 2.4 respectively. To calculate transformation matrix, the rotation angle  $\theta_r$  around  $r$ -axis and the articulation angle  $\theta_q$  around  $q$ -axis are considered.

Here we add two intermediate coordinate systems  $C^{W1}$  and  $C^{W2}$  to connect the coordinate system  $C^{M1}$  and  $C^{M2}$ , which attached to the front body and rear body of articulated shield respectively. The transformation relation is:

$$\begin{aligned}
 C^{M1} &\xrightarrow{\theta_r} C^{W1} \xrightarrow{\theta_q} C^{W2} \xrightarrow{-\theta_r} C^{M2} \\
 C^{M1} - C^{W1} &\quad \mathbf{r}^{W1} = \mathbf{T}_z(\theta_r)(\mathbf{r}^{M1} - \mathbf{r}_O^{M1}) \\
 C^{W1} - C^{W2} &\quad \mathbf{r}^{W2} = \mathbf{T}_y(\theta_q)\mathbf{r}^{W1} \\
 C^{W2} - C^{M2} &\quad \mathbf{r}^{M2} - \mathbf{r}_O^{M2} = \mathbf{T}_z^{-1}(\theta_r)\mathbf{r}^{W2}
 \end{aligned} \tag{2.22}$$

Then,

$$\begin{aligned}
 \mathbf{r}^{M2} - \mathbf{r}_O^{M2} &= \mathbf{T}_z(-\theta_r)\mathbf{T}_y(\theta_q)\mathbf{T}_z(\theta_r)(\mathbf{r}^{M1} - \mathbf{r}_O^{M1}) \\
 &= \mathbf{T}_C(\mathbf{r}^{M1} - \mathbf{r}_O^{M1})
 \end{aligned} \tag{2.23}$$

where  $\mathbf{r}_O^{M1}$ ,  $\mathbf{r}_O^{M2}$  are origins of  $C^{M1}$  and  $C^{M2}$ . Actually they are the same point, which named the crease center. Eq. (2.22) includes the following transformation procedures:

When the  $r$ -axis unit vector for front body and rear body  $\mathbf{e}_{r1}^T$  and  $\mathbf{e}_{r2}^T$  are given,  $\theta_r$  and

$\theta_q$  can be obtained as follows:

1.  $\theta_q$  ( $0 \leq \theta_q < \pi/2$ )

$$\tan \theta_q = \frac{|\mathbf{e}_{r1}^T \times \mathbf{e}_{r2}^T|}{\mathbf{e}_{r1}^T \cdot \mathbf{e}_{r2}^T} \geq 0 \tag{2.24}$$

2.  $\theta_r$  ( $0 \leq \theta_r < 2\pi$ )

Case 1:  $\theta_q = 0$ , straight alignment

$$\theta_r = 0$$

Case 2:  $\theta_q > 0$ , curve alignment

$$\mathbf{b}^{iT} = \frac{\mathbf{e}_{r1}^T \times \mathbf{e}_{r2}^T}{|\mathbf{e}_{r1}^T \times \mathbf{e}_{r2}^T|},$$

$$\mathbf{p}_1^{iT} = \mathbf{b}^{iT} \times \mathbf{e}_{r1}^T,$$

$$\theta_{r1} = \arctan \left( \frac{(\mathbf{e}_{p1}^T \times \mathbf{p}_1^{iT}) \cdot \mathbf{e}_{r1}^T}{\mathbf{e}_{p1}^T \cdot \mathbf{p}_1^{iT}} \right) \quad (2.25)$$

As the same way,  $\mathbf{p}_2^{iT} = \mathbf{b}^{iT} \times \mathbf{e}_{r2}^T$ ,

$$\theta_{r2} = \arctan \left( \frac{(\mathbf{e}_{p2}^T \times \mathbf{p}_2^{iT}) \cdot \mathbf{e}_{r2}^T}{\mathbf{e}_{p2}^T \cdot \mathbf{p}_2^{iT}} \right) \quad (2.26)$$

Here, it can be proved that  $\theta_{r1} = \theta_{r2}$ .

Figure 2.4 shows the relation between articulation angles and direction vectors. When  $\theta_r$  and  $\theta_q$  are determined,  $\theta_{CH}$  and  $\theta_{CV}$  can be obtained as follows.

Case 1:  $\theta_{CH} = \theta_{CV} = 0$

Case 2:

$$0 < |\theta_{CH}| < \frac{\pi}{2},$$

$$\cos \theta_{CH} = \cos \theta_q \sin^2 \theta_r + \cos^2 \theta_r \quad (2.27)$$

$$|\sin \theta_{CH}| = \left( \sin^2 \theta_r (1 - \cos \theta_q) (2 - \sin^2 \theta_r (1 - \cos \theta_q)) \right)^{1/2} \quad (2.28)$$

$$0 < |\theta_{CV}| < \frac{\pi}{2},$$

$$\cos \theta_{CV} = \cos \theta_q \cos^2 \theta_r + \sin^2 \theta_r \quad (2.29)$$

$$|\sin \theta_{CV}| = \left( \cos^2 \theta_r (1 - \cos \theta_q) (2 - \cos^2 \theta_r (1 - \cos \theta_q)) \right)^{\frac{1}{2}} \quad (2.30)$$

where,

$$\begin{aligned} \theta_{CH} &= -\text{sign}(\sin \theta_r) |\theta_{CH}| \\ \theta_{CV} &= \text{sign}(\cos \theta_r) |\theta_{CV}| \end{aligned} \quad (2.31)$$

As shown in Table 2.2

### 2.1.5 Machine Type

As shown in Table 2.3, the machine type is classified as

$$\max(L_1, L_{CSE}, L_2) = \begin{cases} L_1 & \text{Type 1} \\ L_{CSE} & \text{Type 2} \\ L_2 & \text{Type 3} \end{cases}$$

Here as shown in Figure 2.5,

$L_{M1}$ : Length of the front body

$L_{M2}$ : Length of the rear body

$L_{CSE}$ : Length from crease center to erector plane

$$L_1 = L_{M1} - L_{CSE}$$

$$L_2 = L_{M2} - L_{CSE}$$

### 2.1.6 Excavation Stage

For each machine type, four excavation stages are considered, that is

- (1) Excavation stage at straight section;
- (2) Excavation stage around BC section;

- (3) Excavation stage at curve section, and
- (4) excavation stage around EC section.

All of these stages are shown in Figure 2.6 (for machine type 1) and Figure 2.7 (for machine types 2 and 3). On different excavation sections, different operation rules should be considered respectively.

#### **2.1.6.1 Operation Rules at Curve**

Operation rules at curve alignment are based on of the assumptions in section 2.1.1. Table 2.4 shows detailed rules of each type.

#### **2.1.6.2 Operation Rules around BC**

Figure 2.8 shows detailed operation rules (timing at rotation start of front body and rear body) at BC section for all machine types. Operation rules around BC section should ensure shield bodies turn smoothly from a straight line to a curve. Then, the shield should transit some distance to ensure enough space at the inner side of the curve for turning of the front body. Since Type 1 shield has a longer front body, it needs longer transition distance compared with Type 2 and Type 3.

#### **2.1.6.3 Operation Rules around EC**

For machine type 1, just before EC section,  $P_{1I}$  is set to follow the trace of  $P_{2I}$ , which follows the steady contact state at curve alignment. Just after EC section, the contact condition is changed to keep cutter face center  $P_{CF}$  on tunnel center line. This has been shown in Figure 2.9 (a). For machine type 2, the contact condition follows the same condition at curve. This is shown in Figure 2.9 (b). For machine type 3, the contact condition also follows the same condition at curve. It is illustrated in Figure 2.9 (c).

## 2.1.7 Calculation Method for Articulation Angle

### 2.1.7.1 Type 1

The calculation procedure for Type 1 is as follows:

1. Select excavation stage where front body located.
2. Find step number  $k$ .
3. Calculate  $\mathbf{r}_{II}$ ,  $\mathbf{r}_F$ ,  $\mathbf{r}_{CF}$ .
4. Calculate  $\theta_r$ ,  $\theta_q$ ,  $\theta_{CH}$ ,  $\theta_{CV}$ .

Table 2.5 shows judging conditions of Type 1 at different shield positions.

For position 1,

$$\begin{aligned}\theta_r &= \theta_q = 0 \\ \theta_{CH} &= \theta_{CV} = 0\end{aligned}$$

For position 2, the front body at  $P_{II}$  touches the trace of  $P_{2I}$  on  $\mathbf{n}$  vector, as shown in Figure 2.10.

To find step number  $k$  in trace of  $P_{2I}$ , the following conditions should be satisfied:

1.  $P_F$  is located along  $\mathbf{n}$  between  $P_{CSE[k-1]}$  and  $P_{CSE[k]}$
2.  $P_{II}$  is on trace of  $P_{2I}$
3.  $P_C P_F \perp P_F P_{II}$ ,  $P_F P_{OR}$ .

According to the first and second conditions,  $P_F P_{II} = R_M$  can be derived, where  $R_M$  is radius of machine. To find step number  $k$  at curve, the following conditions should be satisfied.

$$([\mathbf{r}_{CSE[k]}^T - \mathbf{r}_C^T] \cdot \mathbf{e}_{r2}^T > 0) \text{ and } (|\mathbf{r}_{CSE[k-1]}^T - \mathbf{r}_C^T| \leq L_{M1}) \quad (2.32)$$

and,

$$[(\mathbf{r}_{CSE[k]}^T - \mathbf{r}_C^T) \cdot \mathbf{n}_{k(2)}^T] \times [(\mathbf{r}_{CSE[k-1]}^T - \mathbf{r}_C^T) \cdot \mathbf{n}_{k-1(2)}^T] \leq 0 \quad (2.33)$$

When step number  $k$  is determined,  $\mathbf{r}_F$  can be calculated by linear interpolation as

$$\mathbf{r}_F^T = \mathbf{r}_{CSE[k-1]}^T + \beta(\mathbf{r}_{CSE[k]}^T - \mathbf{r}_{CSE[k-1]}^T) \quad (0 \leq \beta \leq 1) \quad (2.34)$$

$$\begin{aligned} \theta_x &= \theta_{x[k-1]} + \beta(\theta_{x[k]} - \theta_{x[k-1]}) \\ \theta_y &= \theta_{y[k-1]} + \beta(\theta_{y[k]} - \theta_{y[k-1]}) \\ \theta_z &= \theta_{z[k-1]} + \beta(\theta_{z[k]} - \theta_{z[k-1]}) \\ \mathbf{n}_F^T &= \mathbf{T}_n \mathbf{e}_p^{MR} \end{aligned} \quad (2.35)$$

$\beta$  in Eqs. (2.34) and (2.35) can be solved from

$$(\mathbf{r}_F^T - \mathbf{r}_C^T) \mathbf{n}_F^T = 0 \quad (2.36)$$

Finally  $\mathbf{r}_{lf}^T$  can be determined by

$$\mathbf{r}_{lf}^T = \mathbf{r}_F^T + R_M \mathbf{n}_F^T$$

If step number  $k$  cannot be found by conditions 2.32 and 2.33, it belongs to position 3 in Table 2.5.

For position 3, the front body has passed over EC and the rear body is keeps in curve. Using the last step number  $k$ , the following conditions should be satisfied:

1.  $P_{CF}$  is on  $P_{CSE[k-1]}P_{CSE[k]}$ ;
2.  $P_{CF}P_C = LMl$ .

Then,

$$\mathbf{r}_{CF}^T = \mathbf{r}_{CSE[k-1]}^T + \beta(\mathbf{r}_{CSE[k]}^T - \mathbf{r}_{CSE[k-1]}^T) \quad (2.37)$$

$\beta$  can be obtained from

$$\begin{aligned}
|\mathbf{r}_{CF}^T - \mathbf{r}_C^T|^2 &= L_{M1}^2 \\
\therefore |(\mathbf{r}_{CSE[k-1]}^T - \mathbf{r}_C^T) + \beta(\mathbf{r}_{CSE[k]}^T - \mathbf{r}_{CSE[k-1]}^T)|^2 - L_{M1}^2 &= 0 \\
\therefore \beta^2 |\mathbf{r}_{CSE[k]}^T - \mathbf{r}_{CSE[k-1]}^T|^2 + 2\beta(\mathbf{r}_{CSE[k]}^T - \mathbf{r}_{CSE[k-1]}^T) \cdot (\mathbf{r}_{CSE[k-1]}^T - \mathbf{r}_C^T) \\
&+ |\mathbf{r}_{CSE[k-1]}^T - \mathbf{r}_C^T|^2 - L_{M1}^2 = 0 \quad (0 \leq \beta \leq 1)
\end{aligned} \tag{2.38}$$

Then,

$$\mathbf{e}_{r1}^T = \frac{\mathbf{r}_{CF}^T - \mathbf{r}_C^T}{|\mathbf{r}_{CF}^T - \mathbf{r}_C^T|} \tag{2.39}$$

Since  $\mathbf{e}_{r2}^T$  is the tangent unit vector of alignment at PcSE,  $\theta_r$ ,  $\theta_q$ ,  $\theta_{CH}$ ,  $\theta_{CV}$  can be determined by Eqs. (2.24) ~ (2.31) in section 2.1.4.

### 2.1.7.2 Type 2

The calculation procedure for Type 2 is as follows:

1. Select excavation stage, i.e., straight line, curve and EC, where front body located.
2. Find step number  $k$ .
3. Calculate  $\mathbf{r}_{CF}$  for curve and EC.
4. Calculate  $\theta_r$ ,  $\theta_q$ ,  $\theta_{CH}$ ,  $\theta_{CV}$

Table 2.6 shows judging conditions of Type 2 at different shield positions.

For position 1,

$$\begin{aligned}
\theta_r &= \theta_q = 0 \\
\theta_{CH} &= \theta_{CV} = 0
\end{aligned}$$

For position 2 and position 3, P<sub>1O2</sub> touches the trace of P<sub>2O2</sub> on  $\mathbf{n}$  (refer to Figure 2.11). To find step number  $k$  in trace of P<sub>2O2</sub>, the following conditions should be satisfied:

1. P<sub>F</sub> is along  $\mathbf{n}$  and on P<sub>C</sub>P<sub>CF</sub>.
2. P<sub>1O2</sub> is along  $\mathbf{n}$  and on the trace of P<sub>2O2</sub>.

$$3. \left| \mathbf{r}_{1O2} - \mathbf{r}_C \right|^2 = L_{M1}^2 + R_M^2 = L^2 .$$

To find step number  $k$  at curve and at EC, the condition below should be satisfied.

$$\left( \left| \mathbf{r}_{2O2[k]}^T - \mathbf{r}_C^T \right| - L \right) \times \left( \left| \mathbf{r}_{2O2[k-1]}^T - \mathbf{r}_C^T \right| - L \right) \leq 0 \quad (2.40)$$

When step number  $k$  is determined,  $\mathbf{r}_{CSE}$  and  $\mathbf{r}_{1O2}$  can be calculated by linear interpolation

as:

$$\mathbf{r}_{CSE}^T = \mathbf{r}_{CSE[k-1]}^T + \beta(\mathbf{r}_{CSE[k]}^T - \mathbf{r}_{CSE[k-1]}^T) \quad (0 \leq \beta \leq 1) \quad (2.41)$$

$$\theta_x = \theta_{x[k-1]} + \beta(\theta_{x[k]} - \theta_{x[k-1]})$$

$$\theta_y = \theta_{y[k-1]} + \beta(\theta_{y[k]} - \theta_{y[k-1]})$$

$$\theta_z = \theta_{z[k-1]} + \beta(\theta_{z[k]} - \theta_{z[k-1]}) \quad (2.42)$$

$$\mathbf{n}^T = \mathbf{T}_n \mathbf{e}_p^{MR}$$

$$\mathbf{t}^T = \mathbf{T}_n \mathbf{e}_r^{MR}$$

Then,

$$\mathbf{r}_{1O2}^T = \mathbf{r}_{CSE}^T - R_M \mathbf{n}^T + L_{CSE} \mathbf{t}^T \quad (2.43)$$

$\beta$  in Eqs. (2.41) and (2.42) can be solved from

$$\left| \mathbf{r}_{1O2}^T - \mathbf{r}_C^T \right|^2 - L^2 = 0 \quad (2.44)$$

To determine  $\mathbf{e}_{r_1}^T$ , the followings are defined:

$$\mathbf{e}_1^T = \frac{\mathbf{r}_{1O2}^T - \mathbf{r}_C^T}{\left| \mathbf{r}_{1O2}^T - \mathbf{r}_C^T \right|} \quad (2.45)$$

$$\mathbf{e}_2^T = -\mathbf{n}_F^T \quad (2.46)$$

From  $\mathbf{e}_1^T$  and  $\mathbf{e}_2^T$  the rotation angle from  $x$ -axis to  $\mathbf{e}_1$ ,  $\theta_r(0 \leq \theta_r < 2\pi)$ , and the rotation angle from  $\mathbf{e}_{r1}$  to  $\mathbf{e}_2$ ,  $\theta_q(0 \leq \theta_q \leq \pi/2)$ , can be obtained by Eq. 2.24 to 2.26. And the angle from P<sub>1O2</sub>PC to P<sub>CF</sub>PC,  $\alpha$ , can be represented by

$$\alpha = -\arctan\left(\frac{R_M}{L_{M1}}\right) > 0 \quad (2.47)$$

Using  $\theta_r$  and  $\alpha$ , the unit axial vector of front body  $\mathbf{e}_{r1}^T$  can be expressed as

$$\mathbf{e}_{r1}^T = \mathbf{T}_z(-\theta_r)\mathbf{T}_y(\alpha)\mathbf{T}_z(\theta_r)\mathbf{e}_1^T \quad (2.48)$$

Finally,  $\mathbf{r}_{CF}^T$  can be determined from

$$\mathbf{r}_{CF}^T = \mathbf{r}_C^T + L_{M1}\mathbf{e}_{r1}^T \quad (2.49)$$

Then,  $\theta_r$ ,  $\theta_q$ ,  $\theta_{CH}$ ,  $\theta_{CV}$  can be determined with the same method in Type 1.

### 2.1.7.3 Type 3

For Type 3, the procedure and equations are same with Type 2, except the trace of rear body is given by P<sub>2O1</sub> (refer to Figure 2.12).

Considering the different rules at rotation start of front body and rear body with Type 2, Table 2.6 for Type 2 will be changed as Table 2.7.

### 2.1.8 Calculation Method for Copy Cutter Length

When  $\mathbf{r}_{CF}^T$  is obtained, position of the front body can be determined. Then the required minimum excavation space is given by the outer boundary of the front body and the rear body. Copy cutter length is the length from the circumference of shield at copy cutter position to the excavation surface.

To calculate the required copy cutter length, the following two situations should be considered:

1. Copy cutter follows the trace of edge of front body and rear body, that is, the trace of  $P_{101}$ ,  $P_{202}$ ,  $P_{201}$ , and  $P_{21}$ .
2. Copy cutter follows the trace of skin plate of front body and rear body. In this situation, the trace of the points on skin plate is considered. This trace can be represented by the position vector on the axis of front body or rear body  $\mathbf{r}_*$  and unit normal direction vector to the cross section at  $\mathbf{r}_*$ ,  $\mathbf{k}_*$ , which is the unit axial vector of front body or rear body.

$$\begin{aligned} \mathbf{r}_{*i}^T &= \mathbf{r}_C^T + r_{1i} \mathbf{e}_{r1}^T && \text{for front body} \\ &= \mathbf{r}_{TC}^T + r_{2i} \mathbf{e}_{r2}^T && \text{for rear body} \end{aligned} \quad (2.50)$$

where,

$\mathbf{r}_C^T$ : position vector at crease center

$\mathbf{r}_{TC}^T$ : position vector at tail center

$\mathbf{e}_{r1}^T$ : unit vector in axial direction of front body

$\mathbf{e}_{r2}^T$ : unit vector in axial direction of rear body

$$r_{1i} = (i-1)\Delta r = (i-1) \frac{L_{M1}}{(n_r - 1)}$$

$$r_{2i} = (i-1)\Delta r = (i-1) \frac{L_{M2}}{(n_r - 1)}$$

$n_r$ : number of calculation points along axial direction of front body and rear body

Table 2.8 shows the consideration of  $\mathbf{r}_*$  and  $\mathbf{k}_*$  in this analysis.

Around the circumference of the copy cutter plane, some calculation points are set with equal interval. These calculation points can be given as:

$$\mathbf{r}_{cal[j]}^T = \mathbf{r}_C^T + \mathbf{T}_1 \mathbf{T}_r^{-1}(\theta_{r[j]}) \mathbf{r}_{cal}^{MR1} \quad (2.51)$$

where,

$\mathbf{r}_C^T$ : Crease center, which is also the origin of coordinate system  $C^{M1}$

$\mathbf{T}_1$ : Transformation matrix of the front body, which equals to  $\mathbf{T}_x^{-1}(\theta_x) \mathbf{T}_y^{-1}(\theta_y)$

$\mathbf{T}_r$ : Transformation matrix by circumferential angle  $\theta_{r[j]}$

$$\theta_{r[j]} = (i_q - 1) \Delta\theta \quad (i_q = 1, 2, \dots, n_q)$$

$$\Delta\theta = \frac{2\pi}{n_q}$$

$n_q$ : Number of calculation points around the circumference of copy cutter plane

$$\mathbf{r}_{cal}^{MR1} = [R_M \quad 0 \quad L_{CC}]^T$$

$R_M$ : Radius of shield machine

$L_{CC}$ : Length between Pcc - Pc ( $< L_{MI}$ )

Pcc: Center of copy cutter

Figure 2.13 shows image of copy cutter length  $(\mathbf{r}_{gj}^{MR} - \mathbf{r}_{cal}^{MR})_{PR}$ . To calculate the copy cutter

length, followings are executed.

Procedure A: Determination of the intersection point of a specified cross section of the shield body trace and a specified  $P_R$ - axis of the present shield position  $\mathbf{r}_{G[k-1]}$

In Figure 2.13 and Figure 2.14, calculation point on shield skin plate  $\mathbf{r}_{2S}$ :

$$\mathbf{r}_{2S}^{MR} = [R_M \quad 0 \quad r]^T \quad (2.52)$$

Position vector on shield axis  $\mathbf{r}_{2C}$ :

$$\mathbf{r}_{2C}^{MR} = [0 \quad 0 \quad r]^T \quad (2.53)$$

where,  $R_M$  : Radius of shield machine

$r$  :  $r$  coordinate of  $\mathbf{r}_{2S}$  (unknown parameter)

The position of excavation boundary  $\mathbf{r}_{Gj[k-1]}$ :

$$\mathbf{r}_{Gj[k-1]}^{MR} = [\gamma R_M \quad 0 \quad r]^T = \mathbf{r}_{2C}^{MR} + \gamma(\mathbf{r}_{2S}^{MR} - \mathbf{r}_{2C}^{MR}) \quad (2.54)$$

where  $\gamma$  : Multiple factor (unknown parameter),  $\gamma > 0$

Since  $\mathbf{r}_{Gj[k-1]}$  is on the trace of excavation boundary,

$$(\mathbf{r}_{Gj[k-1]}^{MR} - \mathbf{r}_{*[k-1]}^{MR}) \cdot \mathbf{k}_{*[k-1]}^{MR} = 0 \quad (2.55)$$

Substituting Eq. (2.54) to (2.55),

$$r = -\gamma R_M (\mathbf{k}_{*[k-1]}^{MR})_{p_R} / (\mathbf{k}_{*[k-1]}^{MR})_{r_R} + \mathbf{r}_{*[k-1]}^{MR} \cdot \mathbf{k}_{*[k-1]}^{MR} / (\mathbf{k}_{*[k-1]}^{MR})_{r_R} = a\gamma - b \quad (2.56)$$

At the same time,

$$|\mathbf{r}_{Gj[k-1]} - \mathbf{r}_{*[k-1]}| = R_M^2 \quad (2.57)$$

Substitute Eq. (2.54) to (2.57),

$$\begin{aligned} & (\mathbf{r}_{Gj[k-1]} - \mathbf{r}_{*[k-1]})(\mathbf{r}_{Gj[k-1]} - \mathbf{r}_{*[k-1]}) = R_M^2 \\ & \therefore \left[ \gamma R_M - (\mathbf{r}_{*[k-1]}^{MR})_{p_R} \right]^2 + \left[ -(\mathbf{r}_{*[k-1]}^{MR})_{q_R} \right]^2 + \left[ r - (\mathbf{r}_{*[k-1]}^{MR})_{r_R} \right]^2 = R_M^2 \\ & \therefore \gamma^2 (R_M^2 + a^2) - 2\gamma \left[ R_M (\mathbf{r}_{*[k-1]}^{MR})_{p_R} + a \left[ (b + (\mathbf{r}_{*[k-1]}^{MR})_{r_R}) \right] \right] \\ & \quad + \left[ b^2 + 2b(\mathbf{r}_{*[k-1]}^{MR})_{r_R} + |\mathbf{r}_{*[k-1]}^{MR}|^2 - R_M^2 \right] = 0 \end{aligned} \quad (2.58)$$

Here,  $a$  and  $b$  are defined in Eq. (2.56)

$\gamma$  can be solved in Eq. (2.58). Substituting  $\gamma$  to Eq. (2.56), then  $r$  can be determined.

When  $\gamma$  and  $r$  are obtained,  $\mathbf{r}_{2S}^{MR}$ ,  $\mathbf{r}_{2C}^{MR}$ ,  $\mathbf{r}_{Gj[k-1]}^{MR}$  can be obtained according to their definitions.

Procedure B: Determination of the intersection point of the excavation surface ( $\mathbf{r}_{Gj}$ ) and a specified  $p_R$ - axis from the copy cutter plane  $\mathbf{r}_{gj}$ .

In Figure 2.13 and Figure 2.15, position on shield axis  $\mathbf{r}_{CC}^{MR}$ :

$$\mathbf{r}_{CC}^{MR} = [0 \quad 0 \quad L_{CC}]^T \quad (2.59)$$

The position on the trace of excavation boundary  $\mathbf{r}_{gj}^{MR}$ :

$$\mathbf{r}_{gj}^{MR} = [\gamma R_M \quad 0 \quad L_{CC}]^T = \mathbf{r}_{CC}^{MR} + \gamma(\mathbf{r}_{calj}^{MR} - \mathbf{r}_{CC}^{MR}) \quad (2.60)$$

Step number  $k$  of  $\mathbf{r}_{Gj[k]}$  should satisfy the following condition,

$$\left[ (\mathbf{r}_{Gj[k]}^{MR} - \mathbf{r}_{CC}^{MR}) \mathbf{k}_{CF}^{MR} \right] \times \left[ (\mathbf{r}_{Gj[k-1]}^{MR} - \mathbf{r}_{CC}^{MR}) \mathbf{k}_{CF}^{MR} \right] \leq 0 \quad (k = \text{current}, -1, -2, \dots) \quad (2.61)$$

where,  $\mathbf{k}_{CF}^{MR}$ : unit normal vector of cutter face (axial direction of front body)

Since  $\mathbf{r}_{gj}^{MR}$  is on  $\mathbf{r}_{Gj[k]}^{MR} - \mathbf{r}_{Gj[k-1]}^{MR}$ , then,

$$\mathbf{r}_{gj}^{MR} = \mathbf{r}_{Gj[k-1]}^{MR} + \beta(\mathbf{r}_{Gj[k]}^{MR} - \mathbf{r}_{Gj[k-1]}^{MR}) \quad (0 \leq \beta \leq 1) \quad (2.62)$$

From  $r_R$  component,  $\beta$  can be obtained,

$$\begin{aligned} L_{CC} &= (\mathbf{r}_{Gj[k-1]}^{MR})_{r_R} + \beta(\mathbf{r}_{Gj[k]}^{MR} - \mathbf{r}_{Gj[k-1]}^{MR})_{r_R} \\ \therefore \beta &= \frac{L_{CC} - (\mathbf{r}_{Gj[k-1]}^{MR})_{r_R}}{(\mathbf{r}_{Gj[k]}^{MR} - \mathbf{r}_{Gj[k-1]}^{MR})_{r_R}} \end{aligned} \quad (2.63)$$

From  $p_R$  component,  $\gamma$  can be obtained,

$$\begin{aligned} \gamma R_M &= (\mathbf{r}_{Gj[k-1]}^{MR})_{p_R} + \beta(\mathbf{r}_{Gj[k]}^{MR} - \mathbf{r}_{Gj[k-1]}^{MR})_{p_R} \\ \therefore \gamma &= \frac{1}{R_M} \left[ (\mathbf{r}_{Gj[k-1]}^{MR})_{p_R} + \beta(\mathbf{r}_{Gj[k]}^{MR} - \mathbf{r}_{Gj[k-1]}^{MR})_{p_R} \right] \end{aligned} \quad (2.64)$$

When  $\beta$ ,  $\gamma$  are determined,  $\mathbf{r}_{gj}^{MR}$  can be obtained.

By carrying out the procedure A and procedure B, copy cutter length  $(\mathbf{r}_{gj} - \mathbf{r}_{cal[j]})_{p_R}$  can be determined for each cross section of shield machine in Table 2.8. Finally the copy cutter length, *CCL*, can be obtained.

$$CCL = \max \left( (\mathbf{r}_{gj}^{MR})_{p_R} \dots \right) - R_M \geq 0 \quad (2.65)$$

## 2.2 Simulation Method of H&V Shield Behavior

### 2.2.1 Types of Forces

The kinematic shield model for single circular shield is developed, taking into account shield tunnel engineering practices, namely—the excavated area, the tail clearance, the rotation direction of the cutter disc, sliding of the shield, ground loosening at the shield crown, and the dynamic equilibrium condition (Sugimoto et al. 2002). Applying this model to the front and rear sections of both bodies of the H&V shield individually, the H&V model is developed (Chaiyaput et al. 2015).

For mathematics purposes, the five forces mentioned in the first chapter are represented as follows: force due to self-weight of machine  $f_1$ , force on shield tail  $f_2$ , force due to jack thrust  $f_3$ , force on cutter disc  $f_4$ , and force on shield periphery  $f_5$ , as shown in Figure 2.16. The force due to self-weight of machine  $f_1$  and the force on shield periphery  $f_5$  act on the both sections of two bodies. The force on shield tail  $f_2$  acts only on the rear section, whereas the force at face  $f_4$  is loaded on cutter disc of the front section. The force on jack thrust  $f_3$  is composed of the forces due to shield jack and articulated jack. The force on shield periphery  $f_5$  is due to the ground reaction force acting on shield skin plate and the dynamic friction force on shield skin place. It

is noted that the force due to articulated jack  $f_{32}$  is not necessary to calculate since the summation of the force due to  $f_{32}$  is always zero.

Similar to models previously mentioned, the interaction force between the shield and the ground can be obtained by considering the coefficient of earth pressure  $K$ , which is a function of the distance between the original excavated surface and the shield skin plate shown in Figure 1.21. Furthermore, in the case of soft soil, the ground displacement to shield skin plate can be represented by  $U_n$ . On the other hand, for stiff soil, the self-stabilization of the ground can be expected, which causes the appearance of the gap between the shield skin plate and the excavated surface. This consideration is similar to the touching problem in FE analysis.

The H&V shield behavior is represented by the movement of the shield at the connection point between the left and right body  $P_c$ . The shield behavior during excavation can be obtained by solving the following equilibrium conditions of forces and moments acting on the shield:

$$\begin{bmatrix} \sum_{i=1}^5 (F_{LFi}^M + F_{LRi}^M + F_{RLi}^M + F_{RRi}^M) \\ \sum_{i=1}^5 (M_{LFi}^M + M_{LRi}^M + M_{RLi}^M + M_{RRi}^M) \end{bmatrix} = 0 \quad (2.66)$$

where  $F$  and  $M$  are the force and moment vectors respectively, the first subscripts  $L$  and  $R$  denote the left and right bodies of the H&V shield respectively, the second subscripts  $F$  and  $R$  denote the front and rear sections of each body respectively, and the superscript  $M$  indicates the machine coordinate system.

Another aspect to take into account is the representation of the axis for this method. The coordinate systems change in a way in which  $x$ -axis becomes the vertical one in a downward direction, while the  $z$  - axis is on the horizontal plane, occurring the same with the  $y$  - axis. The origin of the machine coordinate system is selected at the connection point between right and left

bodies. This global coordinate system  $C^T$ , the machine coordinate system  $C^M$ , and the rotated coordinate system or  $C^{MR}$  are shown in Figure 2.17.

### 2.2.1.1 Self-weight of the Shield $f_1$

The self-weight of shield  $W_s$  acts vertically downward in the  $x$ -axis direction at the center of the gravity. In here, the force vector  $F_1^T$  is defined as:

$$F_1^T = \begin{bmatrix} W_s \\ 0 \\ 0 \end{bmatrix} \quad (2.67)$$

The weight of the each body acts at the center of gravity of each body. In this machine coordinate system  $C^M$ ,  $p$  – axis is vertically downward without the rotation of the shield and the  $r$  – axis is the direction of the machine axis, while  $q$  – axis is determined by right hand coordinates system.

### 2.2.1.2 Forces on the Shield Tail $f_2$

The force on the shield tail  $f_2$  is composed of the reaction force on the inner shield surface from the segment  $f_{21}$  and the force due to the wire brush deformation and the applied grease pressure between the individual rows of wire brushes  $f_{22}$ . In the case of  $f_{21}$ , when the shield rotates until the segment ring contacts the shield tail, a reaction force from the segment to the shield is generated. The postural change of the shield during excavation may cause deformation of the wire brush at the shield tail, which generates the unequal pressure acting on the inside of the shield tail.

To calculate the forces, the following information was assumed:

1. The segment is regarded as a rigid body.
2. The shield tail is regarded as a cantilever beam of which the fixed support is at the end of the support girder.

3. The force due to the wire brush deformation has a linear relationship with the deformation of the wire brush and is represented by the distribution of pressure on the shield.

The force calculation of  $f_2$  then is divided in the calculus of reaction forces due to both  $f_{21}$  by using the cantilever beam function and  $f_{22}$  by calculating the deformation of the wire brush and the applied grease pressure if the segment contacts with the shield. Also, it is necessary to calculate the gap between the shield and the segment ring at the segment end  $U_{SE}$ ; calculate the gap between the shield and the segment ring at the end of shield tail,  $U_{ST}$ ; and calculate deformation of the wire brush,  $\Delta U_{WB}$ , by interpolation between  $U_{SE}$  and  $U_{ST}$ .

Force vector on the shield tail,  $F_2$  is defined to consist of the contact force between the segment ring and the inner shield surface,  $F_{21}$  and the interaction force at the shield tail,  $F_{22}$ .

**a) Reaction Force due to  $f_{21}$**

If the shield contacts the segment at the  $i$ th element, the force vector due to  $f_{21}$ ,  $F_{21i}$  can be obtained as:

$$F_{21i}^{MR} = \begin{bmatrix} F_{21i} \Delta l_{21} \\ -\alpha_{ic} (\mu_{ic} F_{21i} + c_{ic}) \text{sign}(CT) \\ -\mu_{ic} F_{21i} - c_{ic} \end{bmatrix} \quad (2.68)$$

where  $\alpha_{ic}$  is the factor of shearing resistance between the shield tail and the segment ring which depends on the cutter torque and has a range between 0 to 1,  $c_{ic}$  and  $\mu_{ic}$  are the mobilized cohesion and the coefficient of mobilized friction between the shield tail and the segment ring respectively,  $F_{21i}$  is the contact force on the  $i$ th element,  $CT$  is the cutter torque with the positive

sign for clockwise rotation of the cutter face of which  $sign(CT)$  is equal to 1 for  $CT>0$ , equal to -1 for  $CT<0$ , and equal to 0 for  $CT=0$ , and  $\Delta l_{21}$  is the width of element in the circumferential direction and can be defined as

$$\Delta l_{21} = \frac{2\pi R_{SI}}{n_C} \quad (2.69)$$

in which  $R_{SI}$  is the inner radius of the shield tail and  $n_C$  is the number of division in the circumferential direction of the shield.

The reaction force on the  $i$ th element per unit width  $F_{21i}$  is calculated as:

$$F_{21i} = -\frac{3U_{21i}E_S I_S}{l_{21i}^3} \quad (2.70)$$

where:

$$U_{21i} = \min(U_{2Ai}, U_{2Ci}) - t_{TD} < 0 \quad (2.71)$$

in which  $U_{21i}$  is the tail clearance at the acting point of  $F_{21i}$ ;  $E_S I_S$  is the bending stiffness of the shield tail per unit width;  $l_{21i}$  is the arm length from the fixed support to the acting point of  $F_{21i}$ ;  $U_{2Ai}$  is the tail clearance at the segment end;  $U_{2Ci}$  is the tail clearance at the end of the shield tail; and  $t_{TD}$  is the thickness of hardening grouting material inside the shield tail.

The position vector of  $F_{21}$  on the  $i$ th acting position,  $\mathbf{r}_{21i}$ , is defined as the contact position between the segment ring and the inner shield surface.

$$\mathbf{r}_{21i}^{MR} = \begin{cases} \text{if } U_{21i} = U_{SEi(p_R)}^{MR}, & \mathbf{r}_{21i}^{MR} = \mathbf{r}_{SEi}^{MR} \\ \text{if } U_{21i} = U_{STi(p_R)}^{MR}, & \mathbf{r}_{21i}^{MR} = \mathbf{r}_{STi}^{MR} \end{cases} \quad (2.72)$$

where  $U_{21i}$  is the tail clearance at the contact position,  $\mathbf{r}_{SEi}$  is the position vector of the segment end on the inner shield skin, and  $\mathbf{r}_{STi}$  is the position vector of the tail end on the inner shield skin.

**b) Reaction Force due to  $f_{22}$**

The force due to  $f_{22}$  on the  $i$ th element  $\mathbf{F}_{22i}^{MR}$  is calculated based on the pressure acting on the inner shield skin at the shield tail,  $P_{Ti}$ , as

$$\mathbf{F}_{22i}^{MR} = A_{22} \begin{bmatrix} -\sigma_{22i} \\ -\alpha_{ws} (\mu_{ws} \sigma_{22i} + c_{ws}) \text{sign}(CT) \\ -(\mu_{ws} \sigma_{22i} + c_{ws}) \end{bmatrix} \quad (2.73)$$

where  $\alpha_{ws}$  is the factor of shearing resistance between the wire brush and the segment ring which depends on the cutter torque and has a range between 0 to 1,  $c_{ws}$  and  $\mu_{ws}$  are the mobilized cohesion and the coefficient of mobilized friction between the wire brush and the segment ring respectively, and  $A_{22}$  is the area of tail element and can be calculated from

$$A_{22} = \Delta_{22} l_{WB} \quad (2.74)$$

where  $\Delta_{22}$  is the width of the tail element which is defined equal to  $\Delta_{21}$ , and  $l_{WB}$  is the length of the wire brush along the shield tail.

In Eq. (2.73) the pressure acting on the inner shield surface due to the deformation of the wire brush and the grease pressure at the  $i$ th tail element  $\sigma_{22i}$  can be found from:

$$\sigma_{22i} = \frac{\sigma_{22Bi} + \sigma_{22Ci}}{2} \quad (2.75)$$

$$\sigma_{22ni} = k_{WB}(t_{WB} - U_{2ni}) + \sigma_{grease} \quad (2.76)$$

where  $n$  is  $B$  or  $C$ , and  $\sigma_{22i}$  is the pressure at the  $i$ th element due to the wire brush deformation,  $k_{WB}$  is the spring constant of the wire brush;  $l_{WB}$  is the original height of the wire brush,  $\sigma_{grease}$  is the applied grease pressure between the individual rows of wire brushes, and  $U_{2ni}$  the tail clearance.

The position vector of  $F_{22i}$  on the  $i$ th element at the shield tail  $r_{22i}$ , can be found from

$$\mathbf{r}_{22i}^{MR} = \begin{bmatrix} R_{SI} \\ 0 \\ -(l_T - l_{22i}) \end{bmatrix} \quad (2.77)$$

where  $l_T$  is the length from  $C^M$  origin to the tail end, and  $l_{22i}$  is the distance from the tail end of shield to the acting position of  $F_{22i}$  in the  $r$ -axis direction and can be defined as

$$l_{22i} = \frac{2P_{1i} + P_{2i}}{3(P_{1i} + P_{2i})} l_{WB} \quad (2.78)$$

where  $P_{1i}$  and  $P_{2i}$  are obtained from

$$P_{ni} = P_{grease} + P_{nWB_i} \quad (2.79)$$

in which  $n=1$  is the position at the first row of the wire brush,  $n=2$  is the position of the wire brush at the tail end,  $P_{grease}$  is the applied grease pressure in the chamber between individual rows of the wire brushes, and  $P_{nWB_i}$  is the pressure on the  $i$ th tail element caused by the wire brush deformation.

### 2.2.1.3 Jack Force $f_3$

The jack thrust acts in the  $r$ -axis direction on the plane where the jacks are mounted. The friction on the interface between the jacking plate and the segment is also taken into account.

Therefore, the force vector due to  $i$ th jack  $\mathbf{F}_{3i}$  can be obtained as

$$\mathbf{F}_{3i}^{MR} = A_J S_i \begin{bmatrix} 0 \\ -\alpha_{sc} (\mu_{sc} \sigma_J + c_{sc}) \text{sign}(CT) \\ \sigma_J \end{bmatrix} \quad (2.80)$$

where  $\alpha_{sc}$  is the factor of shearing resistance between the steel and the concrete segment which depends on the cutter torque and has a range between 0 to 1,  $c_{sc}$  and  $\mu_{sc}$  are the mobilized cohesion and the coefficient of mobilized friction between the steel and the concrete segment respectively,  $A_J$  is the cross-sectional area of the hydraulic jack,  $\sigma_J$  is the applied hydraulic pressure, and  $S_i$  is the status of the  $i$ th jack ( $S_i=1$  for active jack and  $S_i=0$  for inactive jack).

The position vector of the  $i$ th jack measured from the line of origin of  $C^M$  to their center  $\mathbf{r}_{3i}$ , can be defined as

$$\mathbf{r}_{3i}^M = \begin{bmatrix} R_J \cos \theta_{ji} \\ R_J \sin \theta_{ji} \\ -(l_{CJ} + l_{Si}) \end{bmatrix} \quad (2.81)$$

in which  $l_{CJ}$  is the length of the jack at zero stroke;  $l_{Si}$  is the  $i$ th jack stroke;  $R_J$  is the radius of the jack measured from center of the  $i$ th jack to the centroid of all jacks, which coincides with the line of origin of  $C^M$ ; and  $\theta_{ji}$  is the angle between the  $p$ -axis to center of the  $i$ th jack measured in right-handed system as shown in Figure 2.18.

#### 2.2.1.4 Force at the Face $f_4$

The force acting at the face can be divided into three components: force due to the earth pressure acting on the front and rear of CF  $f_{41}$  force due to the earth pressure acting on the periphery of CF  $f_{42}$ ; and force due to weight of the muck in the chamber  $f_{43}$ . To formulate these forces, the following were assumed:

1. Normal earth pressure distribution on the front face is proportional to the initial normal earth pressure.
2. Normal earth pressure distribution on the cutter face periphery is equal to the initial normal earth pressure.
3. Weight of the muck in the chamber is loaded on the shield at the centroid of the chamber.

To calculate the force acting normal to the cutter face, the cutter face is divided into a finite number of small elements in both radial and circumferential directions as shown in Figure 2.19.

##### a) Force Acting on the Front and Rear of CF $f_{41}$

The balance of the pressure normal on the cutter face produces the following conditions:

$$\begin{aligned}\sigma'_{nf} + \sigma_w &= \sigma_{CF} + \sigma_m && \text{for clayey ground} \\ \sigma_{nf} &= \sigma_{CF} + \sigma_m && \text{for sandy ground}\end{aligned}\tag{2.82}$$

where  $\sigma_{nf}$  is the total earth pressure;  $\sigma'_{nf}$  is the effective earth pressure;  $\sigma_w$  is the hydraulic pressure on CF;  $\sigma_{CF}$  is the net pressure acting on CF; and  $\sigma_m$  is the muck pressure at the face.

All the following equations are for clayey ground. In the case of sandy ground, it's necessary to replace  $\sigma_{nf}$  with  $\sigma'_{nf}$  and add  $\sigma_w$  to the normal earth pressure since the earth and water pressures are calculated together for clayey ground but are calculated separately for sandy ground. To model  $\sigma_{nf}$ , the following were assumed:

1.  $\sigma_{nf}$  is proportional to the initial normal earth pressure.

2. The penetration resistance and the cutting resistance depend upon the cutting depth  $t_c$  in Eq. (2.83) or penetration angle  $\theta_p$  in Eq. (2.84).

$$t_c = \frac{v_s}{fp} \quad (2.83)$$

$$\theta_p = \frac{v_s}{2\pi fr} \quad (2.84)$$

where  $v_s$  is the advance speed of the shield,  $f$  is the rotating speed of  $CF$ ,  $p$  is the number of paths of the cutter bit, and  $r$  is the radius of the calculation point in  $CF$ . Since  $p$  and  $r$  are constants for a machine,  $\sigma_{nf} / \sigma_{no}$  is supposed to be a function of  $v_s / fr$ , where  $\sigma_{no}$  is the initial normal earth pressure.

3. The state of earth pressure distribution on  $CF$  may change due to reasons such as local collapse of the ground at the face. Therefore  $\sigma_{nf}$  can be obtained from

$$\sigma_{nf} = F(p, q) \left( a \frac{v_s}{fr} + b \right) \sigma_{no} \quad (2.85)$$

where  $F(p, q)$  is the factor due to the state of earth pressure; and  $a, b$  are constants. The second term in Eq. (2.85) is the first order approximation of the function  $v_s / fr$ .

To calculate the force acting on the front and rear of  $CF$ ,  $CF$  is divided into a finite number of small elements in both radial and circumferential directions. The force vector due to  $f_{41}$ ,  $F_{41}$  can be obtained by summation of the following force acting on the  $ij$ th element of the cutter face:

$$\mathbf{F}_{41ij[k]}^{MR} = A_{41ij} \begin{bmatrix} 0 \\ -(\mu_{ms} \sigma_{CFij[k]} + \tau_{mij[k]}) \text{sign}(CT) \\ \sigma_{CFij[k]} + \sigma_{mij[k]} \end{bmatrix} \quad (2.86)$$

where  $\tau_{mij[k]}$  is the shear resistance on both sides of the cutter face due to the muck pressure;

$$\tau_{mij[k]} = 2 \left\{ (1 - \alpha_o) (\mu_{ms} \sigma_{mij[k]} - c_{ms}) + \alpha_o (\mu_m \sigma_{mij[k]} - c_m) \right\} \quad (2.87)$$

$A_{41ij}$  is the area of the  $ij$ th element on the cutter face;

$$A_{41ij} = \frac{1}{2} (\Delta\theta)(\Delta R)^2 (2i - 1) \quad (i = 1, 2, 3, \dots, n_R) \quad (2.88)$$

$\alpha_o$  is the open ratio of the cutter face;  $c_{ms}$  and  $\mu_{ms}$  are the mobilized cohesion and the coefficient of mobilized friction between the muck and the steel, respectively; and  $c_m$  and  $\mu_m$  are the mobilized cohesion and the coefficient of mobilized friction of muck, respectively.

Velocity of the shield during excavation for the  $ij$ th calculation point at step  $[k]$ ,  $v_{sij[k]}$ , can be obtained as

$$v_{sij[k]} = \frac{|\mathbf{r}_{41ij[k]}^T - \mathbf{r}_{41ij[k-1]}^T|}{\Delta t_{[k]}} \quad (2.89)$$

where  $\Delta t_{[k]}$  is the estimated time for excavation from step  $[k-1]$  to step  $[k]$ ,

$$\Delta t_{[k]} = \frac{|\mathbf{r}_{o[k]}^T - \mathbf{r}_{o[k-1]}^T|}{v_{so[k]}} \quad (2.90)$$

in which  $v_{so[k]}$  is the initial shield velocity measured at the center of shield jack, and  $\mathbf{r}_{so[k-1]}$  and  $\mathbf{r}_{so[k]}$  are the position vectors at the center of shield jack at step  $[k-1]$  and  $[k]$  respectively.

The pressure acting on the cutter face can be illustrated in Figure 2.20. The normal pressure acting on the cutter face  $\sigma_{CF}$ , can be defined in terms of the normal earth pressure and the muck pressure inside the chamber  $\sigma_m$ , as

$$\sigma_{CFij[k]} = \begin{cases} \sigma_{nfi[k]} + P_{wij[k]} - \sigma_{mij[k]} & \text{for cohesionless soil} \\ \sigma_{nfi[k]} - \sigma_{mij[k]} & \text{for cohesive soil} \end{cases} \quad (2.91)$$

where  $P_{wij[k]}$  is the hydraulic pressure on the cutter face,

$$P_{wij[k]} = -\left(\mathbf{r}_{41ij[k]}^T - \mathbf{r}_{w[k]}^T\right) \mathbf{e}_{(x)}^T \gamma_w \quad (2.92)$$

and  $\sigma_{mij[k]}$  is the muck pressure acting normal to the cutter face,

$$\sigma_{mij[k]} = -\left(\mathbf{r}_{41ij[k]}^T - \mathbf{r}_{CF[k]}^T\right) \mathbf{e}_{(x)}^T \gamma_m + \sigma_{mo[k]} \quad (2.93)$$

in which  $\mathbf{r}_{CF[k]}$  is the position vector of the center of the cutter face,  $\gamma_m$  is the unit weight of muck, and  $\sigma_{mo[k]}$  is the initial muck pressure in the chamber.

And from Eq. (2.89)

$$\mathbf{r}_{41ij}^{MR} = \begin{bmatrix} r_{CFij} \\ 0 \\ l_{CF} \end{bmatrix} \quad (2.94)$$

in which  $\mathbf{r}_{41ij}$  is the position vector of  $F_{41ij}$ ,  $r_{CFij}$  is the radius of the  $ij$ th element on CF, and  $l_{CF}$  is the distance from the origin of  $C^M$  to the center of CF.

### **b) Force Acting on the Periphery of CF $f_{42}$**

The normal earth pressure distribution on the cutter face periphery was assumed to be equal to the initial normal earth pressure as shown in Figure 2.20,  $\sigma_{ne} = \sigma_{no}$ . The earth pressure acting in the  $r_R$  - axis direction in  $C^{MR}$  is neglected in the calculation of this force. Thus, the force vector due to  $f_{42}$ ,  $\mathbf{F}_{42}$  can be obtained by summation of the following force on the  $j$ th element of the cutter face periphery:

$$\mathbf{F}_{42j}^{MR} = A_{42j} \begin{bmatrix} -\sigma_{nej} \\ (\mu_{ms}\sigma_{nej[k]} + c_{ms}) \text{sign}(CT) \\ 0 \end{bmatrix} \quad (2.95)$$

where  $\sigma_{nej}$  is the normal earth pressure on the  $j$ th element of the cutter face periphery which can be obtained from

$$\sigma_{nej} = \sigma_{oj(p_R)}^{MR} \quad (2.96)$$

where

$$\sigma_{oj}^{MR} = \mathbf{T}_{Rj} \mathbf{T}_z \mathbf{T}_y \mathbf{T}_x \sigma_{oj}^T \mathbf{T}_x^{-1} \mathbf{T}_y^{-1} \mathbf{T}_z^{-1} \mathbf{T}_{Rj}^{-1} \quad (2.97)$$

and

$$\sigma_{oj(p_R)}^{MR} = \sigma_{oj}^{MR} \mathbf{e}_{(p_R)}^{MR} \quad (2.98)$$

in which  $\mathbf{e}_{(p_R)}$  is the unit vector in the  $p_R$ -axis direction in  $C^{MR}$  which is defined as  $[1 \ 0 \ 0]^T$ ,

and  $A_{42j}$  is the area of the  $j$ th element on the cutter face periphery.

$$A_{42j} = (\Delta\theta) R_{CF} t_{CF} \quad (2.99)$$

where  $t_{CF}$  is the thickness of cutter face as illustrated in Figure 2.21. The position vector of the

$j$ th calculation point on the cutter face periphery  $\mathbf{r}_{42j}^M$ , is illustrated in Figure 2.22 and can be

defined as:

$$\mathbf{r}_{42j}^M = \begin{bmatrix} R_{CF} \cos \theta_j \\ R_{CF} \sin \theta_j \\ l_{CF} \end{bmatrix} \quad (2.100)$$

**c) Force due to the Weight of Muck in Chamber  $f_{43}$**

The slurry or mud is the necessary material to stabilize the tunnel face for closed-type shield tunneling method. In case of the EPB shield tunneling method, the plastic fluidized soil is excavated out by the cutter face, called the muck, and then filled into the chamber to support the face. The muck inside the chamber will be discharged by the screw conveyor, which is expected to prevent the water seepage. In case of the slurry shield tunneling method, the pressurized slurry is encountered against the earth and water pressures at the face. The slurry is mixed with excavated ground, also called the muck, inside the chamber and will be discharged out by the removal pipe. The slurry penetrates the ground to a certain depth through the cutter face and gives cohesion to the ground around the tunnel face.

The weight of the muck inside the chamber is assumed to load on the shield at the center of gravity of the muck, which is assumed to coincide with the centroid of the chamber as illustrated also in Figure 2.5. Thus, the weight of muck inside the chamber  $f_{43}$ ,  $F_{43}$  can be found from

$$\mathbf{F}_{43}^T = \begin{bmatrix} W_m \\ 0 \\ 0 \end{bmatrix} \quad (2.101)$$

where  $W_m$  is the weight of the muck filled in the chamber and can be estimated from the equation

$$W_m = (l_M - l_B - t_{CF}) \times \pi R_{chamber}^2 \times \gamma_m \quad (2.102)$$

in which  $R_{chamber}$  is the inner radius of the chamber. The position vector of the weight of muck

$\mathbf{r}_{43}$ , can be written as

$$\mathbf{r}_{43}^M = \begin{bmatrix} 0 \\ 0 \\ l_m \end{bmatrix} \quad (2.103)$$

where  $l_m$  is the distance from the origin of  $C^M$  to the centroid of the chamber.  $l_m$  is illustrated as

$$l_m = \frac{1}{2}(l_M - t_{CF} + l_B) - l_T \quad (2.104)$$

in which  $l_m$  is the length of shield, and  $l_B$  is the length from the bulkhead to the shield tail.

### 2.2.1.5 Earth Pressure Acting on the Shield Periphery $f_s$

The active earth pressure occurs when the ground at the open face deforms toward the shield periphery. The void between the excavated area and the outer skin plate of shield is generated by over-excavation of the cutter face or the copy cutter. On the other hand, as the shield has transited within the excavated area, some parts of the shield skin plates push the ground, and the passive earth pressure is generated. This situation is caused by control of the shield related with the applied jack thrust and the shield movement direction. The state of earth pressure is also taken into consideration in the earth pressures acting on the shield.

To formulate the force acting on the shield periphery, the next three aspects are assumed:

1. The shield is considered as a rigid body.
2. The ground reaction curve shows the relationship between the ground displacement and the earth pressure acting on the shield periphery, which can be obtained by:

$$K_i(U_i) = \begin{cases} (K_{io} - K_{i\min}) \tanh \left[ \frac{a_i U_i}{K_{io} - K_{i\min}} \right] + K_{io} \\ (K_{io} - K_{i\max}) \tanh \left[ \frac{a_i U_i}{K_{io} - K_{i\max}} \right] + K_{io} \end{cases} \quad (2.105)$$

where in the first case,  $(U_i \leq 0)$ ; in the second case,  $(U_i \geq 0)$ ; and  $(i = v \text{ or } h)$ ;  $K$  is the coefficient of earth pressure which is defined as the earth pressure  $\sigma$  divided by the initial vertical earth pressure  $\sigma_{vo}$  ( $K_i = \sigma_i / \sigma_{vo}$ );  $U$  is the ground displacement;  $a$  is the gradient of

function  $K(U)$ , which represents the coefficient of sub grade reaction  $k(a_i = k_i / \sigma_{vo})$ ; subscripts  $v$  and  $h$  are the vertical and the horizontal directions, respectively; and subscript  $o$  is the initial,  $min$  is the lower limit, and  $max$  is the upper limit of the coefficient of earth pressure.

The coefficient of earth pressure in any direction  $K_\theta$  can be interpolated by using  $K_h$  and  $K_v$  as

$$K_\theta(U_n, \theta) = [K_v(U_n) \cos^2 \theta + K_h(U_n) \sin^2 \theta] \quad (2.106)$$

where  $U_{nij}$  is the normal ground displacement on the shield periphery which is obtained from

$$U_n = \sqrt{(U_v)^2 + (U_h)^2} \quad (2.107)$$

and  $U_h$  and  $U_v$  are the ground displacements in horizontal and vertical directions respectively

and are described in Appendix B.  $\theta_{ij}$  can be estimated from

$$\theta = \tan^{-1} \left( \frac{U_h}{U_v} \right) \quad (2.108)$$

Summation of the following force on the  $ij$ th element is considered as the force acting on the shield periphery  $F_{5ij}$ . It can be obtained as

$$F_{5ij}^{MR} = A_{5ij} \begin{bmatrix} -\sigma_{nsij} \\ -\alpha (\mu_{ms} \sigma_{nsij} + c_{ms}) \text{sign}(CT) \\ -(\mu_{ms} \sigma_{nsij} + c_{ms}) \end{bmatrix} \quad (2.109)$$

where  $\alpha$  is the factor of the shearing resistance between the shield skin plate and the ground which depends on the cutter torque and has a range between 0 to 1, and  $A_{5ij}$  is the area of the  $ij$ th element on the shield periphery. It can be defined as

$$A_{5ij} = \frac{2\pi l_M}{n_C n_L} R_s \quad (2.110)$$

in which  $n_C$  and  $n_L$  are the number of divisions in circumferential and longitudinal directions of the shield respectively. The position vector of the acting point of  $\mathbf{F}_{5ij}$  on the shield periphery  $\mathbf{r}_{5ij}^M$ , is defined as

$$\mathbf{r}_{5ij}^M = \begin{bmatrix} R_s \cos \theta_i \\ R_s \sin \theta_i \\ l_j \end{bmatrix} \quad (2.111)$$

where  $R_s$  is the outer radius of the shield, and  $\theta_i$  is the  $i$ th calculation point angle which is measured away from the  $p$  - axis in a counterclockwise direction around the  $r$  - axis.

### 2.2.2. Summations of Forces, Moments, and Cutter Torque

For convenience in calculation of the summations, the forces and their position vectors for each step of calculation are considered in  $C^M$ . The methods to transform forces and position vectors from one coordinate system to another are described in Appendix C. The moment vector can be obtained by taking the cross product of the position vector and the force vector. Thus, the moment vector due to  $\mathbf{f}_1$  can be expressed as

$$\mathbf{M}_1^M = \mathbf{r}_1^M \times \mathbf{F}_1^M \quad (2.112)$$

and the force and moment vector due to  $\mathbf{f}_{21}$  and  $\mathbf{f}_{22}$  can be

$$\mathbf{F}_2^M = \sum_{i=1}^{n_C} (\mathbf{F}_{21i}^M + \mathbf{F}_{22i}^M) \quad (2.113)$$

$$\mathbf{M}_2^M = \sum_{i=1}^{n_C} (\mathbf{r}_{21i}^M \times \mathbf{F}_{21i}^M + \mathbf{r}_{22i}^M \times \mathbf{F}_{22i}^M) \quad (2.114)$$

The summations of force and moment vectors due to  $\mathbf{f}_3$  can be obtained by summation of each jack force as

$$\mathbf{F}_3^M = \sum_{i=1}^{n_j} \mathbf{F}_{3i}^M \quad (2.115)$$

$$\mathbf{M}_3^M = \sum_{i=1}^{n_j} \mathbf{r}_{3i}^M \times \mathbf{F}_{3i}^M \quad (2.116)$$

where  $n_j$  is the number of shield jack.

The force and moment vectors on the cutter face due to  $\mathbf{f}_{41}$ ,  $\mathbf{f}_{42}$  and  $\mathbf{f}_{43}$  are the summation of the entire forces on each small element of the cutter face and can be written as

$$\mathbf{F}_4^M = \sum_{i=1}^{n_R} \sum_{j=1}^{n_\theta} \mathbf{F}_{41ij}^M + \sum_{j=1}^{n_\theta} \mathbf{F}_{42j}^M + \mathbf{F}_{43}^M \quad (2.117)$$

$$\mathbf{M}_4^M = \sum_{i=1}^{n_R} \sum_{j=1}^{n_\theta} \mathbf{r}_{41ij}^M \times \mathbf{F}_{41ij}^M + \sum_{j=1}^{n_\theta} \mathbf{r}_{42j}^M \times \mathbf{F}_{42j}^M + \mathbf{r}_{43}^M \times \mathbf{F}_{43}^M \quad (2.118)$$

The resistance of the cutter torque due to the earth pressure on the cutter face is the moment caused by  $\mathbf{f}_4$  around the  $r$  - axis and can be expressed as

$$CT = \mathbf{M}_{4(r)}^M \quad (2.119)$$

The summations of force and moment vectors due to  $\mathbf{f}_5$  on each small element of the shield periphery can be written as

$$\mathbf{F}_5^M = \sum_{i=1}^{n_L} \sum_{j=1}^{n_C} \mathbf{F}_{5ij}^M \quad (2.120)$$

$$\mathbf{M}_5^M = \sum_{i=1}^{n_L} \sum_{j=1}^{n_C} \mathbf{r}_{5ij}^M \times \mathbf{F}_{5ij}^M \quad (2.121)$$

## 2.3 Simulation Algorithms

### 2.3.1 General

Figure 2.23 shows the component of the model, as follows:

1. Ground properties. The ground properties, i.e.,  $K_o$ ,  $\mu_{ms}$ ,  $c_{ms}$ , etc., are the parameters. The reverse analysis is used to confirm proper value of the ground properties during shield excavation.
2. Shield operation. The shield operation parameters, i.e.,  $F_{3r}$ ,  $M_{3p}$ ,  $M_{3q}$ , etc., are the affecting factors on the shield behavior.
3. Shield behavior. The position and rotation of the shield are the major factors affecting the ground displacement around the shield. The shield tunneling simulation takes into account the shield tunneling behavior, i.e.,  $\Delta x$ ,  $\Delta y$ ,  $\Delta z$ , etc.

The relationship between the applications and the parameters is shown in Table 2.9. .

### 2.3.2 Simulation Techniques

The procedure of the shield tunneling simulation is explained. The shield tunneling behavior is represented by the movement of the shield in the  $x$ ,  $y$ , and  $z$  directions ( $\Delta x$ ,  $\Delta y$ , and  $\Delta z$ ) and the shield postures (yawing angle  $\phi_y$ , pitching angle  $\phi_p$ , and rolling angle  $\phi_r$ ). Since the change of  $\phi$  is limited in practice, the factor of shearing resistance due to the cutter torque  $\alpha$  was adopted as the parameter instead of  $\phi$ . The shield behavior during excavation can be obtained by solving the following equilibrium conditions of forces and moments:

$$\begin{bmatrix} \sum_{i=1}^5 F_i^M \\ \sum_{i=1}^5 M_i^M \end{bmatrix} = 0 \quad (2.122)$$

and the residual  $v$  is

$$\mathbf{v} = - \begin{bmatrix} \sum_{i=1}^5 \mathbf{F}_i^M \\ \sum_{i=1}^5 \mathbf{M}_i^M \end{bmatrix} \quad (2.123)$$

The shield tunneling behavior can be obtained so that the residual square sum  $SSQ$  becomes minimum.

$$SSQ = \mathbf{v}^T \mathbf{W} \mathbf{v} \quad (2.124)$$

where  $\mathbf{W}$  is the diagonal matrix of weighting factor.

The steps for simulation are resumed as:

1. Input the of parameters (ground/slurry properties, shield dimensions, jack thrust)
2. Give the initial values for  $\Delta x, \Delta y, \Delta z, \Phi_y, \Phi_p, \alpha$
3. Shield positions led to the calculus of  $\mathbf{F}_1, \mathbf{F}_3$  and  $\mathbf{M}_1, \mathbf{M}_3$  directly,
4.  $\mathbf{F}_2$  and  $\mathbf{M}_2$  are obtained with the values of the position of the shield tail, the position of the end of the segment, the gap between shield tail and segment, the contact position and deformation of the wire brush, the force and pressure on shield tail, and the external load on the shield tail,
5.  $\mathbf{F}_4$  and  $\mathbf{M}_4$  are obtained by: position vector for each calculation point, velocity, normal earth pressure and the earth pressure acting on cutter face.
6.  $\mathbf{F}_5$  and  $\mathbf{M}_5$  are obtained by: ground displacement, ground reaction curve, earth pressure acting on shield periphery and external load on shield periphery.
7. Once having all the forces and the moments, make the summations necessary

$$(\sum \mathbf{F}_p, \sum \mathbf{F}_q, \sum \mathbf{F}_r, \sum \mathbf{M}_p, \sum \mathbf{M}_q \text{ and } \sum \mathbf{M}_r)$$

8. If there is convergence, then the process is over. On the contrary, a revision of  $\Delta x, \Delta y, \Delta z, \Phi_y, \Phi_p, \alpha$  is necessary and the process starts again at point number 3.

Note that the optimization technique, Lavenberg-Marquardt method, is applied to minimize the residual square sum for the  $\Delta x, \Delta y, \Delta z, \Phi_y, \Phi_p, \alpha$  values.

### 2.3.3 Indexes of Shield Tunneling Behavior

Since a shield performs in three-dimensional space, the shield behavior has six degrees of freedom, so the traces of shield in the horizontal and vertical planes,  $\phi_y$ ,  $\phi_p$ , and  $C$  represent the shield behavior adequately. Since it is difficult to examine the simulation process in detail by using the trace of the shield and it is also impossible to compare the simulation results of  $\Delta x$ ,  $\Delta y$  and  $\Delta z$  with the observed one, the following normalized parameters were adopted to represent the simulation results: (1) the tilt angle from the shield trace onto the machine axis on the horizontal and vertical planes  $\theta_{xT}$  and  $\theta_{yT}$ , which show sliding of the shield in the horizontal and vertical directions respectively; (2) the tunnel alignment parameters, namely the curvature on the horizontal and vertical planes  $\kappa_h$  and  $\kappa_v$ , and the velocity of shield  $v_s$  which represents the shield advancement within two successive steps. The indexes of shield behavior are summarized as  $\phi_y, \phi_p, \alpha, \theta_{xT}, \theta_{yT}, \kappa_h, \kappa_v$ , and  $v_s$ . Here, it is considered that traces of the shield,  $\phi_y, \phi_p$ , and  $\alpha$  show the configuration of the shield behavior, whereas  $\theta_{xT}, \theta_{yT}, \kappa_h, \kappa_v$ , and  $v_s$  show detail of the shield behavior. The sign conventions of  $\theta_{xT}, \theta_{yT}, \kappa_h$ , and  $\kappa_v$  rely on the right-hand system, i.e., the positive sign of  $\theta_{xT}, \theta_{yT}, \kappa_h$ , and  $\kappa_v$  indicate rotation of shield to the right, downward, a rightward curve, and a downhill curve respectively. The calculations of the significant alignment parameters can be summarized as follows.

### 2.3.3.1 Curvature on the Vertical Plane

On the vertical plane ( $xz$  plane), as shown in Figure 2.24,  $\kappa_v$  at step  $[k]$  can be obtained from

$$\kappa_{v[k]} = \frac{\Delta\theta_{y[k]}}{\Delta l_{[k]}} \quad (2.125)$$

where

$$\Delta\theta_{y[k]} = \phi_{p[k]} - \phi_{p[k-1]} \quad (2.126)$$

and

$$\Delta l_{[k]} = \sqrt{(\Delta x_{[k]}^*)^2 + (\Delta y_{[k]}^*)^2 + (\Delta z_{[k]}^*)^2} \quad (2.127)$$

where  $\Delta x^*$ ,  $\Delta y^*$ , and  $\Delta z^*$  are defined similar to  $\Delta x$ ,  $\Delta y$ , and  $\Delta z$  respectively.

Thus, the radius of curvature on the vertical plane,  $R_v$ , is an inversion of  $\kappa_v$  as

$$R_{v[k]} = \frac{1}{\kappa_{v[k]}} \quad (2.128)$$

The meaning of  $R_{v[k]}$  can be explained as: if  $R_{v[k]} > 0$ , the vertical curve is downhill curve; if  $R_{v[k]} < 0$ , the vertical curve is uphill curve; and it becomes straight line when  $R_{v[k]} = 0$ .

### 2.3.3.2 Tilt Angle on the Vertical Plane

$\theta_{yT}$  at step  $[k]$  can be calculated from

$$\theta_{yT[k]} = \phi_{p[k]} - \theta_{yp[k]} - \frac{\Delta\theta_{y[k]}}{2} \quad (2.129)$$

where

$$\theta_{yp[k]} = \tan^{-1} \left[ \frac{\Delta x_{[k]}^*}{\sqrt{(\Delta y_{[k]}^*)^2 + (\Delta z_{[k]}^*)^2}} \right] \quad (2.130)$$

in which  $\theta_{yp[k]}$  is in the range of  $-\pi/2 \sim \pi/2$ . The meaning of  $\theta_{yT[k]}$  can be explained as: if  $\theta_{yT[k]} > 0$ , the shield rotates downward from the tunnel alignment; if  $\theta_{yT[k]} < 0$ , the shield rotates upwards from the tunnel alignment; and the shield moves in a horizontal straight line and coincides with the tunnel alignment when  $\theta_{yT[k]} = 0$ . The definitions of used parameters are also illustrated in Figure 2.24.

### 2.3.3.3 Curvature on the Horizontal Plane

On the horizontal plane ( $yz$  plane), as shown in Figure 2.25,  $\kappa_h$  at step  $[k]$  can be defined as

$$\kappa_{h[k]} = \frac{\Delta\theta_{x[k]}}{\Delta l_{x[k]}} \quad (2.131)$$

where

$$\Delta\theta_{x[k]} = \phi_{y[k]} - \phi_{y[k-1]} \quad (2.132)$$

and

$$\Delta l_{x[k]} = \sqrt{(\Delta y_{[k]}^*)^2 + (\Delta z_{[k]}^*)^2} \quad (2.133)$$

The radius of curvature on the horizontal plane,  $R_h$ , can be determined from an inversion of  $\kappa_h$  as

$$R_{h[k]} = \frac{1}{\kappa_{h[k]}} \quad (2.134)$$

The meaning of  $R_{h[k]}$  can be explained as: if  $R_{h[k]} > 0$ , the radius of horizontal curvature is in a rightward curve; if  $R_{h[k]} < 0$ , the radius of horizontal curvature is in a leftward curve; and it becomes straight line when  $R_{h[k]} = 0$ .

### 2.3.3.4 Tilt Angle on the Horizontal Plane

$\theta_{xT}$  at step  $[k]$  can be obtained as

$$\theta_{xT[k]} = \frac{\pi}{2} - \theta_{xp[k]} - \frac{\Delta\theta_{x[k]}}{2} \quad (2.135)$$

where

$$\theta_{xp[k]} = \tan^{-1} \left[ \frac{\Delta z_{[k]}^*}{\Delta y_{[k]}^*} \right] \quad (2.136)$$

in which  $\theta_{xp[k]}$  is in the range of  $0 \sim 2\pi$ . The meaning of  $\theta_{xT[k]}$  can be explained as: the shield rotates from the tunnel alignment to the right when  $\theta_{xT[k]} > 0$ , if  $\theta_{xT[k]} < 0$  the shield rotates from the tunnel alignment to the left, and when  $\theta_{xT[k]} = 0$  the shield moves in a vertical straight line and coincides with the tunnel alignment.

## CHAPTER 3: SENSITIVITY ANALYSES

### 3.1 Introduction

#### 3.1.1 Analysis Data

Table 3.1 shows the used data of the shield. In this research the machine is composed of the left and right bodies. The alignment in the left body is straight for the horizontal and vertical movements, while the right body rotates around the left body. The shield moves on the horizontal straight alignment for a planned distance of 20 m. Table 3.2 shows the characteristics of the ground properties. Here, as ground stiffness parameters, SPT-N values were assumed 30 and 50.

#### 3.1.2 Analysis Parameters

Sensitivity analyses are carried out to examine the influence of the model parameters on the shield tunneling behavior. For the analysis of this study, four parameter groups were used, since these parameters are considered to be a predominant factor on shield behavior.

1. CCL (Copy Cutter Length) parameters:

The reduction effectiveness rates of CCL were 0.00 (default), 0.25, 0.50, 0.75, and 1.00. Here the maximum copy cutter length CCL is 400 mm. Then as the CCL 400, 300, 200, 100, 0 mm are considered.

2. Crease angle  $\theta_C$  and pitching angle  $\phi_{PRR}$

As a default, the pitching angle of the right rear body  $\phi_{PRR}$  is zero, since the right rear body was assumed to be parallel to the left rear body. The articulation angle of the right body  $\theta_C$  is calculated, based on the geometric conditions so that the rear body is inside the excavation surface. As an alternative, under the pitching angle of the right front body in constant, the

articulation angle of the right body takes  $\theta_G$ ,  $0.5\theta_G$  and  $0.0$ . That is, the pitching angle of the right rear body  $\phi_{pRR}$  is  $0.0$ ,  $-0.5\theta_G$  and  $-\theta_G$  respectively. Note that the result of Parameter 1 is the case with  $\phi_{pRR}=0$ .

### 3. Share of jack force for both bodies

As a default, the jack force is set by sequential analysis on the external load acting on each body. As an alternative, under the total jack force is constant, the share of the total jack force for each body is changed, that is, the jack thrust at the left body per the total jack force is  $0.2$ ,  $0.4$ ,  $0.6$  and  $0.8$ .

### 4. Ground stiffness

SPT-N value =  $30$  and  $50$  are used, as medium stiff soil and very stiff soil respectively.

Table 3.3 shows the analysis case in this study

## 3.2 Parameter 1: Copy Cutter Length

### 3.2.1 Shield Behavior

Figure 3.1 and Figure 3.2 shows a part of the results of the CCL (Copy Cutter Length) parameters study. From Figure 3.1, the following are found:

- 1) Case (a) and (b) show almost same results;
- 2) Case (d), the shield stops before the 10-meter distance; and
- 3) In Case (c),  $\phi_p$  decreases, that is, the machine starts to go up.

These can be explained as follows:

- 1) When the reduction rate increases, the advance becomes more difficult and the excavation speed decreases due to the increase of the skin friction; and

2) When the reduction rate increases, the machine rotates to upward since the overcutting space at the crown decreases.

From Figure 3.2, the followings are found:

1) The curvature on the horizontal and vertical planes  $\kappa_h$  and  $\kappa_v$  are around 0, which points out that the alignment of the shield during excavation is likely a straight line;

2) The fluctuation of  $\theta_{xT}$  is compatible with  $\phi_y$ , both decrease together;

3) The  $\theta_{yT}$  becomes around 120 min after the articulation starts, where the positive sign shows that the shield axis direction is downward from the shield movement direction in vertical plane. These indicate that the shield moves on the horizontal plane with the machine axis slightly downward.

### 3.2.2 Trace

Figure 3.3 shows the trace of the shield. The followings are found:

1) On both vertical and horizontal planes, the calculated and planned trace of the left body part of the machine follows the same route, but the calculated trace of the right body on the vertical plane shows a slightly higher with distance;

2) In the first three cases, the calculated and the planned distances have a good correlation;

3) In case(d), the CCL affects significantly the final distance. Here the change of the calculated distance indicates a change of velocities.

### 3.2.3 Force

Figure 3.4 shows the total of the forces and moments with distance. The followings are found:

1) Case (a) and (b) are almost same.

2) Case (c) shows a stop before 20 m and the moment of  $f_5 M_{5p}$  increases compared to the first two cases.

3) In case (d), as the effective rate decreases, the velocity decreases, the moment of  $f_5 M_{5p}$  decreases (force at the shield periphery) and the  $M_{4p}$  increases.

### 3.2.4 Gap Around Shield Periphery

Figure 3.5 shows the distance from the initiated excavation surface to the shield periphery in normal direction (here after called “gap around the shield periphery”). The shield periphery was unfolded as a flat plate, leaving the crown of the shield on the middle section of every image. The upper part is the front body of the machine, while the lower part is the rear body. The right and left hand sides correspond to the right and left bodies respectively. The white section is the connection point between the two shields at rear part. From Figure 3.5, the following are found

1) In case of the left body, the gap around the shield periphery,  $U_n$  for the reduction rates less than 0.5, is smooth and larger than -20 mm, which indicates that the left body is inside of the excavation area with a little bit rightward rotation of the shield.

The  $U_n$  for the reduction rate 0.75 is between 50mm and 30mm and shows the dense contour line, which indicates that the left body rotates upward as the right body rotation.

2) On the other hand, in the case of the right body, the range of  $U_n$  is much wider than that of the left body. And as the reduction rate increases, the minimum value of the  $U_n$  decreases and the maximum value of  $U_n$  increases.

3) Except for the reduction rate 0.75, the  $U_n$  distribution at the right front body is almost constant along the machine axis and smaller at the crown part, and the  $U_n$  distribution at the right rear body shows that the right rear body keeps horizontally against the ascent tunnel alignment of the right body,

4) The  $U_n$  distribution for the reduction rate 0.75 shows that the left body rotates upward as the right body rotates upward, even the articulation mechanism is used.

### 3.2.5 Effective Normal Earth Pressure

Figure 3.6 show the effective normal earth pressure  $\sigma'_n$ . From Figure 3.6, the followings are found:

1) Case (a) and (b) show the almost same results.  $\sigma'_n$  is slightly more pressure at the invert of the shield center on the right front body and at the crown of the left rear body, while the other part does not show significant pressure.

2) In case (c),  $\sigma'_n$  is a little more obvious. Case (d) has a major ground reaction, especially at the position  $U_n$  is positive value in Figure 3.5.

These are because in the case of reduction rate 0.75, the right body rotates to upward to fit for the initial excavation surface due to not enough overcutting and the left body also rotates to upward with the rotation of the right rear body. As a results, the skin friction increases and the shield velocity decreases.

### 3.2.6 Summary

The influence of the copy cutter length on behavior can be summarized as follows:

1) In case of the reduction rate 0.00, the trace of the shield and the yawing, pitching and rolling angles of the shield almost follow the planned values. This means that the shield can be controlled along the planned alignment more precisely when the operational parameters are adjusted.

2) In case of the reduction rate 0.00 (CCL=400 mm) and 0.25 (CCL=300 mm), the shield behavior are almost same. This means that the copy cutter length 300 mm is enough to construct a spiral tunnel in this case.

3) In case of the reduction rate 0.50 (CCL = 200 mm), the pitching angle of the shield shows upward and the velocity of the shield decreases a little bit. This is because due to not enough overcutting the right front body touches the excavation surface, the friction around the shield increases and the shield rotates upward.

4) In case of the reduction rate 0.75 (CCL = 100 mm), the tendency in case of reduction rate 0.50 is emphasized, and the distribution of the ground reaction force acting on the skin plate at the left body shows that the left body rotates upwards. This is because the gap between the excavation surface and the skin plate becomes smaller.

### 3.3 Parameter 2: Crease Angle $\theta_{CV}$ and Pitching Angle $\phi_{PRR}$

In this section, the influence of the crease angle of the right body and the pitching angle of the right rear body on shield behavior is discussed in following three cases:

$$1) (\theta_{CV}, \phi_{PRR}) = (\theta_{CV}, 0) \text{ (Corresponds section 3.2: Parameter 1, from Figure 3.1 to Figure 3.6)}$$

$$2) (\theta_{CV}, \phi_{PRR}) = (0.5\theta_{CV}, -0.5\theta_{CV})$$

$$3) (\theta_{CV}, \phi_{PRR}) = (0, -\theta_{CV})$$

From Figure 3.7 to Figure 3.16 show the results with the reduction rate change, which are similar to the ones in Parameter 1. Therefore, the influence of  $(\theta_{CV}, \phi_{PRR})$  on shield behavior at each reduction rate will be discussed.

#### 3.3.1 Shield Behavior

From Figure 3.1, Figure 3.2, Figure 3.7 and Figure 3.8, the followings are found:

1) At each reduction rate, the pitching angle of shield  $\phi_p$  decreases when  $|\theta_{CV}|$  decreases with  $\theta_{CV} > 0$  and  $|\phi_{PRR}|$  increases with  $\phi_{PRR} < 0$ .

2) In case of reduction rate 0.00 and 0.25 and  $\phi_{\text{pRR}} = 0, -0.5\theta_{\text{CV}}$  and  $-\theta_{\text{CV}}$  when  $|\theta_{\text{CV}}|$  decreases with  $\theta_{\text{CV}} > 0$  and  $|\phi_{\text{pRR}}|$  increases with  $\phi_{\text{pRR}} < 0$  the velocity of shield  $v_s$  decreases and stops before 20 m distance.

3) In case of reduction rate 0.50,  $v_s$  increases when  $(\theta_{\text{CV}}, \phi_{\text{pRR}})$  changes from  $(\theta_{\text{CV}}, 0)$  to  $(0.5\theta_{\text{CV}}, -0.5\theta_{\text{CV}})$ . However  $v_s$  decreases when  $(\theta_{\text{CV}}, \phi_{\text{pRR}})$  changes from  $(0.5\theta_{\text{CV}}, -0.5\theta_{\text{CV}})$  to  $(0, -\theta_{\text{CV}})$ . This indicates that with reduction 0.50 and  $\phi_{\text{pRR}} = -0.5\theta_{\text{CV}}$ ,  $v_s$  achieves the largest value although the shield still stops before 20 m distance.

4) In case of reduction rate 0.75, when  $(\theta_{\text{CV}}, \phi_{\text{pRR}}) = (0, -\theta_{\text{CV}})$  the shield moves back because the friction on skin plate is so high and the rotation of the right body is limited due to the small CCL (100 mm). On the other hand, when  $(\theta_{\text{CV}}, \phi_{\text{pRR}}) = (0.5\theta_{\text{CV}}, -0.5\theta_{\text{CV}})$ ,  $v_s$  increases and the shield just stops around 15 m distance, which is longer than the one at  $(\theta_{\text{CV}}, \phi_{\text{pRR}}) = (\theta_{\text{CV}}, 0)$

5) At each reduction rate,  $\theta_{yT}$  decreases when  $|\theta_{\text{CV}}|$  decreases with  $\theta_{\text{CV}} > 0$  and  $|\phi_{\text{pRR}}|$  increases with  $\phi_{\text{pRR}} < 0$  after articulation start ( $\theta_{yT} = 120$  min, 60 min, 0 min in  $\phi_{\text{pRR}} = 0, -\theta_{\text{CV}}/2, -\theta_{\text{CV}}$  respectively). On the other hand, the curvature on the vertical plane  $\kappa_v$  also decreases and becomes to the negative value around the articulation point ( $\kappa_v$  is about 0, -0.025 and -0.05 in  $\phi_{\text{pRR}} = 0, -\theta_{\text{CV}}/2, -\theta_{\text{CV}}$  respectively). This points out that the alignment of shield around the articulation point  $\phi_{\text{pRR}} = -\theta_{\text{CV}}/2, -\theta_{\text{CV}}$  is an upward vertical curve.

### 3.3.2 Trace

Except for the tendency in Parameter 1, from Figure 3.3, 3.9 and 3.10, it is found that the difference between the calculated and the planned trace on vertical plane in  $\phi_{pRR} = -\theta_{CV}$  is larger than the one in  $\phi_{pRR} = 0, -\theta_{CV} / 2$ .

### 3.3.3 Force

From Figure 3.4, 3.11, 3.12, it is found that, at each reduction rate, the force of  $f_3, F_{3p}$  increases with  $F_{3p} < 0$  and the force of  $f_4, F_{4p}$  decreases with  $F_{4p} > 0$  when  $|\theta_{CV}|$  decreases with  $\theta_{CV} > 0$  and  $|\phi_{pRR}|$  increases with  $\phi_{pRR} < 0$ . Then, the  $F_{3p}$  and  $F_{4p}$  are around zero in  $\phi_{pRR} = -\theta_{CV}$ .

### 3.3.4 Gap Around Shield Periphery

From Figure 3.5, 3.13 and 3.14, the followings are found with each reduction rate:

1) In case of the left body, the range of the gap around the shield periphery  $U_n$ , increases when  $|\theta_{CV}|$  decreases with  $\theta_{CV} > 0$  and  $|\phi_{pRR}|$  increases with  $\phi_{pRR} < 0$ . On the left spring line, the gap increases. This means that  $|U_n|$  increases with  $U_n < 0$  and achieves more than 20 mm in  $\phi_{pRR} = -\theta_{CV}$ . On the right spring line,  $|U_n|$  decreases with  $U_n < 0$  until  $U_n > 0$  and achieves more than 0 mm in  $\phi_{pRR} = -\theta_{CV}$ . This indicates that the left body is still inside of the excavation area with a little bit rightward rotation of the shield and the ground reaction force acting on the left body at the right spring line increases lightly.

2) In case of the right body, the gap distributing around the crown of the right front body and the bottom of the tail right body decreases ( $|U_n|$  decreases with  $U_n < 0$ ). The reverse tendency

occurs around the tail crown of the right rear body ( $|U_n|$  increases with  $U_n < 0$ ). This indicates that the right body moves on an upward vertical curve.

Except for reduction rate 0.75, the gap around the left spring line of the right front body decreases until the shield touches and pushes on the excavation surface when  $|\theta_{CV}|$  decreases with  $\theta_{CV} > 0$  and  $|\phi_{pRR}|$  increases with  $\phi_{pRR} < 0$ .

### 3.3.5 Effective Normal Earth Pressure

From Figure 3.6, 3.15 and 3.16, with each reduction rate value, when  $|\theta_{CV}|$  decreases with  $\theta_{CV} > 0$  and  $|\phi_{pRR}|$  increases with  $\phi_{pRR} < 0$ , the followings are found:

- 1) In case of the left body, the effective normal earth pressure  $\sigma'_n$  around the crown of the tail left body and the right spring line of the left front body increases.
- 2) In case of the right body, the  $\sigma'_n$  around the left spring line of the right front body increases.

Actually, the above mentioned results are reasonable and coincide with the relationship  $U_n$ - $\sigma'_n$  because the  $\sigma'_n$  increases at the position where the shield starts to touch the excavation surface ( $U_n > 0$ ).

### 3.5.6 Summary

The influence of the crease angle of the right body  $\theta_{CV}$  and pitching angle of the right rear body  $\phi_{pRR}$  can be summarized as follows:

- 1) The pitching angle  $\phi_p$  cannot follow the planned value in  $\phi_{pRR} = -\theta_{CV} / 2, -\theta_{CV}$ . This means that with the inappropriate value of  $\theta_{CV}$  and  $\phi_{pRR}$ , it is impossible to control the shield.
- 2) The velocity  $v_s$  decreases and stops before the planned distance because the friction on skin

plate increases due to the ill-suited movement of the right body during rotation ( $\theta_{CV}$  and  $\phi_{PRR}$  not suitable) even if the large CCL is used (CCL=400 mm).

3) The effective normal earth pressure  $\sigma'_n$  on the left body has a trivial change when the  $\theta_{CV}$  and  $\phi_{PRR}$  change since the left body is on a straight line.

### 3.4 Parameter 3: Share of Jack Force For Both Bodies

In Case No. 350023 and 350083 as shown in Table 3.3, the shield moved back during the analysis and finally the analysis was terminated. This is considered as follows:

1) The overcutting at the left body is only 10 mm since the tunnel alignment is straight line, while at the right body, the overcutting is done by copy cutter and the articulation is also applied. Then the friction resistance between the ground and the skin plate at the left body is larger than that at the right body.

2) In Case No.350023, the jack thrust at the right body is larger than that at the left body. Then since the large horizontal moment to left turn is generated, the H&V shield rotates to leftward. On the other hand in Case No.350083, the tendency is reverse and the H&V shield rotates to rightward.

3) Due to the small overcutting at the left body, the frictional resistance around the skin plate at the left body increases as the shield rotates.

4) Finally the total jack thrust is short against the frictional resistance around the skin plate and the face pressure, then the shield moved back.

Therefore, the results in Case No. 350043 and Case No. 350063 were shown and discussed in the next section.

### 3.4.1 Shield Behavior

The shield behavior are shown in Figure 3.17. Comparing both Case (a) (Case No.350043) and Case (b) (Case No. 350063) in Figure 3.17, the followings are found:

- 1) The total advanced distance in Case (b) is a little bit longer than that in Case (a).
- 2) The yawing angle  $\phi_y$  in Case (b) shows that the shield takes a right turn, and that in Case (a) shows that the shield takes a left turn, respectively. Furthermore the rotation angle of the shield at last in Case (b) is a little bit smaller than that in Case (a).
- 3) The tendency of the pitching angle  $\phi_p$  and the rolling angle  $\phi_r$  is almost same at the both cases. The  $\phi_p$  is close to zero before the shield enters to the spiral part, but increases gradually at the spiral part. The  $\phi_r$  follows the planned  $\phi_r$ .
- 4) The  $v_s$  in Case (b) is a little bit larger than that in Case (a).

These can be explained as follows: in Case (b), the absolute value of the  $\phi_y$  at last is a little bit smaller than that in Case (a); therefore the frictional resistance around the skin plate is smaller, especially at the left body; the velocity of the shield is larger; and the advanced distance of the shield is longer, compared with those in Case (a).

### 3.4.2 Trace

Figure 3.18 shows the trace of the shield. The followings are found:

- 1) On the vertical plane, in both Case (a) and Case (b), the calculated trace of the right body on the vertical plane shows than the planned trace.
- 2) On the horizontal planes, in Case (a) the shield moves leftward from the planned trace, while in Case (b) the opposite tendency occurs due to the moment created by the difference of the jack force on the left and the right body.

### 3.4.3 Force

Figure 3.19 shows the total of the forces and moment with distance. The followings are found:

- 1) The moment of  $f_3$ ,  $M_{3p}$  changes the sign from negative to positive; and
- 2)  $M_{3r}$  increases when the share of jack force increases from 0.4 to 0.6.

This is due to the difference between the jack forces on both body.

### 3.4.4 Gap Around Shield Periphery

The gap from the initial excavated surface to the shield skin plate in normal direction  $U_n$  is shown in Figure 3.20, where the left side and the right side are the left body and right body, respectively, and the shield skin plate is unfolded as a flat plate, that is, the vertical axis shows the length of the shield, and the horizontal axis represents the circumference of the shield. From Figure 3.20 the followings were found:

- 1) In Case (b), at the left body, the passive state of the ground is developed drastically at the left spring line in the rear part (90 degrees), and the active state occurred at the opposite site.
- 2) In Case (b), at the right body, the passive state of the ground appears below the spring line of the front body and around the crown at the shield tail of the rear body.
- 3) In Case (a), the magnitude of the normal distance  $U_n$  is a little bit larger than that in Case (b).
- 4) In case of the left body, the tendency of the distribution of the active state and the passive state in Case (a) is reverse against that in Case (b).
- 5) The magnitude of the  $U_n$  in the left body is much smaller than that of the right body.

There can be consider as follows:

- 1) The shield rotates to rightward and leftward in Case (b) and Case (a) respectively.

2) The overcutting by copy cutter and articulation angle are applied to the right body, while those are not applied to the left body.

3) The overall distribution of the  $U_n$  is reasonable from the viewpoint of the geometric condition based on the interaction between the shield skin plate and the excavated surface of the ground.

### 3.4.5 Effective Normal Earth Pressure

The effective normal earth pressure acting on the shield periphery  $\sigma'_n$  is plotted in Figure 3.21. From Figure 3.21, the followings are found:

- 1) The normal effective earth pressure  $\sigma'_n$  is close to zero at the main part.
- 2) In the case of the left body, the distribution of the  $\sigma'_n$  in Case (b) is reverse against that in Case (a).
- 3) In the case of the right body, the distribution of the  $\sigma'_n$  show the same tendency for the both Case (b) and Case (a).
- 4) There are considered to be the reflection of the distribution of the  $U_n$  and the stiffness of the ground.

### 3.4.6 Summary

The influence of the share of the jack force can be summarized as follows:

- 1) The share of jack thrust on each body gives much influence to the shield behavior, especially in yawing angle  $\phi_y$  and velocity  $v_s$ , even the total amount of the jack thrust is constant.
- 2) As the jack thrust at the right body increases, the shield takes a left turn, the frictional resistance around the left body increases, then the shield velocity  $v_s$  decreases and finally the shield moved back in the analysis.

3) With the changes of the share of jack thrust on each body, the distribution of the  $U_n$  and  $\sigma_n$  are reasonable from the view point of the geometric condition between the ground and the skin plate.

### 3.5 Parameter 4: Ground Stiffness

#### 3.5.1 Shield Behavior

Figure 3.22 shows the shield behavior of parameter study on ground stiffness. From Figure 3.22 the followings are found:

- 1) The velocity  $v_s$  in Case (b) is very higher than that in Case(a)
- 2) The  $\phi_p$ ,  $\phi_y$  and  $v_s$  don't follow the planned value.

#### 3.5.2 Trace

Figure 3.23 shows the trace of shield with the influence of the ground stiffness. The followings are found:

1) On the vertical planes, the calculated trace of both body in Case(b) is lower than the planned one, while in Case(a) only the calculated trace of right body is slightly higher than the planned one and the left body follows its planned trace.

2) On the horizontal planes, the left body and the right body in both Cases follow the planned trace. These are because the shield moves more than the planned distance since the shield velocity  $v_s$  in Case(b) is so fast.

- 3) In Case(a) the calculated trace matches the planned one, compared with Case(b).

#### 3.5.3 Force

Figure 3.24 shows the total of the forces and moments with distance. It is found that the magnitude of  $f_s$  moment,  $|M_{sp}|$  in Case(b) is less than the one in Case(a)

#### 3.5.4 Gap Around Shield Periphery

Figure 3.25 shows the distribution of the  $U_n$  in Case(a) and Case(b). The following are found:

1) The distribution tendency is almost similar.

2) The  $U_n$  around the bottom of the end of right front body in Case(b) increases a little bit compared to that in Case(a).

### 3.5.5 Effective Normal Earth Pressure

Figure 3.26 shows the effective normal earth pressure acting on the shield periphery  $\sigma'_n$  in Case(a) and Case(b). From this figure, it is found that the distribution tendency is almost similar.

### 3.5.6 Summary

The influence of the ground stiffness can be summarized as follow:

1) The ground with high stiffness can help machine, permitting the rotation more easily, increasing the velocity.

2) The stiffness of the ground may not be influence to the effective normal earth pressure.

## CHAPTER 4: APPLICATION

### 4.1 Site Description

The target tunnel is Tachiaigawa rainwater discharge tube, where two tunnels are constructed at the same time by the H&V shield. The first one built by the left body of the H&V shield (Tunnel A) is in a horizontal alignment including a leftward curve and a straight line. The second one created by the right body of the H&V shield (Tunnel B) is parallel with Tunnel A in a horizontal plane before rotation around Tunnel A from the rightward transverse direction to the upward vertical one. The plane and longitudinal view of the tunnel and spiral steps are shown in Figure 4.1.

In this study, the segmental rings at the sharp curve and at the spiral section were used for the analysis; that is, the analysis length is about 220 m. The overburden depth around the analysis area is about 24 m, and the groundwater level is TP-0.97 m. The ground properties are shown in Table 4.1.

The ground reaction curves,  $K-U_n$  relationships, used in the kinematic shield model, for Ylc, Toc, Tos, Tog, and Eds layers are shown in Figure 4.2. The dimensions of the tunnel and the shield are shown in Table 4.2 and Figure 4.3 where LF, LR, RF, and RR are the left front, left rear, right front, and right rear bodies respectively. Tunnels A and B are constructed in layers Ylc, Toc, Tog, Tos, and Eds, as shown in the longitudinal tunnel view of Figure 4.1 by the H&V shield with 2.925 m in the outer radius of both shields and 8.5 m for the left and 7.8 m for the right body in total length.

### 4.2 Simulation of H&V Shield at a Sharp Curve

### 4.2.1 Operation Data

The input data used for simulation are shown in Figure 4.4. The tunneling operations are jack thrust  $F_{3r}$ , horizontal jack moment  $M_{3p}$  (+: right turn), vertical jack moment  $M_{3q}$  (+: downward), cutter face rotation direction  $CF$  (1: counterclockwise direction, viewed from shield tail), copy cutter length  $CCL$ , area of applied copy cutter  $CC$  range, and articulation angle in horizontal direction  $\theta_H$  (+: left-turn), which are employed to control the shield position and the shield behavior during excavation. The behavior of both shields is defined as yawing angle  $\phi_y$  (+: right turn), pitching angle  $\phi_p$  (+: downward), and rolling angle  $\phi_r$  (+: clockwise direction, viewed from shield tail). The excavation conditions are shield velocity  $v_s$ , slurry pressure  $\sigma_m$ , and slurry density  $\gamma_m$  in the chamber, which is usually controlled to stabilize the tunnel face.

$F_{3r}$  of about 10 MN is applied to the shield to drive the shield forward against earth pressure at the face and friction on the shield skin plate as its advance. Since both tunnel planned alignments at the analysis area are horizontal leftward curves,  $M_{3p}$  is applied to negotiate the horizontal moment due to normal earth pressure around skin plate  $M_{5p}$ , which gets much influence of no earth pressure around the connection point of the rear body.  $M_{3q}$  is mainly applied against the vertical moment due to the earth pressure on the cutter disc and the self-weight of the shield. The value of the abovementioned three parameters is determined through two steps.

First, the forces and moments generated on the H&V shield are calculated without the jack force ( $F_{3r}$ ,  $M_{3p}$ , and  $M_{3q}$  are zero). The used simulation model has been presented in the previous chapter. From the results of this step, the initial values of the jack force are defined. Second, those values will be modified aiming to keep the H&V shield following the planned tunnel alignment. The most optimal values will be obtained when the agreement between the calculated and planned data has been achieved.

$CF$  defines the rotation direction of cutter torque, which is generated due to the shearing resistance on the cutter disc, and its rotation direction causes the shield rolling around its axis.

Therefore, the rotation direction of the cutter disc is alternately controlled to maintain the use of facilities inside the shield. Since the tunnel is excavated at the curved alignment, the copy cutter is employed at around the left spring line of the shield for the leftward curve. The copy cutter is used to increase the excavated area around the cutter disc, which reduces the ground reaction force acting on the skin plate and makes a shield easily translate or rotate to this field.  $\theta_H$  of the left and right bodies at the leftward curve are about 270 min and 240 min respectively, which correspond to the radius of curvature of the horizontal alignment of both tunnels. It means that the horizontal curve radius of Tunnel A is less than that of Tunnel B. The use of articulation of shield is to fit the skin plate to the excavated area by cutter disk and copy cutter, which also reduces the ground reaction force acting on the surface plate and makes a shield easily translate or rotate.

$\phi_y$  shows that both bodies' rotation follow the planned horizontal tunnel alignment at the leftward curve.  $\phi_p$  and  $\phi_r$  are zero because the H&V shield is on a horizontal plane and its components (the left and right bodies) do not rotate around their axis.

Shield velocity  $v_s$  of 0.025 m/min and  $\gamma_m$  of 13.5 kN/m<sup>3</sup> were set, based on the experience. To stabilize the face,  $\sigma_m$  about 334 kPa is applied based on the lateral earth pressure at the tunnel face.

## 4.2.2 Simulation Results

The shield behavior in the sharp curve is then simulated from ring numbers 1 to 71 using the operational control data and the excavation condition in Figure 4.4.

### 4.2.2.1 H&V Shield Behavior

Figure 4.5 shows the planned alignment and the calculated traces of the left and right bodies of the H&V shield on vertical and horizontal planes. The calculated and planned time-dependent parameters  $\phi_y$ ,  $\phi_p$ ,  $\phi_r$ , and  $v_s$  are compared in Figure 4.6. Figure 4.5 shows that the maximum difference between the planned alignment and the calculated traces is 1.8 cm and 2.7 cm for the

vertical position of the left and right bodies respectively and is 32.5 cm for the horizontal position of both bodies. In Figure 4.6, the calculated  $\phi_r$  indicates that the shield performs good negotiation to the sharp leftward curve. The calculated  $\phi_p$  shows the lookup of 30 min at the end of the leftward curve (around the distance 40 m), compared with the planned  $\phi_p$  and the  $\phi_p$  along the longitudinal tunnel alignment up to the distance 33 m is within 15 m lookup. The calculated  $\phi_r$  at the sharp curve gradually decreases from the start to the end of the curve up to 24 min; that is, the H&V shield rotates to counterclockwise viewed from tail. The calculated  $v_s$ , with the maximum difference from the planned  $v_s$  just 0.6 mm/min, nearly coincides with the planned one. Therefore, these figures, in general, show overall good agreement between the calculations and the plan of shield behavior. Considering the change of geological conditions along the longitudinal tunnel alignment and the connection condition between the right and left rear bodies of the H&V shield, these differences can be adjustable by updating the shield operation on time, based on real-time measurement on shield position, rotation, etc.

#### 4.2.2.2 Ground-shield Interaction

The forces and moments described hereafter are considered at the distance of 4.345 m on the straight line and 22.574 m on the sharp curve as an example. The distance between the original excavated surface and the shield skin plate  $U_n$  around the shield skin plate are shown in Figures 4.7 and 4.9, and the effective normal earth pressure acting on the shield periphery  $\sigma_n'$  is plotted in Figures 4.8 and 4.10, where the shield skin plate is unfolded as a flat plate; that is, the vertical axis shows the length of the shield and the horizontal axis represents the circumference of the shield.  $\sigma_n'$  is determined by applying  $U_n$  to the ground reaction curve in Figure 4.2.

In case of excavation at the straight line, the following are found from Figure 4.7:

1)  $U_n$  at almost all of the area is a negative value. This is because of the overcutting by cutter face and copy cutter.

2)  $U_n$  becomes positive in a little area at the invert around the tail of both bodies, where the H&V shield skin plate pushes the ground. At the opposite side (the crown around the tail of both bodies),  $U_n$  becomes negative, where the earth pressure is in active state. These characteristics result from the equilibrium condition.

3) The contour line becomes intense at the right spring line (from 180 to 360 degrees) around the cutter face of both bodies. This comes from the application of copy cutter shown in the copy cutter range of Figure 4.4.

4) The distribution of  $U_n$  at the both right and left bodies is almost same. This phenomenon is natural when the shield is in the straight line and prepares to enter the leftward curve.

From Figure 4.8, the following are found:

1)  $\sigma_n'$  is close to zero in the almost area because of the self-stabilization of the ground due to the gap between the excavated surface and the shield skin plate.

2) The high intensity of  $\sigma_n'$  appears in the area where  $U_n$  is positive, which is reasonable from the viewpoint of ground-structure interaction.

3)  $\sigma_n'$  is zero at the area where the copy cutter is applied. This means that the shield does not touch the ground.

4)  $\sigma_n'$  around both spring lines of both bodies is smaller than that at the invert and crown of both bodies. This is because the horizontal effective earth pressure is smaller than the vertical one due to smaller  $K_{ho}$  than  $K_{vo}$ , as shown in Table 4.1.

When the H&V shield excavates at the sharp curve, the following are found from Figure 4.9:

1)  $U_n$  at the almost area is negative. This corresponds to the overcutting by cutter face and copy cutter.

2)  $U_n$  becomes positive along the invert of the rear left body and around the end of the right spring line of the rear right body. The H&V shield pushes the ground at these locations, whereas  $U_n$  at the opposite side becomes negative. These characteristics result from the equilibrium condition and correspond to the leftward curve of the tunnel alignment.

3) The contour line at the crown and the invert of both bodies becomes intense. This is because of the application of copy cutter shown on the copy cutter range of Figure 4.4.

4)  $U_n$  along the left spring line at the middle position of each body is larger than that at the end position of each body, while  $U_n$  along the right spring line has a reverse tendency. These come from the geometric condition between the shield and the excavated area.

From Figure 4.10, the following are found:

1) The intensity of  $\sigma_n'$  also appears in the area where  $U_n$  is positive due to ground-structure interaction.

2)  $\sigma_n'$  is close to zero in the almost area. This can be explained as the same reasons in Figure 4.8.

#### 4.2.2.3 Forces and Moments Acting on the Shield

The forces and moments acting on the shield at the distance 4.345 m and 22.574 m are summarized in Tables 4.3 and 4.4 respectively, where  $F$  and  $M$  are the force and the moment acting on the shield respectively; the subscripts  $p$ ,  $q$ , and  $r$  are the directions in the machine coordinate system in Figure 2.16; and the subscript numbers are the types of the forces in Figure 2.16. From these tables, the following are found:

1) The forces and moments in these tables indicate that they satisfy the equilibrium conditions.

2) The total amount of each component of forces and moments at the connection point is the interaction one between the left and right bodies. The forces in transverse direction  $F_q$  acting at the connection point between the left and right bodies is about 3,000 kN. Since the connection

area has no earth pressure, each body pushes the opposite side body. The moment around shield axis  $M_r$  from the right body to the left body at the connection point is about  $-3400$  kN-m. This means that the right body generates the  $M_r$ , so that the left body rotates around the shield axis to a counterclockwise direction. This calculated  $M_r$  coincides with the rolling angle  $\phi_r$  of the left and right bodies in Figure 4.6. Other components of forces and moments are not so large.

3) This result indicates that proper shield operation of the left and right bodies is necessary to escape excess forces and moments at the connection point, taking the interaction forces and moments at the connection point into account.

### 4.3 Simulation of H&V Shield at the Spiral Section

#### 4.3.1 Operation data

The input data used for simulation at the spiral section are shown in Figure 4.11. The function of tunneling operations has been mentioned in section 4.2.1. In this section, the modification of the value of jack force, articulation angle and copy cutter range and length will be presented.

$F_{3r}$  of from 10 to 14 MN is applied to the both left and right body shield not only to drive the H&V shield forward against earth pressure at the face and friction on the shield skin plate but also to suppress the eccentric moment acting on the connection point between the left and right body. Since the planned alignments of Tunnel B at the analysis area is spiral curve,  $M_{3pR}$  of right body is set to zero. The equality of  $M_{3qL}$  and  $M_{3qR}$  is applied along alignment of Tunnel A and B against the vertical moment due to the earth pressure on the cutter disc and the self-weight of the shield. The value of the above mentioned three parameters is determined through two steps similar to the method it is at a sharp curve.

Since the alignment of Tunnel A is straight line and the one of Tunnel B is a spiral curve, the copy cutter is only employed at around the crown of the right body at the beginning and the end half of the spiral section. The copy cutter is used to increase the excavated area around the

cutter disc, which reduces the ground reaction force acting on the skin plate and makes the right body easily rotate to this field.

$\theta_H$  and  $\theta_V$  of the left body are zero for straight line.  $\theta_H$  of the right body is about 10 min along this area for the leftward movement of right body.  $\theta_V$  of the right body increases from zero to 240 min and decreases to 30 min quickly around the beginning of spiral section.  $\theta_V$  of the right body keeps the constant value, 30 min, along the beginning half alignment of spiral section for upward movement of right body. After that the  $\theta_V$  increases gradually up to 240 min and keeps that constant value until the right body finishes the rotation at the end of the spiral section.  $\theta_V$  decrease to zero quickly when the right body returns to the straight line and H&V shield continues to excavate the ground with the vertical multi-circular section.

$\phi_y$  and  $\phi_p$  show that both bodies' rotation follows the planned tunnel alignment at the spiral section that are the straight line alignment of Tunnel A and the spiral curve alignment of Tunnel B.  $\phi_r$  of both body increases gradually up from 0 to 90 degrees because the left body rotates around its axis and the right body rotates around the axis of the left body from the horizontal multi circular shape to the vertical one.

### 4.3.2 Simulation Results

The shield behavior in the spiral section is then simulated from ring numbers 71 to 360, using the operational control data and the excavation condition in Figure 3.11.

#### 4.3.2.1 H&V Shield Behavior

Figure 4.12 shows the planned alignment and the calculated traces of the left and right bodies of the H&V shield on vertical and horizontal planes. The calculated and planned time-dependent parameters  $\phi_y$ ,  $\phi_p$ ,  $\phi_r$ , and  $v_s$  are compared in Figure 4.13. Figure 4.12 shows that the maximum difference between the planned alignment and the calculated traces is 39.5 cm and 40.2 cm for the vertical position of the left and right bodies respectively and is 133.8 cm and 130.7 cm for the horizontal position of the left and right bodies respectively.

In Figure 4.13, the calculated  $\phi_y$  indicates that the shield performs good negotiation to almost the spiral section. However, after the H&V shield passes the end-point of the spiral section at the distance 186.5 m, the difference between the planned and calculated  $\phi_y$  achieves the maximum value, 262 min, because of the tendency of the leftward movement of the machine outside of the spiral section.

The calculated  $\phi_p$  shows the lookup of about 130 min and 59 min at the distance from 49 to 95 m and from 135 to 170 m respectively. Around outside of the spiral section, the calculated  $\phi_p$  shows the tendency of the downward movement of the machine with the maximum difference between the planned and calculated  $\phi_p$  about 130 min.

The calculated  $\phi_r$  at the spiral section nearly coincides with the planned one when the maximum difference between the planned and calculated  $\phi_r$  is just 175.5 min at the distance 162.2 m when the right body rotates around 5,400 min.

The calculated  $v_s$ , with the maximum difference from the planned  $v_s$ , is 1.13 mm/min, nearly coincides with the planned one.

Although the maximum differences between the planned alignment and the calculated traces are not small (40.2 cm for the vertical position and 133.8 cm for the horizontal position), considering the complicated conditions during excavation in spiral section such as the change of geological conditions and the connection condition between the right and left rear bodies, these differences can be accepted as the good results in simulation of H&V shield behavior.

#### 4.3.2.2 Ground-shield Interaction

The forces and moments described hereafter are considered at the distance of 125.5 m on the spiral curve. The distance between the original excavated surface and the shield skin plate  $U_n$  around the shield skin plate are shown in Figures 4.14 and the effective normal earth pressure acting on the shield periphery  $\sigma_n'$  is plotted in Figures 4.15, where the shield skin plate is unfolded as a flat plate; that is, the vertical axis shows the length of the shield, and the horizontal

axis represents the circumference of the shield.  $\sigma_n'$  is determined by applying  $U_n$  to the ground reaction curve in Figure 4.2.

From Figure 4.14 the following are found:

1)  $U_n$  at more than a half of the area at the left spring line of the left body and the right spring line of the right body is a negative value because of the overcutting by cutter face and copy cutter.

2)  $U_n$  becomes positive in the rest area at the right spring line of the left body and the left spring line of the right body, where the H&V shield skin plate pushes the ground. At the opposite side,  $U_n$  becomes negative, where the earth pressure is in active state. These characteristics result from the equilibrium condition.

3) The contour line becomes intense at the crown of right rear body. This comes from the application of copy cutter shown in the copy cutter range of Figure 4.11.

4) The distribution of  $U_n$  at the left body is simple. This phenomenon is natural when the left body shield is in the straight line.

From Figure 4.15, the following are found:

1)  $\sigma_n'$  is close to zero in the almost area because of the self-stabilization of the ground due to the gap between the excavated surface and the shield skin plate.

2) The high intensity of  $\sigma_n'$  appears in the area where  $U_n$  is positive, which is reasonable from the viewpoint of ground-structure interaction.

3)  $\sigma_n'$  is zero at the area where the copy cutter is applied. This means that the shield does not touch the ground.

4)  $\sigma_n'$  around right spring lines of left body and left spring line of right body is larger than that at the invert and crown of both bodies. This is because the horizontal effective earth pressure is smaller than the vertical one due to smaller  $K_{ho}$  than  $K_{vo}$ , as shown in Table 4.1. Both spring lines are becoming the invert and crown when H&V shield is rotating.

### 3.3.2.3 Forces and Moments Acting on the Shield

The forces and moments acting on the shield at the distance 125.5 m are summarized in Tables 4.5, where  $F$  and  $M$  are the force and the moment acting on the shield; the subscripts  $p$ ,  $q$ , and  $r$  are the directions in the machine coordinate system in Figure 2.16; and the subscript numbers are the types of the forces in Figure 2.16. From these tables, the following are found:

1) the forces and moments in these tables indicate that they satisfy the equilibrium conditions.

2) the total amount of each component of forces and moments at the connection point is the interaction between the left and right bodies. The forces in transverse direction  $F_q$  acting at the connection point between the left and right bodies is about 20000 kN. Since the connection area has no earth pressure, each body pushes the opposite side body. At this distance the right body is on the higher level than the position of the left body, and the force acting on the connection point is larger by gravity. The moment around the shield axis  $M_r$  from the right body to the left body at the connection point is about  $-2700$  kN-m. This means that the right body generates the  $M_r$  so that the left body rotates around the shield axis to a counterclockwise direction. The moment around the  $p$  axis  $M_p$  and  $q$  axis  $M_q$  are about 40150 kN-m and  $-20230$  kN-m respectively. This is because the right body is on the spiral curve. It needs a large moment to rotate itself from horizontal direction to the vertical one.

3) This result indicates that proper shield operation of the left and right bodies is necessary to escape excess forces and moments at the connection point, taking the interaction forces and moments at the connection point into account.

## CHAPTER 5: CONCLUSIONS

In this study, the kinematic model of the loads acting on the H&V shield during excavation and the simulation algorithms were developed based on a model for articulated shield. This kinematic model was used to simulate the shield behavior during the excavation based on equilibrium conditions, taking into account the ground displacement around the shield. More explicitly, the model took into account the following: the gap between the shield and the excavated area around the shield, the dynamic equilibrium conditions, the cutter face rotating direction, sliding of the shield in the vertical and the horizontal directions, local collapse of the ground, the gap between the shield and the segment, etc. Furthermore, from the viewpoint of the shield tunneling behavior, the model was verified by carrying out the sensitivity analyses on the model parameters and applying it to a planned shield tunneling.

The conclusions of the entire study can be summarized as follows:

1. The operational parameters calculated by the proposed control method is valid for a sharp curve, but it is not so effective for spiral part.
2. The H&V shield behavior provided by the proposed H&V kinematic shield model is reasonable from the view point of theory.
3. The proposed model shows that the H&V shield can construct a spiral tunnel from horizontal multi-circular shape to vertical one.
4. To rotate the right body around the left body, the following were found:
  - 4.1. An articulation of the body is very effective to carry out a spiral excavation.
  - 4.2. It is better to escape the copy cutter use, since the overcutting by copy cutter changes the advance direction due to the generated horizontal and vertical transverse forces.
  - 4.3. The jack force is effective to control the advance direction of the shield and not to control the rolling of the shield.

- 4.4. Rolling shield jacks will be effective for the rolling of the shield.
- 4.5. These operational parameters cannot be considered by the shield kinematic model for a single shield and an articulated shield.
5. Through the sensitivity analyses and the application of the model to the site, it was found that each model parameters has the following characteristics:
  - 5.1 The effective rate of the copy cutter is important to reduce the friction because of the contact between the machine and the ground. This is important because the friction reduces the velocity and therefore the capacity of work in the better time. The bigger the reduction rate, the bigger the reduction on the tunneling speed.
  - 5.2 The swing angle between the left rear body and right rear body around the transverse axis ( $q$ -axis) decreases from zero degree, the normal earth pressure acting on the skin plate shows a stress concentration more especially at the right body and the velocity decreases, since the friction on the skin plate increases due to the inclination of the right body. But the swing angle does not affect so much the normal earth pressure of the left body, since the left body is on a straight line.
  - 5.3 The thrust of the jack force affects the velocity of the machine directly, since the jack force pushes the machine forward; therefore, the bigger the jack force, the bigger the excavation speed. However, if the jack force is bigger on the right side, then the machine turn left. Because of its rotation, the velocity is drastically reduced, the advanced distance reduced. On the other hand, when a major percentage of the total jack thrust is on the left body, the machine turn right. In this case, the velocity is also reduced, but not as much as in the contrary case. In the case of stiff ground, a large jack force is required to increase the velocity since the sensitivity of the earth pressure at the face to the speed of the shield advance is high. Also, the jack moment is effective for rotating the shield.

- 5.4 The stiffness of the ground has a very important influence on the tunneling machine. The stiffness actually helps the machine, permitting the rotation more easily, increasing the velocity and the reached distance if the overcutting is carried out properly. However, both types of ground in this study show a similar trend and behavior, especially the pitching and the direction angle.

## REFERENCES

- Fujita, K. (1989), Underground construction, tunnel, underground transportation, Special lecture B, *Proceedings of 12th International Conference on Soil Mechanics and Foundation Engineering*, Rio de Janeiro, Vol. 5, pp. 2159-2176.
- Huang, H. W., Liu, Y. J. and Xie, X. Y. (2003), Application of GPR to grouting distribution behind segment in shield tunnel, *Rock and Soil Mechanics*, Vol. 24 Supp., pp. 353-356.
- JGS (1996), *Introduction to Shield Tunneling Method*, JGS, 261 p. (in Japanese)
- JSCE (1986), *Standard Specification for Shield Tunneling Method*, JSCE, 290 p. (in Japanese)
- JSSMFE (1993), *Underground Construction in Soft Ground in Japan*, JSSMFE, 76 p.
- Kanayasu, S., Yamamoto, Y. and Kitahara, Y. (1995), Stability of excavation face in earth pressure balanced shield, *Proceedings of the International Symposium on Underground Construction in Soft Ground*, Fujita & Kusakabe (Eds), Balkema, Rotterdam, pp. 265-268.
- Khazaei, S., Shimada, H., Kawai, T., Yotsumoto, J. and Matsui, K. (2006), Monitoring of over cutting area and lubrication distribution in a large slurry pipe jacking operation, *Geotechnical and Geological Engineering*, Vol. 24, pp. 735-755.
- Kishio, T., Ohta, H., Nakai, N., Hashimoto, T. and Hayakawa, K. (1995), Reducing ground settlement caused by shield tunneling in soft clay, *Proceedings of the International Symposium on Underground Construction in Soft Ground*, Fujita & Kusakabe (Eds), Balkema, Rotterdam, pp. 257-260.
- Kurihara, K. (1998), Current mechanized shield tunneling methods in Japan, *Proceedings of International Congress on Tunnel and Underground Works, Tunnels and Metropolises*, Negro Jr & Ferreira (Eds), Balkema, Rotterdam, pp. 615-622.

- Kuwahara, H., Harada, M., Seno, Y. and Takeuchi, M. (1988), Application of fuzzy reasoning to the control of shield tunnelling, *Proceedings of Japan Society of Civil Engineer*, JSCE, No.391/VI-8, pp. 169-178. (in Japanese)
- Mair, R. J. (1995), Geotechnical aspects of tunnelling in soft ground, *Proceedings of the International Symposium on Underground Construction in Soft Ground*, Fujita & Kusakabe (Eds), Balkema, Rotterdam, pp. 13-22.
- Makata, H. (1980), Ground settlement prevention measures in sewer shield tunneling work (Part 1), *Bulletin of Japan Sewage Works Association*, JSA, Vol. 17, No. 191, pp. 9-19. (in Japanese)
- Makata, H. (1981), *Ground settlement prevention measures in sewer shield tunneling work with soft ground (Based on survey of Shinozaki trunk line)*, D. Eng. Thesis.
- Sakai, K. and Hoshiya, M. (1987), Prediction and control of behaviors on driving shields using Kalman filter theory, *Journal of Japan Society of Civil Engineers*, JSCE, No.385/VI-7, pp.69-78. (in Japanese)
- Sakai, K. and Hoshiya, M. (1993), Direction control method of shield tunnelling machines and its observed behaviours in some various ground conditions, *Journal of Japan Society of Civil Engineers*, JSCE, No.459/I-22, pp.139-148. (in Japanese)
- Shimizu, Y., Furukawa, K., Imai, K. and Suzuki, M. (1992), Study of the moving characteristics of a shield tunneling machines (2nd Report), *Journal of Japan Society Mechanical Engineers*, JSME, 58(554), 121-128. (in Japanese)
- Shimizu, Y. and Nishida, S. (1996), Moving characteristics of shield tunneling machine, *Journal of Japan Society of Civil Engineers*, JSCE, No.535/III-34, pp.103-114. (in Japanese)
- Shimizu, Y., Obayashi, M., Asada, K. and Suzuki, M. (1994), Movement of shield tunneling machine of articulate type and model experiment, *Journal of Japan Society Mechanical Engineers*, JSME, 60(571), pp.134-140. (in Japanese)

- Shimizu, Y. and Suzuki, M. (1992), Study of the moving characteristics of a shield tunneling machines, *Journal of Japan Society of Mechanical Engineers*, JSME, Vol. 58, No. 550, pp. 155-161. (in Japanese)
- Shimizu, Y., Suzuki, M. (1994), Movement characteristics and control method of shield tunneling machine of articulate type, *Journal of Japan Society Mechanical Engineers*, JSME, 60(571), pp.141-148. (in Japanese)
- Shimizu, Y., Yamazato, K. and Nishida, S. (1997), Estimation of shield movement with FEM, *Journal of Japan Society of Civil Engineers*, JSCE, No.575/III-40, pp.243-248. (in Japanese)
- Sugimoto, M. and Tamamura, K. (1992), Study of acting load on shield machine based on In-situ measurements, *Proceedings of 2nd Symposium on Tunnel Engineering*, JSCE, pp. 83-88. (in Japanese)
- Sugimoto, M. and Sramoon, a. (2002). Theoretical model of shield behaviour during excavation. I: Theory., *Journal of Geotechnical and Geoenvironmental Engineering*, ASCE, Vol. 128, No. 2, 138-155.
- Yamada, K., Yoshida, T., Makata, H. and Hashimoto, S. (1988), Behavior of ground displacement due to shield thrusting in alluvial subsoils and its prediction analysis, *Japan Society of Civil Engineers Collection of Theses*, JSCE, No. 373, pp. 103-111. (in Japanese)
- Sramoon, A. (2001) Study on shield tunneling behaviors by kinematic shield model, PhD thesis, Nagaoka Univ. of Technology, Niigata, Japan.
- Chen, J. (2008) Study on calculation method of overcutting space and articulation angle during curved excavation by articulated shield, PhD thesis, Nagaoka Univ. of Technology, Niigata, Japan.

- Chaiyaput, S., Huynh, T. N., and Sugimoto, M. (2015) “Influence of copy cutter length on H&V shield behavior”, *15th Asian Regional Conference on Soil Mechanics and Geotechnical Engineering (15ARC)*, Fukuoka, Japan, ISSMGE.
- Huynh, T. N., Chen, J., and Sugimoto, M. (2015) “Analysis on shield operational parameters to steer articulated shield”, *15th Asian Regional Conference on Soil Mechanics and Geotechnical Engineering (15ARC)*, Fukuoka, Japan, ISSMGE.
- Maidl, B., Herrenknecht, M., Maidl, U., and Wehrmeyer, G. (2012) *Mechanized shield tunnelling*, 2nd edition, Ernst & Sohn, Berlin, Germany.
- Muto, M., Ito, T., Usui, H., and Ishido, A. (2015) “Drive shield TBM longitudinally under a small river using the H&V shield spiral technique”, *Tunnel and Underground Space, Japan Tunnelling Association*, 46(2), 17–23 (in Japanese).
- Shield Tunnelling Association in Japan (2011a) *Technical note on multi-circular face shield method*, 6th edition, Japan, STA (in Japanese).
- Shield Tunnelling Association in Japan (2011b) *Technical note on Horizontal & vertical variation shield method*, 6th edition, Japan, STA (in Japanese).
- Sonoda, T., Hagiwara, H., Osaki, H., Noguchi T., and Nakamura, M. (1992) “Construction of underground space by a new shield tunnelling method: Spiral tunnelling and ramification of multi-circular face shield”, *Tunnelling and Underground Space Technology*, 7(4), 355–361.
- Sugimoto, M., Sramoon, A., Konishi, S., and Sato, Y. (2007) “Simulation of shield tunneling behavior along a curved alignment in a multilayered ground”, *J. of Geotechnical and Geoenvironmental Engineering, ASCE*, 133(6), 684–694.

# APPENDIX

## APPENDIX A

### ALIGNMENT OF SHIELD TUNNEL

In the geometric design of the shield tunnel, the design and the setting out of the straight and curve alignments are important aspects of the tunnel engineering works. The initial design is usually based on a series of straight sections whose positions are defined largely by the topography and the geological function of the area. The intersections of pairs of straights are then connected by a curve.

#### A.1 Circular curve

Two straight lines are connected by a circular curve of radius,  $R_{hi}$ , as shown in Figure A.1. When the straight lines project forward, it will cross each other at the intersection point ( $IP_i$ ). The angle  $\Delta_i$  at  $IP_i$  is called the angle of intersection and equals the angle measured from the beginning of curve ( $BC_i$ ) to the end of curve ( $EC_i$ ) around the center of curve ( $O_i$ ). The distance  $BC_iIP_i$  and  $EC_iIP_i$  are the tangent lengths,  $TL_i$ , which can be expressed as

$$TL_i = R_{hi} \tan\left(\frac{\Delta_i}{2}\right) \quad (i = 1, 2, 3, \dots, m) \quad (\text{A.1})$$

where  $m$  is the number of the intersection point. The length of curve from  $BC_i$  to  $EC_i$ ,  $CL_i$ , can be defined as

$$CL_i = R_{hi} \Delta_i \quad (i = 1, 2, 3, \dots, m) \quad (\text{A.2})$$

The main chord,  $C_i$ , is the straight distance from  $BC_i$  to  $EC_i$

$$C_i = 2R_{hi} \sin\left(\frac{\Delta_i}{2}\right) \quad (i = 1, 2, 3, \dots, m) \quad (\text{A.3})$$

The apex distance,  $AL_i$ , is the distance from  $A_i$  to  $IP_i$

$$AL_i = R_{hi} \left[ \sec\left(\frac{\Delta_i}{2}\right) - 1 \right] \quad (i = 1, 2, 3, \dots, m) \quad (\text{A.4})$$

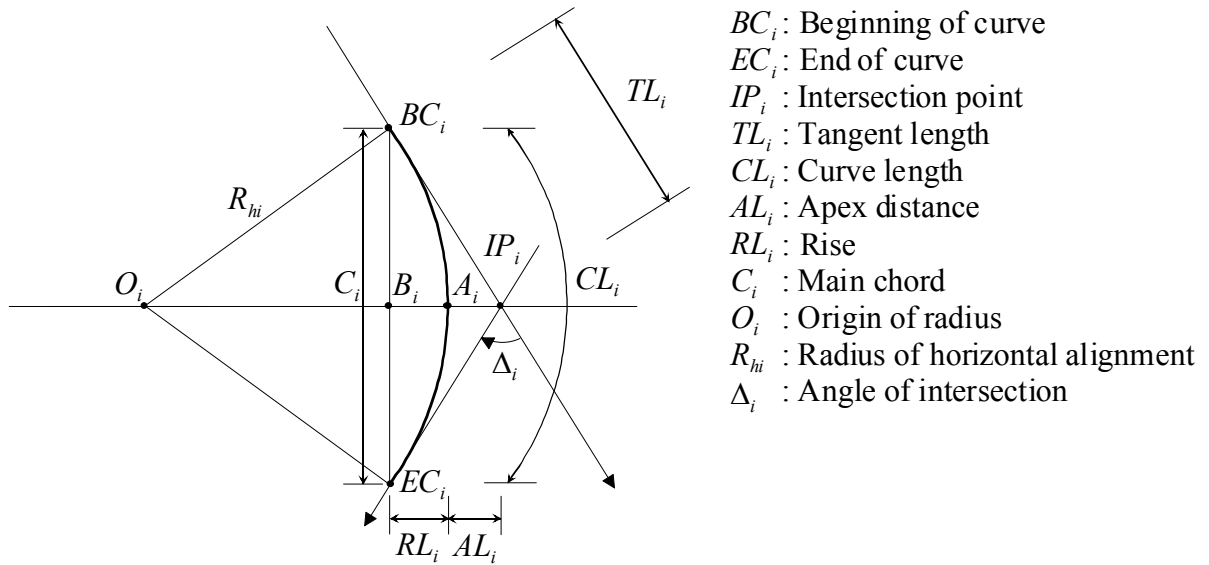


Figure A.1 Configuration of circular curve.

and  $A_iB_i$  is the rise,  $RL_i$ , which can be obtained from

$$RL_i = R_{hi} \left[ 1 - \cos\left(\frac{\Delta_i}{2}\right) \right] \quad (i = 1, 2, 3, \dots, m) \quad (A.5)$$

These equations should be deduced using a curve diagram (Refer to Figure A.1).

## A.2 Transition curve

Primary functions of a transition curve are:

1. To accomplish gradual transition from the straight to circular curve, so that curvature changes from zero to a finite value.
2. To change curvature in compound and reverse curve cases, so that gradual change of curvature introduced from curve to curve.

### A.2.1 Clothoid curve

An ideal transition curve is that which introduces centrifugal force  $F$  at a gradual rate (by time  $t$ ) i.e.  $F$  should be proportional to  $t$ . Centrifugal force at any radius  $r$  is given by

$$F = \frac{Wv^2}{gr} \propto t. \text{ Assuming that the speed of the vehicle that is negotiating the curve is constant, so}$$

$r$  and the time  $t$  have an inverse proportion relation. Then,  $lr = \text{const}$ . Thus, the fundamental

requirement of a transition curve is that its radius is of curvature at any given point should vary inversely as the distance from the beginning of the curve. Such a curve is called clothoid and is known as an ideal transition.

$C$  : Starting point of clothoid (K.A.)

$M$  : Center of circular curve through ending point of clothoid  
(K.E.)

$OX$  : Major tangential line (tangential line through origin of clothoid)

$X, Y$  : Coordinate of K.E.

$L$  : Length of clothoid

$R$  : Radius of circular curve through K.E.

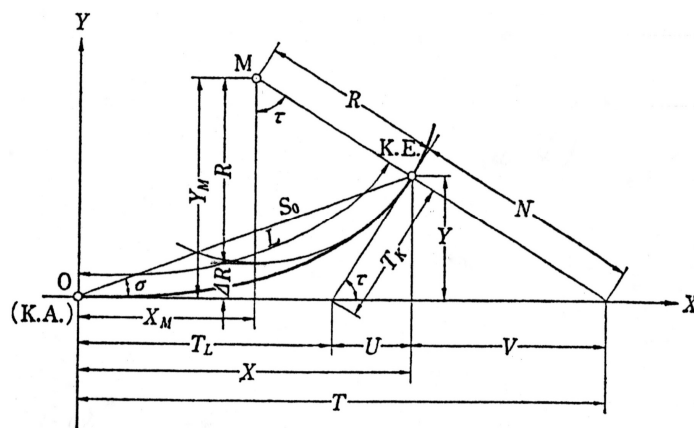


Figure A.2 Components and symbols in clothoid curve.

When defining  $R$  as radius of the curve and  $L$  as length from starting point of the curve, if the curve which satisfies the condition that the product of  $R$  and  $L$  is constant, i.e.  $RL = A^2$  ( $A$ : constant value), it is named clothoid curve.  $A$  is the representative parameter of clothoid. Figure A.2 shows components and symbols of the clothoid curve. During actual calculation, dimensionless expression is used usually. If setting  $r = R/A$  and  $l = L/A$ , the unit clothoid  $rl = 1$  can be obtained. To discuss geometric relations of each component in

clothoid, the unit clothoid is considered firstly. Actual results can be obtained by multiplying results of the unit clothoid by the scale parameter  $A$ . In calculation, two transcendental functions named as Fresnel Integrals are used to determine the horizontal and vertical coordinate by setting the starting point of clothoid as origin.

Set  $P$  as a any point with curvature radius  $r$  on clothoid curve, since  $dl = d\tau \cdot r$ ,

$$r \cdot l = A^2 \quad \frac{1}{r} = \frac{l}{A^2} \quad \frac{d\tau}{dl} = \frac{l}{A^2} \quad (\text{A.6})$$

Integrate it,

$$\tau = l^2 / 2A^2 = l^2 / 2RL = l / 2r \quad (\text{A.7})$$

And,

$$r = A^2 / l = A^2 / \sqrt{2\tau} \quad (\text{A.8})$$

$$dx = dl \cos \tau, \quad dy = dl \sin \tau \quad (\text{A.9})$$

Submit Eqs.(A.6) and Eqs.(A.8) to Eqs.(A.9),

$$dx = (A / \sqrt{2\pi}) \cos \tau d\tau \quad dy = (A / \sqrt{2\pi}) \sin \tau d\tau \quad (\text{A.10})$$

Integrate it,

$$\begin{aligned} x &= \frac{A}{\sqrt{2}} \int_0^\tau \frac{\cos \tau}{\sqrt{\tau}} d\tau \\ y &= \frac{A}{\sqrt{2}} \int_0^\tau \frac{\sin \tau}{\sqrt{\tau}} d\tau \end{aligned} \quad (\text{A.11})$$

Eqs.(A.11) is called Fresnel Integrals, in which,

$$\begin{aligned} \cos \tau &= 1 - \frac{\tau^2}{2!} + \frac{\tau^4}{4!} - \frac{\tau^6}{6!} + \dots \\ \sin \tau &= \tau - \frac{\tau^3}{3!} + \frac{\tau^5}{5!} - \frac{\tau^7}{7!} + \dots \end{aligned}$$

Then, Eqs.(A.11) can be represented as

$$\begin{aligned} x &= A\sqrt{2\tau} \left( 1 - \frac{\tau^2}{10} + \frac{\tau^4}{216} - \frac{\tau^6}{9360} + \dots \right) \\ y &= A \frac{\sqrt{2\tau}}{3} \tau \left( 1 - \frac{\tau^2}{14} + \frac{\tau^4}{440} - \frac{\tau^6}{25200} + \dots \right) \end{aligned} \quad (\text{A.12})$$

Submit  $A = \sqrt{rl}$ ,  $\tau = \frac{l}{2r}$  to it,

$$\begin{aligned} x &= l \left( 1 - \frac{l^2}{40r^2} + \frac{l^4}{3456r^4} - \frac{l^6}{599040r^6} + \dots \right) \\ y &= \frac{l^2}{6r} \left( 1 - \frac{l^2}{56r^2} + \frac{l^4}{7040r^4} - \frac{l^6}{1612800r^6} + \dots \right) \end{aligned} \quad (\text{A.13})$$

And,

$$\begin{aligned} \Delta r &= y + r \cos \tau - r \\ x_M &= x - r \sin \tau \\ t_K &= y \cos \tau \\ t_L &= x - y \cot \tau \\ S_0 &= y \cos \tau \end{aligned} \quad (\text{A.14})$$

### A.2.2 Parabolic curve

For vertical alignment, quadratic parabolic curve is adopted as a transition curve usually, which is shown in Figure A.3.

To describe the parabolic curve, the following equations are used.

$$y = \frac{1}{2K} x^2 + i_1 x \quad (\text{A.15})$$

Set slope  $i$  at any point be proportional to  $x$  represented as

$$i = \frac{1}{K} x + i_1 \quad (\text{A.16})$$

Then radius of any point  $R$ ,

$$R = \frac{\left[ 1 + \left( \frac{dy}{dx} \right)^2 \right]^{\frac{3}{2}}}{\frac{d^2 y}{dx^2}} = K(1 + i^2)^{\frac{3}{2}} \quad (\text{A.17})$$

Since  $i^2$  is extremely smaller than 1,

$$R \cong K \quad (\text{A.18})$$

From Eqs.(A.16),

$$R \cong K = \frac{x}{i - i_1} = \frac{l}{i_2 - i_1} \quad (\text{A.19})$$

Then,

$$y = \frac{i_2 - i_1}{2l} x^2 + i_1 x \quad (\text{A.20})$$

So the height  $y_v$  at changing point of slope,

$$y_v = \frac{i_2 - i_1}{2l} l_1^2 \quad (\text{A.21})$$

Since height  $y_B$  at point B, which obtained from parabolic curve is

$$y_B = \frac{i_2 - i_1}{2l} l^2 + i_1 l \quad (\text{A.22})$$

height  $y_B$  at point B, which obtained from straight line is

$$y_B = i_1 l_1 + i_2 l_2 \quad (\text{A.23})$$

Since Eqs.(A.22) should equal to Eqs.(A.23), i.e.,

$$\frac{1}{2}(i_2 - i_1)(l_1 + l_2) + i_1(l_1 + l_2) = i_1 l_1 + i_2 l_2 \quad (\text{A.23})$$

Then,

$$(l_1 - l_2)(i_1 - i_2) = 0 \quad (\text{A.24})$$

Since there are different slope in parabolic curve,  $i_1 \neq i_2$ ,

$$l_1 = l_2 \quad (\text{A.25})$$

Finally, Eqs.(A.21) is changed as

$$y_v = \frac{1}{8}(i_2 - i_1)l \quad (\text{A.26})$$

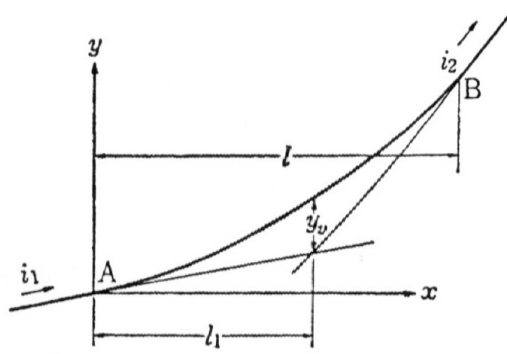


Figure A.3 Components and symbols in parabolic curve.

## APPENDIX B

## GAP FROM INITIAL EXCAVATION SURFACE TO SHIELD SKIN PLATE DURING SHIELD TUNNELING

In order to precisely predict the ground displacement around the shield periphery, the over-excavation, position of the shield, rotation of the shield, *etc.*, should be taken into consideration. To simplify the problem, the shield is assumed as a rigid body. The method to calculate the ground displacement around the shield periphery can be performed as: (i) calculates the cutter face position, (ii) calculates the calculation point on the shield periphery, and (iii) calculates the ground displacement around the shield periphery. The calculation procedures are explained as follows;

### B.1 Trace of center of cutter face

To calculate the excavated area caused by the cutter face in the ground, position of the cutter face during the shield excavation have to determine, taking into account the shield tunneling behavior. Thus, the position vector of the origin of  $C^M$ ,  $r_o$ , can be defined as

$$\mathbf{r}_o^T = \mathbf{r}_D^T + \mathbf{T}_x^{-1} \mathbf{r}_E^{T*} - \mathbf{T}_x^{-1} \mathbf{T}_y^{-1} \mathbf{T}_z^{-1} \mathbf{r}_M^M \quad (\text{B.1})$$

where  $r_D$  is the position vector of predetermined surveying point,  $r_E$  is the deviation vector between the predetermined surveying point and the actual surveying point,  $r_M$  is the position vector of the surveying point which usually measured at the center of erector inside the shield, super suffix  $T^*$  denotes the  $C^T$  rotates around the  $x$ -axis, and  $T_x$ ,  $T_y$  and  $T_z$  are the transformation matrices which defined in Appendix H.

The position vector of the center of cutter face at step  $[k]$ ,  $r_{CF[k]}$ , can be obtained from

$$\mathbf{r}_{CF[k]}^T = \mathbf{r}_o^T + l_{CF} \mathbf{k}_{[k]}^T \quad (\text{B.7})$$

in which  $l_{CF}$  is the distance from the center of cutter face to the origin of  $\mathbf{C}^M$ , and the direction vector of cutter face,  $\mathbf{k}_{[k]}$ , is defined as

$$\mathbf{k}_{[k]}^T = \mathbf{T}_x^{-1} \mathbf{T}_y^{-1} \mathbf{T}_z^{-1} \mathbf{k}_{[k](r)}^M \quad (\text{B.8})$$

where  $\mathbf{k}_{[k](r)}$  is the unit vector in the  $r$ -axis direction defined as  $[0 \ 0 \ 1]^T$ .

The trace of the center of cutter face is illustrated in Figure B.1, and its unit vector from step  $[k-1]$  to step  $[k]$ ,  $\mathbf{e}_{CF[k]}$ , can be calculated as

$$\mathbf{e}_{CF[k]}^T = \frac{\mathbf{r}_{CF[k]}^T - \mathbf{r}_{CF[k-1]}^T}{\left| \mathbf{r}_{CF[k]}^T - \mathbf{r}_{CF[k-1]}^T \right|} \quad (\text{B.9})$$

and the unit vector at the rotation axis of the shield,  $\mathbf{e}_{E[k]}$ , is

$$\mathbf{e}_{E[k]}^T = \mathbf{k}_{[k-1]}^T \mathbf{e}_{CF[k]}^T \quad (\text{B.10})$$

The physical meaning of  $\mathbf{e}_{E[k]}^T$  is explained as: If  $\mathbf{e}_{E[k]}^T \cdot \mathbf{e}_{(x)}^T > 0$ , it is shown that the cutter face rotates in counter-clockwise direction around the  $x$ -axis, otherwise the cutter face rotates in clockwise direction. If  $(\mathbf{e}_{E[k]}^T \times \mathbf{k}_{[k-1]}^T) \cdot \mathbf{e}_{(x)}^T > 0$ , it is shown that the cutter face rotates nose down, otherwise the cutter face rotates look up. Here  $\mathbf{e}_{(x)}$  is the unit vector in the  $x$ -axis direction defined as  $[1 \ 0 \ 0]^T$ . Figure B.2 illustrates movement direction of the shield.

## B.2 Position vector of calculation point on the shield periphery

Position vector of the  $ij$ th calculation point on the shield periphery,  $\mathbf{r}_{calij}$ , are defined as

$$\mathbf{r}_{calij}^M = \begin{bmatrix} \mathbf{r}_{calij(p)}^M \\ \mathbf{r}_{calij(q)}^M \\ \mathbf{r}_{calij(r)}^M \end{bmatrix} = \begin{bmatrix} R_s \cos \theta_i \\ R_s \sin \theta_i \\ l_j \end{bmatrix} \quad (\text{B.11})$$

where  $R_s$  is the outer radius of the shield,  $\theta_i$  is the  $i$ th calculation angle which measured from the  $p$ -axis in counter clockwise direction around the  $r$ -axis,

$$\theta_i = (i-1)\Delta\theta + \theta_o \quad (i = 1, 2, 3, \dots, n_C) \quad (\text{B.12})$$

in which  $\theta_o$  is the angle at the calculation point  $i=1$ ,  $\Delta\theta$  is the increment angle which obtained from  $\Delta\theta = 2\pi/n_C$ , and  $n_C$  is the number of mesh in circumferential direction of the shield.  $l_j$  is the distance from the shield tail to the center of  $j$ th mesh which obtained from

$$l_j = (j-1)\Delta l + \frac{\Delta l}{2} + l_o \quad (j = 1, 2, 3, \dots, n_L) \quad (\text{B.13})$$

where  $l_o$  is the distance from the origin of  $\mathbf{C}^M$  to the shield tail,  $\Delta l$  is the length increment in axial direction of the shield which obtained from  $\Delta l = l_M/n_L$ , in which  $l_M$  is the length of shield, and  $n_L$  is the number of mesh in longitudinal direction of the shield. The definition of  $\theta_i$  and  $l_j$  are illustrated in Figure B.3.  $\mathbf{r}_{calij}$  in  $\mathbf{C}^M$  can be transformed to  $\mathbf{C}^T$  as

$$\mathbf{r}_{calij}^T = \mathbf{T}_x^{-1} \mathbf{T}_y^{-1} \mathbf{T}_z^{-1} \mathbf{r}_{calij}^M + \mathbf{r}_o^T \quad (\text{B.14})$$

The calculation points  $i$  and  $j$  will be existed between two successive steps  $[k]$  and  $[k+1]$  if

$$\left[ (\mathbf{r}_{calij}^T - \mathbf{r}_{CF[k]}^T) \cdot \mathbf{k}_{[k]}^T \right] \left[ (\mathbf{r}_{calij}^T - \mathbf{r}_{CF[k+1]}^T) \cdot \mathbf{k}_{[k+1]}^T \right] \leq 0 \quad (\text{B.15})$$

If the calculation point, at step  $[c]$ , is in between the two cutter face positions, at step  $[k]$  and  $[k+1]$ , then the position vector of the cutter face center at the  $ij$ th calculation point,  $\mathbf{r}_{[c]ij}$ , can be obtained by linear interpolation as

$$\mathbf{r}_{[c]ij}^T = \mathbf{r}_{CF[k]}^T + \beta_{ij} \left( \mathbf{r}_{CF[k+1]}^T - \mathbf{r}_{CF[k]}^T \right) \quad (\text{B.16})$$

where  $\beta_{ij}$  is the multiplier quantity which ranges between 0 to 1. The direction vector of the shield axis at any calculation point for the step  $[c]$ ,  $\mathbf{k}_{[c]ij}$ , is obtained as

$$\mathbf{k}_{[c]ij}^T = \frac{\mathbf{k}_{[c]ij}^{\prime T}}{|\mathbf{k}_{[c]ij}^{\prime T}|} \quad (\text{B.17})$$

in which

$$\mathbf{k}_{[c]ij}^{\prime T} = \mathbf{k}_{[k]}^T + \beta_{ij} (\mathbf{k}_{[k+1]}^T - \mathbf{k}_{[k]}^T) \quad (\text{B.18})$$

The definition for unit vector of the intermediate step, step  $[c]$ , is illustrated in Figure B.4.

Since the cutter face is perpendicular to the shield axis, thus, we can define

$$(\mathbf{r}_{calij}^T - \mathbf{r}_{[c]ij}^T) \cdot \mathbf{k}_{[c]ij}^T = 0 \quad (\text{B.19})$$

Substituting the Eqs (B.16) and (B.17) into Eq (B.19) yields;

$$\begin{aligned} & \beta_{ij}^2 \left[ (\mathbf{r}_{CF[k+1]}^T - \mathbf{r}_{CF[k]}^T) \cdot (\mathbf{k}_{[k]}^T - \mathbf{k}_{[k+1]}^T) \right] \\ & - \beta_{ij} \left[ (\mathbf{r}_{calij}^T - \mathbf{r}_{CF[k]}^T) \cdot (\mathbf{k}_{[k]}^T - \mathbf{k}_{[k+1]}^T) + (\mathbf{r}_{CF[k+1]}^T - \mathbf{r}_{CF[k]}^T) \cdot \mathbf{k}_{[k]}^T \right] + (\mathbf{r}_{calij}^T - \mathbf{r}_{CF[k]}^T) \cdot \mathbf{k}_{[k]}^T = 0 \end{aligned} \quad (\text{B.20})$$

By solving this quadratic equation,  $\beta_{ij}$  will be obtained. And if  $\mathbf{k}_{[k]}^T \approx \mathbf{k}_{[k+1]}^T$  then  $\beta_{ij}$  can be approximated as

$$\beta_{ij} = \frac{(\mathbf{r}_{calij}^T - \mathbf{r}_{CF[k]}^T) \cdot \mathbf{k}_{[k]}^T}{(\mathbf{r}_{CF[k+1]}^T - \mathbf{r}_{CF[k]}^T) \cdot \mathbf{k}_{[k]}^T} \quad (\text{B.21})$$

### B.3 Gap around the shield periphery

The position vector from the center of cutter face to the  $ij$ th calculation point,  $\Delta \mathbf{r}_{[c]ij}$ , is obtained from

$$\Delta \mathbf{r}_{[c]ij}^T = \mathbf{r}_{calij}^T - \mathbf{r}_{[c]ij}^T \quad (\text{B.22})$$

The ground displacement vector at the  $ij$ th calculation point on the shield periphery,  $\mathbf{U}_{ij}$ , is calculated from

$$\mathbf{U}_{ij}^T = \frac{l_{[c]ij} - l_{EXij}}{l_{[c]ij}} \Delta \mathbf{r}_{[c]ij}^T \quad (\text{B.23})$$

where  $l_{EXij}$  is the radius of excavation which can be defined for the shield excavation without using the copy cutter as

$$l_{EXij} = R_{CF} \quad (\text{B.24})$$

If the shield excavates using the copy cutter, the excavated radius becomes

$$l_{EXij} = R_{CF} + l_{cp[k]} \quad (\text{B.25})$$

where  $R_{CF}$  is the radius of cutter face,  $l_{cp[k]}$  is the length of copy cutter used, and  $l_{[c]ij}$  can be defined as follow

$$l_{[c]ij} = \left| \Delta \mathbf{r}_{[c]ij}^T \right| \quad (\text{B.26})$$

The definition of  $U_{ij}$  is illustrated in Figure B.5. The vertical and horizontal ground displacements,  $U_{vij}$  and  $U_{hij}$ , in plane perpendicular to the shield axis can be estimated from

$$U_{vij} = \left| U_{ij(x)}^T \right| \times \text{sign}(l_{[c]ij} - l_{EXij}) \quad (\text{B.27})$$

and

$$U_{hij} = \sqrt{(U_{ij(y)}^T)^2 + (U_{ij(z)}^T)^2} \times \text{sign}(l_{[c]ij} - l_{EXij}) \quad (\text{B.28})$$

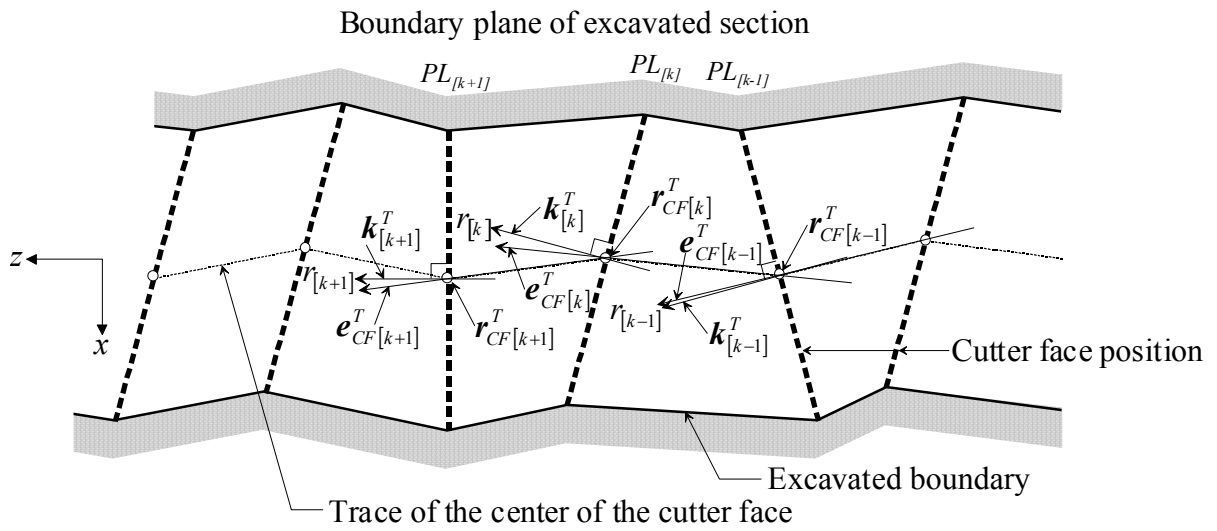


Figure B.1 Trace of the center of the cutter face.

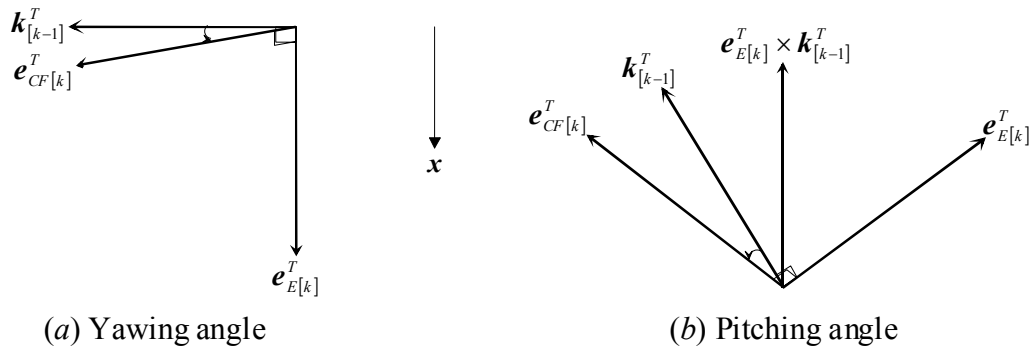


Figure B.2 Definition of shield movement direction.

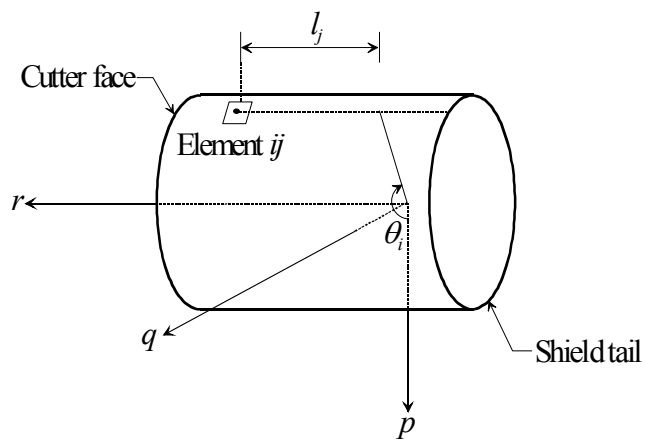


Figure B.3 Definitions of  $\theta_i$  and  $l_j$ .

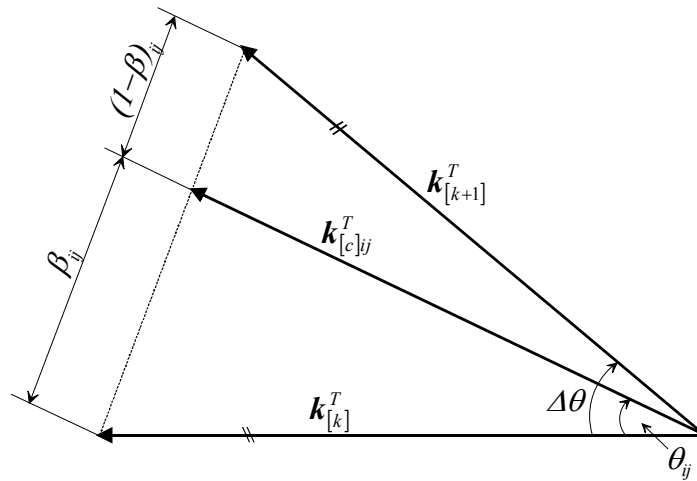


Figure B.4 Definition of unit vector for intermediate step [c].

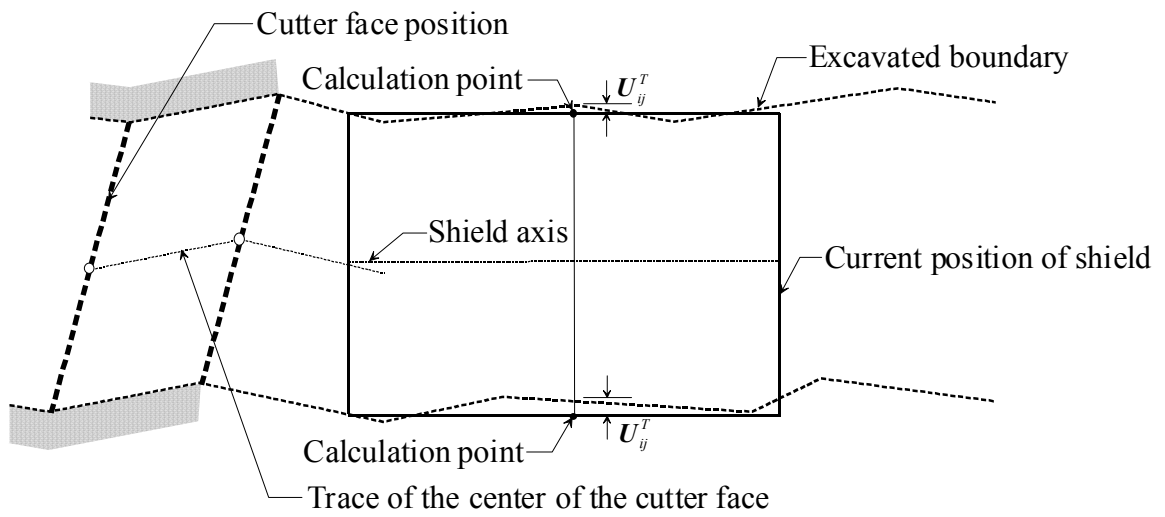


Figure B.5 Definition of ground displacement.

## APPENDIX C

### TRANSFORMATION MATRICES

Here, the cartesian coordinate system is assumed to be *right handed system* which used throughout the research work. Three coordinate systems are used to formulate the position, force, and moment, which related to each other as described in Chapter 2 and shown in Figure 2.2. Thus, the position, the force, and the moment vectors transformation are described. It is noted that the transformation matrix " $T$ " here is an ordinary transformation matrix " $T^{-1}$ "

#### C.1 Position vector transformation

##### C.1.1 Relationships between $C^T$ and $C^M$

$$\begin{bmatrix} p \\ q \\ r \end{bmatrix} = \mathbf{T}_z \mathbf{T}_y \mathbf{T}_x \begin{bmatrix} x - x_o \\ y - y_o \\ z - z_o \end{bmatrix} \quad (\text{C.1})$$

$$\begin{bmatrix} x - x_o \\ y - y_o \\ z - z_o \end{bmatrix} = \mathbf{T}_x^{-1} \mathbf{T}_y^{-1} \mathbf{T}_z^{-1} \begin{bmatrix} p \\ q \\ r \end{bmatrix} \quad (\text{C.2})$$

where

$$\mathbf{T}_x = \begin{bmatrix} 1 & 0 & 0 \\ 0 & \cos \theta_x & \sin \theta_x \\ 0 & -\sin \theta_x & \cos \theta_x \end{bmatrix} \quad (\text{C.3})$$

$$\mathbf{T}_y = \begin{bmatrix} \cos \theta_y & 0 & -\sin \theta_y \\ 0 & 1 & 0 \\ \sin \theta_y & 0 & \cos \theta_y \end{bmatrix} \quad (\text{C.4})$$

$$\mathbf{T}_z = \begin{bmatrix} \cos \theta_z & \sin \theta_z & 0 \\ -\sin \theta_z & \cos \theta_z & 0 \\ 0 & 0 & 1 \end{bmatrix} \quad (\text{C.5})$$

$$\mathbf{T}_x^{-1} = \begin{bmatrix} 1 & 0 & 0 \\ 0 & \cos \theta_x & -\sin \theta_x \\ 0 & \sin \theta_x & \cos \theta_x \end{bmatrix} \quad (\text{C.6})$$

$$\mathbf{T}_y^{-1} = \begin{bmatrix} \cos \theta_y & 0 & \sin \theta_y \\ 0 & 1 & 0 \\ -\sin \theta_y & 0 & \cos \theta_y \end{bmatrix} \quad (\text{C.7})$$

and

$$\mathbf{T}_z^{-1} = \begin{bmatrix} \cos \theta_z & -\sin \theta_z & 0 \\ \sin \theta_z & \cos \theta_z & 0 \\ 0 & 0 & 1 \end{bmatrix} \quad (\text{C.8})$$

The yawing angle  $\phi_y$ , the pitching angle  $\phi_p$ , and the rolling angle  $\phi_r$ , which are measured by an inclinometer in the shield, can be converted into  $\theta_x$ ,  $\theta_y$ , and  $\theta_z$  as follows:

$$\begin{aligned} \theta_x &= \phi_y \\ \theta_y &= \begin{cases} \phi_p & \text{(measured by torque balanced type)} \\ \tan^{-1}(\tan \phi_p \cos \phi_r) & \text{(measured by gravity type)} \end{cases} \\ \theta_z &= \begin{cases} \tan^{-1}(\sin \phi_r / \cos \phi_p) & \text{(measured by torque balanced type)} \\ \phi_r & \text{(measured by gravity type)} \end{cases} \end{aligned} \quad (\text{C.9})$$

Here, note that  $\phi_y$ ,  $\phi_p$  and  $\phi_r$  are measured at the same time after the shield rotation.

### C.1.2 Relationships between $\mathbf{C}^M$ and $\mathbf{C}^{MR}$

$$\begin{bmatrix} p_R \\ q_R \\ r_R \end{bmatrix} = \mathbf{T}_R \begin{bmatrix} p \\ q \\ r \end{bmatrix} \quad (\text{C.10})$$

$$\begin{bmatrix} p \\ q \\ r \end{bmatrix} = \mathbf{T}_R^{-1} \begin{bmatrix} p_R \\ q_R \\ r_R \end{bmatrix} \quad (\text{C.11})$$

where

$$\mathbf{T}_R = \begin{bmatrix} \cos \theta_R & \sin \theta_R & 0 \\ -\sin \theta_R & \cos \theta_R & 0 \\ 0 & 0 & 1 \end{bmatrix} \quad (\text{C.12})$$

and

$$\mathbf{T}_R^{-1} = \begin{bmatrix} \cos \theta_R & -\sin \theta_R & 0 \\ \sin \theta_R & \cos \theta_R & 0 \\ 0 & 0 & 1 \end{bmatrix} \quad (\text{C.13})$$

## C.2 Stress tensor, Force and moment vectors transformation

### C.2.1 Stress tensor transformation

Stress tensor in  $\mathbf{C}^T$  is

$$\sigma^T = \begin{bmatrix} \sigma_{xx}^T & \sigma_{yx}^T & \sigma_{zx}^T \\ \sigma_{xy}^T & \sigma_{yy}^T & \sigma_{zy}^T \\ \sigma_{xz}^T & \sigma_{yz}^T & \sigma_{zz}^T \end{bmatrix} \quad (\text{C.14})$$

Stress tensor in  $\mathbf{C}^M$  is

$$\sigma^M = \begin{bmatrix} \sigma_{pp}^M & \sigma_{qp}^M & \sigma_{rp}^M \\ \sigma_{pq}^M & \sigma_{qq}^M & \sigma_{rq}^M \\ \sigma_{pr}^M & \sigma_{qr}^M & \sigma_{rr}^M \end{bmatrix} \quad (\text{C.15})$$

Stress tensor in  $\mathbf{C}^{MR}$  is

$$\sigma^{MR} = \begin{bmatrix} \sigma_{pp}^{MR} & \sigma_{qp}^{MR} & \sigma_{rp}^{MR} \\ \sigma_{pq}^{MR} & \sigma_{qq}^{MR} & \sigma_{rq}^{MR} \\ \sigma_{pr}^{MR} & \sigma_{qr}^{MR} & \sigma_{rr}^{MR} \end{bmatrix} \quad (\text{C.16})$$

#### C.2.1.1 Relationships between $\sigma^T$ and $\sigma^M$

$$\sigma^M = \mathbf{T}_z \mathbf{T}_y \mathbf{T}_x \sigma^T \mathbf{T}_x^{-1} \mathbf{T}_y^{-1} \mathbf{T}_z^{-1} \quad (\text{C.17})$$

$$\sigma^T = \mathbf{T}_x^{-1} \mathbf{T}_y^{-1} \mathbf{T}_z^{-1} \sigma^M \mathbf{T}_z \mathbf{T}_y \mathbf{T}_x \quad (\text{C.18})$$

### C.2.1.2 Relationships between $\sigma^M$ and $\sigma^{MR}$

$$\sigma^{MR} = \mathbf{T}_R \sigma^M \mathbf{T}_R^{-1} \quad (\text{C.19})$$

$$\sigma^M = \mathbf{T}_R^{-1} \sigma^{MR} \mathbf{T}_R \quad (\text{C.20})$$

### C.2.2 Force vector transformation

Force vector in  $\mathbf{C}^T$  is

$$\mathbf{F}^T = \begin{bmatrix} F_x \\ F_y \\ F_z \end{bmatrix} \quad (\text{C.21})$$

Force vector in  $\mathbf{C}^M$  is

$$\mathbf{F}^M = \begin{bmatrix} F_p \\ F_q \\ F_r \end{bmatrix} \quad (\text{C.22})$$

Force vector in  $\mathbf{C}^{MR}$  is

$$\mathbf{F}^{MR} = \begin{bmatrix} F_{p_R} \\ F_{q_R} \\ F_{r_R} \end{bmatrix} \quad (\text{C.23})$$

#### C.2.2.1 Relationships between $\mathbf{F}^T$ and $\mathbf{F}^M$

$$\mathbf{F}^M = \mathbf{T}_z \mathbf{T}_y \mathbf{T}_x \mathbf{F}^T \quad (\text{C.24})$$

$$\mathbf{F}^T = \mathbf{T}_x^{-1} \mathbf{T}_y^{-1} \mathbf{T}_z^{-1} \mathbf{F}^M \quad (\text{C.25})$$

#### C.2.2.2 Relationships between $\mathbf{F}^M$ and $\mathbf{F}^{MR}$

$$\mathbf{F}^{MR} = \mathbf{T}_R \mathbf{F}^M \quad (\text{C.26})$$

$$\mathbf{F}^M = \mathbf{T}_R^{-1} \mathbf{F}^{MR} \quad (\text{C.27})$$

### C.2.3 Moment vector transformation

Moment vector in  $\mathbf{C}^T$  is

$$\mathbf{M}^T = \begin{bmatrix} M_x \\ M_y \\ M_z \end{bmatrix} \quad (\text{C.28})$$

Moment vector in  $\mathbf{C}^M$  is

$$\mathbf{M}^M = \begin{bmatrix} M_p \\ M_q \\ M_r \end{bmatrix} \quad (\text{C.29})$$

Moment vector in  $\mathbf{C}^{MR}$  is

$$\mathbf{M}^{MR} = \begin{bmatrix} M_{pR} \\ M_{qR} \\ M_{rR} \end{bmatrix} \quad (\text{C.30})$$

### C.2.3.1 Relationships between $\mathbf{M}^T$ and $\mathbf{M}^M$

$$\mathbf{M}^M = \mathbf{T}_z \mathbf{T}_y \mathbf{T}_x \mathbf{M}^T \quad (\text{C.31})$$

$$\mathbf{M}^T = \mathbf{T}_x^{-1} \mathbf{T}_y^{-1} \mathbf{T}_z^{-1} \mathbf{M}^M \quad (\text{C.32})$$

### C.2.3.2 Relationships between $\mathbf{M}^M$ and $\mathbf{M}^{MR}$

$$\mathbf{M}^{MR} = \mathbf{T}_R \mathbf{M}^M \quad (\text{C.33})$$

$$\mathbf{M}^M = \mathbf{T}_R^{-1} \mathbf{M}^{MR} \quad (\text{C.34})$$

# **TABLES**

Table 1.1 Selection of shield (JSCE, 1986).

Shield type		Open face type shield				Supported face type shield (Blind shield)	Balanced face type shield								
		Manual		Semi-mechanical			EPB shield		Slurry shield						
							Without additives		With additives						
Soil type	Alluvial cohesive soil	ℓ	-Face stability -Ground settlement	ℓ	-Face stability -Ground settlement	ℓ	-Soil properties to be check -Control amount of dug soil	ℓ	-Difficult with very soft soil -Control amount of dug soil	◆	-Priority given to work without additives	ℓ	-Difficult with very soft soil -Check slurry burst		
	Diluvial cohesive soil	ℓ	-Declined digging -Intercalation of permeable sand	ℓ	-Intercalation of permeable sand	ℓ	-Intercalation of permeable sand -Blockage of slit and chamber	ℓ	-Impossible to dig	ℓ	-Maintenance of fluidity	◆	-Priority given to work without additives	ℓ	-Provision of secondary processing facilities
	Soft rock (Silt stone/ Mud stone)	ℓ	-Difficult to dig	ℓ	-Intercalation of permeable sand -Abrasion of cutter bit	ℓ	-Intercalation of permeable sand -Abrasion of cutter bit	ℓ	-Impossible to dig	◆	-Priority given to slurry type	◆	-If ground is intercalated with permeable sand	◆	-If ground is intercalated with permeable sand
	Loose sandy soil	ℓ	-Difficult to keep face stability	ℓ	-Difficult to keep face stability	ℓ	-Difficult to keep face stability	ℓ	-Impossible to dig	ℓ	-Granule content	ℓ	-Advanced control amount of dug soil	ℓ	-Advanced control amount of dug soil -Preserved slurry quality
	Consolidated sandy soil	ℓ	-Face stability -Groundwater level and permeability	ℓ	-Face stability -Groundwater level and permeability	ℓ	-Face stability -Groundwater level and permeability	ℓ	-Impossible to dig	ℓ	-Granule content	ℓ	-Abrasion of cutter bit -Quantity of additives	ℓ	-Preserved slurry quality
	Gravel	ℓ	-Face stability -Groundwater level and permeability	ℓ	-Face stability -Groundwater level and permeability	ℓ	-Face stability -Groundwater level and permeability	ℓ	-Impossible to dig	ℓ	-Granule content	ℓ	-Abrasion of cutter bit -Quantity of additives	ℓ	-Slurry loss prevention -Transportation in fluid form
	Gravel with boulders	ℓ	-High risk in digging work	ℓ	-Self-supporting face -Groundwater level and permeability -Amount of over excavation	ℓ	-Difficult to remove boulders -Abrasion of cutter bit and face plate	ℓ	-Impossible to dig	ℓ	-Granule content -Abrasion of cutter bit -Gravel crushing apparatus -Diameter of screw conveyor	ℓ	-Abrasion of cutter bit -Gravel crushing apparatus -Diameter of screw conveyor	ℓ	-Slurry loss prevention -Gravel crushing apparatus -Transportation in fluid form
Adaptability to changed ground conditions		-Easily adaptable: in many cases the use of auxiliary construction work is necessary to ensure face stability		-Digging machine changeable -Same requirement as for manual digging applicable to face stability		-Digging machine not changeable -Same requirement as for manual digging applicable to face stability		-Difficult to applicable -Conversion to manual digging possible		-Adaptable -Pre-installation of additive feed apparatus required		-Adaptable -Wide range of applicable soil properties		-Adaptable -Wide range of applicable soil properties	

Table 1.2 Summary of changes of earth pressure during shield tunneling operation with passing of time  
(Revised from JSSMFE, 1993).

Step	Description	Ground Movement	Earth Pressure
I	[Prior to arrival of shield at the face] No supporting pressure at the face (Open type shield without compressed air).	Ground displacement moves towards the shield face.	Earth pressure becomes active.
	Balance between the pressure at the face during tunneling work.	No ground displacement.	No change in earth pressure.
	Supporting pressure at face (Slurry pressure, mud pressure and/or air pressure).	Outward ground displacement from the shield face.	Earth pressure becomes passive.
II	[Arrival of shield at the face] Earth pressure at the tunnel face is greater than the face supporting pressure.	Ground displacement towards the tunnel cavity.	Earth pressure shifts towards active side.
	Face supporting pressure is slurry or mud pressure.	No ground displacement.	No change in earth pressure.
	Face supporting pressure is air pressure.	Ground displacement is enlarged the tunnel cavity	Earth pressure shifts towards passive side.
III	[Passing of shield] Part of the face supporting pressure is conveyed to the tunnel face.	The opening surface towards the tunnel cavity to be supported by the shield.	Earth pressure shifts towards active side and shearing between the ground and the shield occurs.
	When the shield has moved as snake-like motion.	Shield periphery moves to push the ground and the cavity between the shield and the ground is created by an over-excavation and the ground displacement towards that cavity.	Earth pressure shifts towards passive side in pushing area whereas active earth pressure occurs in cavity area and shearing between the ground and the shield also occurs.
IV	[Passing of shield tail and completion of backfill grouting] Delay in the backfill grouting or delay in the hardening of the backfill materials.	Ground displacement towards the tunnel cavity.	Earth pressure shifts towards active side.
	Immediately backfill grouting after passing of the shield tail.	No ground displacement.	No change in earth pressure.
	Backfill is grouted by high grouting pressure.	Ground displacement is enlarged the tunnel cavity.	Earth pressure shifts towards passive side.
VI	[After backfill grouting] Long term consolidation settlement and creep deformation of the backfill materials.	Ground displacement towards the tunnel cavity.	Earth pressure shifts towards active side.

Table 1.3 Proportion of settlement by settlement type (*Makata, 1981 and Yamada et al., 1988*).

Settlement Soil type	Preconsolidation settlement	Settlement at front face	Tail settlement	Settlement by tail void	Following settlement
Cohesive soil	6 %	5 %	8 %	34 %	47 %
Sandy soil	0 %	3 %	31 %	60 %	6 %

Table 2.1 Parameters at  $\beta = 0, 1/2, 1$ .

		$k-1$		$k$		
$\beta$	0	1/2	1	0	1/2	1
$\alpha$		1	0	1	0	
$\mathbf{r}$	$\mathbf{r}_{k-2(2)}$	$\mathbf{r}_{k-1(1)}$	$\mathbf{r}_{k-1(2)}$	$\mathbf{r}_{k(1)}$	$\mathbf{r}_{k(2)}$	
$\mathbf{k}$	$\mathbf{k}_{k-2(2)}$		$\mathbf{k}_{k-1(2)}$		$\mathbf{k}_{k(2)}$	
$\mathbf{t}$		$\mathbf{t}_{k-1(1)}$		$\mathbf{t}_{k(1)}$		
$\mathbf{n}$	$\mathbf{n}_{k-2(2)}$	$\mathbf{n}_{k-1(1)}$	$\mathbf{n}_{k-1(2)}$	$\mathbf{n}_{k(1)}$	$\mathbf{n}_{k(2)}$	
$\mathbf{b}$	$\mathbf{b}_{k-2(2)}$	$\mathbf{b}_{k-1(1)}$	$\mathbf{b}_{k-1(2)}$	$\mathbf{b}_{k(1)}$	$\mathbf{b}_{k(2)}$	
$\theta_x$	$\theta_{xk-2(2)}$	$\theta_{xk-1(1)}$	$\theta_{xk-1(2)}$	$\theta_{xk(1)}$	$\theta_{xk(2)}$	
$\theta_y$	$\theta_{yk-2(2)}$	$\theta_{yk-1(1)}$	$\theta_{yk-1(2)}$	$\theta_{yk(1)}$	$\theta_{yk(2)}$	
$\theta_z$	$\theta_{zk-2(2)}$	$\theta_{zk-1(1)}$	$\theta_{zk-1(2)}$	$\theta_{zk(1)}$	$\theta_{zk(2)}$	
$\mathbf{T}$	$\mathbf{T}_{k-2(2)}$	$\mathbf{T}_{k-1(1)}$	$\mathbf{T}_{k-1(2)}$	$\mathbf{T}_{k(1)}$	$\mathbf{T}_{k(2)}$	
$\mathbf{T}_n$	$\mathbf{T}_{nk-2(2)}$	$\mathbf{T}_{nk-1(1)}$	$\mathbf{T}_{nk-1(2)}$	$\mathbf{T}_{nk(1)}$	$\mathbf{T}_{nk(2)}$	

$\theta_z$  ( $\theta_{zR}$ ): rotation angle from  $p$ -axis to  $\mathbf{n}$  around  $r$ -axis

Table 2.2 Operational sign.

$\theta_r$	$\theta_{CV}$ $x$	$-\theta_{CH}$ $y$
0	+	0
	+	+
$\pi/2$	0	+
	-	+
$\pi$	-	0
	-	-
$3\pi/2$	0	-
	+	-
$2\pi$	+	0

Table 2.3 Machine types.

Machine type	$\max(L_1, L_{CSE}, L_2)$
1	$L_1$
2	$L_{CSE}$
3	$L_2$

Table 2.4 Operation rule at curve.

Machine type	Rule
1	Front body touches the trace of $P_{21}$ on $\mathbf{n}$ (Refer to Figure 2.10)
2	$P_{102}$ touches the trace of $P_{202}$ on $\mathbf{n-t}$ plane (Refer to Figure 2.11)
3	$P_{102}$ touches the trace of $P_{201}$ on $\mathbf{n-t}$ plane (Refer to Figure 2.12)

Note: symbols are shown in Figure 2.9

Table 2.5 Judging conditions of Type 1 for shield position.

Position	Judging condition	Note
1	RB on straight line; $(\mathbf{r}_C - \mathbf{r}_{BHC}) \cdot \mathbf{e}_{r2} \leq 0$ and $(\mathbf{r}_C - \mathbf{r}_{BVC}) \cdot \mathbf{e}_{r2} \leq 0$	Straight line
2	RB on curve; $(\mathbf{r}_{CF} - \mathbf{r}_C) \cdot \mathbf{n}_{CF} \leq 0$	Curve
3	RB on curve; $(\mathbf{r}_{CF} - \mathbf{r}_C) \cdot \mathbf{n}_{CF} > 0$	EC

Note:  $\mathbf{r}_C$  : position vector at crease center point

$\mathbf{r}_{BHC}$ : position vector at beginning point of horizontal curve

$\mathbf{r}_{BVC}$ : position vector at beginning point of vertical curve

$\mathbf{r}_{CF}$  : position vector at center point of cutter face

$\mathbf{n}_{CF}$  : principal normal vector of the curve at at center point of cutter face

Table 2.6 Judging conditions of Type 2 for shield position.

Position	Judging condition	Note
1	RB on straight line; $(\mathbf{r}_C - \mathbf{r}_{BHC}) \cdot \mathbf{e}_{r2} \leq -L_1$ and $(\mathbf{r}_C - \mathbf{r}_{BVC}) \cdot \mathbf{e}_{r2} \leq -L_1$	Straight line
2	RB on curve; $(\mathbf{r}_{CF} - \mathbf{r}_{EHC}) \cdot \mathbf{k}_{EHC} \leq L_{CSE}$ or $(\mathbf{r}_{CF} - \mathbf{r}_{EVC}) \cdot \mathbf{k}_{EVC} \leq L_{CSE}$	Curve
3	RB on curve; not case 2	EC

Note:  $\mathbf{r}_C$  : position vector at crease center point

$\mathbf{r}_{BHC}$  : position vector at beginning point of horizontal curve

$\mathbf{r}_{BVC}$  : position vector at beginning point of vertical curve

$\mathbf{r}_{EHC}$  : position vector at end point of horizontal curve

$\mathbf{r}_{EVC}$  : position vector at end point of vertical curve

$\mathbf{r}_{CF}$  : position vector at center point of cutter face

$\mathbf{k}_{EHC}$  : tangent vector of the horizontal curve at end point of horizontal curve

$\mathbf{k}_{EVC}$  : tangent vector of the vertical curve at end point of vertical curve

Table 2.7 Judging conditions of Type 3 for shield position.

Position	Judging condition	Note
1	RB on straight line; $(\mathbf{r}_C - \mathbf{r}_{BHC}) \cdot \mathbf{e}_{r2} \leq L_2 - L_{M1}$ and $(\mathbf{r}_C - \mathbf{r}_{BVC}) \cdot \mathbf{e}_{r2} \leq L_2 - L_{M1}$	Straight line
2	RB on curve; $(\mathbf{r}_{CF} - \mathbf{r}_{EHC}) \cdot \mathbf{k}_{EHC} \leq -L_2$ or $(\mathbf{r}_{CF} - \mathbf{r}_{EVC}) \cdot \mathbf{k}_{EVC} \leq -L_2$	Curve
3	RB on curve; not case 2	EC

Note:  $\mathbf{r}_C$  : position vector at crease center point

$\mathbf{r}_{BHC}$  : position vector at beginning point of horizontal curve

$\mathbf{r}_{BVC}$  : position vector at beginning point of vertical curve

$\mathbf{r}_{EHC}$  : position vector at end point of horizontal curve

$\mathbf{r}_{EVC}$  : position vector at end point of vertical curve

$\mathbf{r}_{CF}$  : position vector at center point of cutter face

$\mathbf{k}_{EHC}$  : tangent vector of the horizontal curve at end point of horizontal curve

$\mathbf{k}_{EVC}$  : tangent vector of the vertical curve at end point of vertical curve

Table 2.8 Position vector  $\mathbf{r}_*$  and unit normal direction vector  $\mathbf{k}_*$  in analysis.

Body	Cross section	$\mathbf{r}_*$	$\mathbf{k}_*$
Front body	P1C	$\mathbf{r}_C^T + r_{ir} \mathbf{e}_{r1}^T$	$\mathbf{e}_{r1}^T$
Rear body	P2C	$\mathbf{r}_{TC}^T + r_{ir} \mathbf{e}_{r2}^T$	$\mathbf{e}_{r2}^T$

Table 2.9 Relationship between applications of shield model and affecting factors.

Applications	Ground properties	Shield behavior	Shield Operation
Simulator	Known	<i>Unknown</i>	Known
Controller	Known	Known	<b>Unknown</b>
Reverse analysis	<i>Unknown</i>	Known	Known

Table 3.1 Shield data used in the analysis

		Units	Data					
Whole body			Left body			Right body		
<b>1 Self weight</b>								
Weight	kN	2600.00				2500.00		
Center of gravity(p,q,r)	m	0.000	0.000	0.383	0.000	0.000	0.266	
<b>2 Tail</b>								
Width of segment	m	0.600			0.600			
Outer radius of segment	m	2.800			2.800			
Inner radius of shield tail	m	2.880			2.880			
Thickness of shield tail	m	0.045			0.045			
Young's modulus of steel	kN/m <sup>2</sup>	2.1x10 <sup>8</sup>			2.1x10 <sup>8</sup>			
Original thickness of wire brush	m	0.123	0.123	0.123	0.123	0.123	0.123	
Length of wire brush	m	0.160	0.160	0.160	0.160	0.160	0.160	
Wire brush position from tail	m	0.870	0.504	0.144	0.870	0.504	0.144	
Spring constant of wire brush & Pos.	kN/m <sup>3</sup>							
<b>3 Jack</b>								
Number of jack		20			20			
Angle of No.1 jack	deg	-162.000			-162.000			
Rotate direction(1:unlock -1:clock)		1			1			
Radius of jack	m	2.525			2.525			
Cross section area of jack	m <sup>2</sup>	0.05102			0.05102			
Length of jack (stroke=0)(fix-spreader)	m	3.190			3.190			
<b>4 Cutter face</b>								
Number of path		3.000			3.000			
Coef. of cutter torque		1.000	0.000		1.000	0.000		
Thickness of cutter face	m	0.400			0.400			
Close ratio of cutter face		0.682			0.682			
CC extend/shrink angle, Velocity	deg m/min	30.000	0.000	0.000	30.000	0.000	0.000	
<b>5 Friction</b>								
Coef. of friction MYU-jc		0.300			0.300			
Adhesion C -jc	kN/m <sup>2</sup>	0.000			0.000			
Resistance ratio for Jack		0.400			0.400			
Coef. of friction MYU-tc		0.300			0.300			
Adhesion C -tc	kN/m <sup>2</sup>	0.000			0.000			
Resistance ratio for Tail		0.400			0.400			
Coef. of friction MYU-Wc		0.150			0.150			
Adhesion C -Wc	kN/m	0.000			0.000			
Resistance ratio for Tail		0.400			0.400			
Coef. of friction MYU-gr		0.010			0.010			
Adhesion C -gr	kN/m <sup>2</sup>	0.100			0.100			
Resistance ratio for Grease		0.400			0.400			
<b>6 Dimension</b>								
Radius of machine	m	2.925			2.925			
Radius of excavation	m	2.935			2.935			
Radius of fish tail	m	0.600			0.600			
Radius of chamber	m	2.895			2.895			
Length of machine	m	8.250			7.800			
Length (CF-Bulk head)	m	1.470			1.020			
Length (CF-End of girder)	m	4.935			4.585			
Length (CF-Shield jack fixed point)	m	2.490			2.040			
Length (CF-CM)	m	4.300			3.850			
Surveying point(p,q,r)	m	0.000	0.000	0.000	0.000	0.000	0.000	
Center of elector(p,q,r)	m	0.000	0.000	-2.380	0.000	0.000	-2.380	
<b>A:Articulate part</b>								
<b>1 Articulate jack</b>								
Number of jack		14			14			
Angle of No.1 jack	deg	-154.286			-154.286			
Rotate direction(1:unlock -1:clock)		1			1			
Radius of jack	m	1.980			1.980			
Cross section area of J (Extend/Shrink)	m <sup>2</sup>	0.05714	1.00000		0.05714	0.00000		
Length of jack (Front - Rear)	m	1.680			1.680			
<b>2 Dimension</b>								
Length (CF-Crease jack fixed point)	m	2.720			2.270			
Articulate point(p,q,r)	m	0.000	0.000	0.000	0.000	0.000	0.000	
<b>F:Front body</b>								
<b>1 Self weight</b>								
Weight	kN	1300.00			1200.00			
Center of gravity(p,q,r)	m	0.000	0.000	2.028	0.000	0.000	1.922	
<b>2 Dimension</b>								
Length of machine	m	4.300			3.850			
<b>R:Rear body</b>								
<b>1 Self weight</b>								
Weight	kN	1300.00			1300.00			
Center of gravity(p,q,r)	m	0.000	0.000	-1.262	0.000	0.000	-1.262	
<b>2 Dimension</b>								
Length of machine	m	3.950			3.950			

Table 3.2 Ground parameters

Characteristics		N=30	N=50
1. Density	(kN/m <sup>3</sup> )	19.200	19.200
Submerged density	(kN/m <sup>3</sup> )	9.200	9.200
Water density	(kN/m <sup>3</sup> )	10.000	10.000
Specific gravity		2.720	2.720
2. Cohesion	(kN/m <sup>2</sup> )	0.000	0.000
Internal friction angle	(deg)	40.000	45.000
IP	(%)	0.000	0.000
Soil type (1:sand 2:clay)		1.000	1.000
3. Coef. of earth pressure $K_{Ha}$		0.000	0.000
$K_{H0}$		0.357	0.293
$K_{Hp}$		5.000	5.000
Coef. of earth pressure $K_{Va}$		0.000	0.000
$K_{V0}$		1.000	1.000
$K_{Vp}$		5.000	5.000
Coef. of ground reaction $k_H$	(kN/m <sup>3</sup> )	30000.00	50000.00
$k_v$	(kN/m <sup>3</sup> )	30000.00	50000.00
Coef. of friction $MYU_{-ms}$		0.100	0.100
Adhesion $C_{-ms}$	(kN/m <sup>2</sup> )	0.000	0.000
Coef. of friction $MYU_{-m}$		0.000	0.000
Adhesion $C_{-m}$	(kN/m <sup>2</sup> )	0.000	0.000
Coef. of normal pressure at CF a		30.000	30.000
b		1.000	1.000
Resistance ratio for CT $\alpha$		0.000	0.000
Coef. of Logistic curve $a_H$		0.000	0.000
Coef. of Logistic curve $a_v$		0.000	0.000
Coef. of friction $MYU_{-CF}$		0.100	0.100
Adhesion $C_{-CF}$	(kN/m <sup>2</sup> )	0.000	0.000
dummy		0.000	0.000
E	(kN/m <sup>2</sup> )	84000	140000
E(N値)	(kN/m <sup>2</sup> )	42000	70000
E(c)	(kN/m <sup>2</sup> )		
kH	(kN/m <sup>3</sup> )	35193	58655
kH(N値)	(kN/m <sup>3</sup> )	17597	29328
kH(c)	(kN/m <sup>3</sup> )		
kH	(kN/m <sup>3</sup> )	30000	50000
kH(use)	(kN/m <sup>3</sup> )	30000	50000
KH0		0.357	0.293
KH0			
KHa(use)		0.000	0.000
KH0(use)		0.357	0.293
KHp(use)		5.000	5.000
KHa by Rankin		0.217	0.172
KHp by Rankin		4.599	5.828

Table 3.3 Analysis case

Case No.	Parameter No.	Reduction rate of CCL	$\theta_{cv}$	$\phi_{pRR}$	Share of jack force $\beta=F_{3L}/(F_{3L}+F_{3R})$	SPT N value	Note				
100003	1	0.00	$\theta_{cv}$	0	Planned	30	Default				
125003		0.25									
150003		0.50									
175003		0.75									
200103		0.00									
225103	2	0.25	$0.5\theta_{cv}$	$-0.5\theta_{cv}$	Planned	30					
250103		0.50									
275103		0.75									
200203		0.00									
225203		0.25									
250203		0.50						0	$-\theta_{cv}$	Planned	30
275203		0.75									
350023	3	0.50	$\theta_{cv}$	0	0.2	30					
350043					0.4						
350063					0.6						
350083					0.8						
450005					4			0.50	$\theta_{cv}$	0	Planned

Table 4.1 Ground properties

Ground layer	Ylc	Toc	Tos	Tog	Eds
Unit weight (kN/m <sup>3</sup> )	17.5	17	19	20	19
Cohesion (kN/m <sup>2</sup> )	8	98	9.8	0	0
Internal friction angle (deg)	0	0	35	40	35
$K_{ha}$ ( $\sim K_{hmin}$ )	0.7	0	0	0	0
$K_{ho}$	0.817	1	0.426	0.357	0.426
$K_{hp}$ ( $\sim K_{hmax}$ )	2.714	5	5	5	5
$K_{va}$ ( $\sim K_{vmin}$ )	0.7	0	0	0	0
$K_{vo}$	1	1	1	1	1
$K_{vp}$ ( $\sim K_{vmax}$ )	2.714	5	5	5	5
$k_h$ (MN/m <sup>3</sup> )	8.1	13.6	37.1	49.3	47.3
$k_v$ (MN/m <sup>3</sup> )	8.1	13.6	37.1	49.3	47.3
Coeff. of friction	0.1	0.1	0.1	0.1	0.1

Table 4.2 Dimensions of tunnel and shield

Item	Component	Left body	Right body
Shield	Outer radius (m)	2.925	2.925
	Total length (m)	8.5	7.8
	Length of front body (m)	4.6	3.9
	Length of rear body (m)	3.9	3.9
	Self-weight (kN)	2830	2750
Shield jack	Number of jacks	20	20
	Radius of jack (m)	2.6	2.6
Articulated jack	Number of jacks	12	12
	Radius of jack (m)	2.025	2.025
Segment	Outer radius (m)	2.8 , 2.85	2.8 , 2.85
	Width (m)	0.501 , 1.2	0.561 , 1.2
Tunnel	Horizontal curve radius (m)	50	55.94
Ground	Ground water level (m)	TP-0.97	
	Overburden depth (m)	24	

Table 4.3 Force and moment acting on shield (at distance 4.345m)

Type	Body	Force and moment components (kN, kN-m)					
		$F_p$	$F_q$	$F_r$	$M_p$	$M_q$	$M_r$
$f_1$	Front left	1340	0	-5	-16	6271	-3980
	Rear left	1490	0	-6	-18	2131	-4425
	Front right	1260	0	-5	14	5569	3742
	Rear right	1490	0	-6	17	2131	4425
$f_2$	Front left	0	0	0	0	0	0
	Rear left	0	0	0	0	0	0
	Front right	0	0	0	0	0	0
	Rear right	0	0	0	0	0	0
$f_3$	Front left	0	0	0	0	0	0
	Rear left	0	0	11211	32791	-9647	0
	Front right	0	0	0	0	0	0
	Rear right	0	0	10893	-32110	-7464	0
$f_4$	Front left	331	39	-10595	-31737	2090	2435
	Rear left	0	0	0	0	0	0
	Front right	154	-38	-10592	31694	986	-2924
	Rear right	0	0	0	0	0	0
$f_5$	Front left	-537	57	-159	-549	-2398	1595
	Rear left	-2618	-2568	-302	-266	1027	7774
	Front right	-372	41	-139	311	-1591	-1104
	Rear right	-2538	2469	-293	-132	895	-7539
$\Sigma\phi$	Left body	7	-2472	143	205	-526	3399
	Right body	-7	2472	-143	-205	526	-3399
	Whole body	0	0	0	0	0	0

Table 4.4 Force and moment acting on shield (at distance 22.574m)

Type	Body	Force and moment components (kN, kN-m)					
		$F_p$	$F_q$	$F_r$	$M_p$	$M_q$	$M_r$
$f_1$	Front left	1340	5	-5	-39	6261	-4234
	Rear left	1490	6	-5	-24	2131	-4425
	Front right	1260	5	-4	-9	5563	3553
	Rear right	1490	6	-5	8	2131	4425
$f_2$	Front left	0	0	0	0	0	0
	Rear left	0	0	0	0	0	0
	Front right	0	0	0	0	0	0
	Rear right	0	0	0	0	0	0
$f_3$	Front left	0	0	0	0	0	0
	Rear left	-1	0	10647	31142	-6589	4
	Front right	0	0	0	0	0	0
	Rear right	1	0	10802	-36357	-5689	4
$f_4$	Front left	349	-794	-10411	-29224	2327	2243
	Rear left	0	0	0	0	0	0
	Front right	167	-772	-10570	33313	666	-2911
	Rear right	0	0	0	0	0	0
$f_5$	Front left	-1242	63	-33	-408	-5510	3901
	Rear left	-1979	-2270	-107	631	31	5879
	Front right	-688	136	-69	-267	-2965	-1945
	Rear right	-2186	3615	-239	1234	1645	-6494
$\Sigma$	Left body	-43	-2990	86	2078	-1349	3368
	Right body	43	2990	-86	-2078	1349	-3368
	Whole body	0	0	0	0	0	0

Table 4.5 Force and moment acting on shield (at distance 125.5m)

Type	Body	Force and moment components (kN, kN-m)					
		$F_p$	$F_q$	$F_r$	$M_p$	$M_q$	$M_r$
$f_1$	Front left	870	1019	4	-4710	4027	-2583
	Rear left	967	1134	4	-1554	1336	-2872
	Front right	818	959	3	-4194	3570	2281
	Rear right	967	1134	4	-1579	1337	2872
$f_2$	Front left	0	0	0	0	0	0
	Rear left	0	0	0	0	0	0
	Front right	0	0	0	0	0	0
	Rear right	0	0	0	0	0	0
$f_3$	Front left	0	0	0	0	0	0
	Rear left	187	219	13631	46406	8452	-771
	Front right	0	0	0	0	0	0
	Rear right	-187	-219	13631	-40492	8452	-419
$f_4$	Front left	31	110	-10444	-32965	1328	3302
	Rear left	0	0	0	0	0	0
	Front right	864	173	-8625	24996	2732	-392
	Rear right	0	0	0	0	0	0
$f_5$	Front left	933	11360	-1737	-44129	3778	-2298
	Rear left	-2686	6170	-1566	-3192	1307	7937
	Front right	-8140	-13766	-2760	54179	-28944	-22922
	Rear right	5377	-8293	-2144	7233	-7377	15866
$\Sigma f$	Left body	301	20012	-109	-40145	20230	2714
	Right body	-301	-20012	109	40145	-20230	-2714
	Whole body	0	0	0	0	0	0

# FIGURES

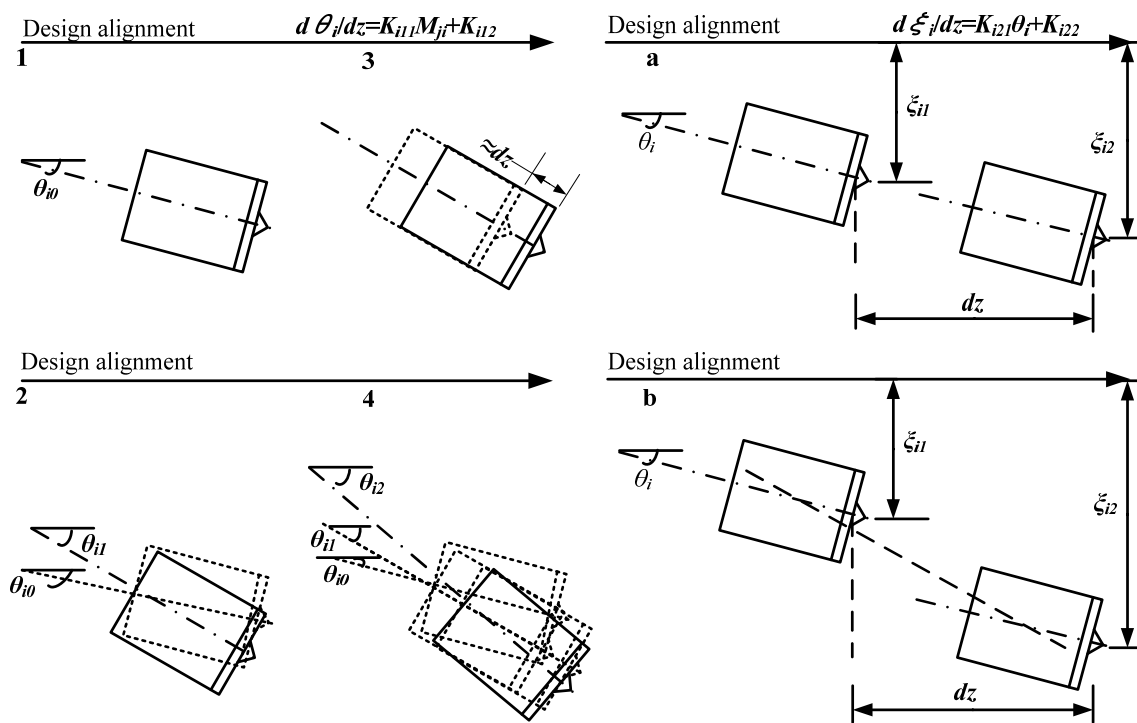


Figure 1.1 Mechanism of shield movement (Shimizu and Suzuki, 1992).

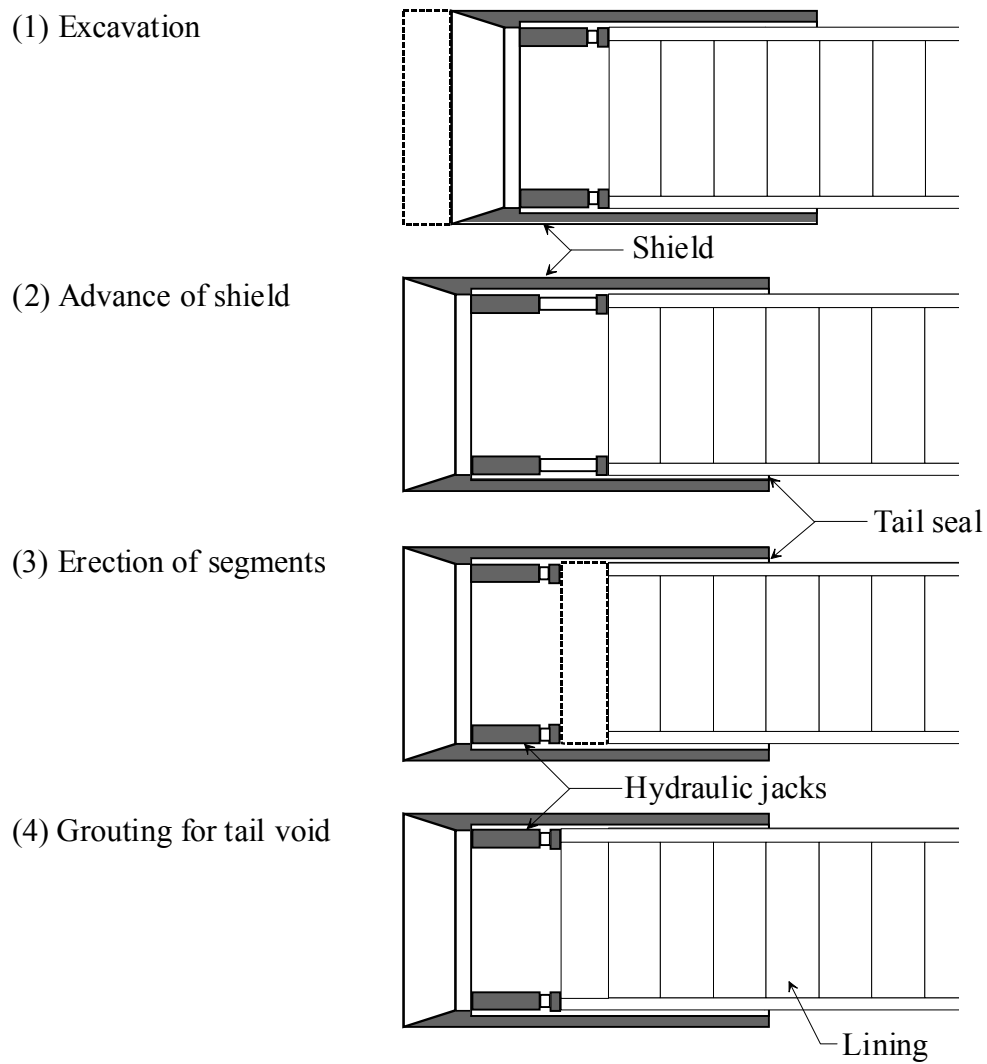


Figure 1.2 Construction sequences of shield tunneling works (Fujita, 1989).

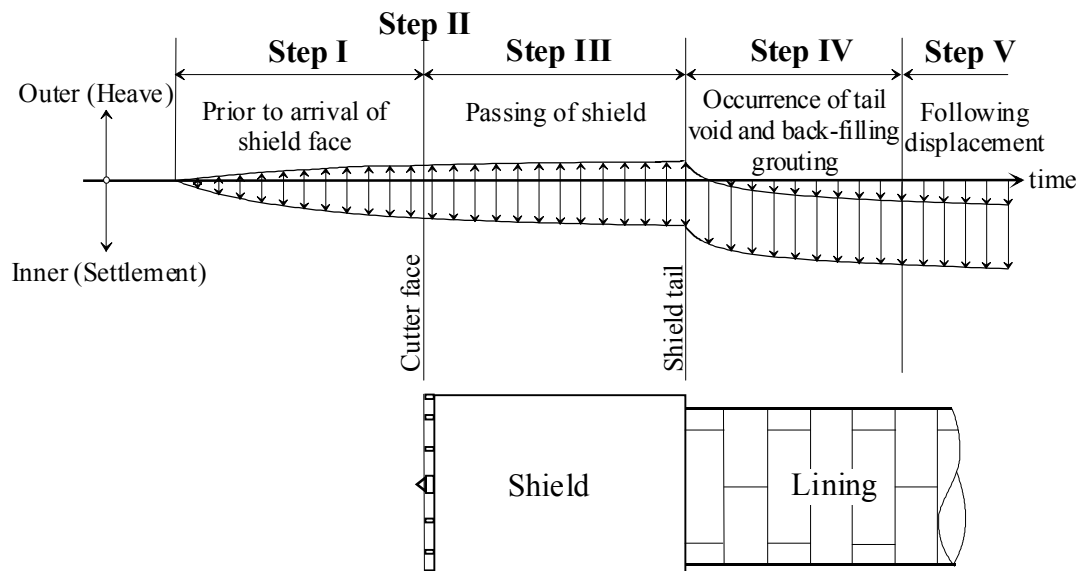


Figure 1.3 Illustration of ground movement caused by shield tunneling work (JSSMFE, 1993).

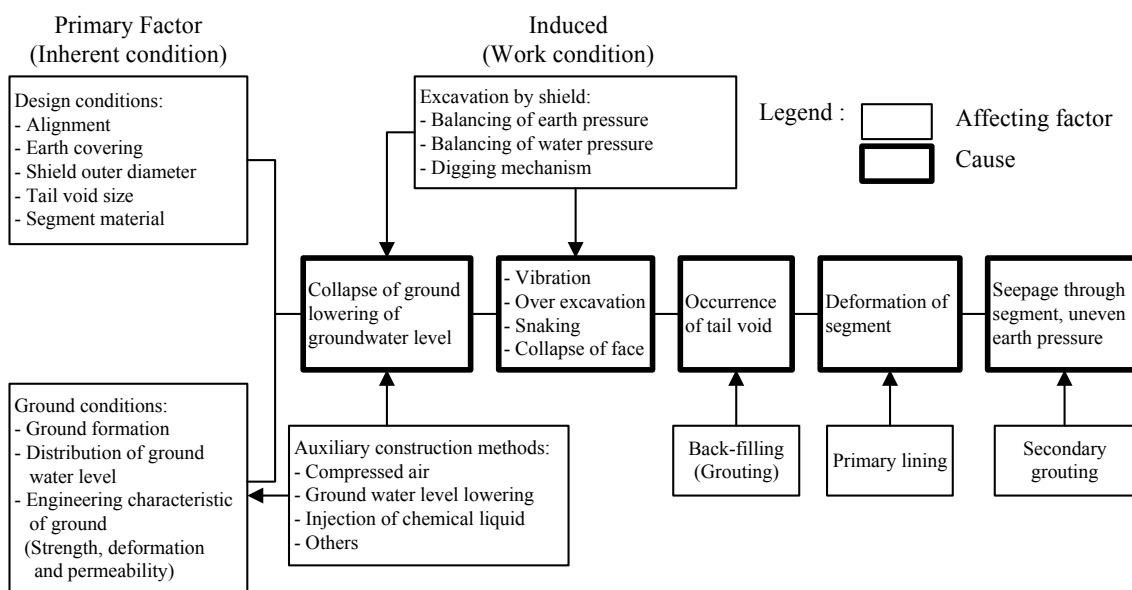


Figure 1.4 Relationships between ground displacement and affecting factors (Makata, 1980).

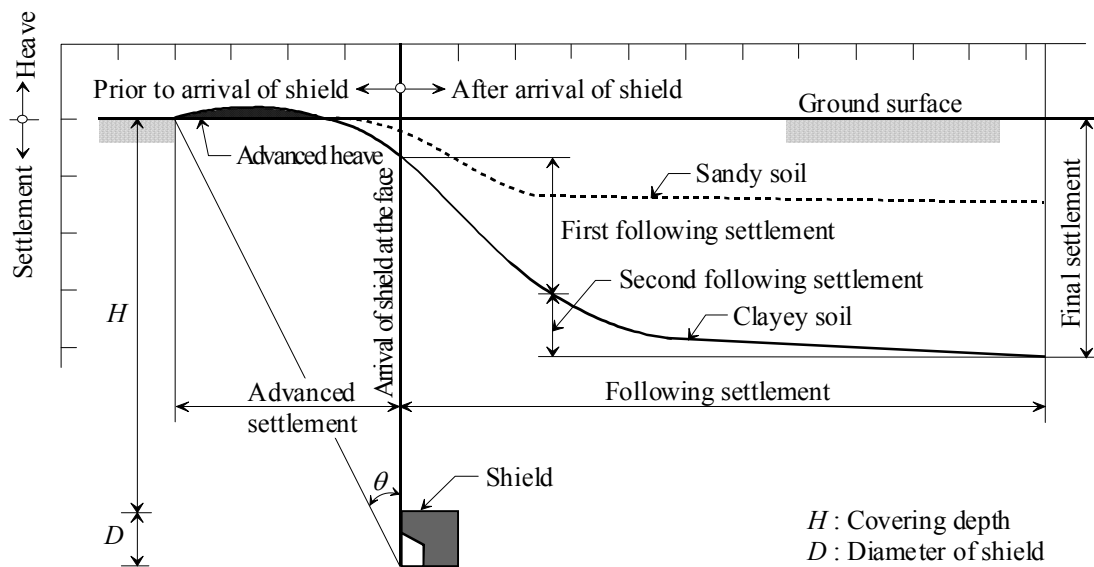


Figure 1.5 Ground surface settlement in longitudinal direction (JGS, 1996).

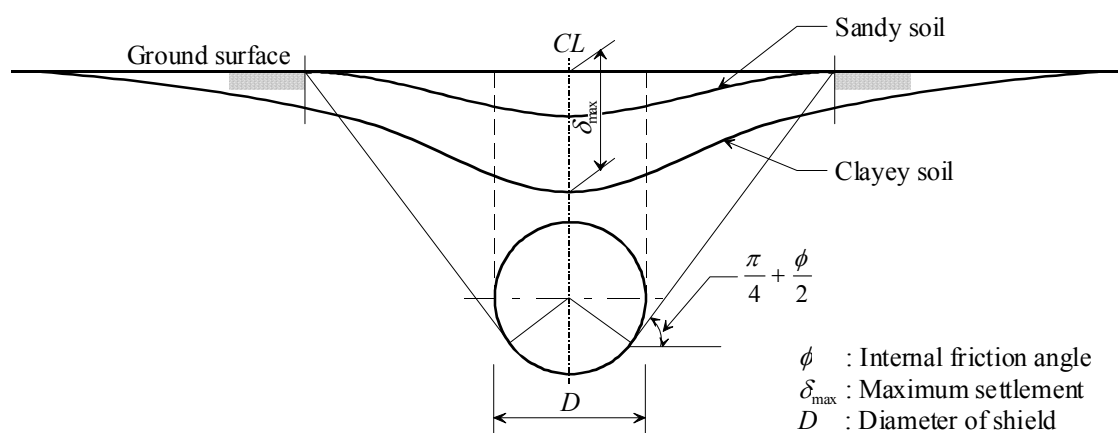


Figure 1.6 Ground surface settlement in transverse direction (JGS, 1996).

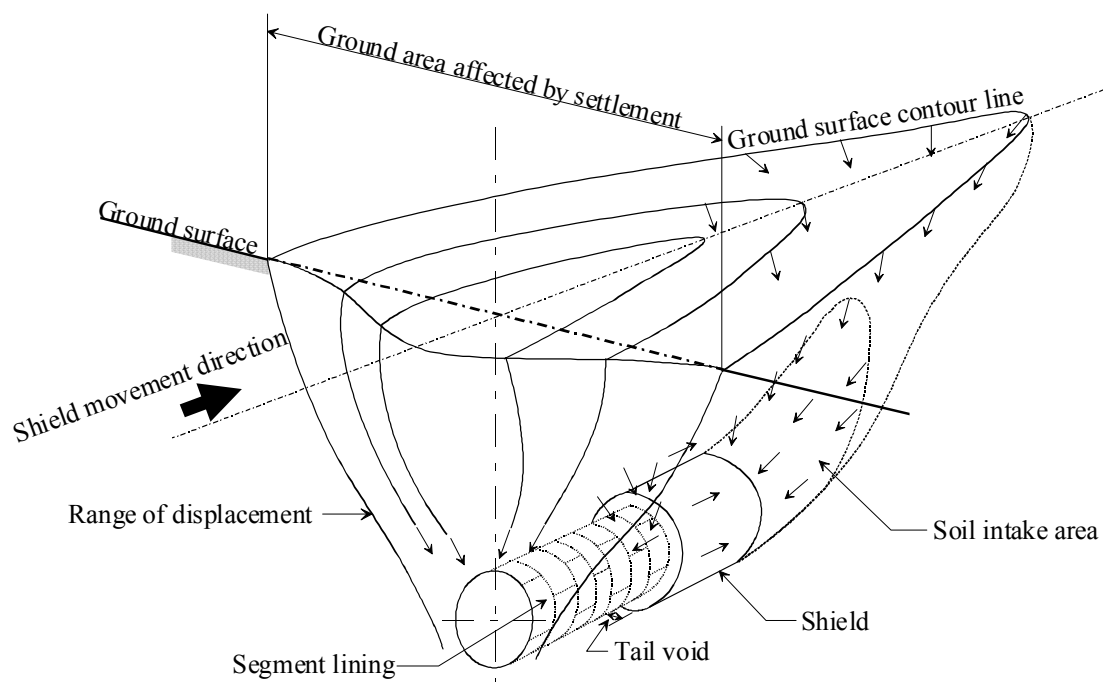


Figure 1.7 Three dimensional displacement of ground around the cutter face for clayey soil (JGS, 1996).

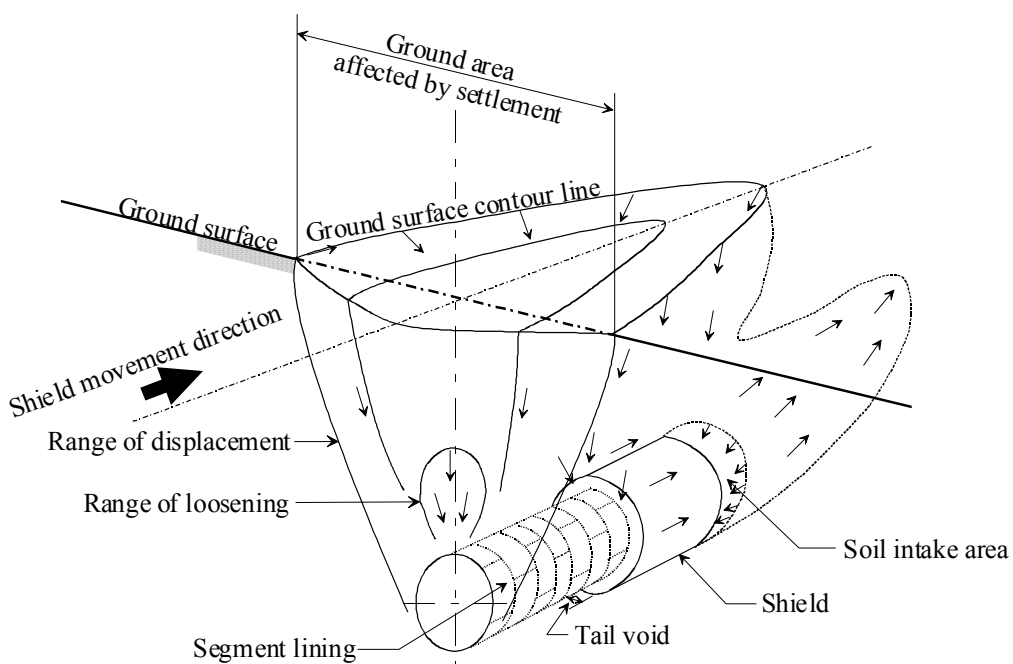


Figure 1.8 Three dimensional displacement of ground around the cutter face for sandy soil (JGS, 1996).

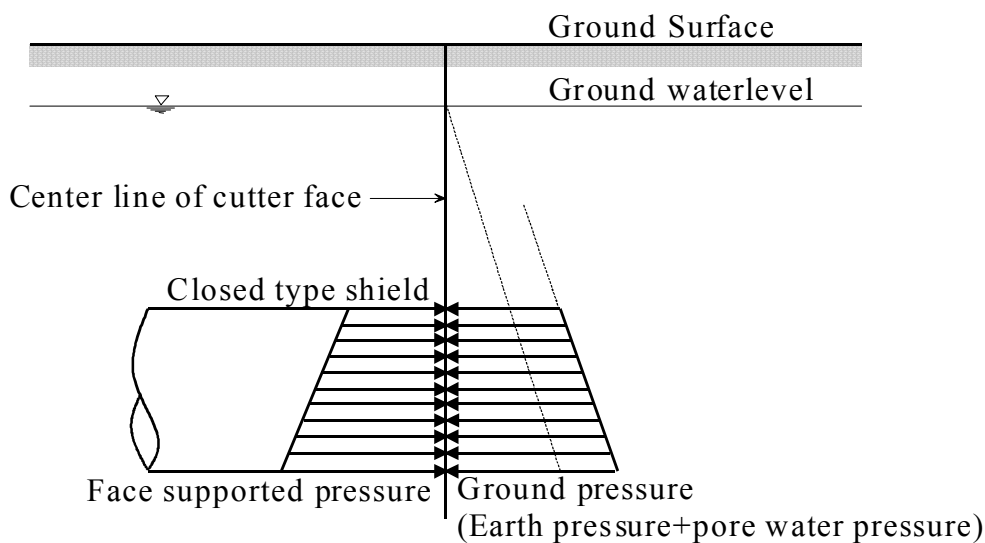


Figure 1.9 Illustration of pressure acting on cutter face (Kanayasu et al., 1995).

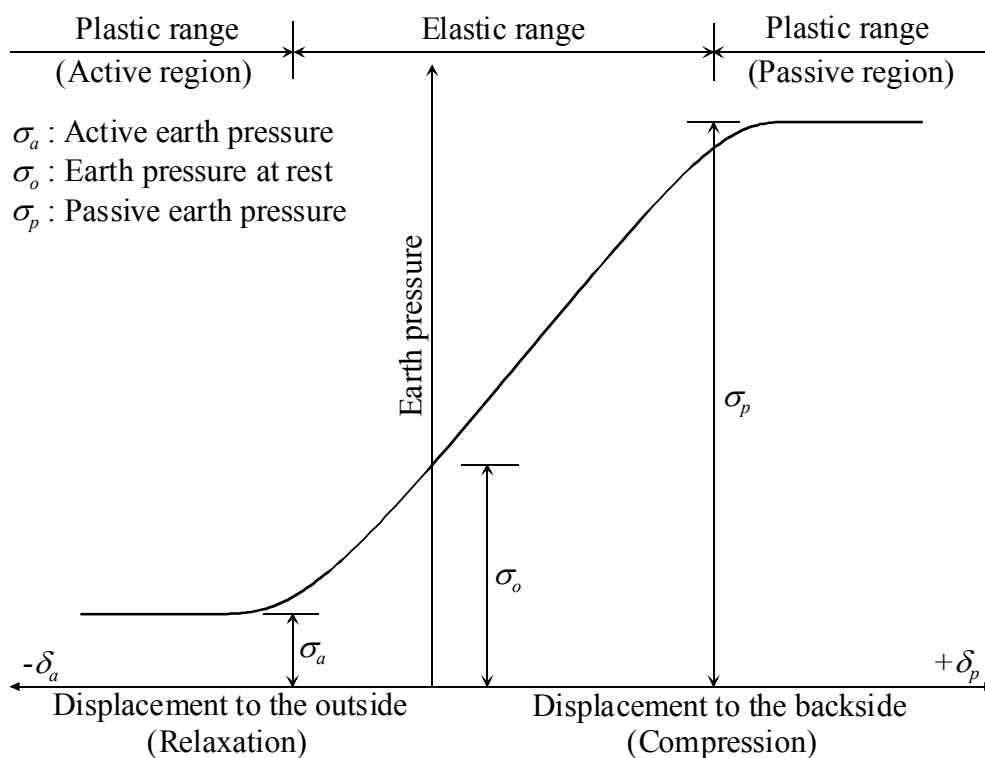


Figure 1.10 Relationship between earth pressure and deformation (Sugimoto et al., 1992).

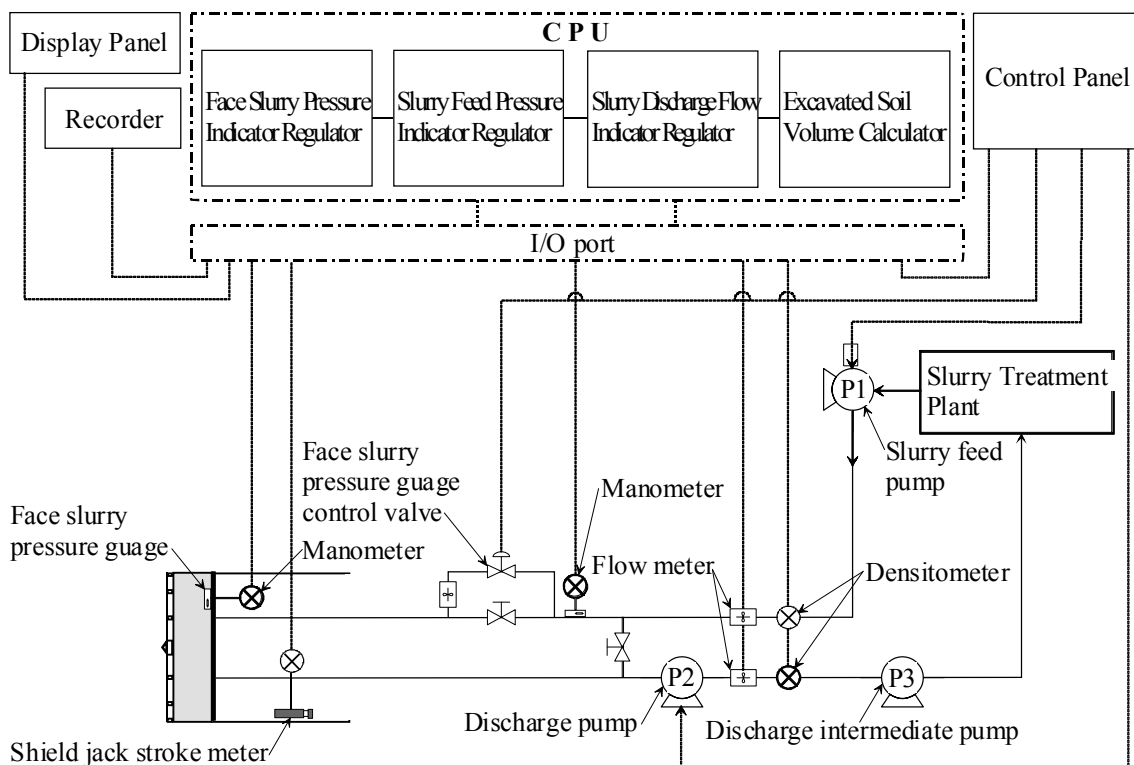


Figure 1.11 An example of control system for face stabilization and excavated soil volume of slurry shield.

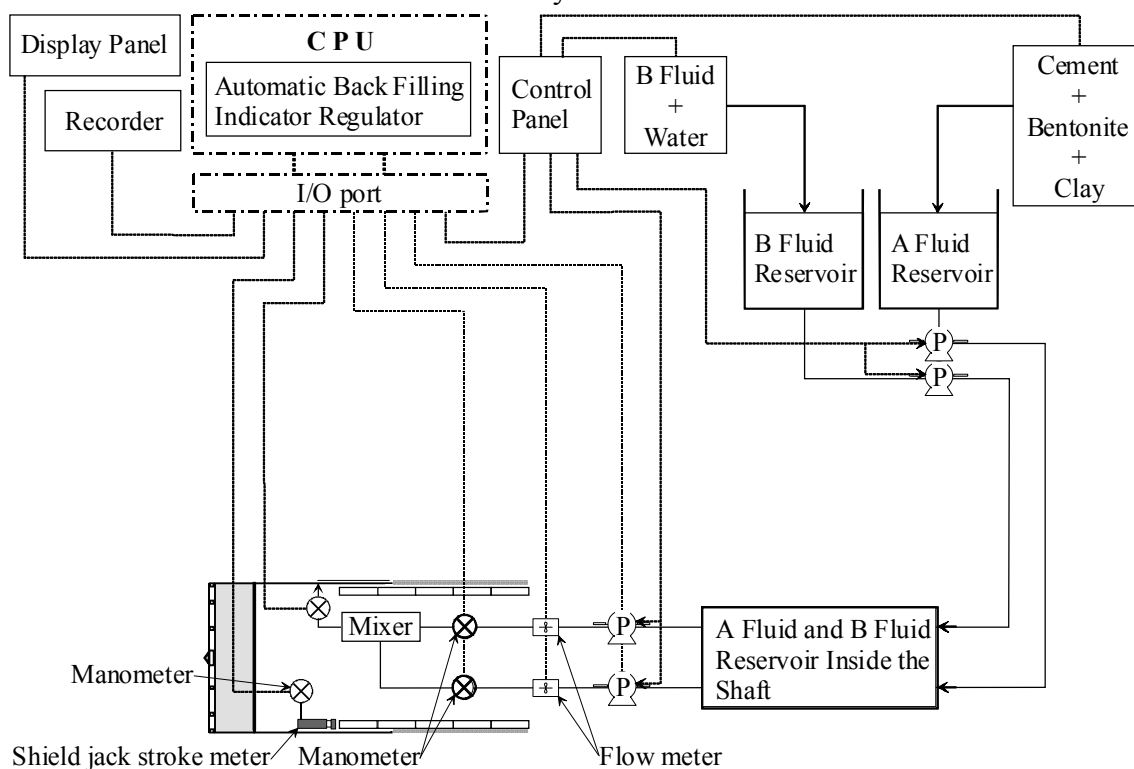


Figure 1.12 An example of automatic back filling control system.

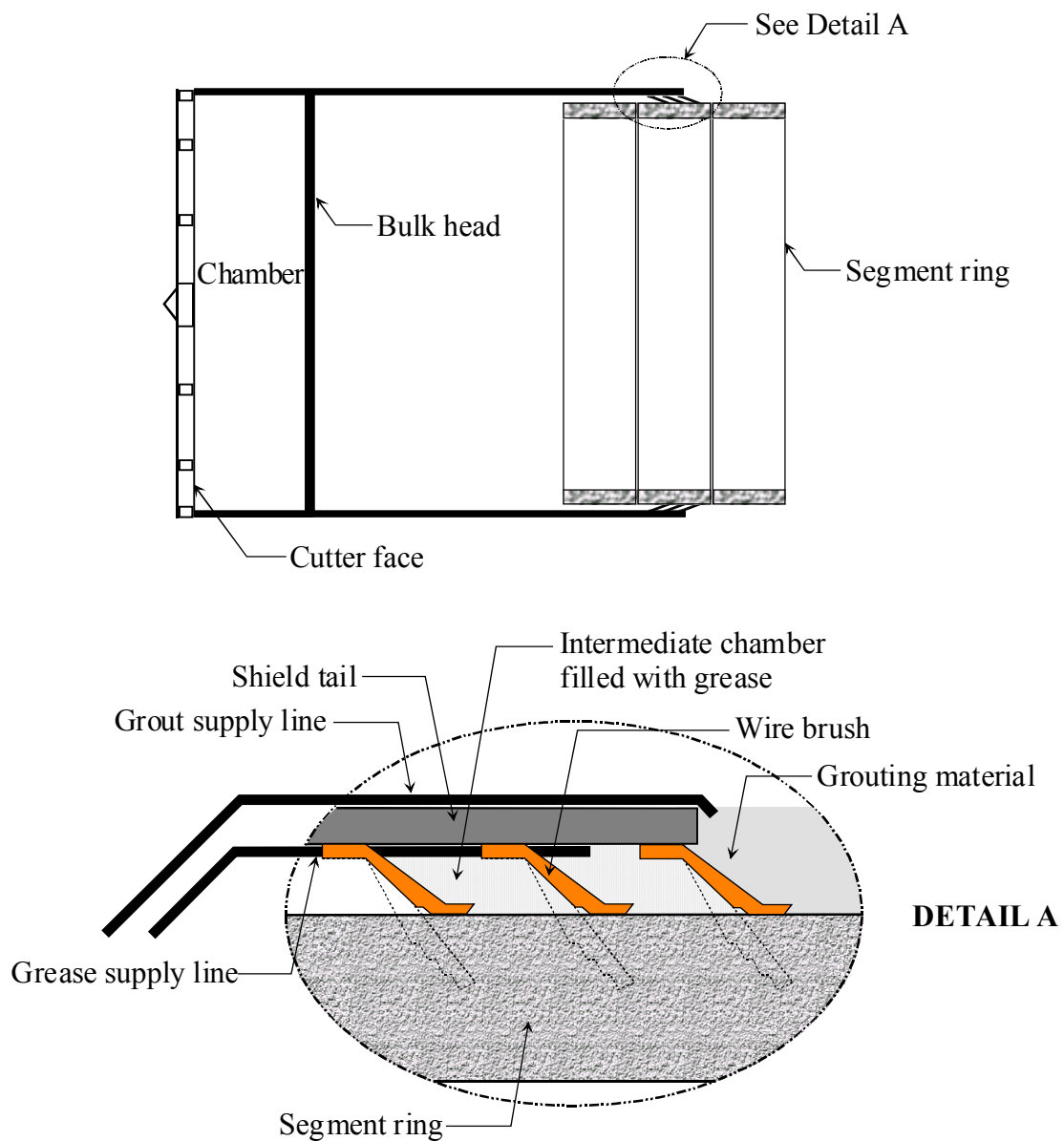


Figure 1.13 Installation of wire brush seal on the inside shield tail.

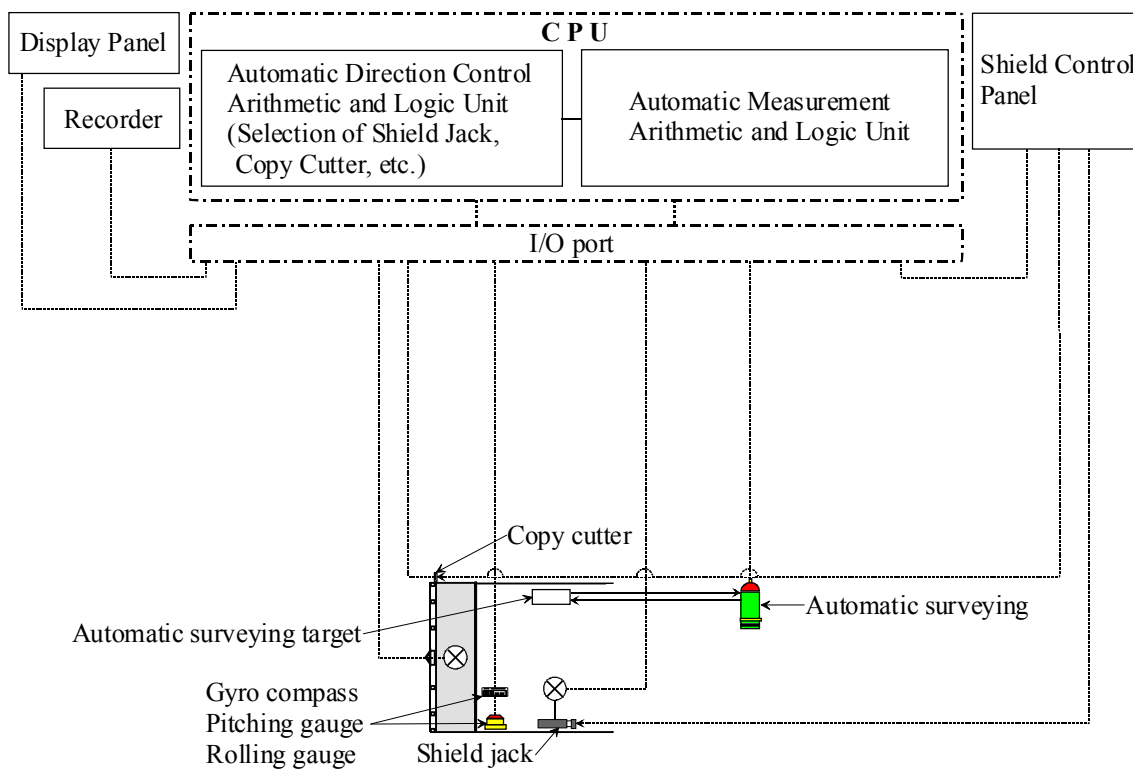


Figure 1.14 An example of automatic shield direction control system.

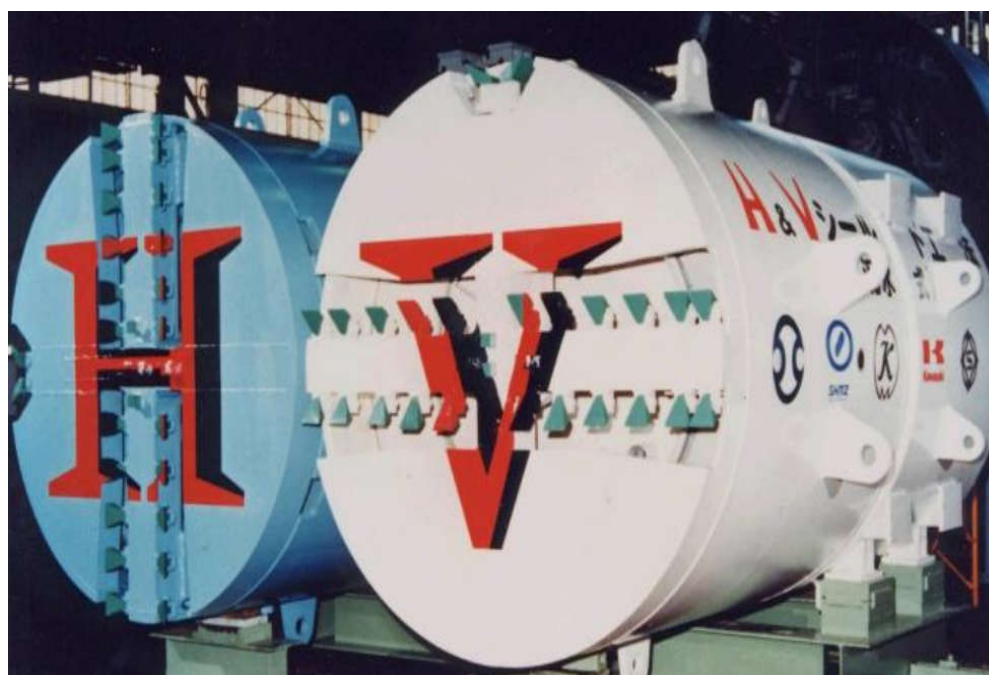
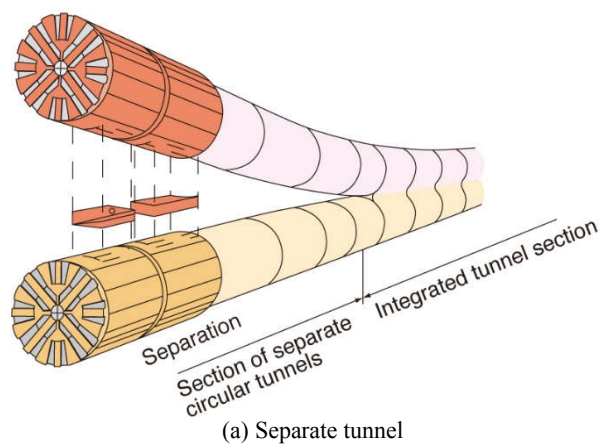
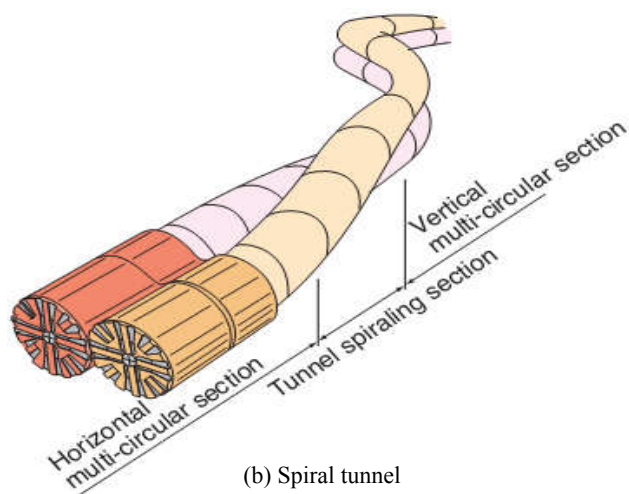


Figure 1.15 H&V shield. (STA 2011b)



(a) Separate tunnel



(b) Spiral tunnel

Figure 1.16 Utilization of H&V shield. (STA 2011b)

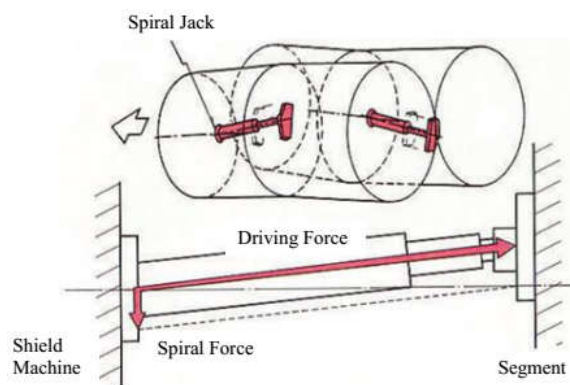


Figure 1.17 Spiral jack. (STA 2011b)

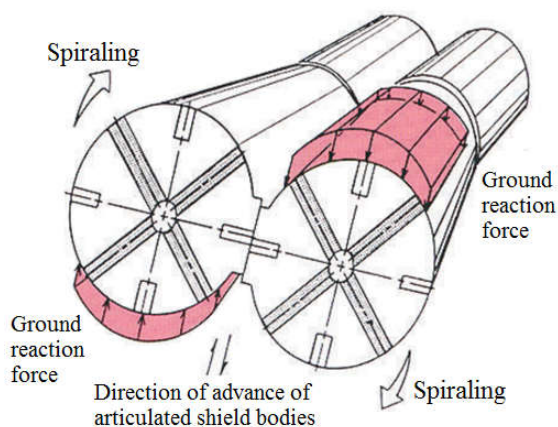


Figure 1.18 Copy cutter and articulated mechanism in excavation. (STA 2011b)

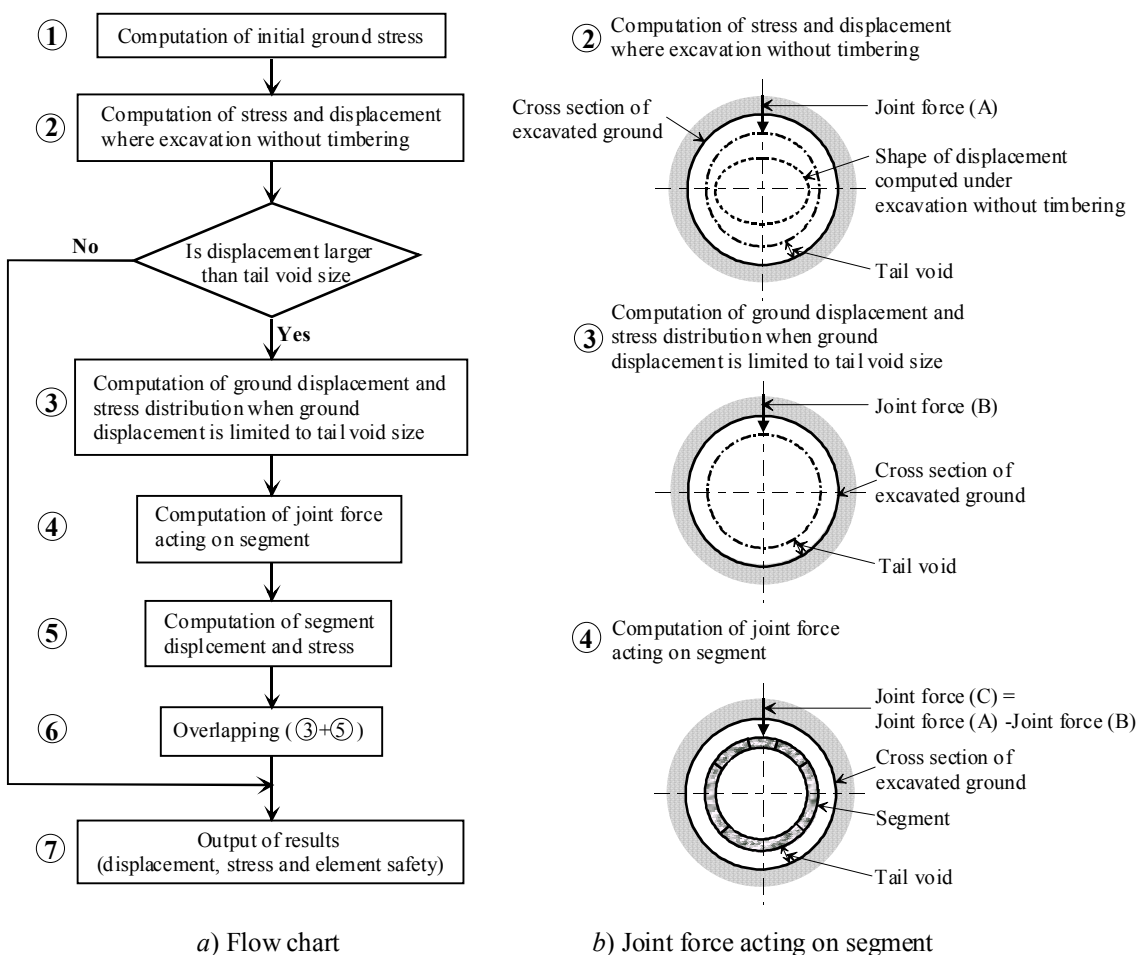


Figure 1.19 Model to analyze taking tail void and segment rigidity into consideration (Yamada et al., 1979).

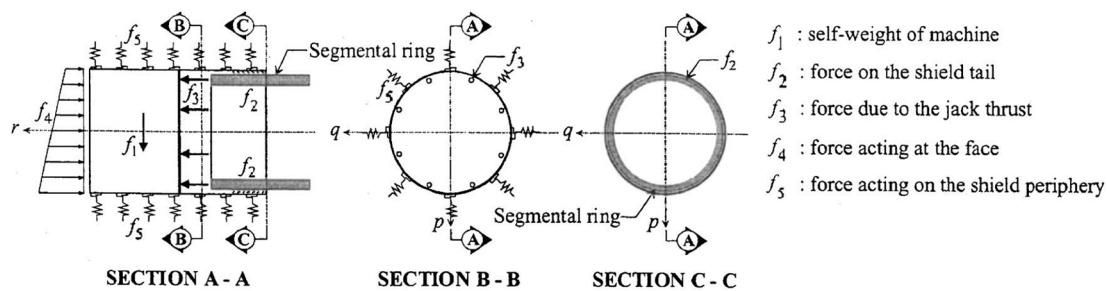


Figure 1.20 Model of loads acting on shield (Sugimoto and Sramoon 2002).

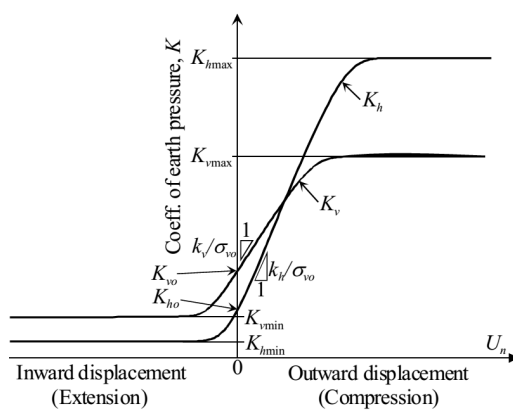


Figure 1.21 Ground reaction curve.

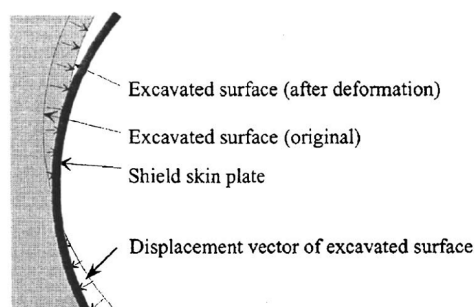
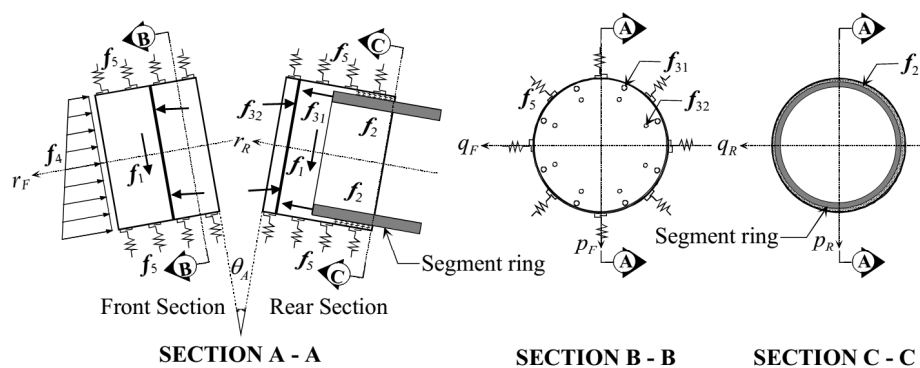


Figure 1.22 Definition of displacement of excavated surface for stiff ground



$f_1$  : self-weight of machine                       $f_2$  : force on the shield tail                       $f_{31}$  : force due to the shield jack thrust  
 $f_{32}$  : force due to the articulate jack thrust                       $f_4$  : force acting at the face                       $f_5$  : force acting on the shield periphery  
 $\theta_A$  : articulated angle

Figure 1.23 Model of load acting on both of right and left body of H&V shield.

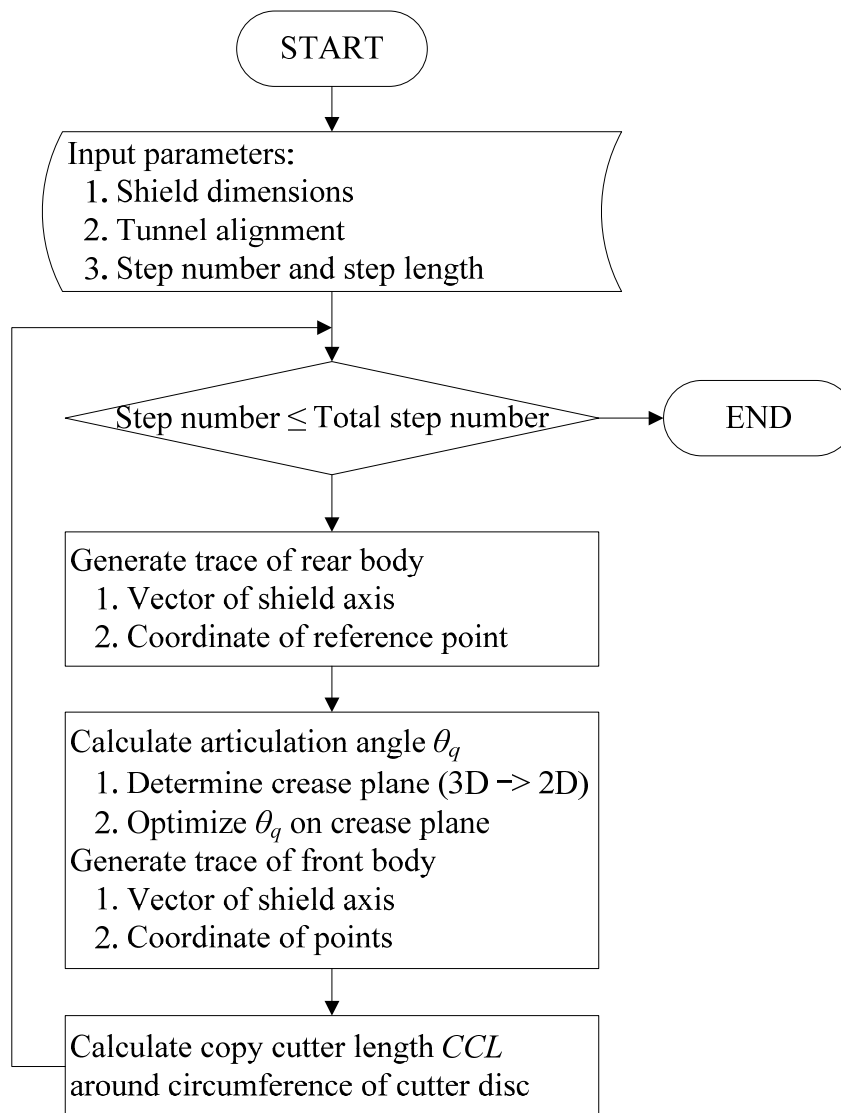


Figure 2.1 Flowchart of numerical procedure for articulation angle and copy cutter length.

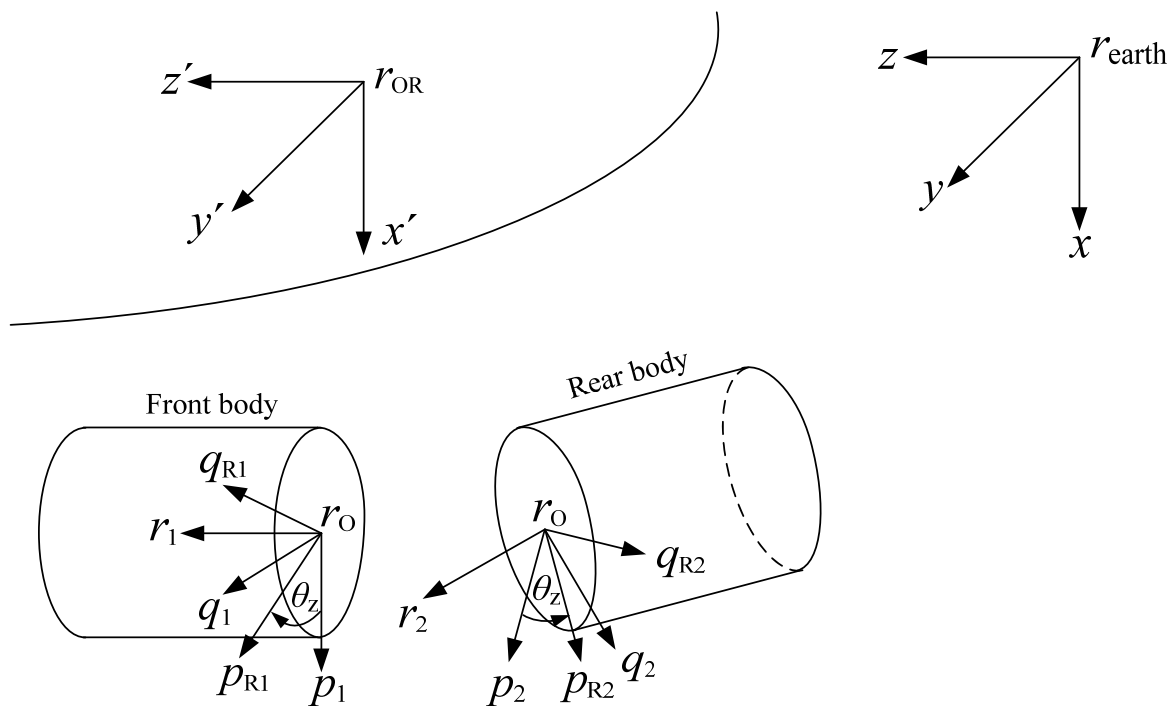


Figure 2.2 Coordinate systems.

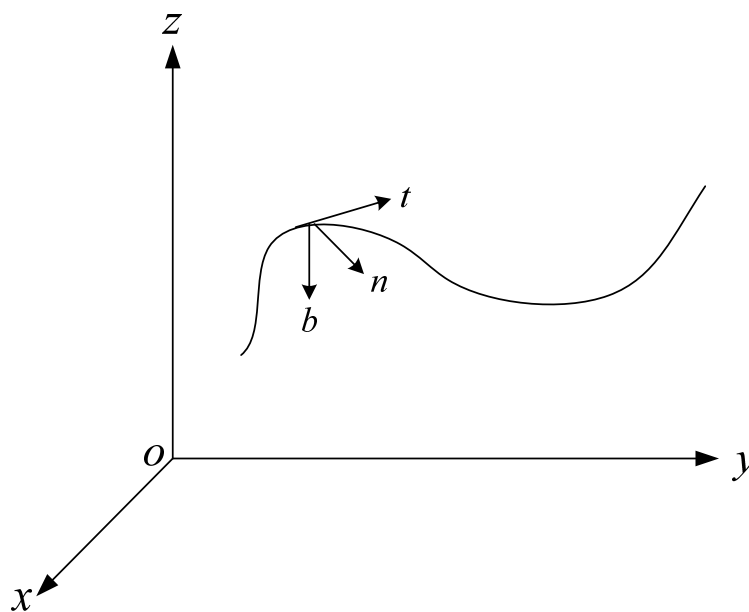


Figure 2.3 Fundamental unit vectors of a spatial curve.

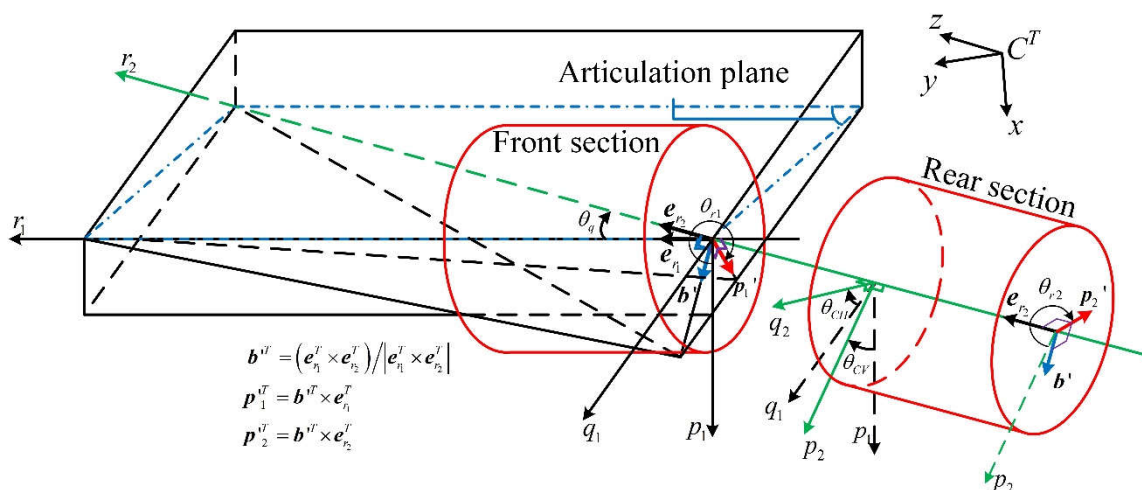


Figure 2.4 Relation between articulation angle and direction vectors.

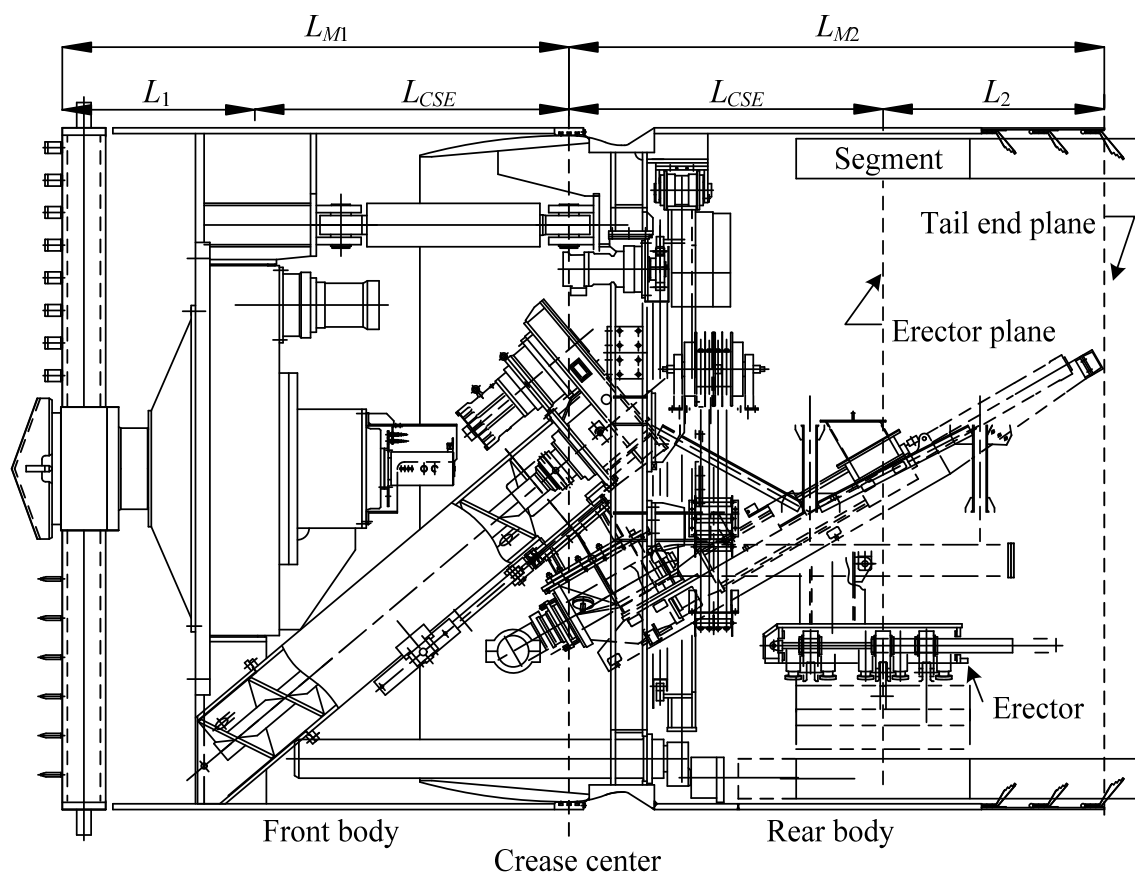


Figure 2.5 Dimension of articulated shield.

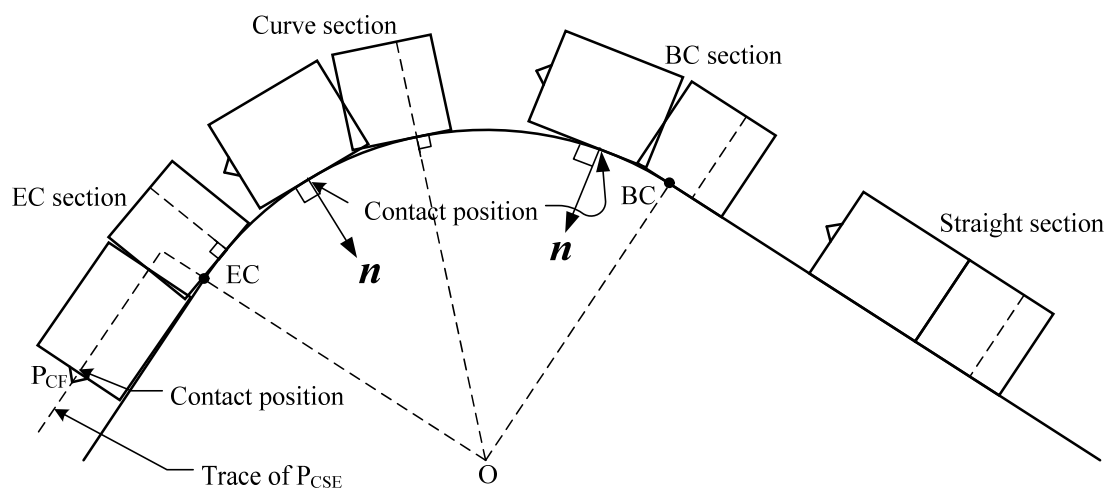


Figure 2.6 Crease Type 1.

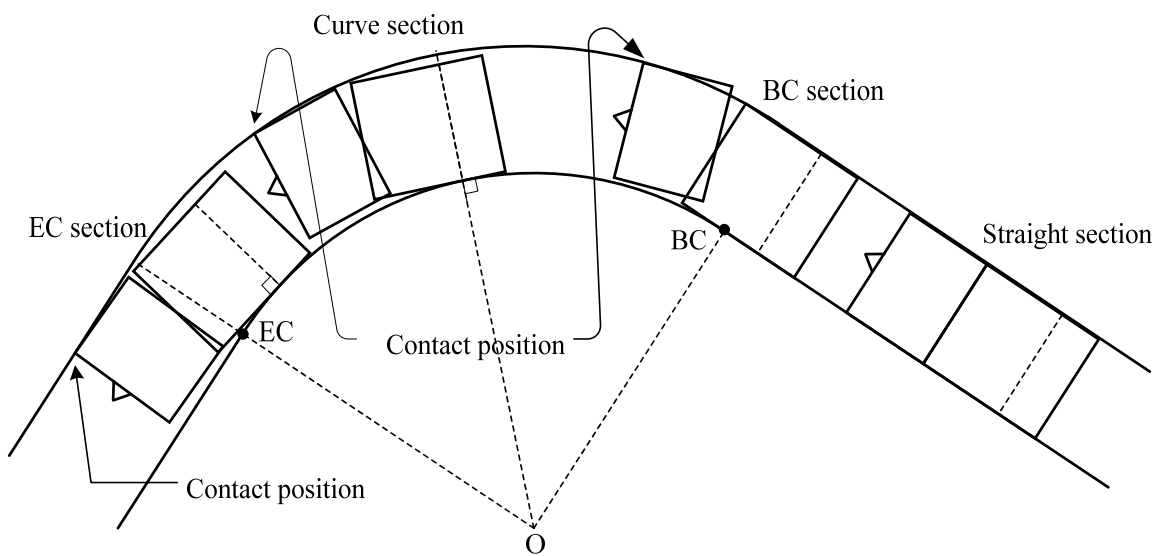
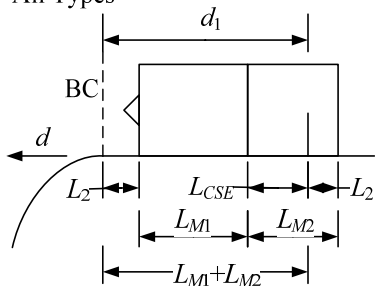


Figure 2.7 Crease Type 2 and Type 3.

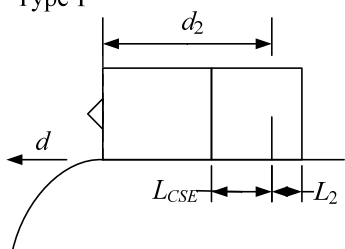
1. CC starts at outer side of curve

All Types

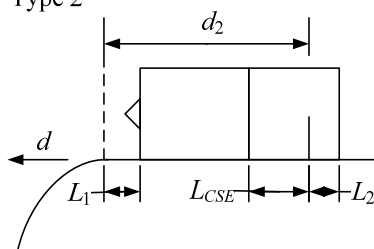


2. CC starts at inner side of curve

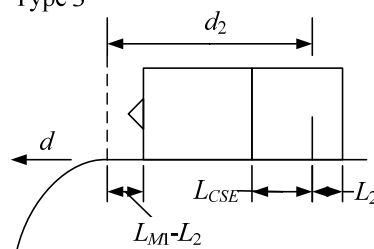
Type 1



Type 2

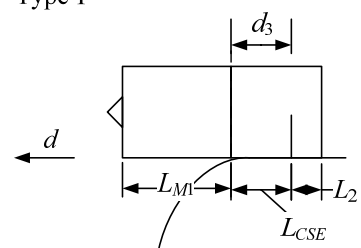


Type 3

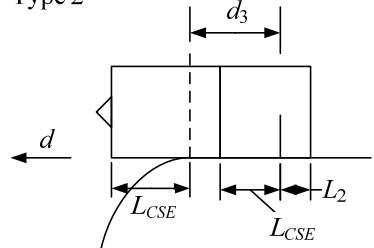


3. FB rotation starts

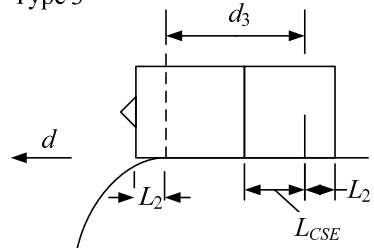
Type 1



Type 2



Type 3



4. RB rotation starts =  $\theta_q$  change end

All Types

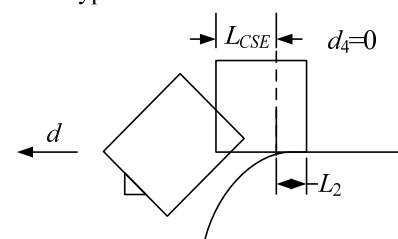


Figure 2.8 Operation rules at BC section for all types.

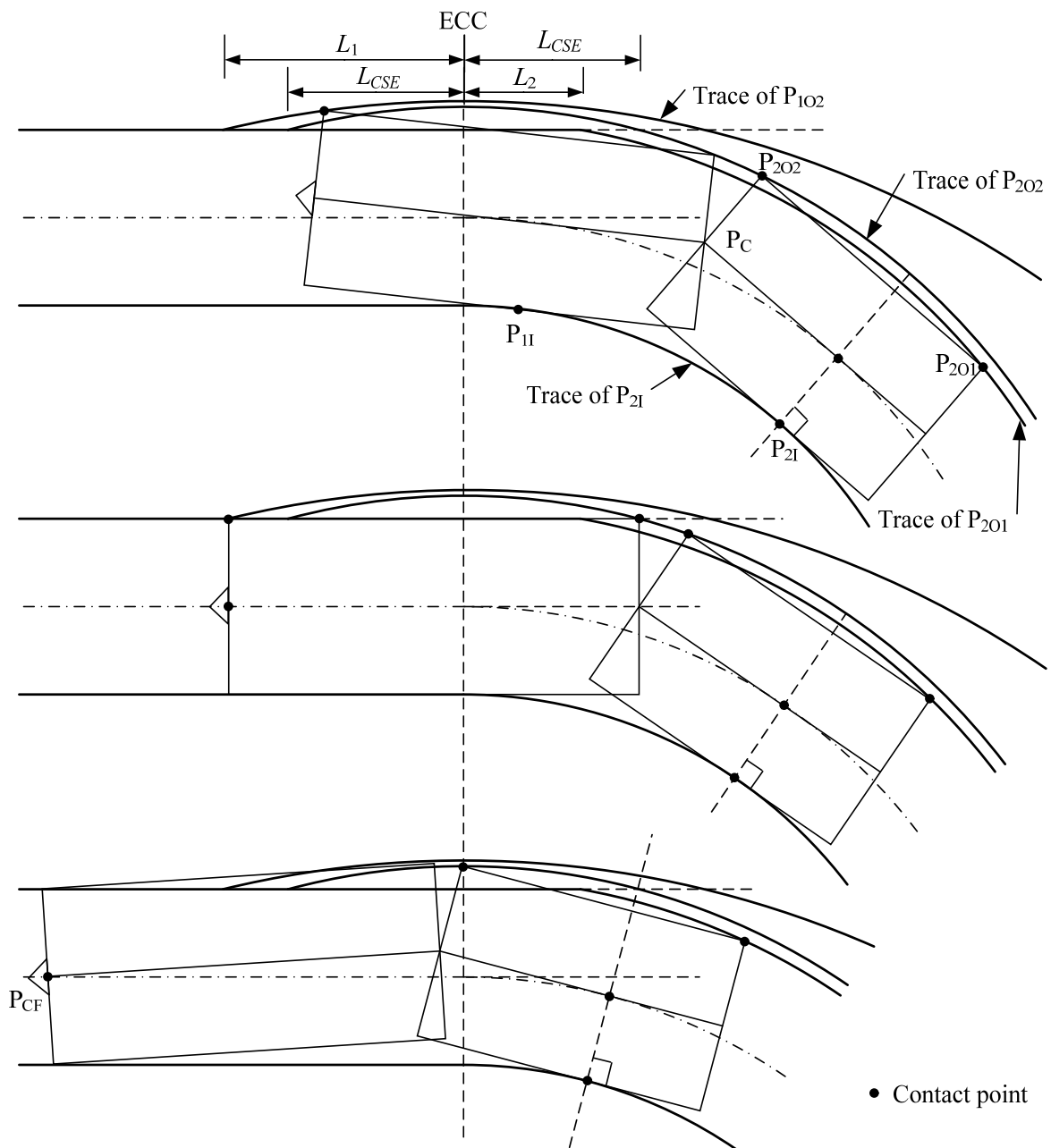


Figure 2.9 (a) Operation rules at EC section for Type1.

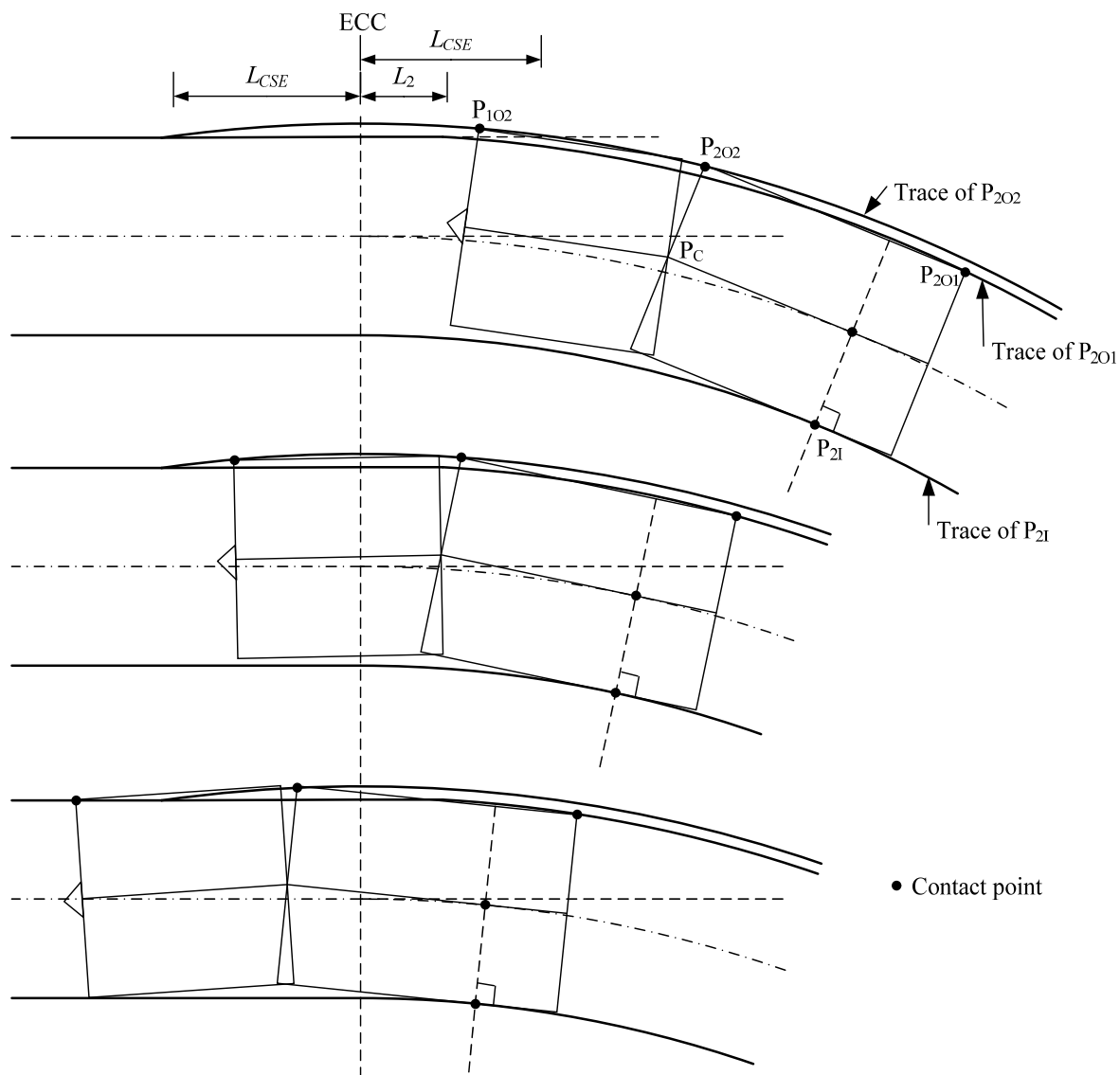


Figure 2.9 (b) Operation rules at EC section for Type2.

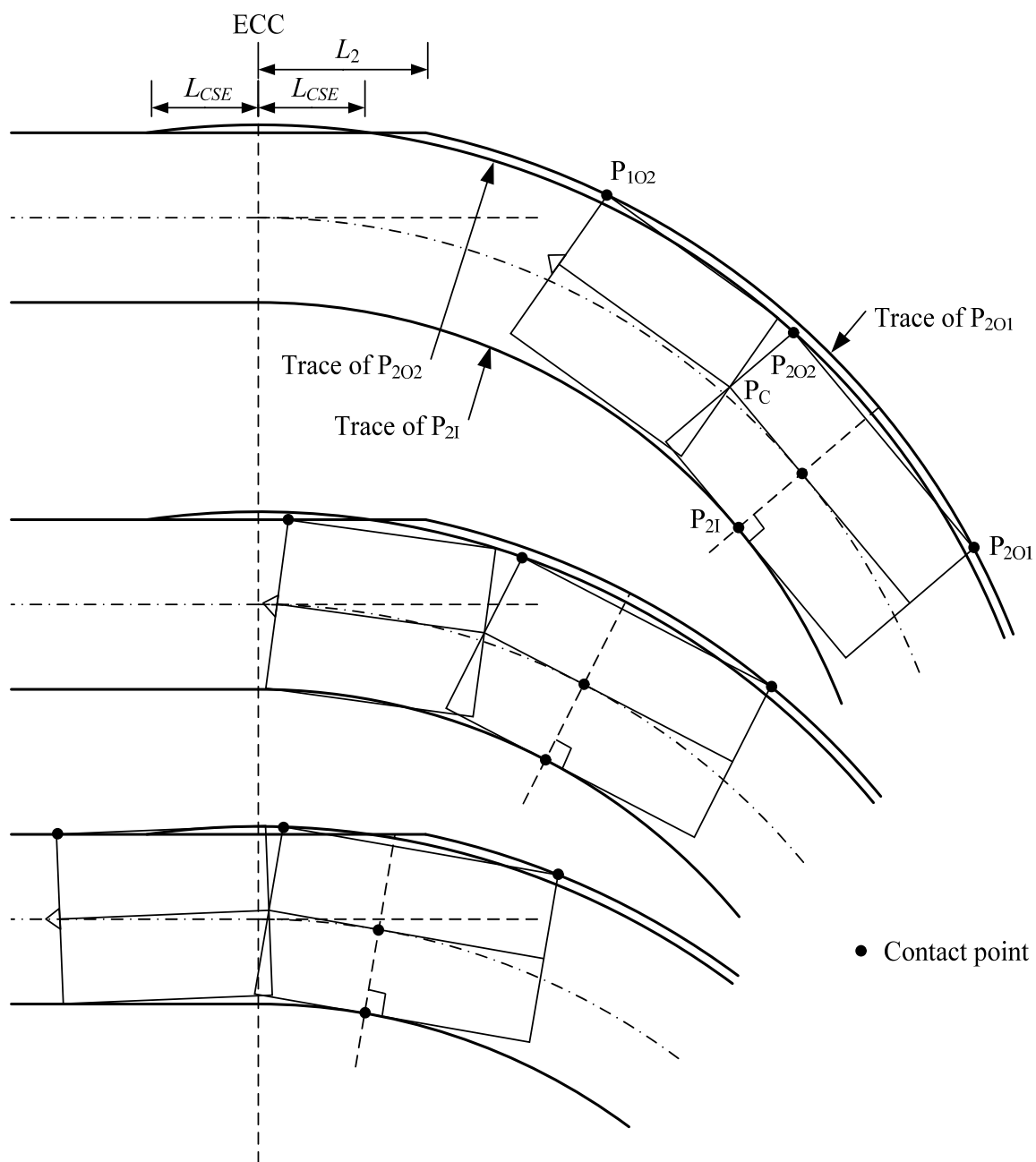


Figure 2.9 (c) Operation rules at EC section for Type3.

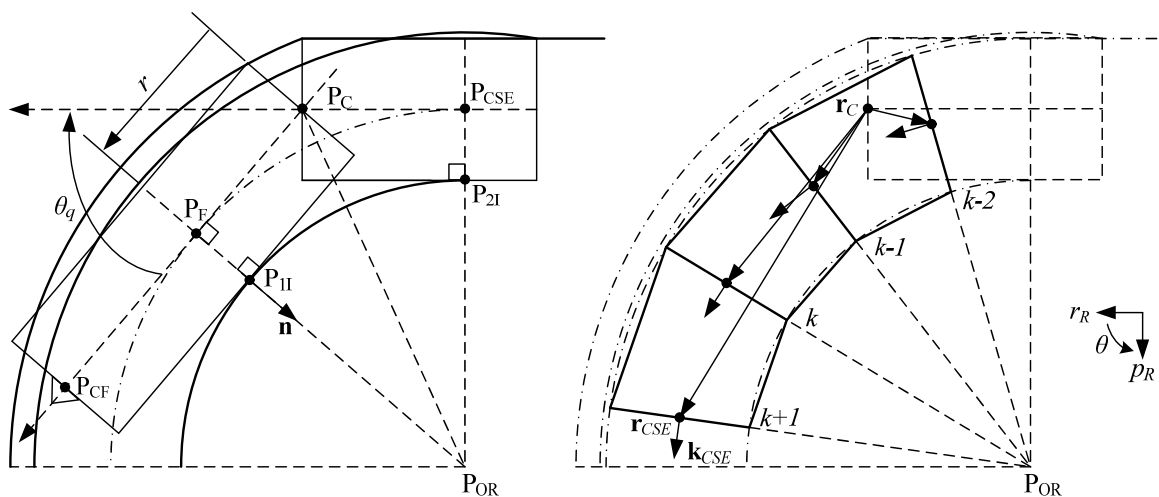


Figure 2.10 Contact condition of Type 1 at curve section.

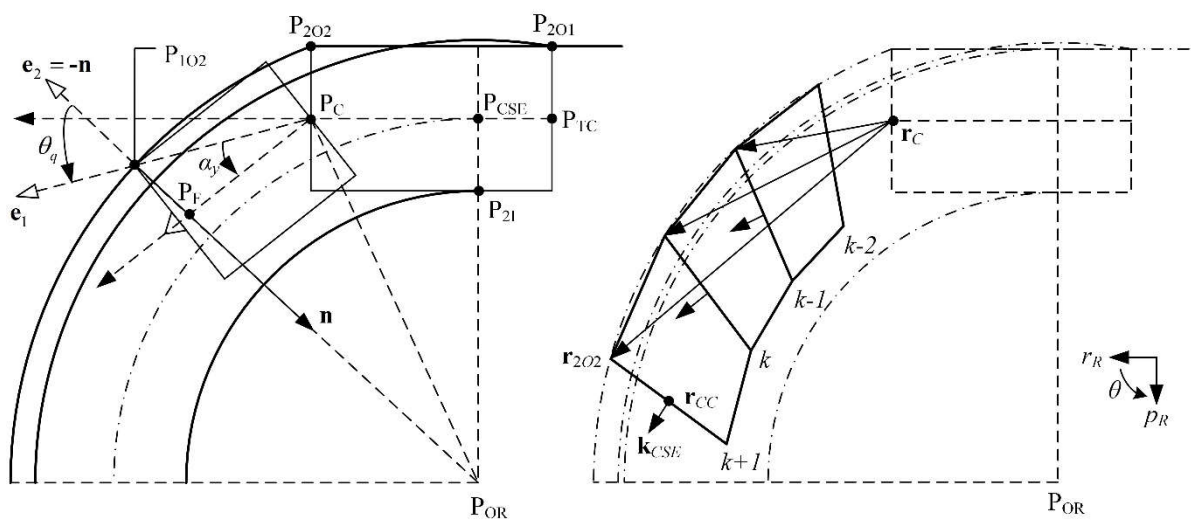


Figure 2.11 Contact condition of Type 2 at curve section.

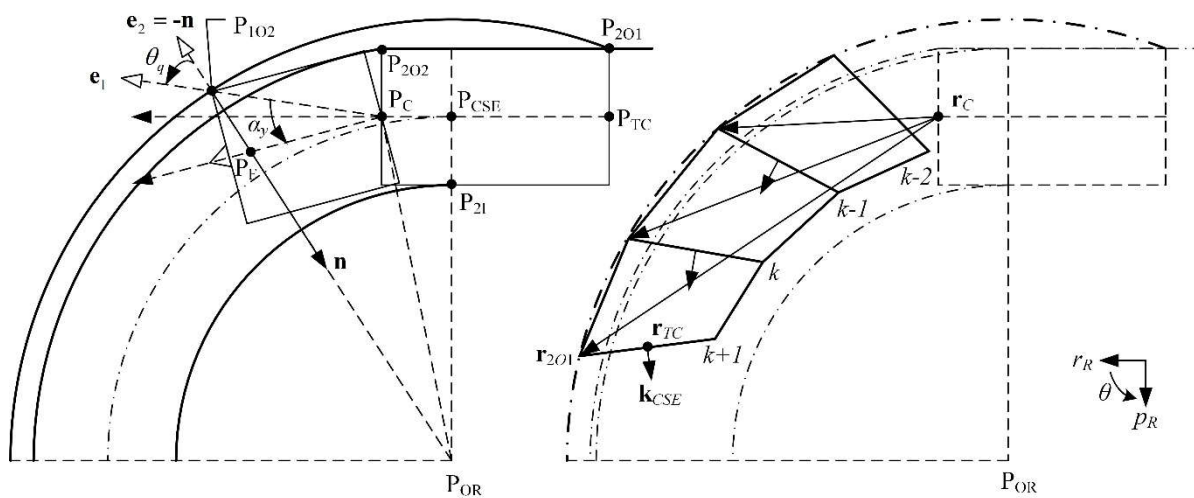


Figure 2.12 Contact condition of Type 3 at curve section.

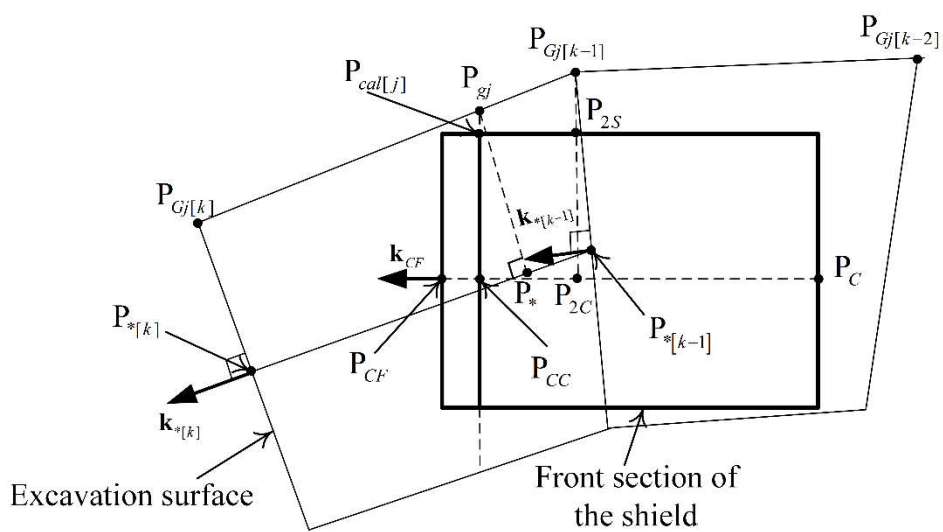


Figure 2.13 Concept to calculate copy cutter length.

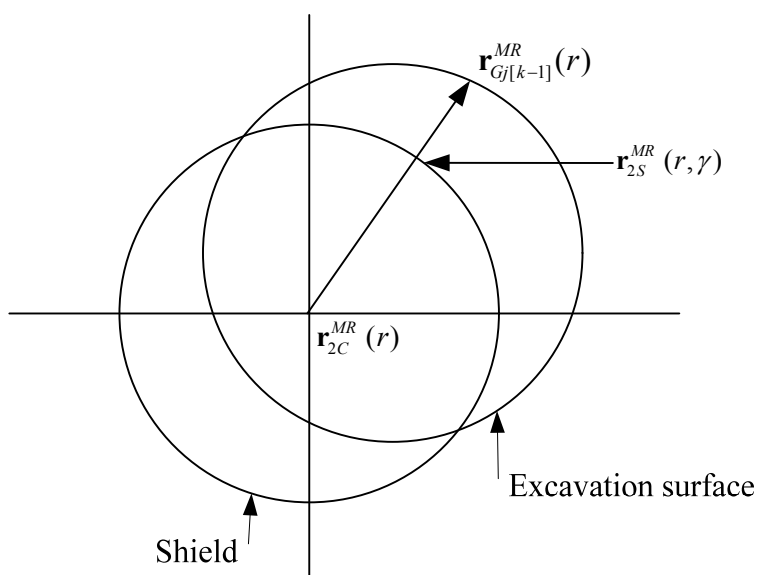


Figure 2.14 Calculation points for Procedure A.

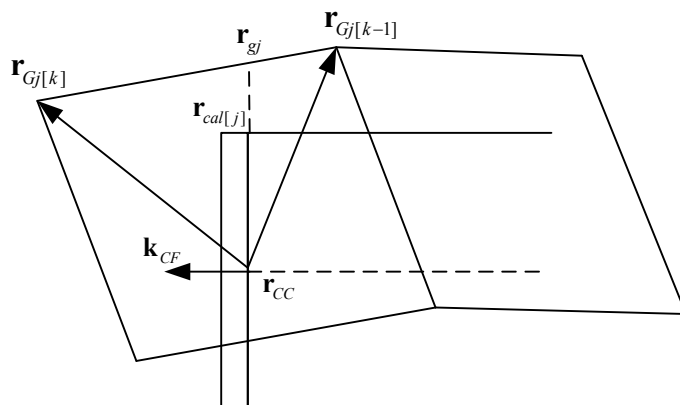


Figure 2.15 Calculation points for Procedure B.

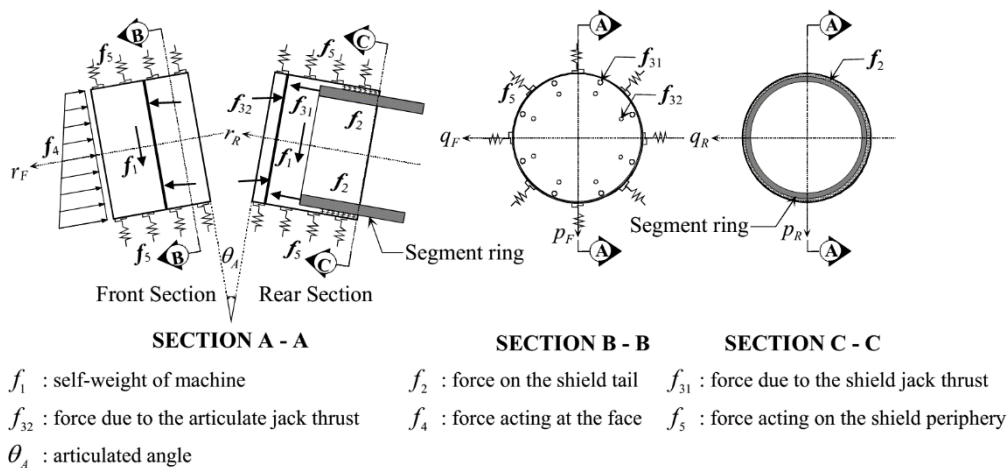


Figure 2.16: Model of load acting on both front body and rear body of H&V shield

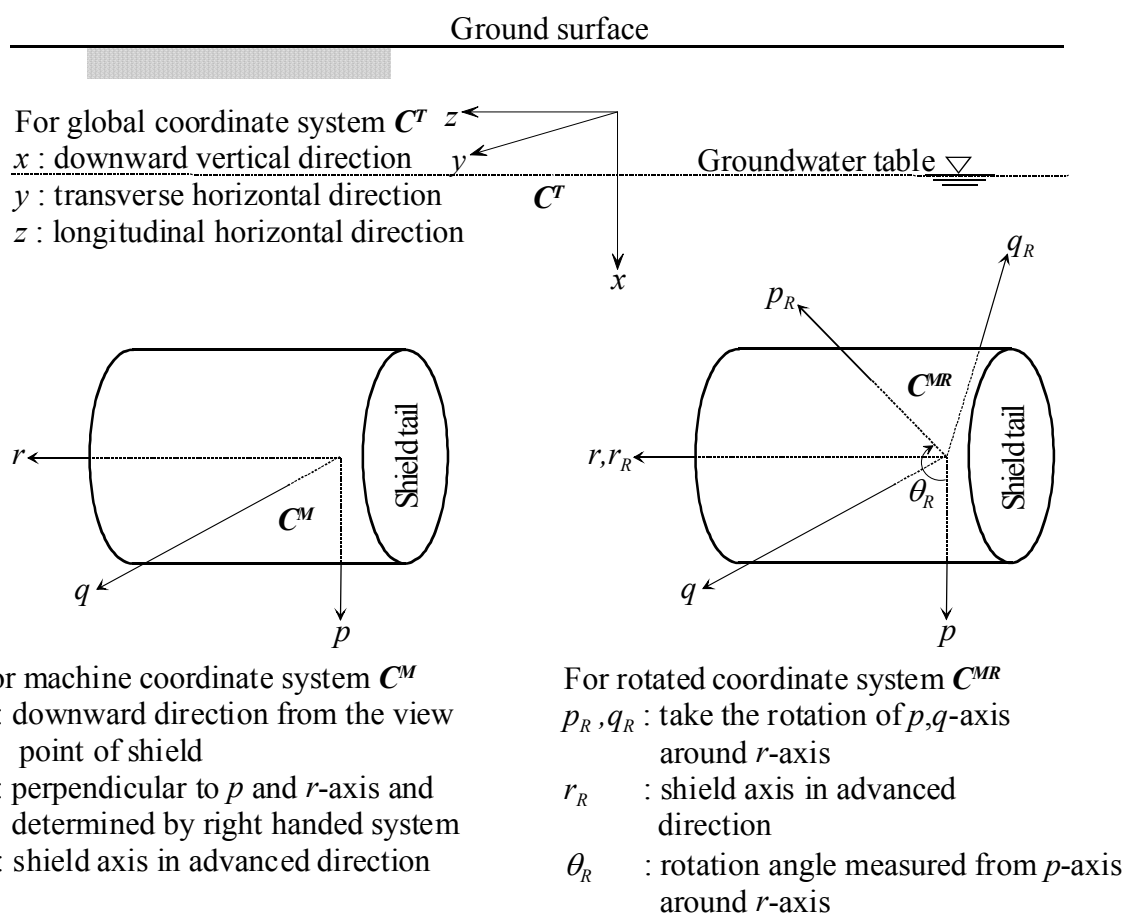


Figure 2.17 Coordinate systems.

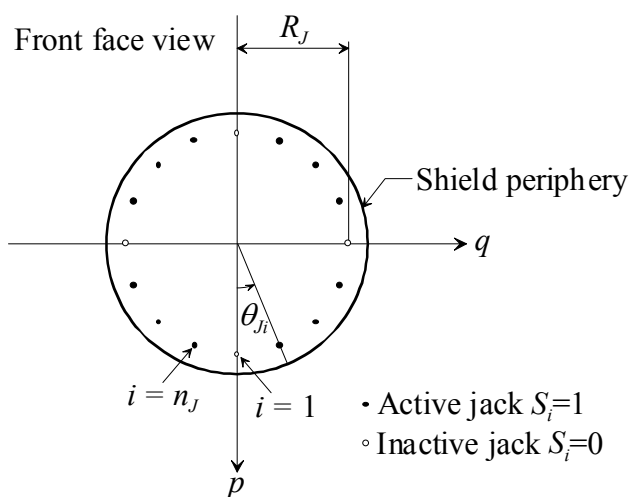


Figure 2.18 Definition of jack position measurement.

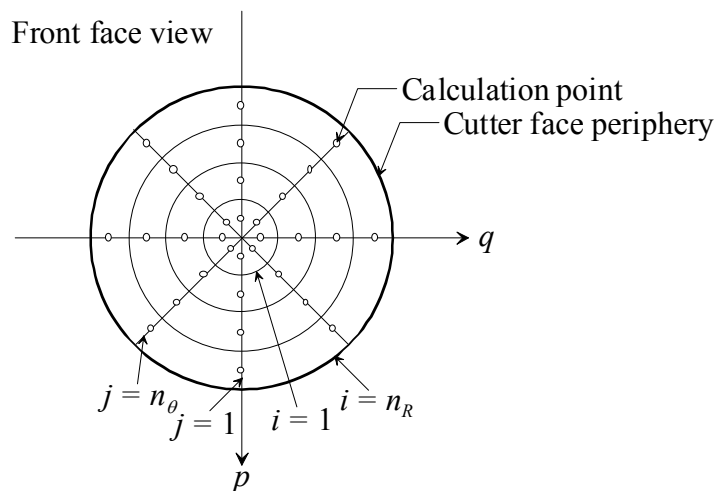


Figure 2.19 Definition of division on front face.

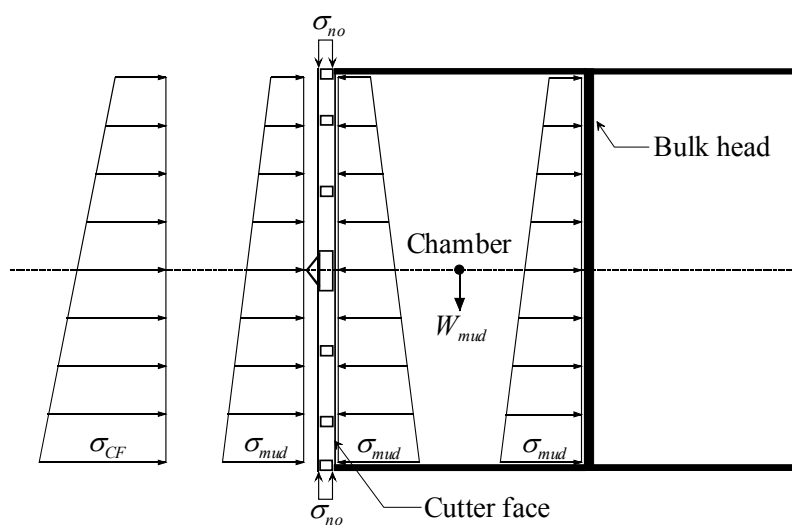


Figure 2.20 Pressure on cutter face.

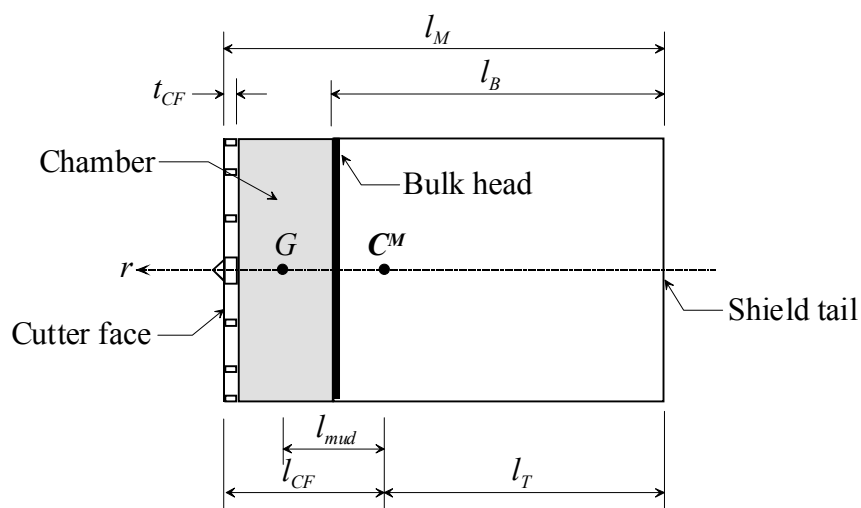


Figure 2.21 Definition of length measured on shield.

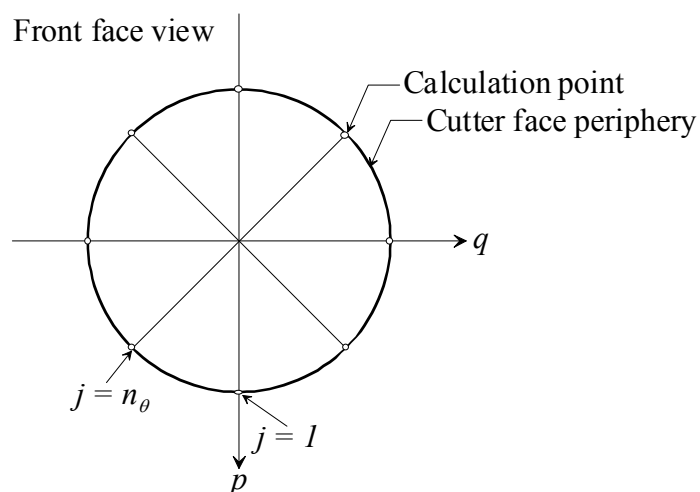


Figure 2.22 Definition of calculation point on cutter face periphery.

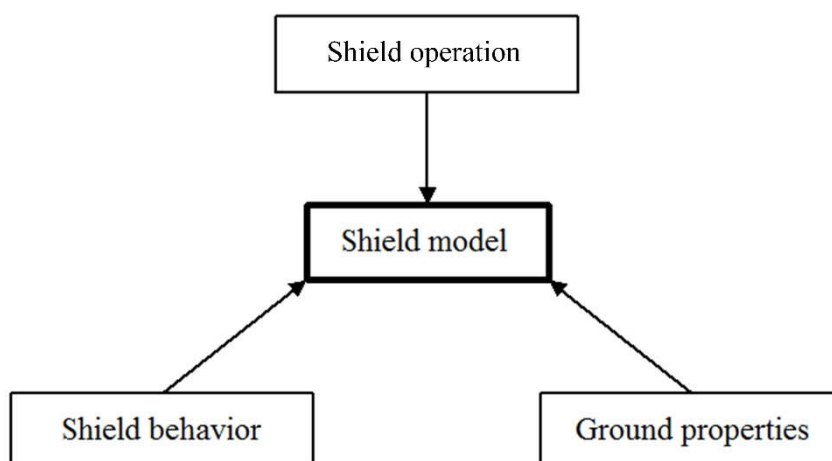
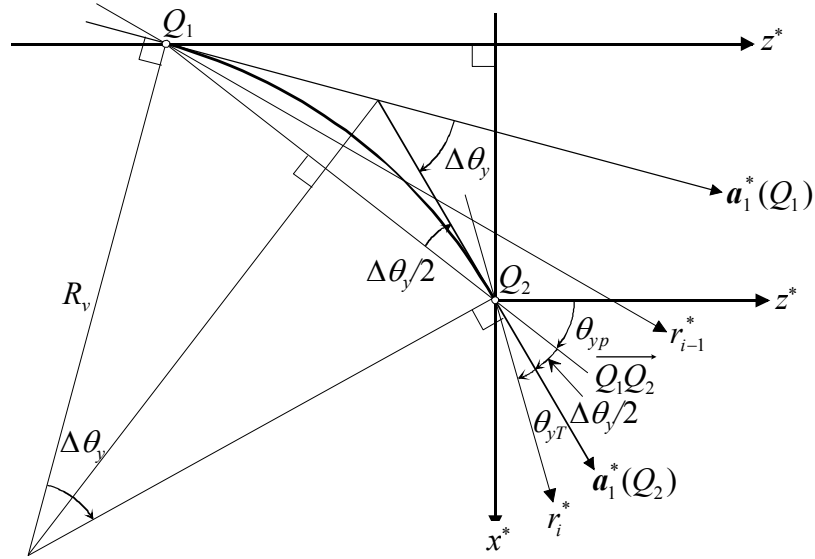
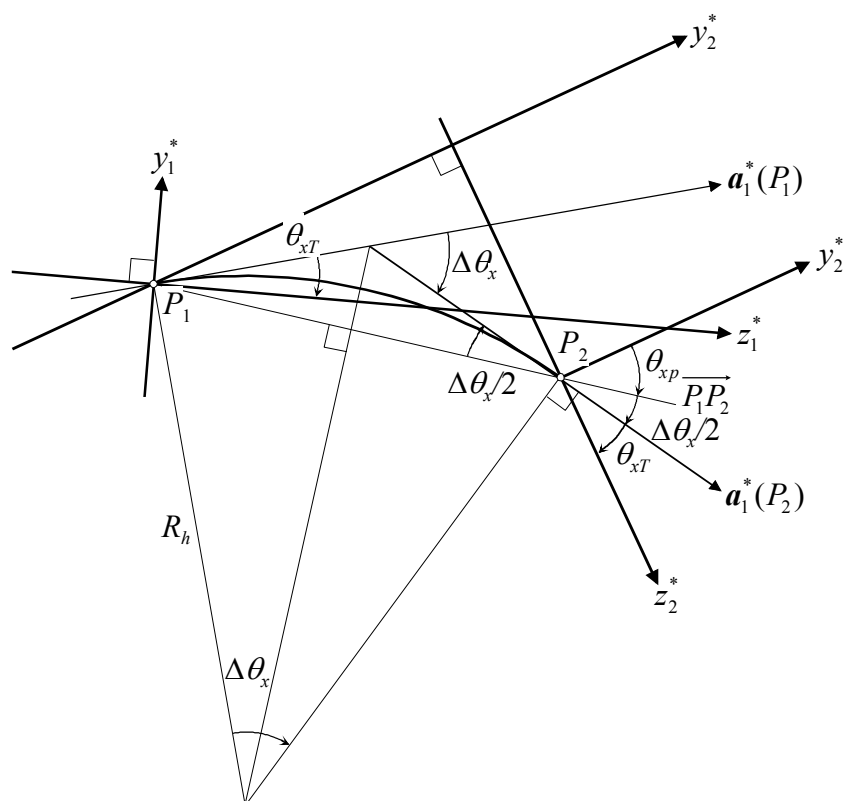


Figure 2. 23 Factors affecting shield model.



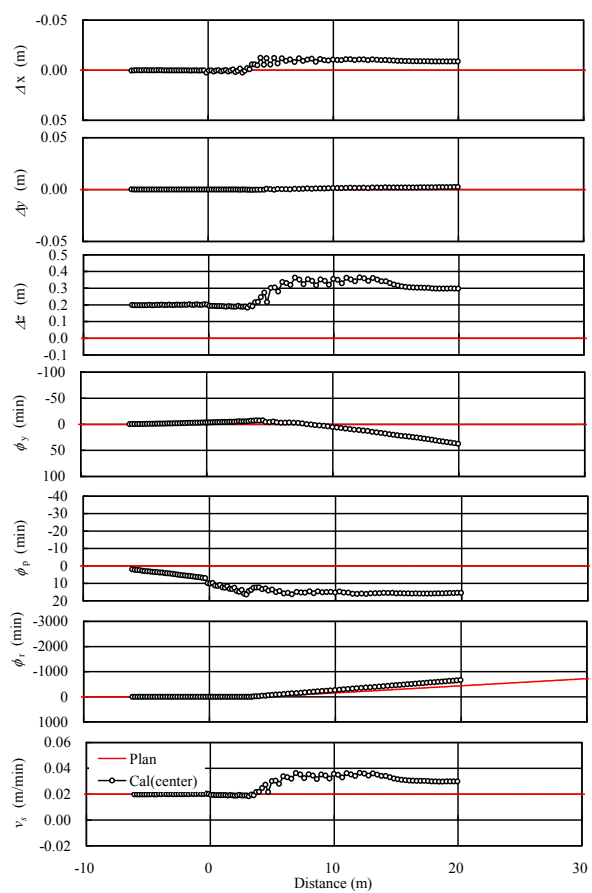
- $\mathbf{a}_1^*(Q_i)$  : Projection of tangential unit vector  $\mathbf{a}_1(Q_i)$  of point  $Q_1$  and  $Q_2$  on vertical plane
- $z^*$  : Projection of tunnel alignment on vertical plane
- $x^*$  :  $x$ -axis of  $\mathbf{C}^T$
- $r_i^*$  : Projection of shield axis on  $x^*z^*$  plane
- $\Delta\theta_y$  : Rotation angle of  $r^*$ -axis around  $y^*$ -axis
- $\theta_{vT}$  : Tilt angle from the shield trace onto the shield axis on vertical plane
- $\theta_{vp}$  : Angle from  $z^*$ -axis to chord  $Q_1Q_2$
- $R_v$  : Radius of curvature on vertical plane

Figure 2.24 Description of  $R_v$  and  $\theta_{vT}$

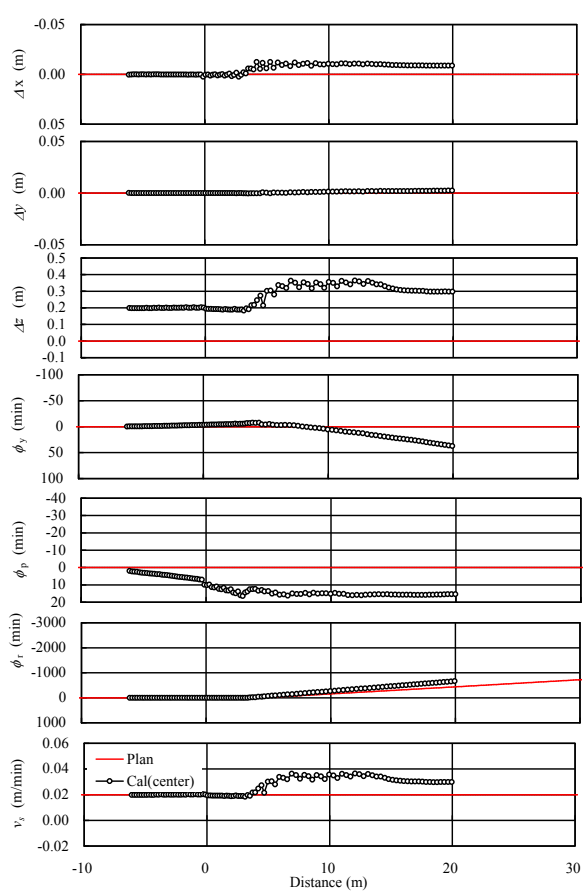


- $\mathbf{a}_1^*(P_i)$  : Projection of tangential unit vector  $\mathbf{a}_1(P_i)$  of point  $P_1$  and  $P_2$  on horizontal plane
- $z_i^*$  : Projection of shield axis at  $P_i$  on vertical plane
- $\Delta\theta_x$  : Rotation angle of  $z^*$ -axis around  $x^*$ -axis
- $\theta_{xT}$  : Tilt angle from the shield trace onto the shield axis on horizontal plane
- $\theta_{xp}$  : Angle from  $y_2^*$ -axis to chord  $P_1P_2$
- $R_h$  : Radius of curvature on horizontal plane

Figure 2.25 Description of  $R_h$  and  $\theta_{xT}$

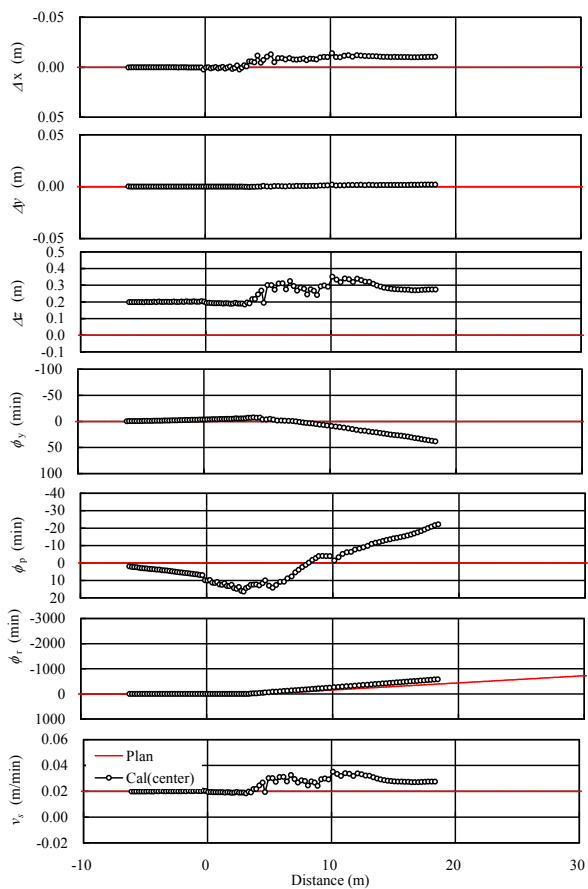


(a) Case No. 100003

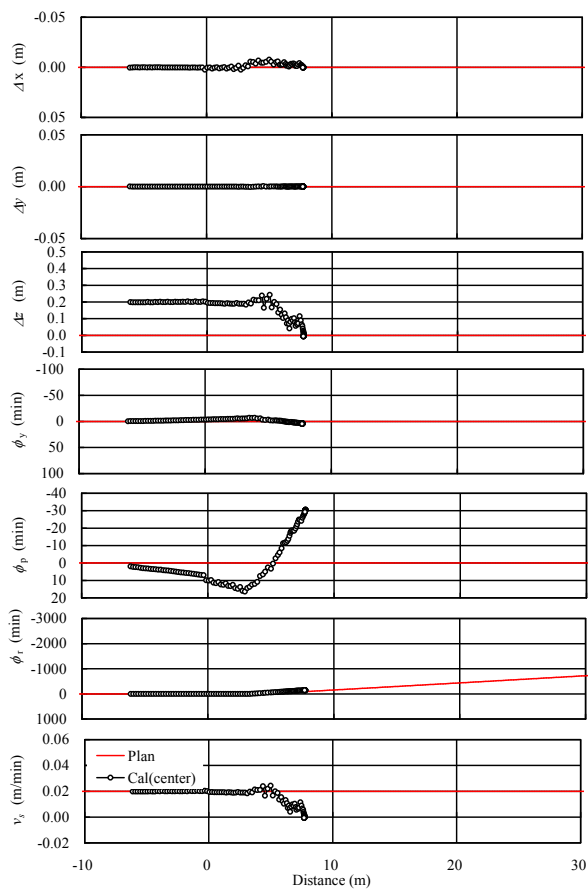


(b) Case No. 125003

Figure 3.1 Shield behavior (Parameter 1: CCL)

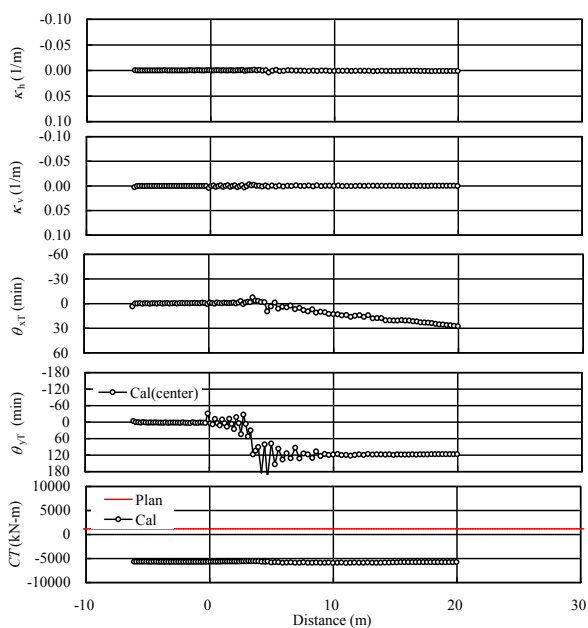


(c) Case No. 150003

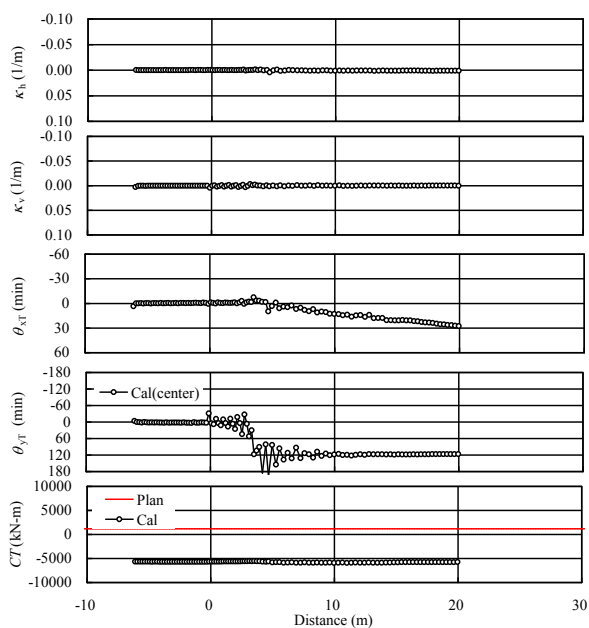


(d) Case No. 175003

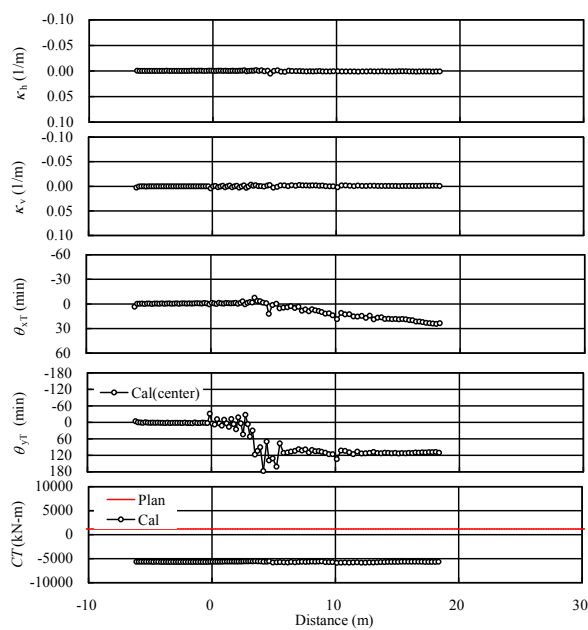
Figure 3.1 Shield behavior (Parameter 1: CCL)



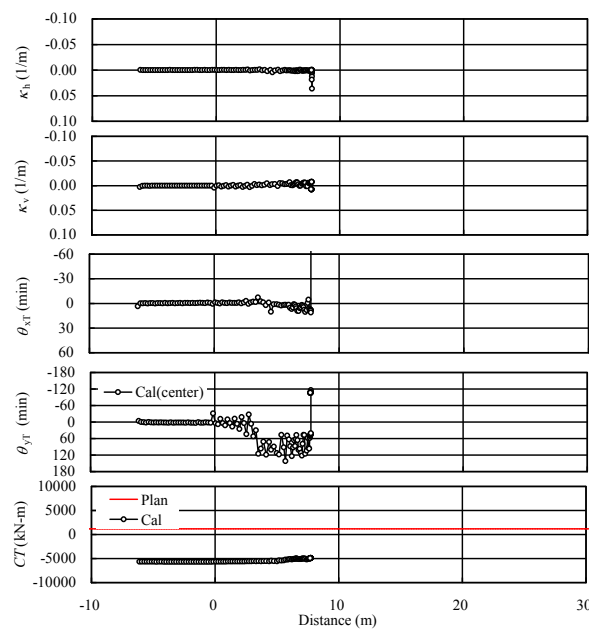
(a) Case No. 100003



(b) Case No. 125003

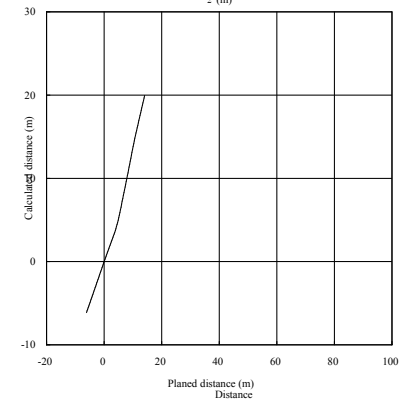
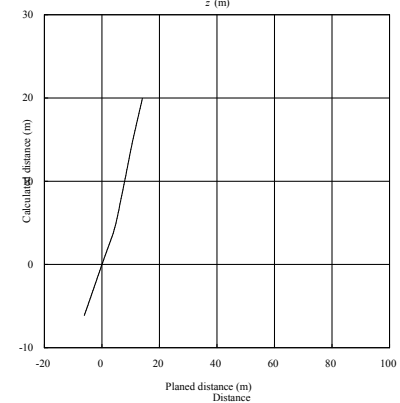
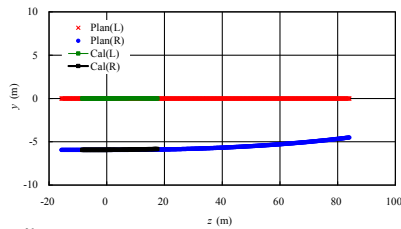
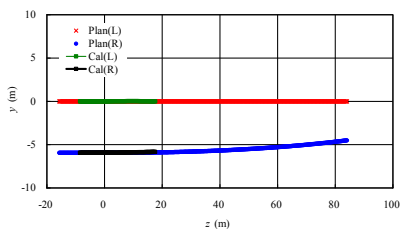
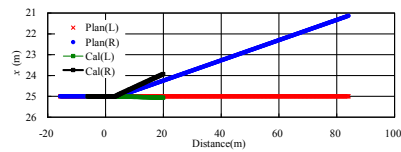
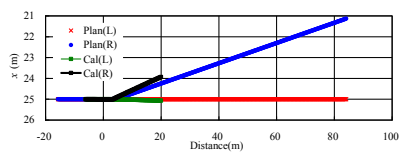


(c) Case No. 150003



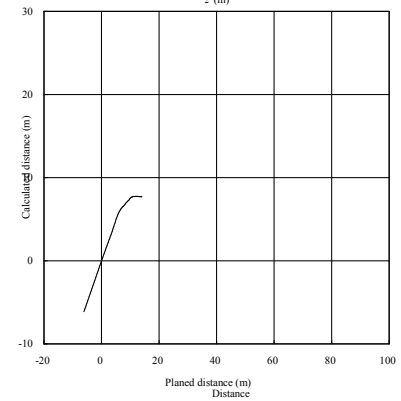
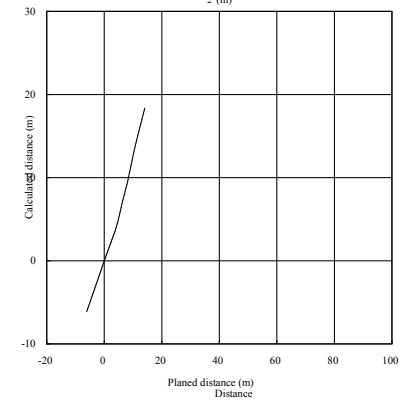
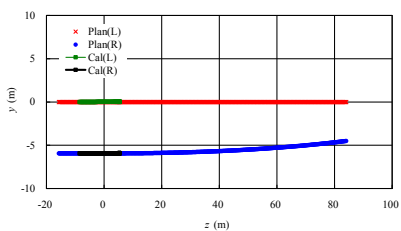
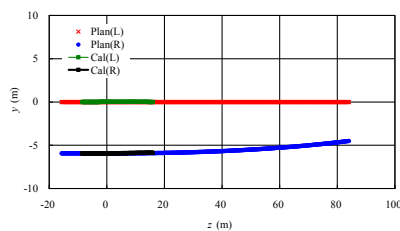
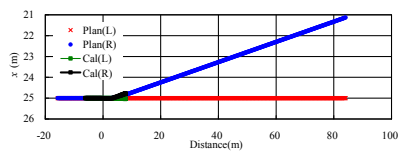
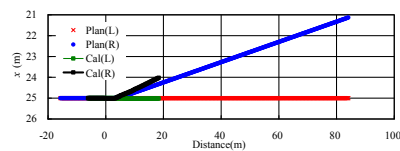
(d) Case No. 175003

Figure 3.2 Shield behavior (curvatures and tilt angles on the horizontal and vertical planes)  
(Parameter 1: CCL)



(a) Case No. 100003

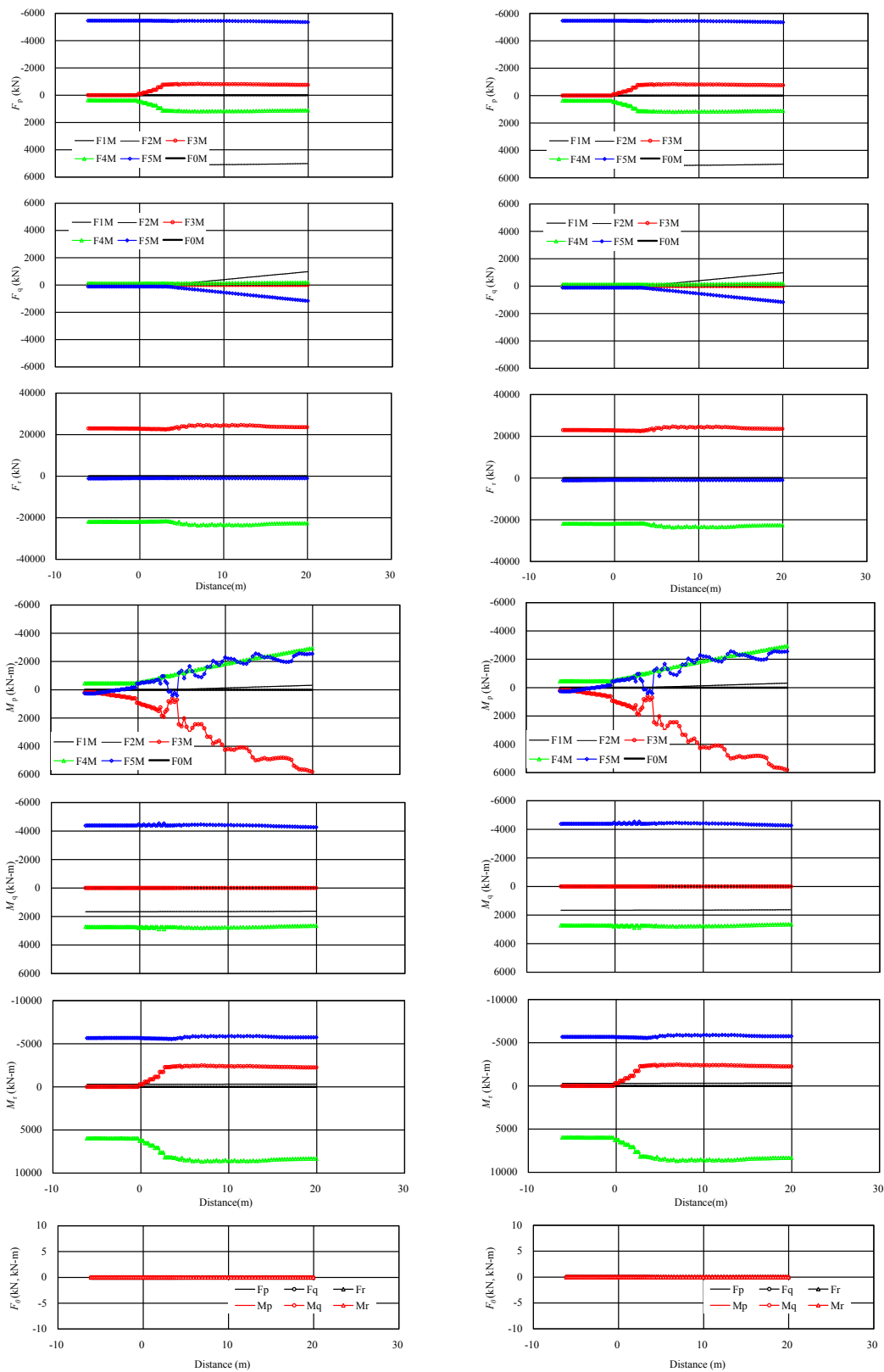
(b) Case No. 125003



(c) Case No. 150003

(d) Case No. 175003

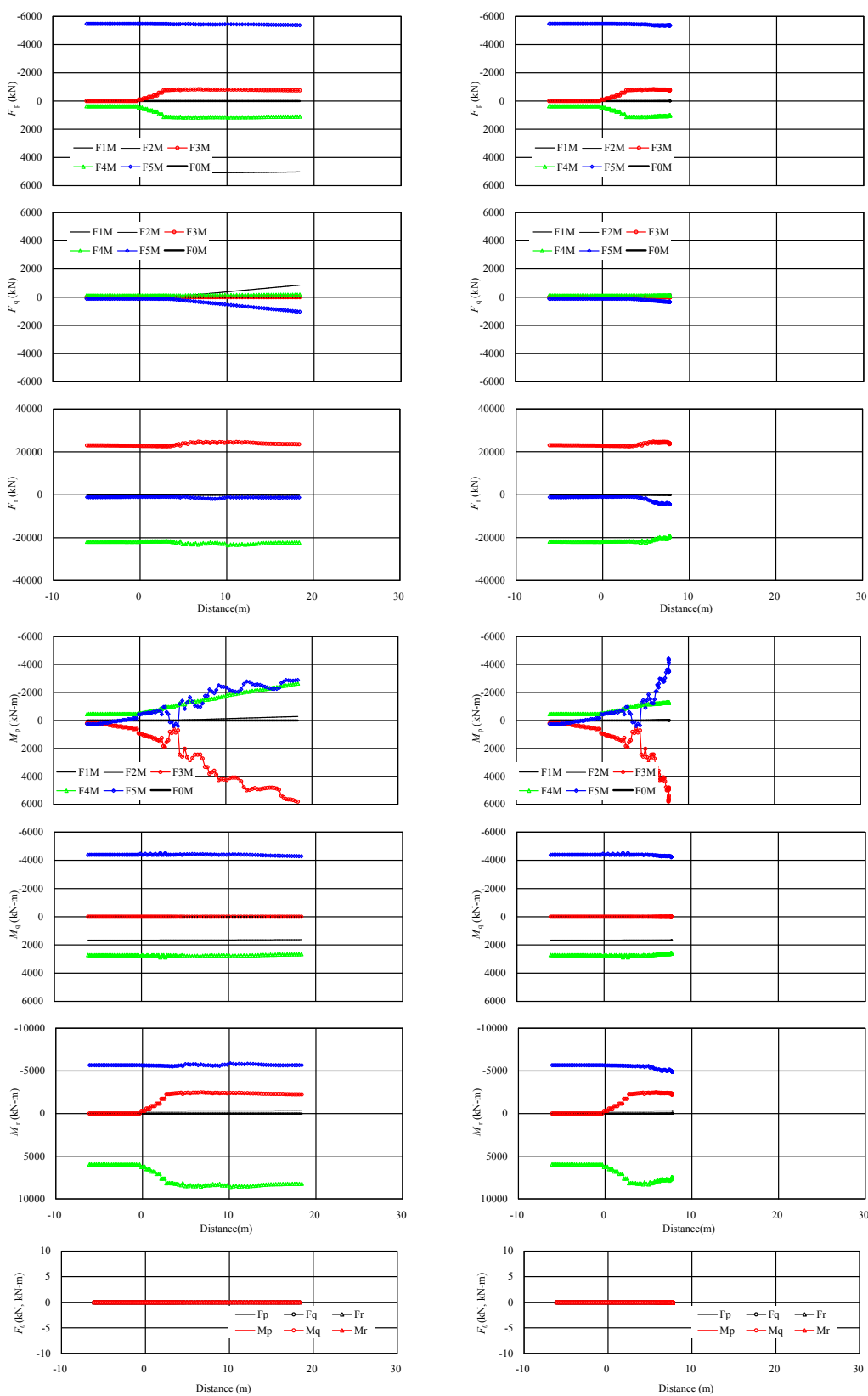
Figure 3.3 Trace of shield on the vertical and horizontal plan (Parameter 1: CCL)



(a) Case No. 100003

(b) Case No. 125003

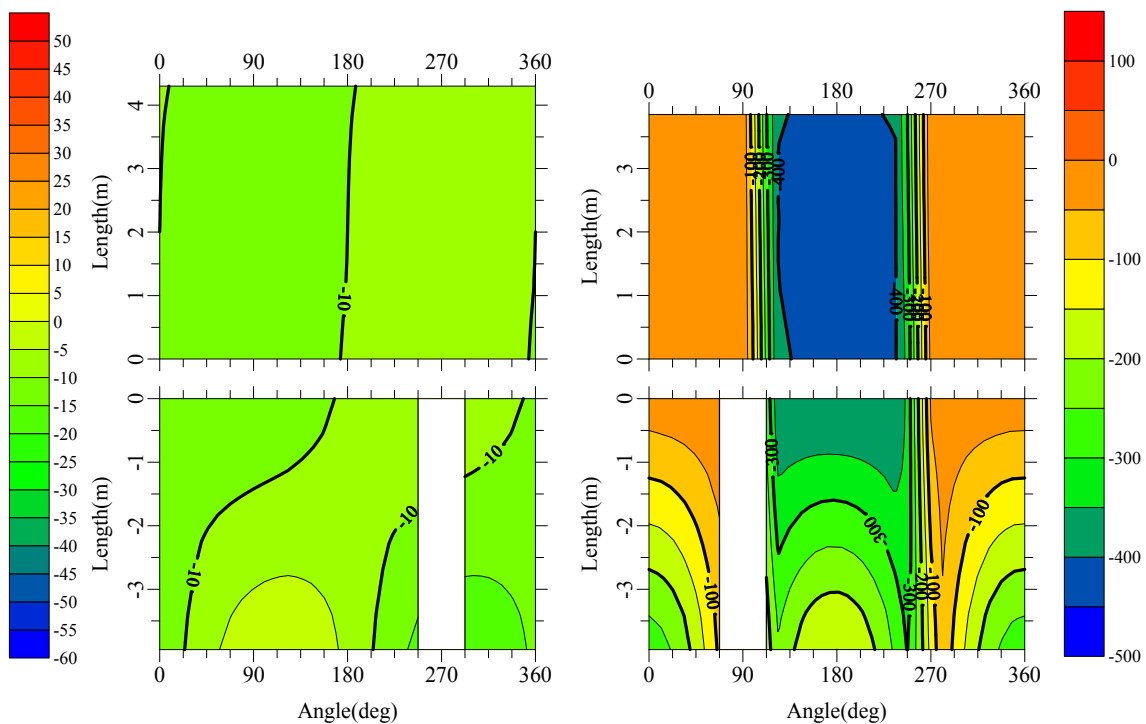
Figure 3.4 Forces and Moments against distance (Parameter 1: CCL)



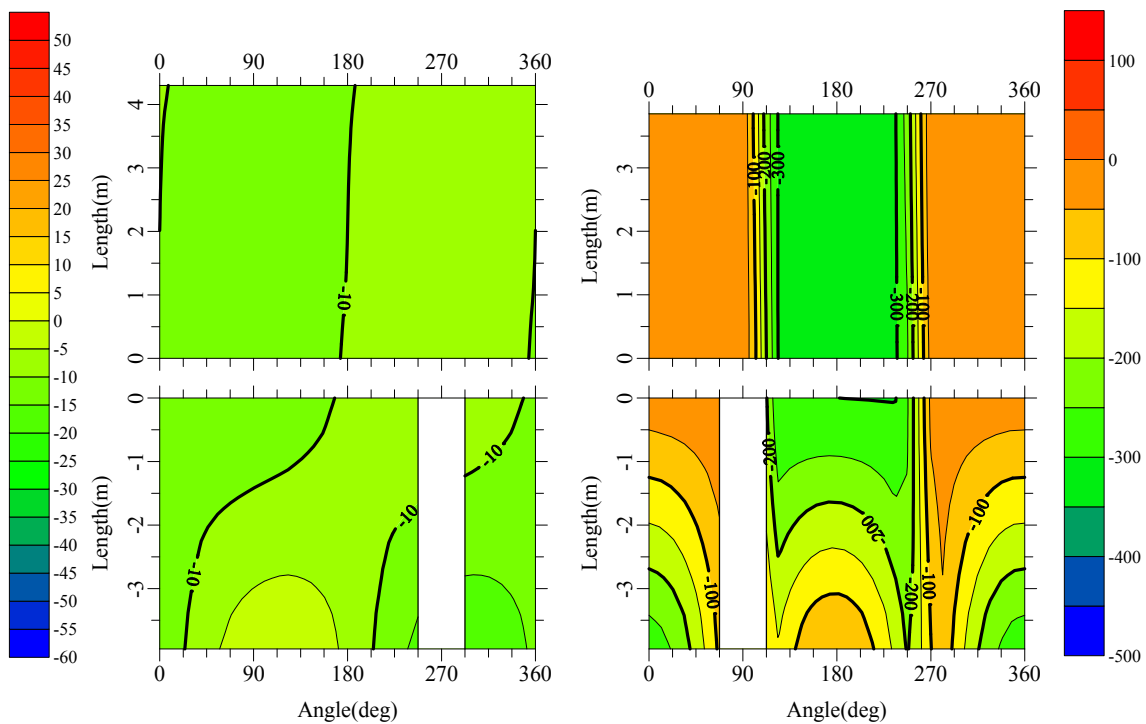
(c) Case No. 150003

(d) Case No. 175003

Figure 3.4 Forces and moments against distance (Parameter 1: CCL)

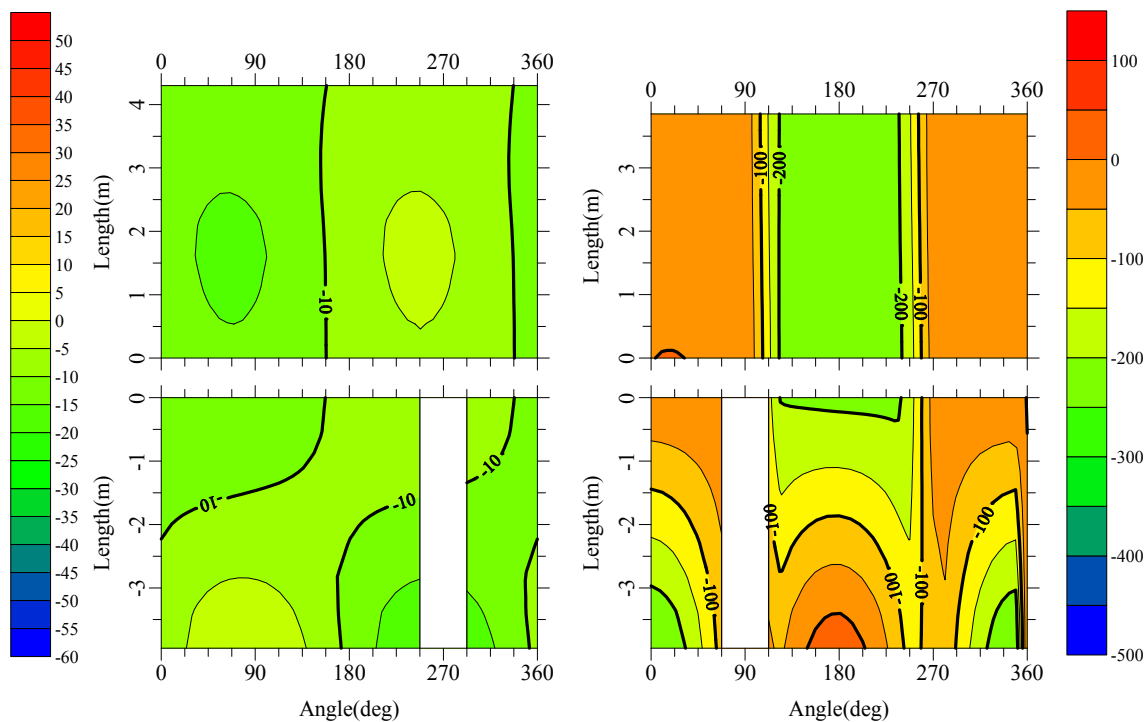


(a) Case 100003

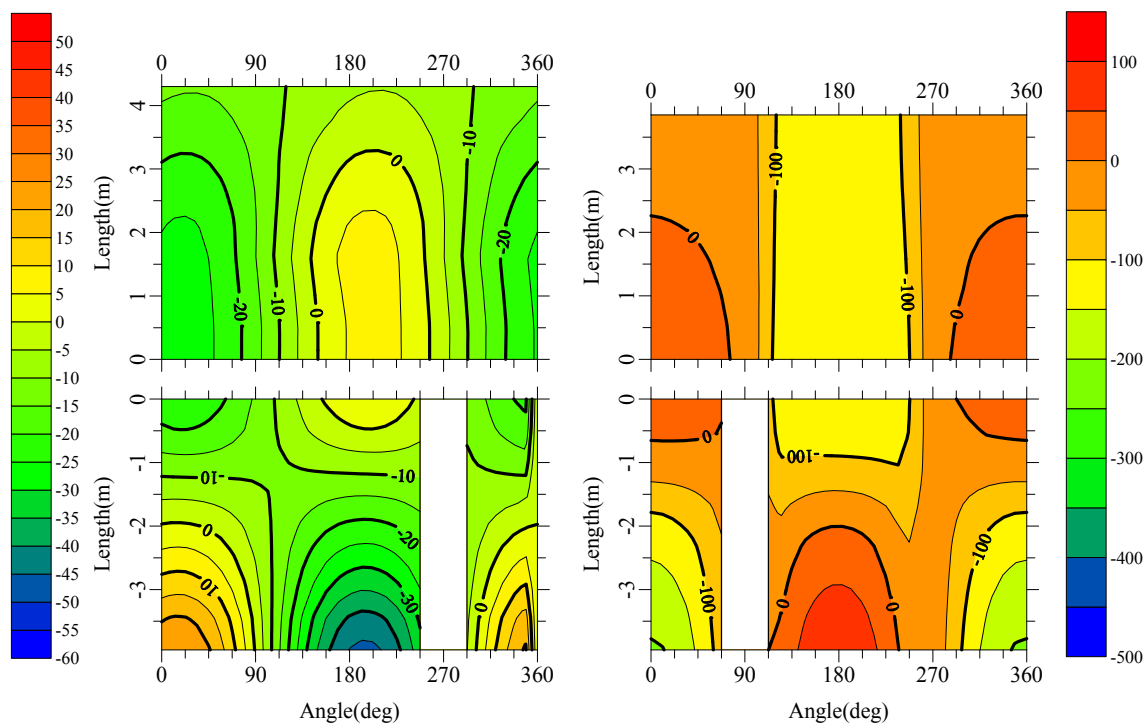


(b) Case 125003

Figure 3.5 Gap around the shield periphery (Parameter 1: CCL)

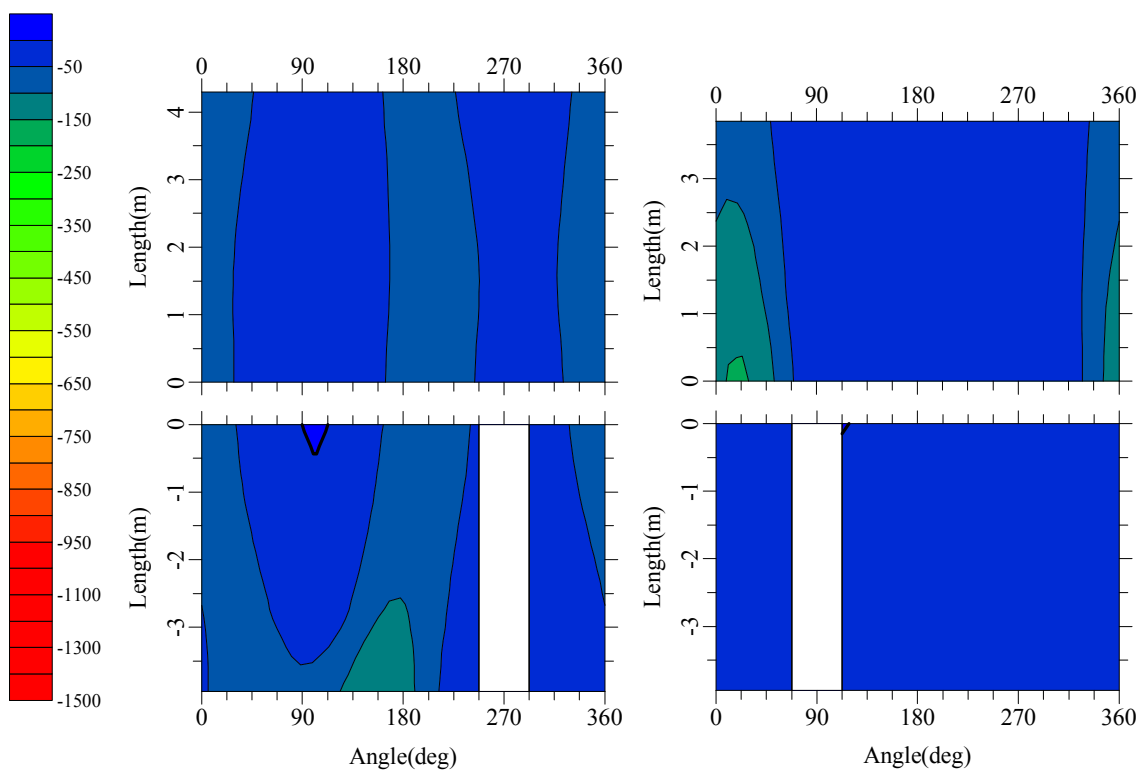


(c) Case 150003

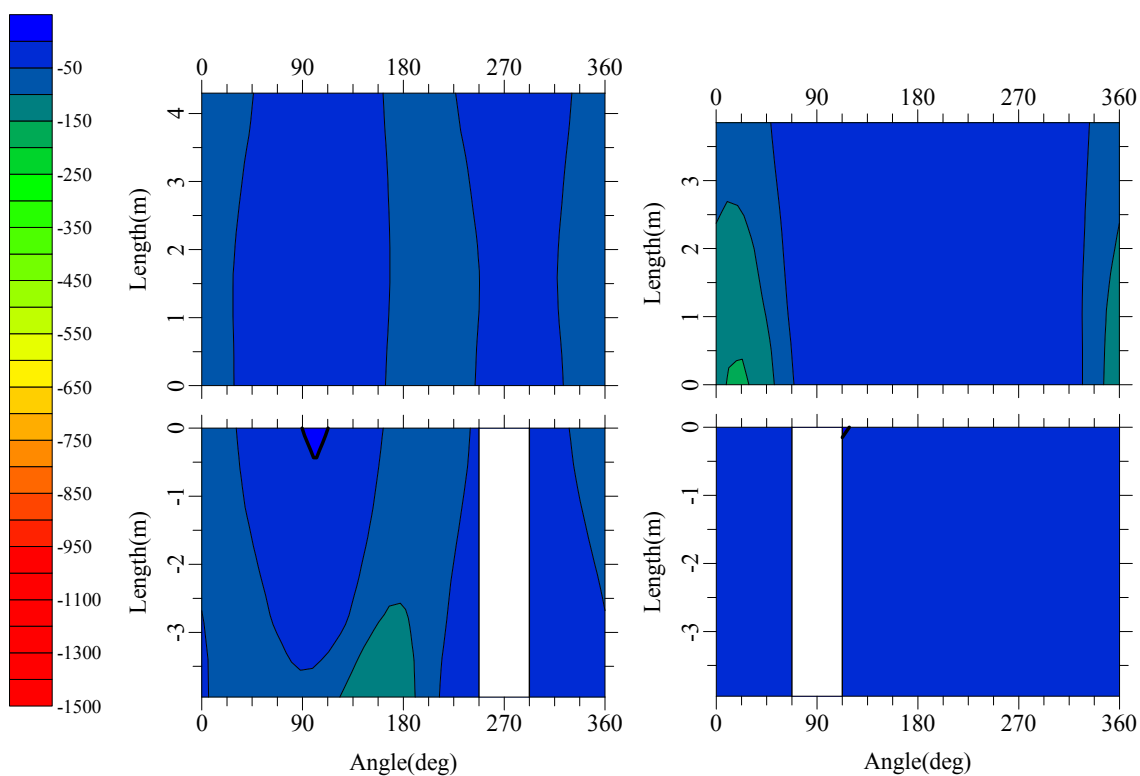


(d) Case 175003

Figure 3.5 Gap around the shield periphery (Parameter 1: CCL)

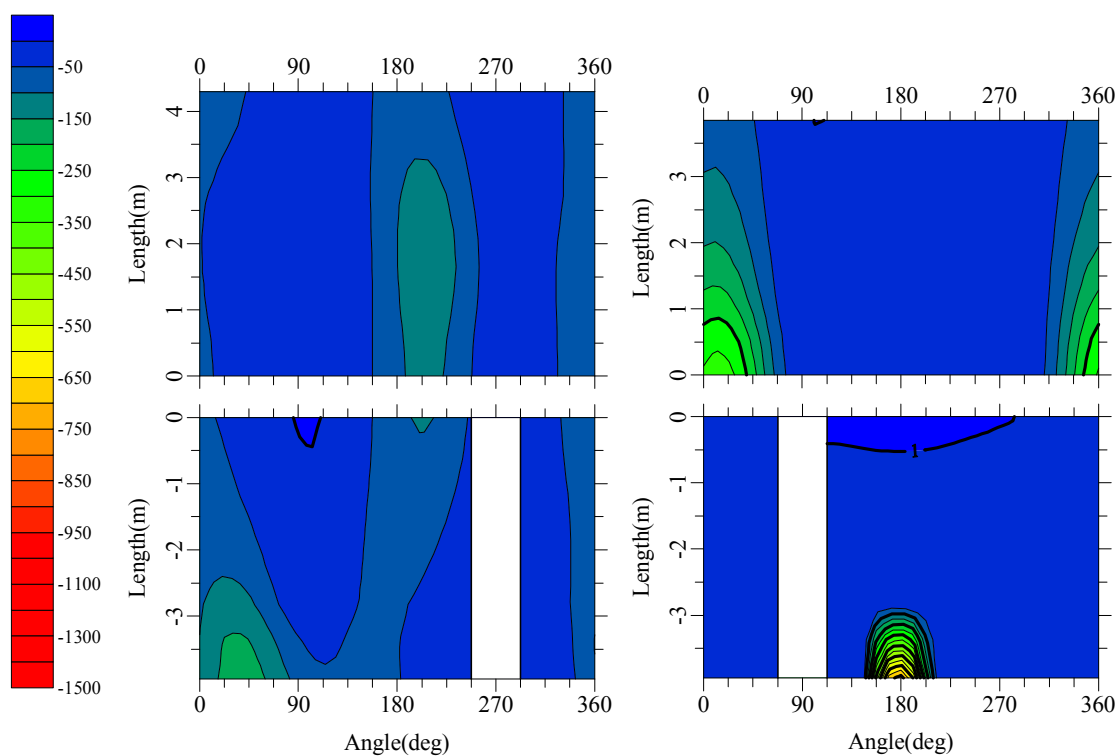


(a) Case 100003

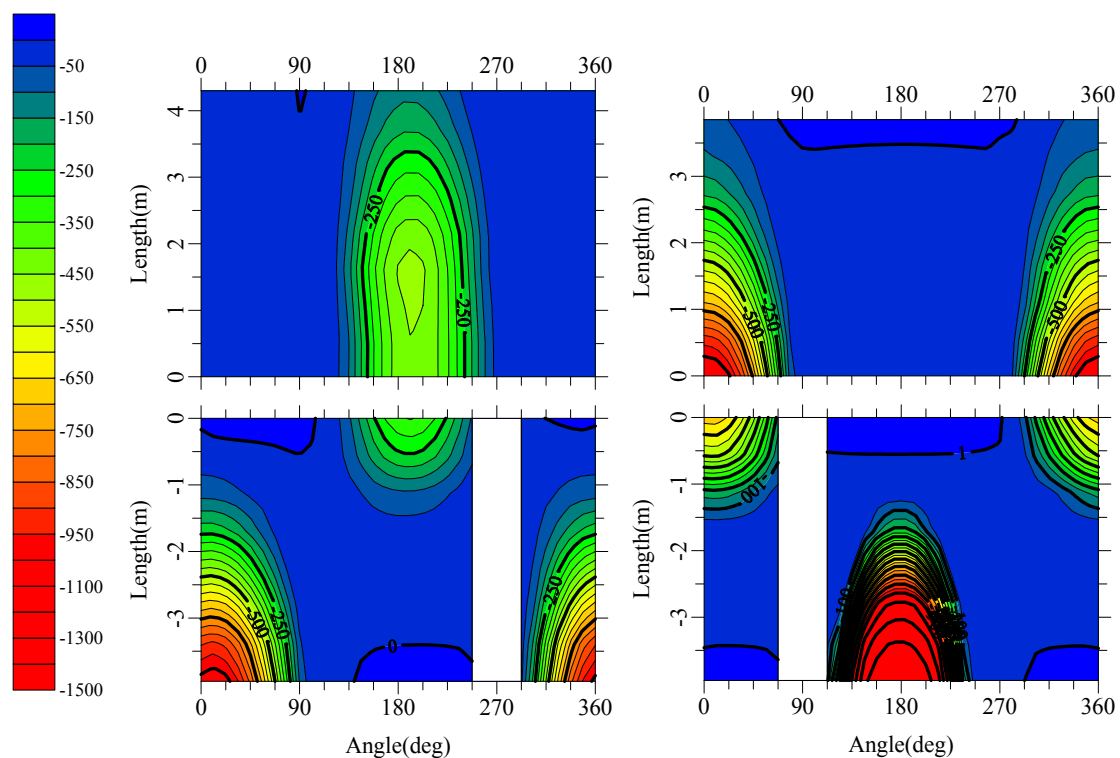


(b) Case 125003

Figure 3.6 Effective normal earth pressure on the shield periphery (Parameter 1: CCL)

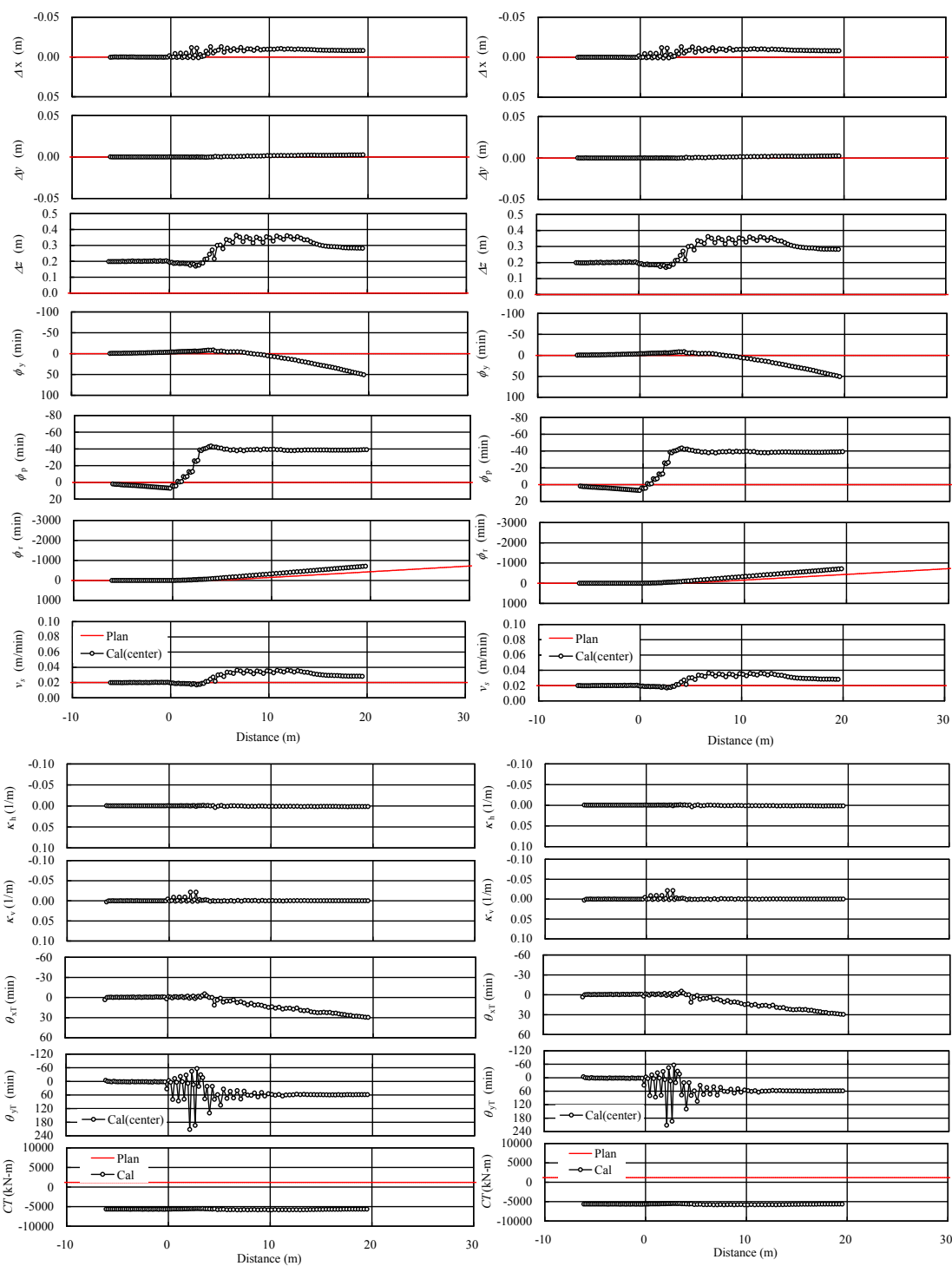


(c) Case 150003



(d) Case 175003

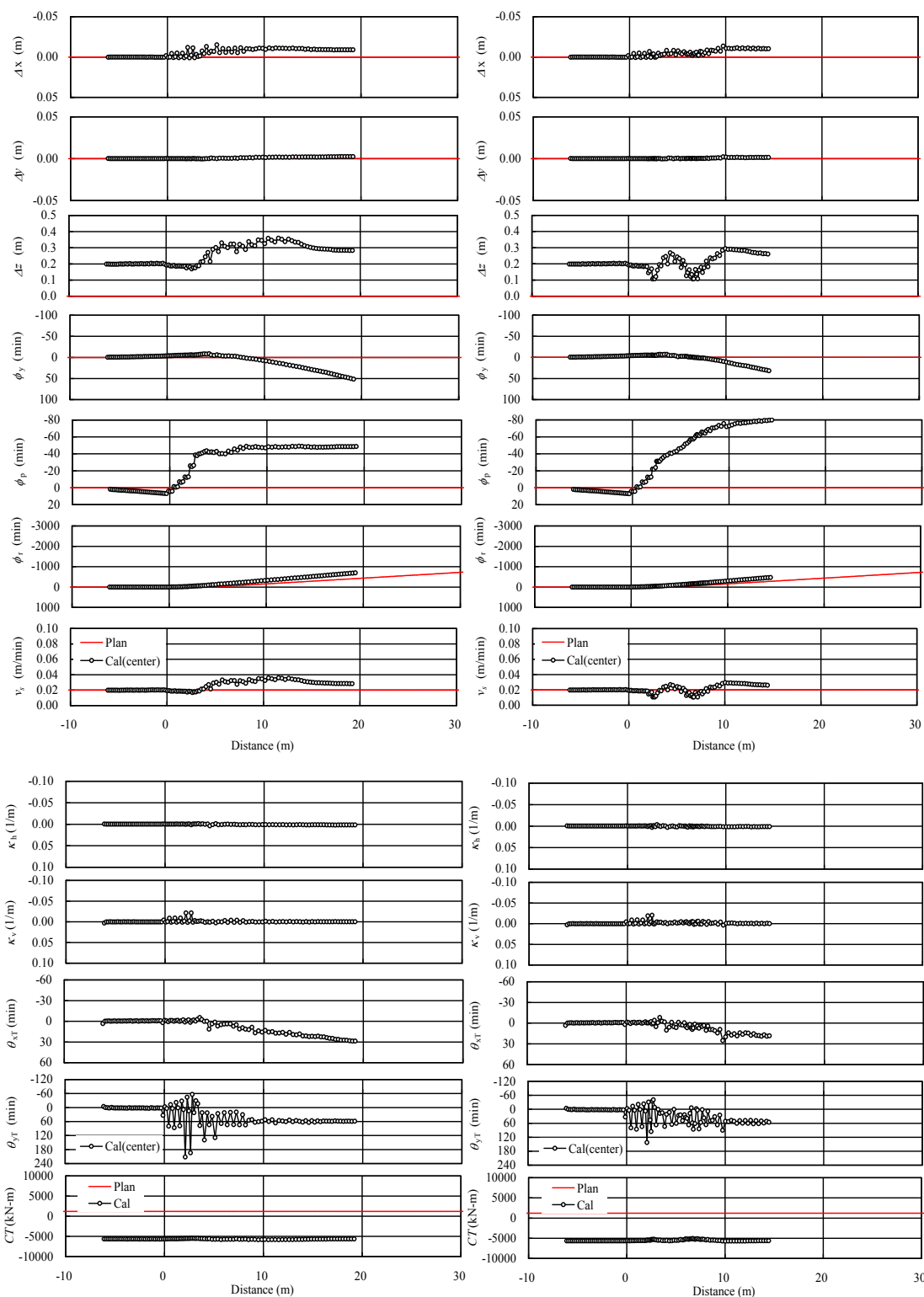
Figure 3.6 Effective normal earth pressure on the shield periphery (Parameter 1: CCL)



(a) Case No. 200103

(b) Case No. 225103

Figure 3.7 Shield Behavior (Parameter 2: Crease Angle and Pitching Angle,  $\phi_{pRR} = -0.5\theta_{CV}$ )

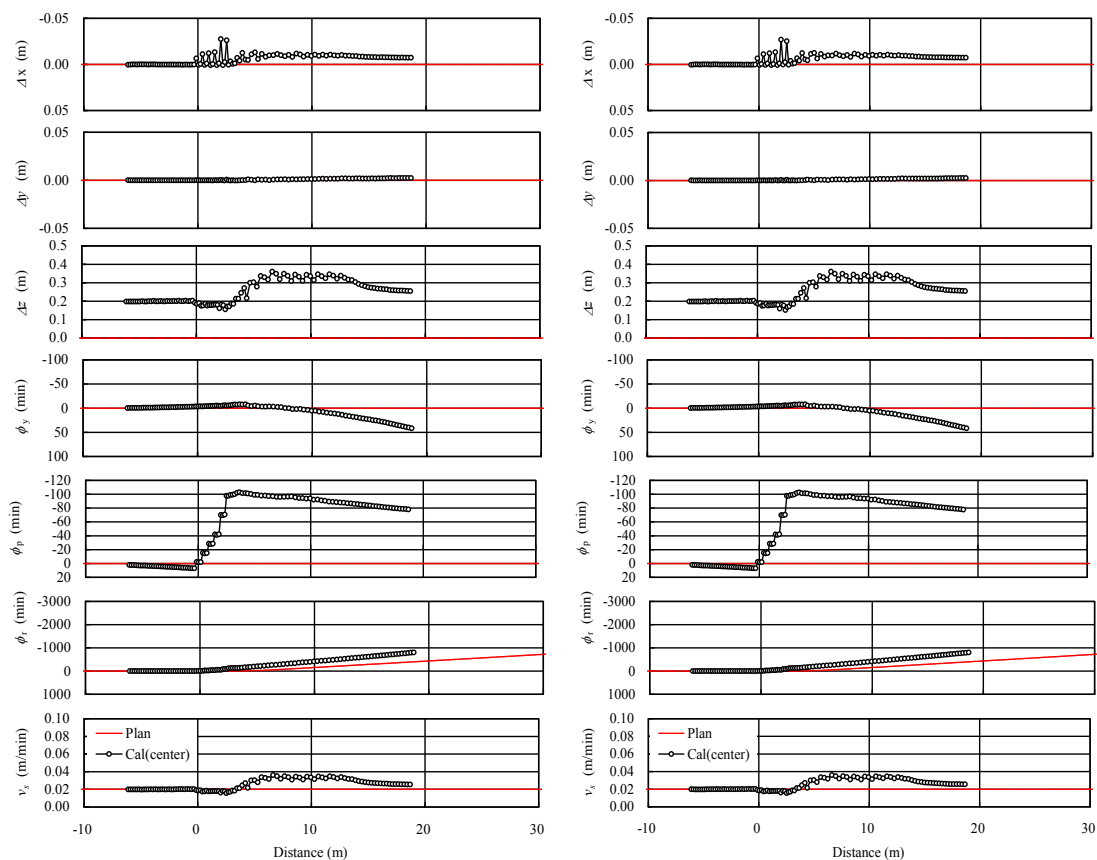


(c) Case No. 250103

(d) Case No. 275103

Figure 3.7 Shield Behavior (Parameter 2: Crease Angle and Pitching Angle,  $\phi_{pRR} = -0.5\theta_{CV}$ )

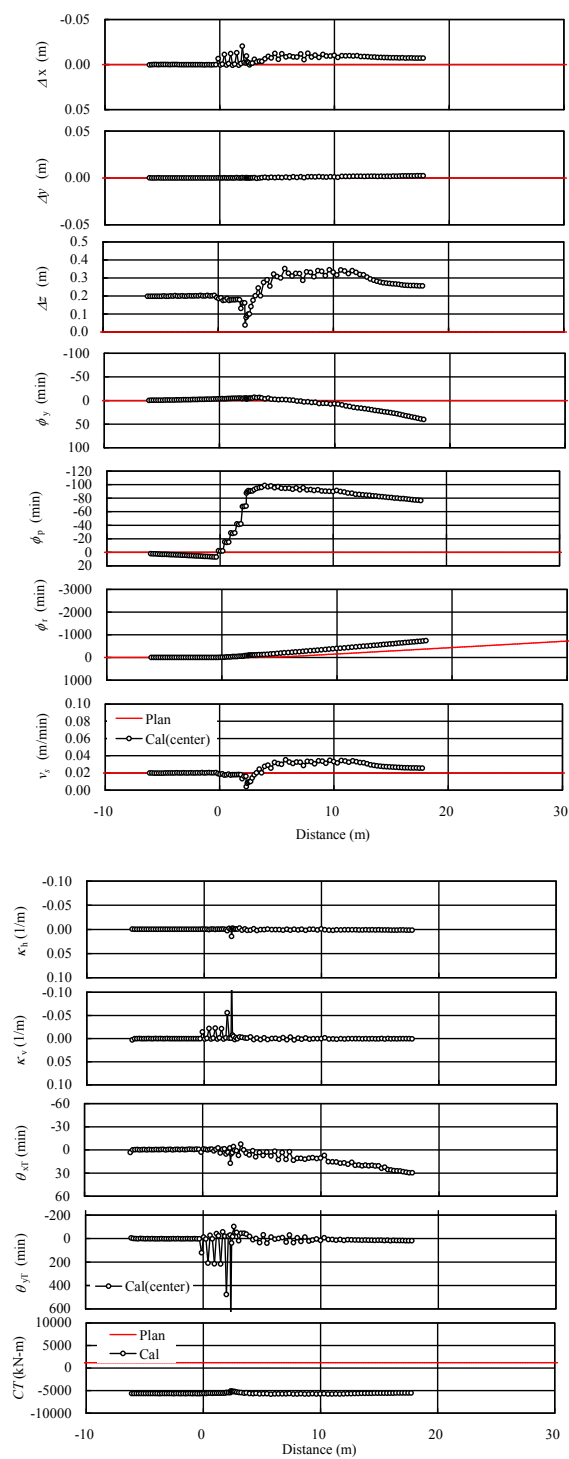
Condition 1)



(a) Case No. 200203

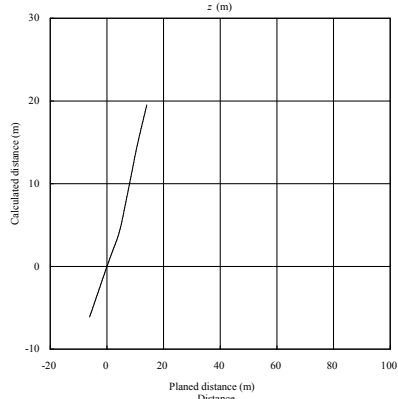
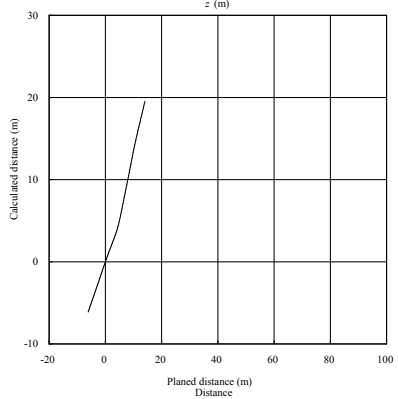
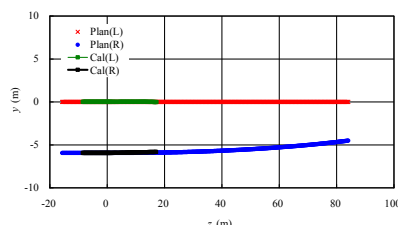
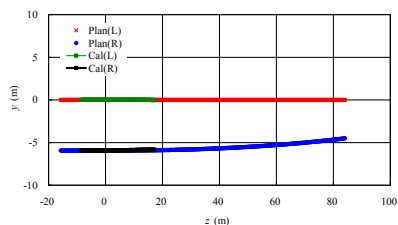
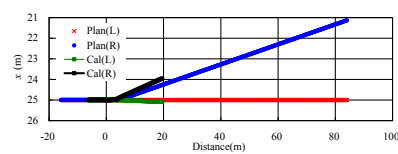
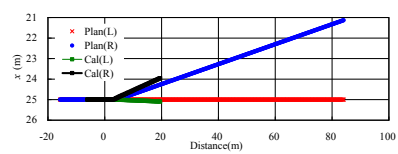
(b) Case No. 225203

Figure 3.8 Shield Behavior (Parameter 2: Crease Angle and Pitching Angle,  $\phi_{PRR} = -\theta_{CV}$ )



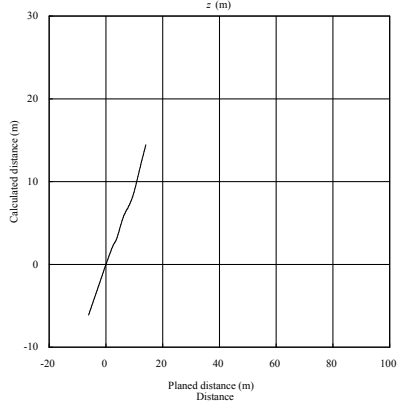
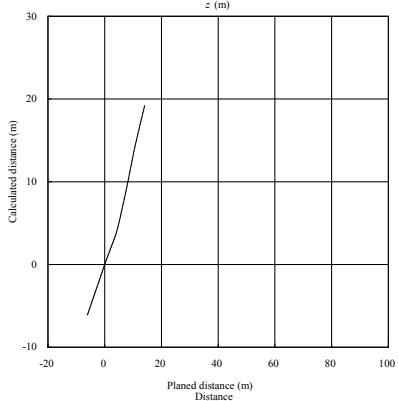
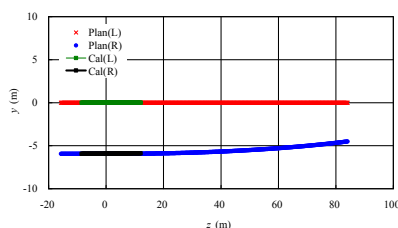
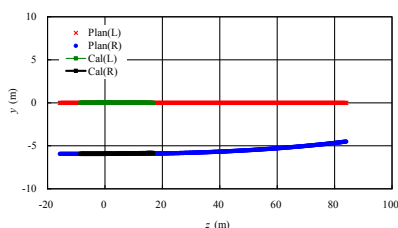
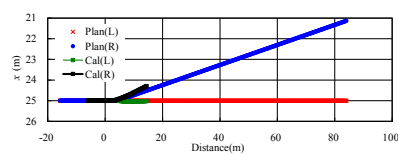
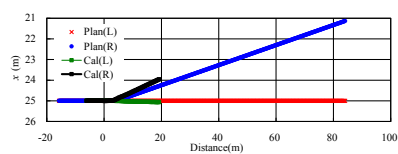
c) Case No. 250203

Figure 3.8 Shield Behavior (Parameter 2: Crease Angle and Pitching Angle,  $\phi_{PRR} = -\theta_{CV}$ )



(a) Case No. 200103

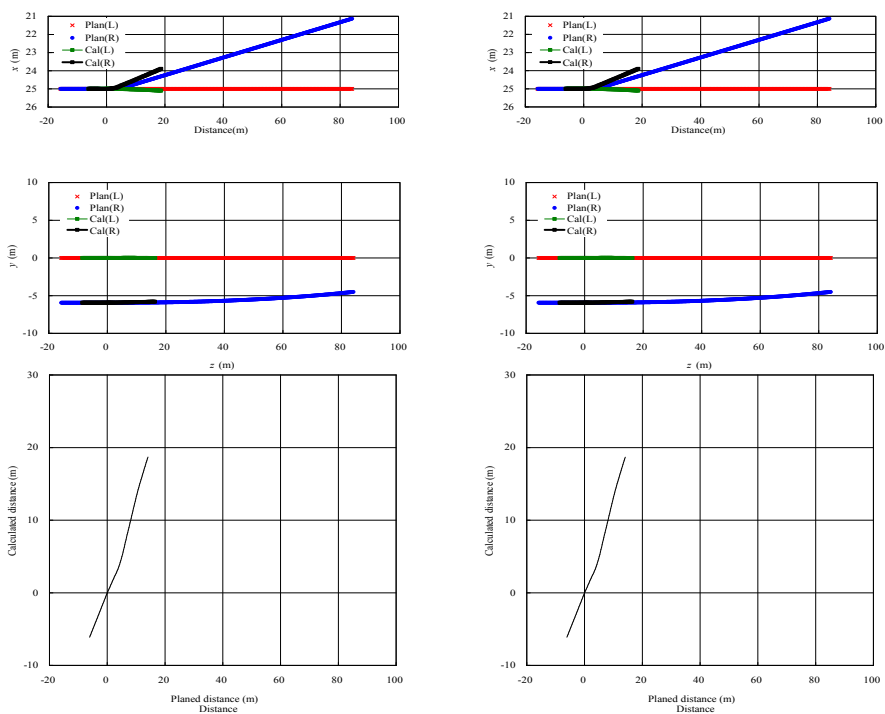
(b) Case No. 225103



(c) Case No. 250103

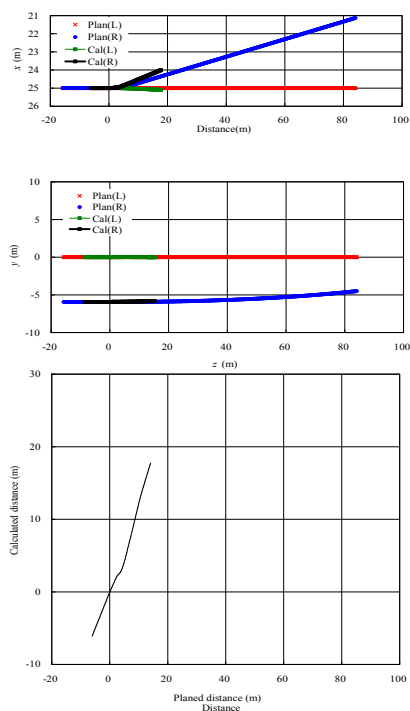
(d) Case No. 275103

Figure 3.9 Trace of shield on the vertical and horizontal plane (Parameter 2: Crease Angle and Pitching Angle,  $\phi_{pRR} = -0.5\theta_{CV}$ )



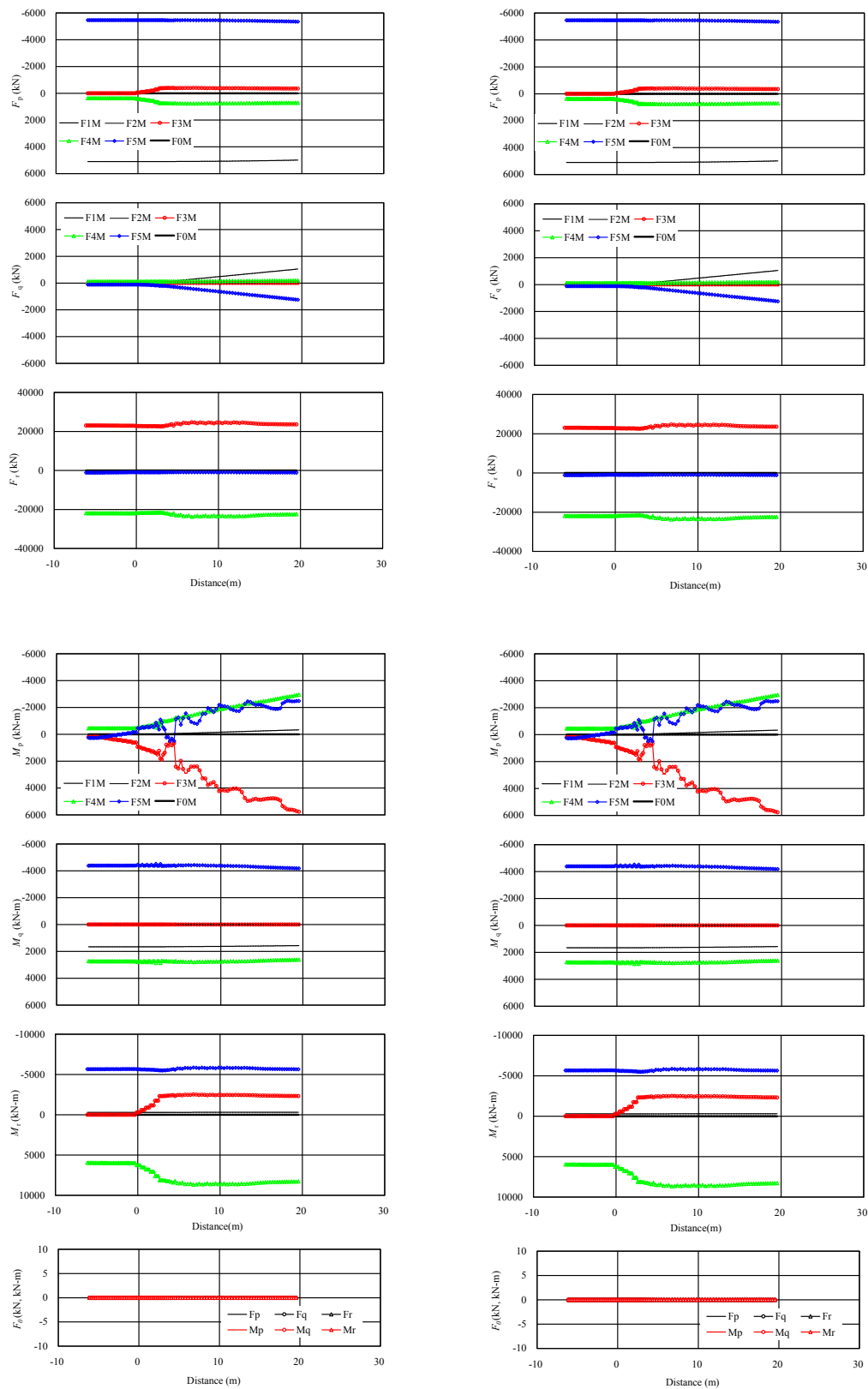
(a) Case No. 200203

(b) Case No. 225203



(c) Case No. 250203

Figure 3.10 Trace of shield on the vertical and horizontal plane (Parameter 2: Crease Angle and Pitching Angle,  $\phi_{PRR} = -\theta_{cv}$ )

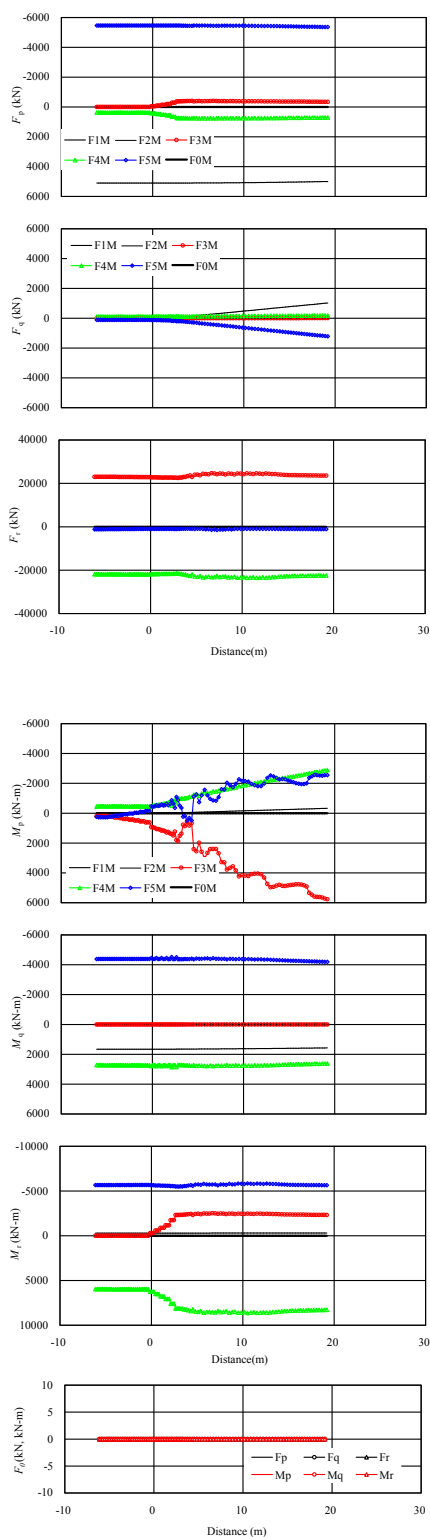


(a) Case No. 200103

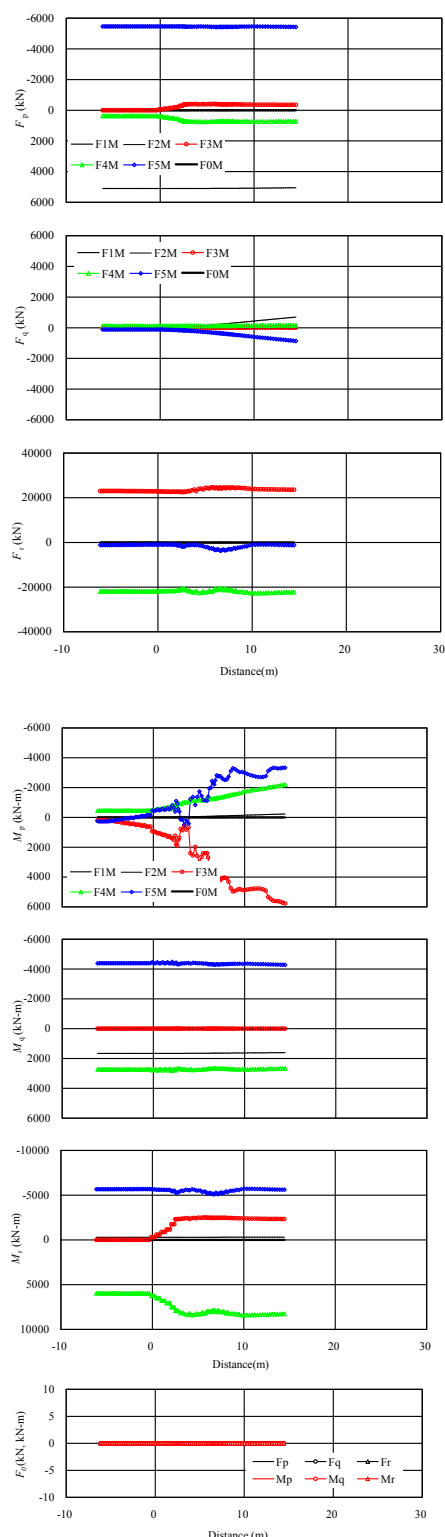
(b) Case No. 225103

Figure 3.11 Forces and Moments against distance (Parameter 2: Crease Angle and Pitching

$$\text{Angle, } \phi_{pRR} = -0.5\theta_{CV})$$



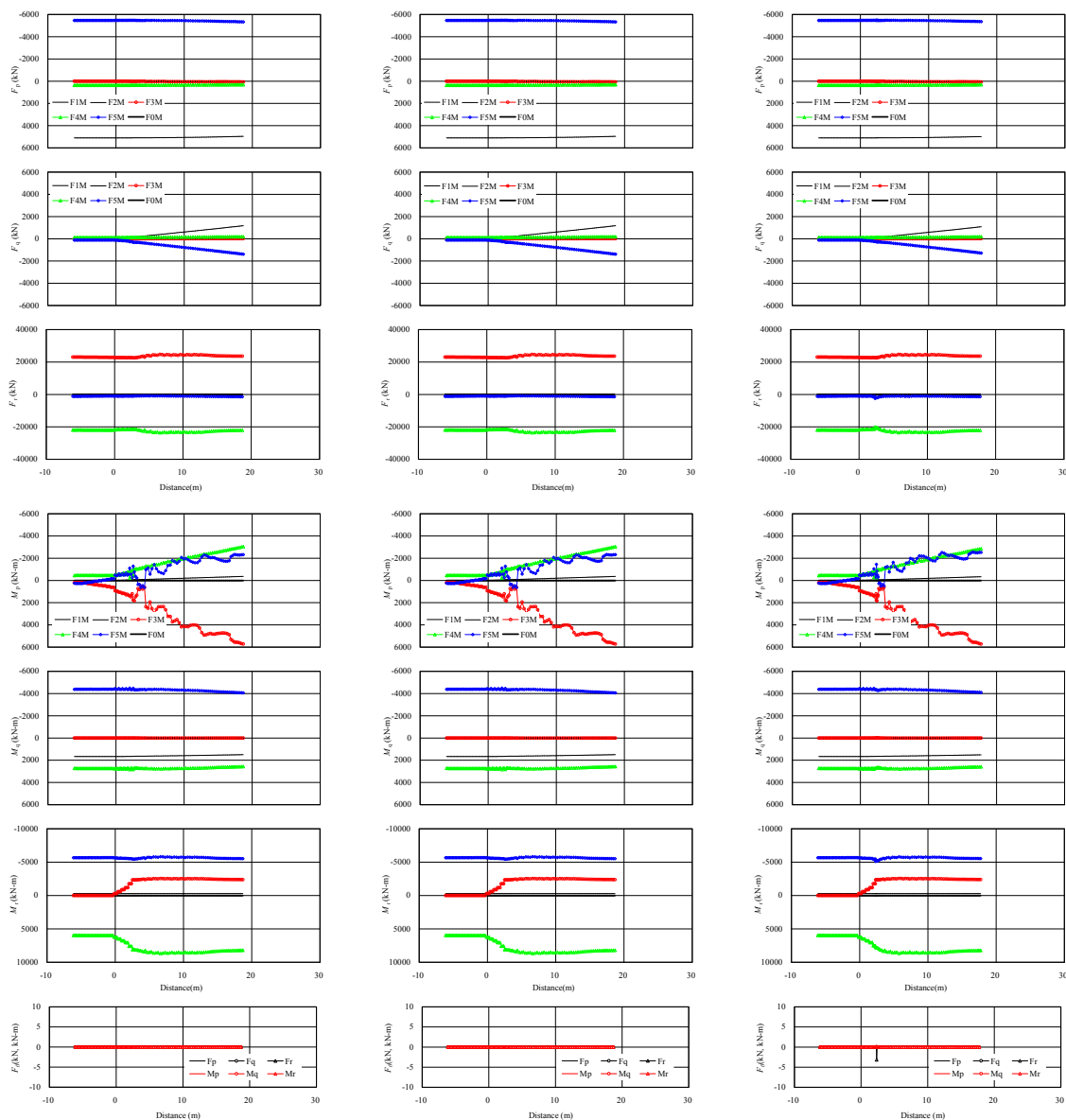
(c) Case No. 250103



(d) Case No. 275103

Figure 3.11 Forces and moments against distance (Parameter 2: Crease Angle and Pitching

$$\text{Angle, } \phi_{\text{pRR}} = -0.5\theta_{\text{CV}})$$



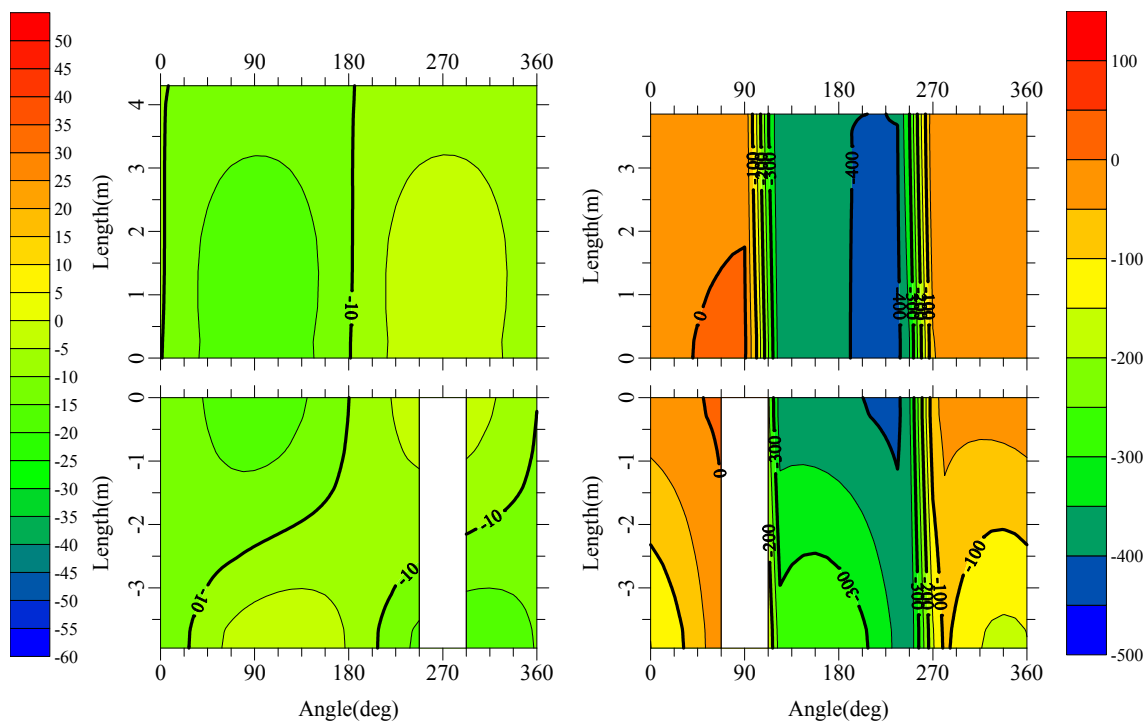
(a) Case No. 200203

(b) Case No. 225203

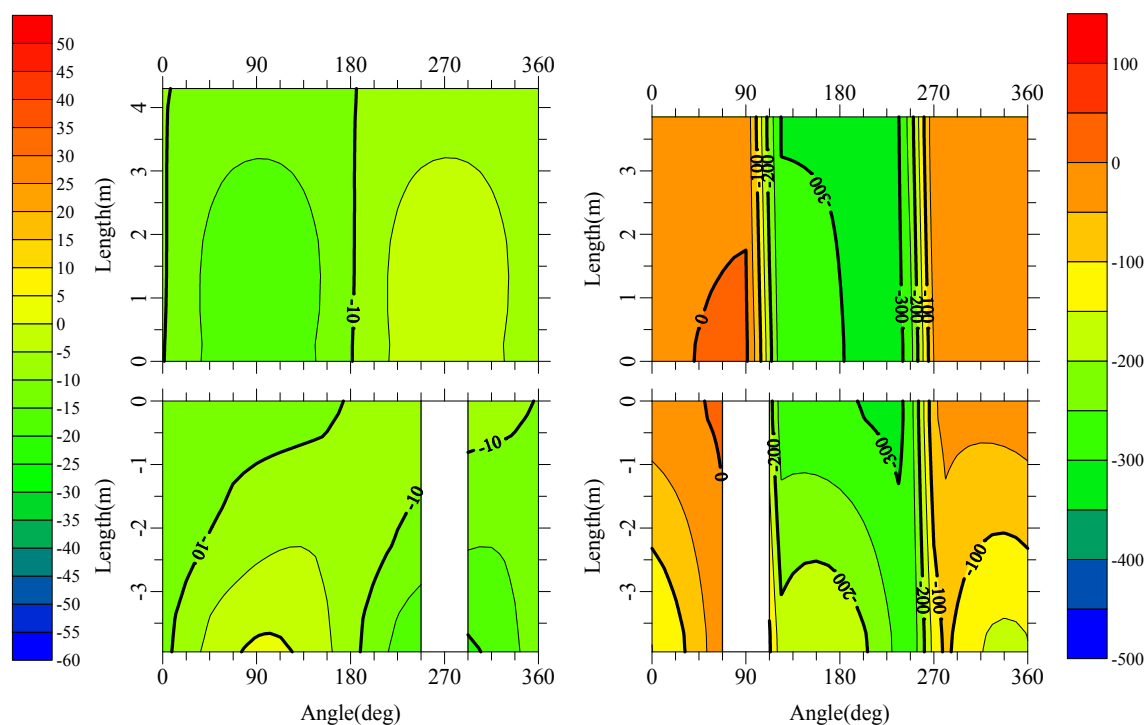
(c) Case No. 250203

Figure 3.12 Forces and Moments against distance (Parameter 2: Crease Angle and Pitching

$$\text{Angle, } \phi_{\text{pRR}} = -\theta_{\text{CV}})$$



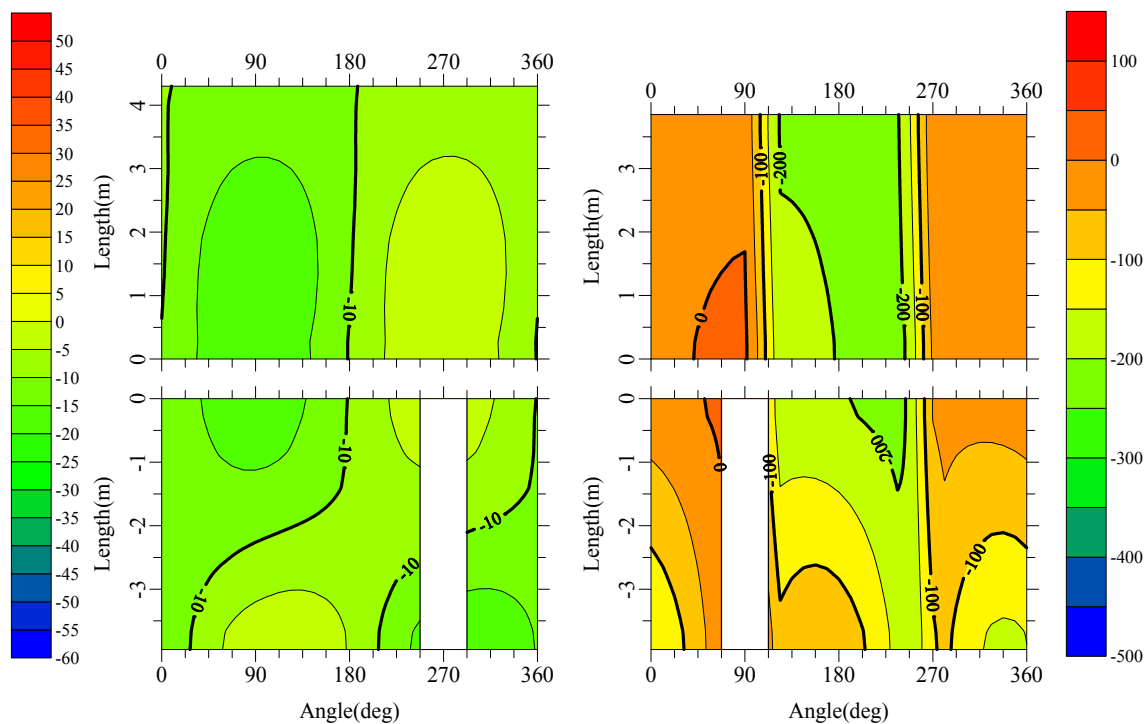
(a) Case200103



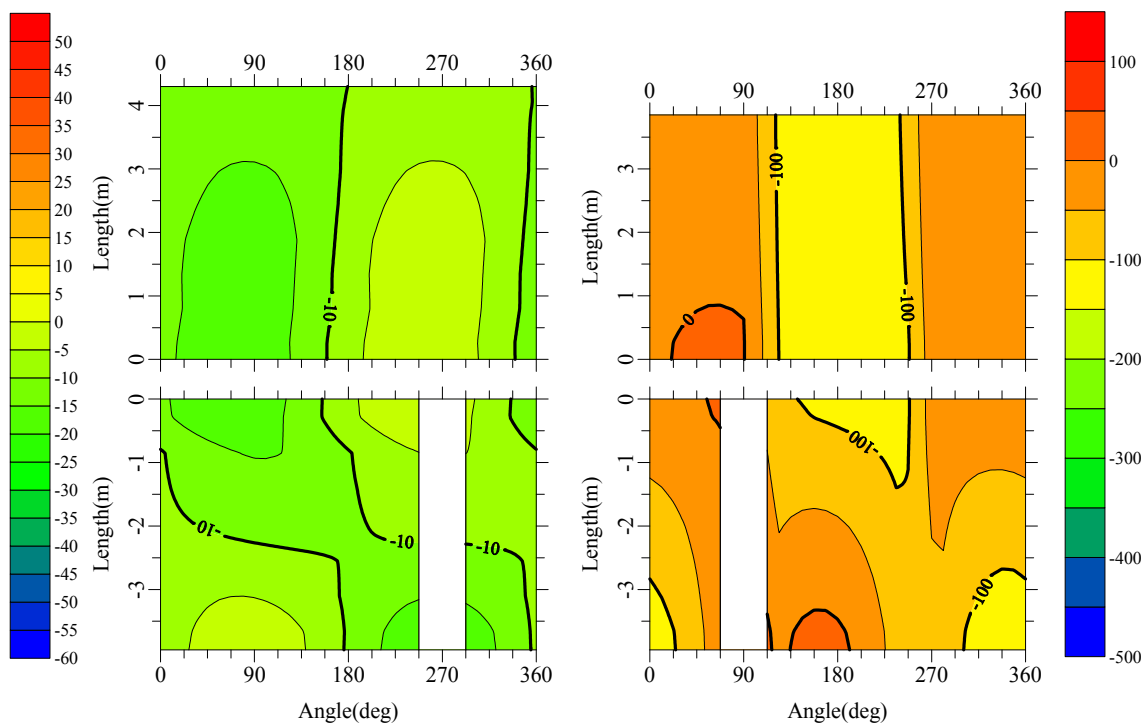
(b) Case 225103

Figure 3.13 Gap around the shield periphery (Parameter 2: Crease Angle and Pitching Angle,

$$\phi_{pRR} = -0.5\theta_{CV})$$



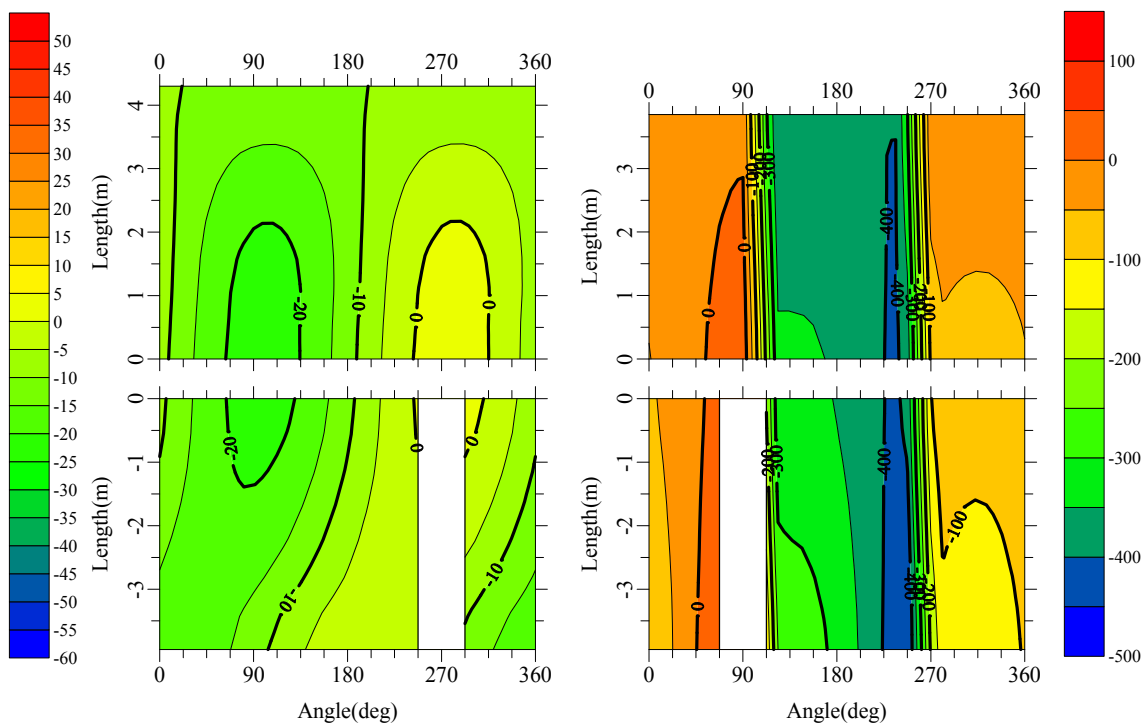
(c) Case 250103



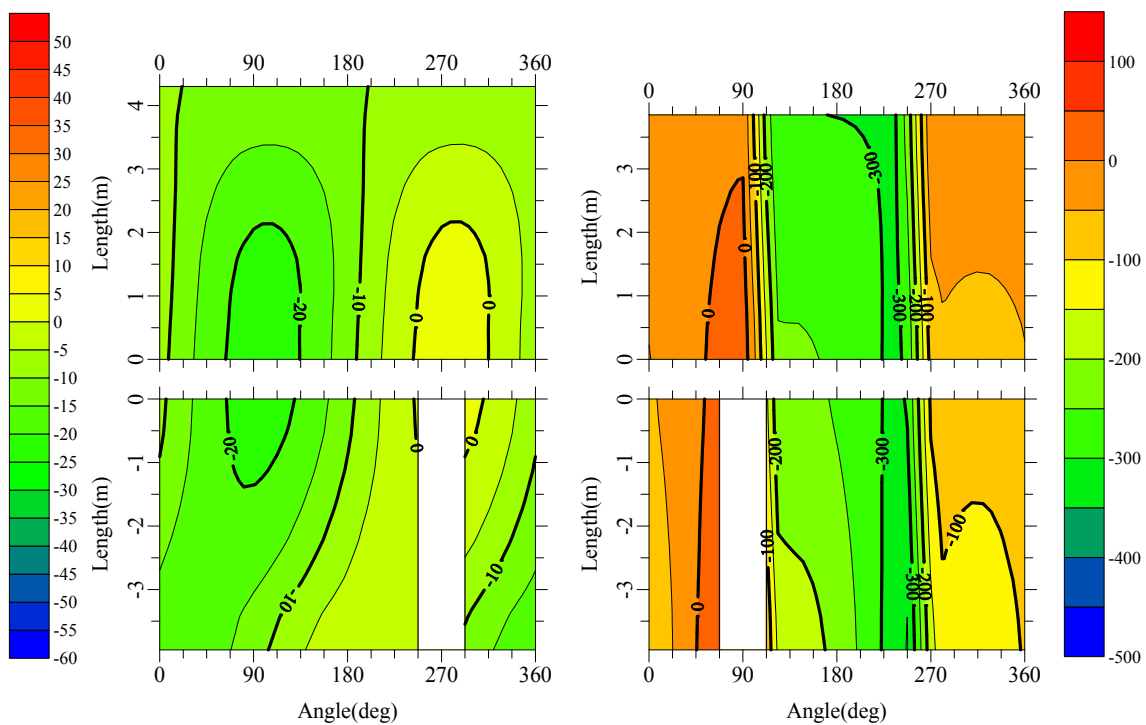
(d) Case 275103

Figure 3.13 Gap around the shield periphery (Parameter 2: Crease Angle and Pitching Angle,

$$\phi_{pRR} = -0.5\theta_{CV})$$



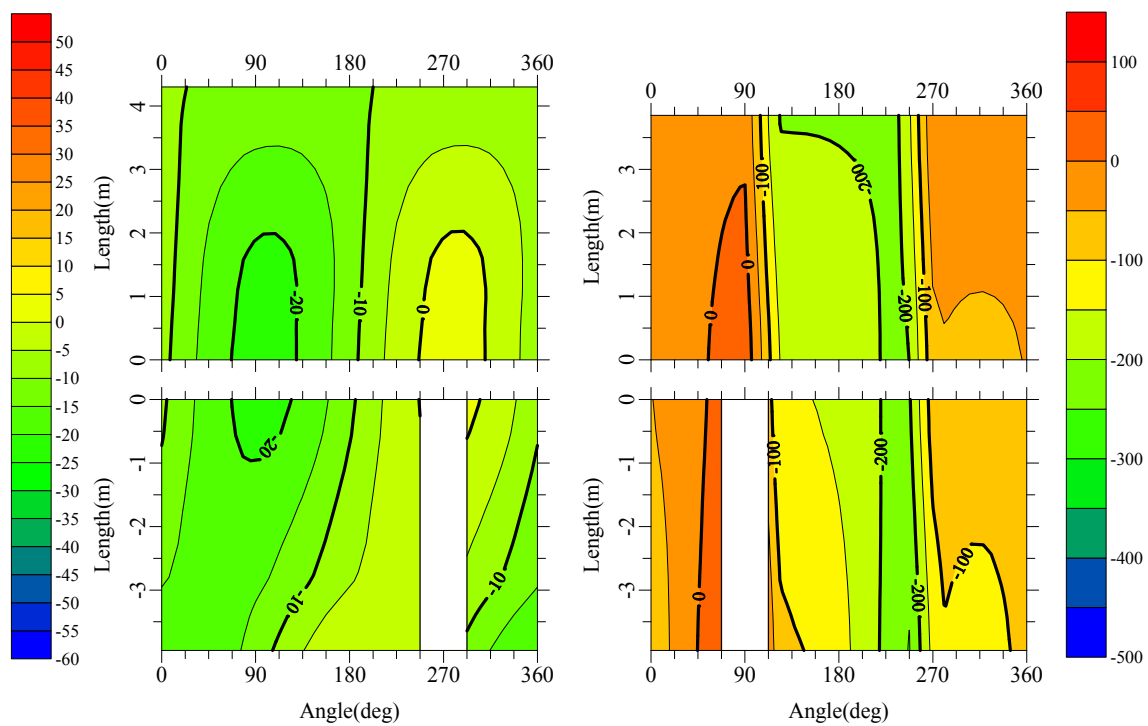
(a) Case 200203



(b) Case 225203

Figure 3.14 Gap around the shield periphery (Parameter 2: Crease Angle and Pitching Angle,

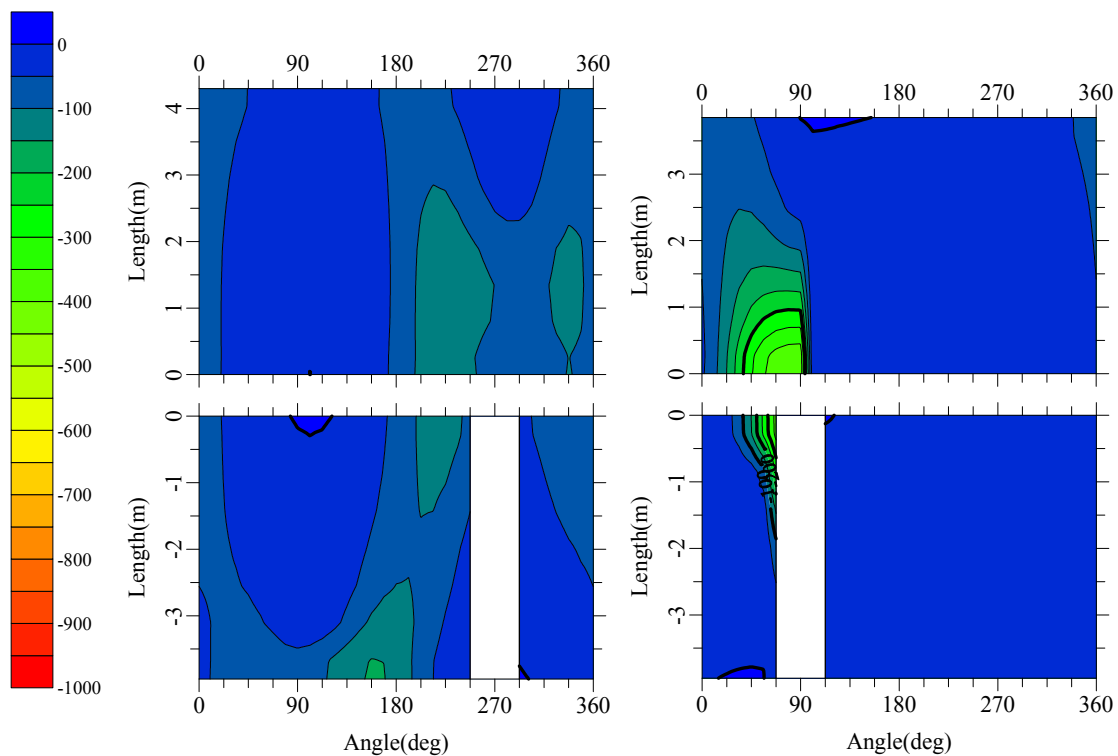
$$\phi_{\text{PRR}} = -\theta_{\text{CV}})$$



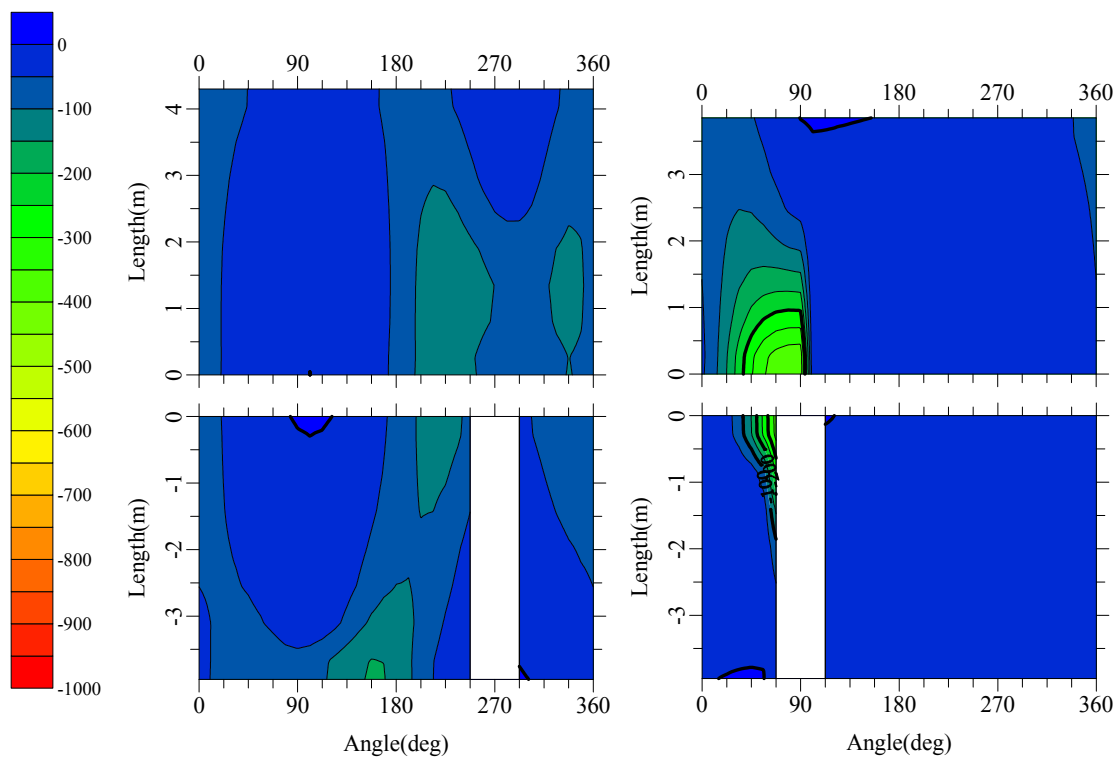
(c) Case 250203

Figure 3.14 Gap around the shield periphery (Parameter 2: Crease Angle and Pitching Angle,

$$\phi_{pRR} = -\theta_{cv})$$



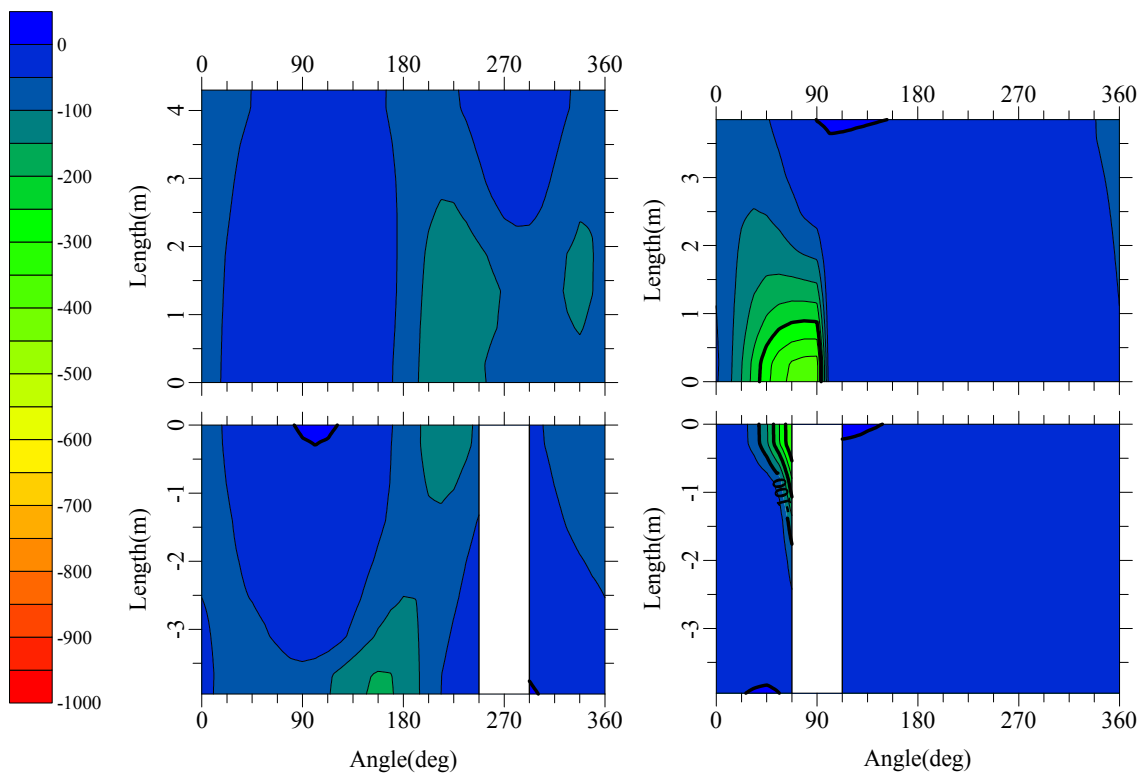
(a) Case 200103



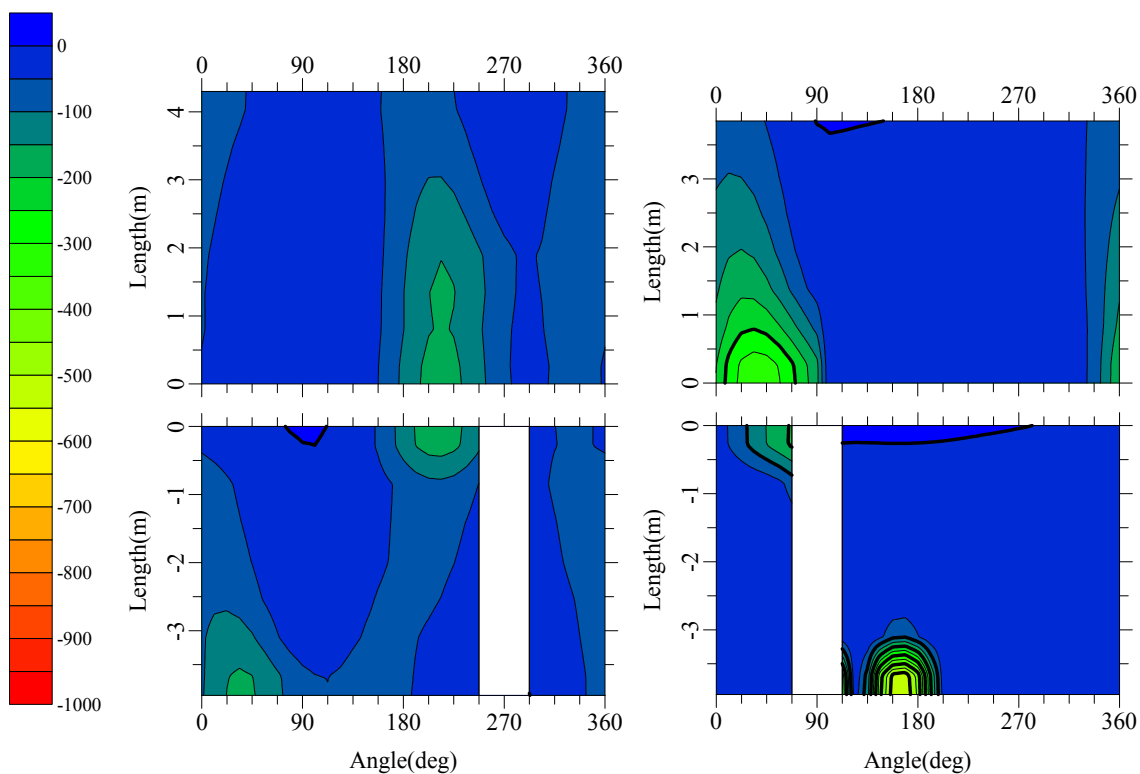
(b) Case 225103

Figure 3.15 Normal effective earth pressure on the shield periphery (Parameter 2: Crease

$$\text{Angle and Pitching Angle, } \phi_{pRR} = -0.5\theta_{cv}$$



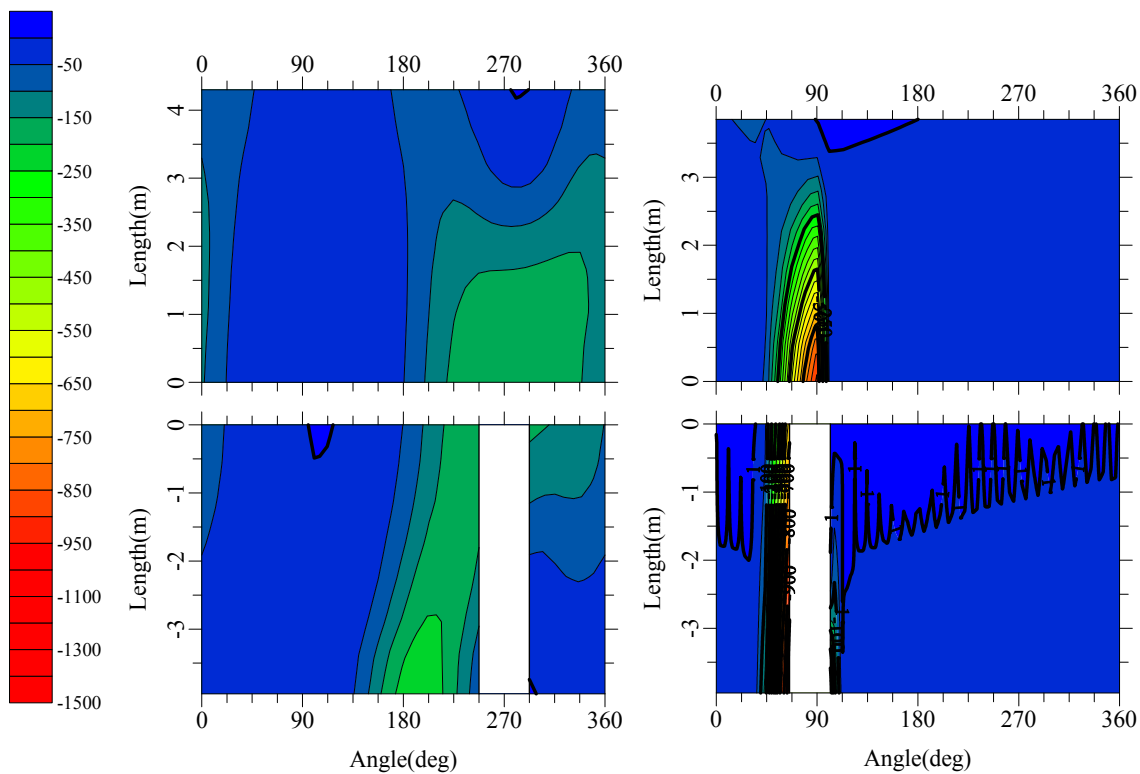
(c) Case 250103



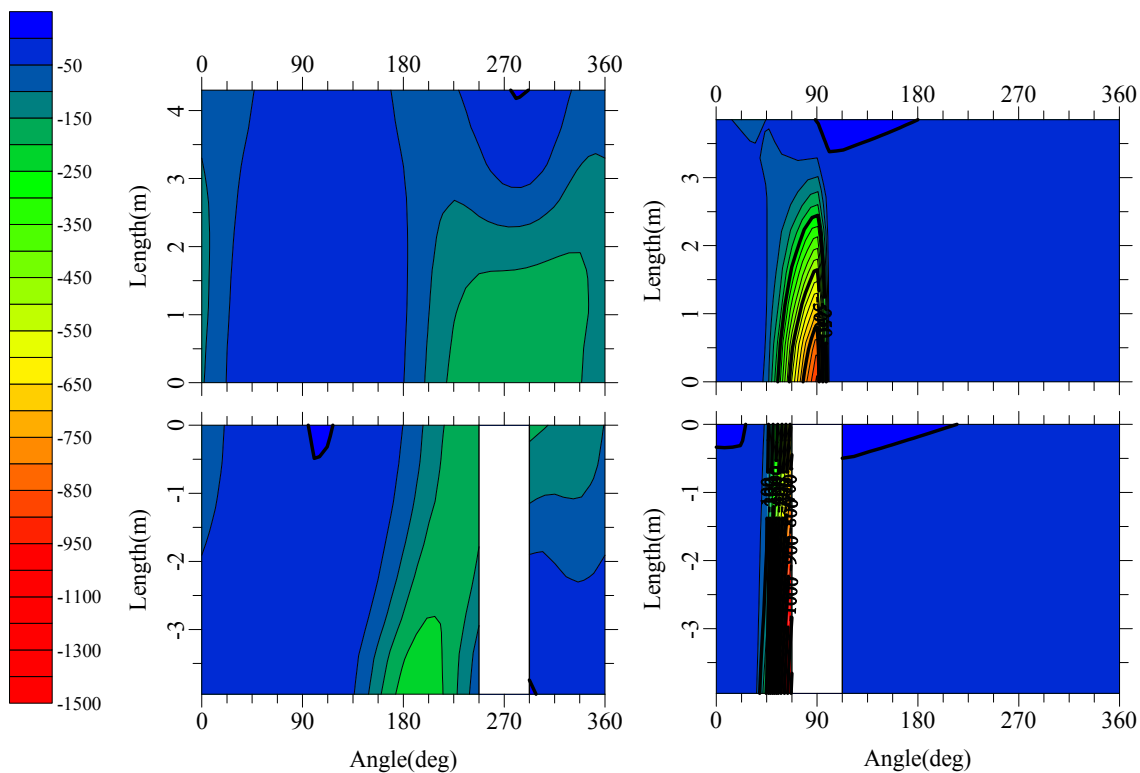
(d) Case 275103

Figure 3.15 Normal effective earth pressure on the shield periphery (Parameter 2: Crease

$$\text{Angle and Pitching Angle, } \phi_{\text{PRR}} = -0.5\theta_{\text{CV}})$$



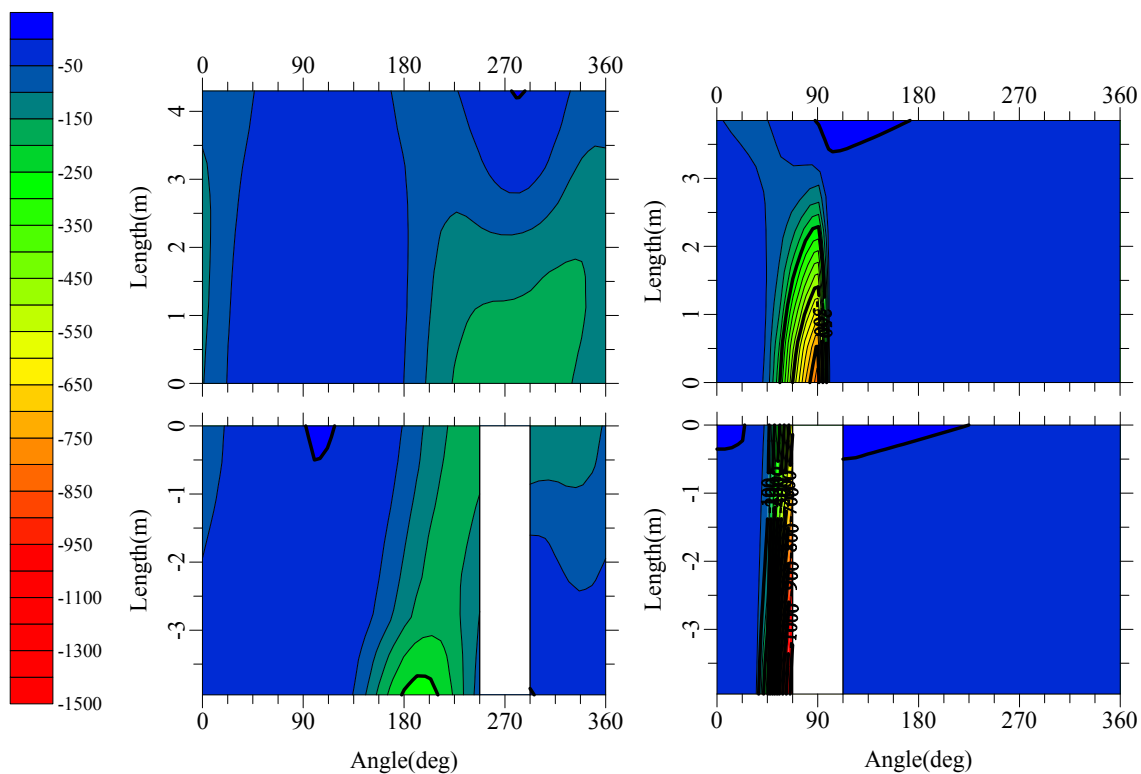
(a) Case 200203



(b) Case 225203

Figure 3.16 Normal effective earth pressure on the shield periphery (Parameter 2: Crease

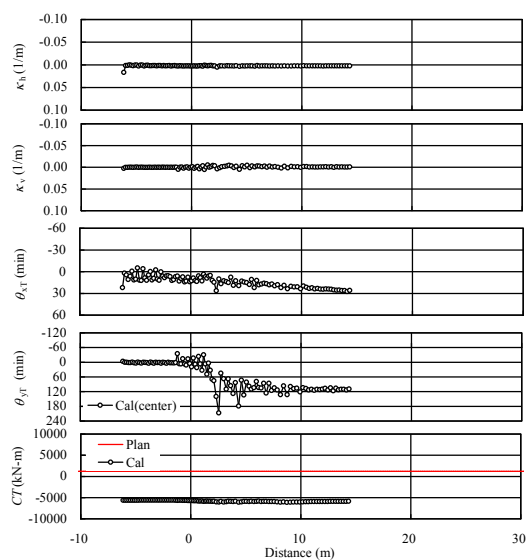
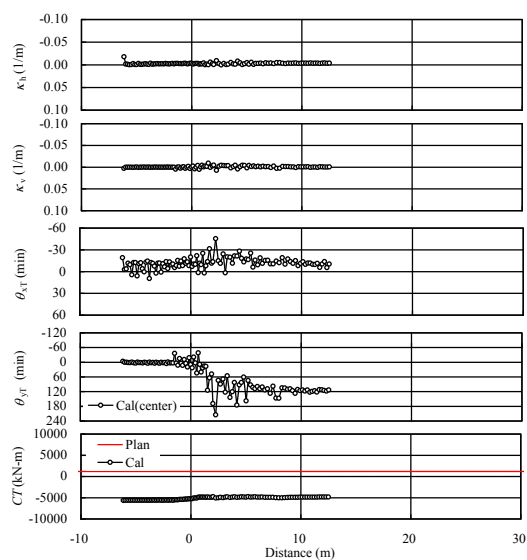
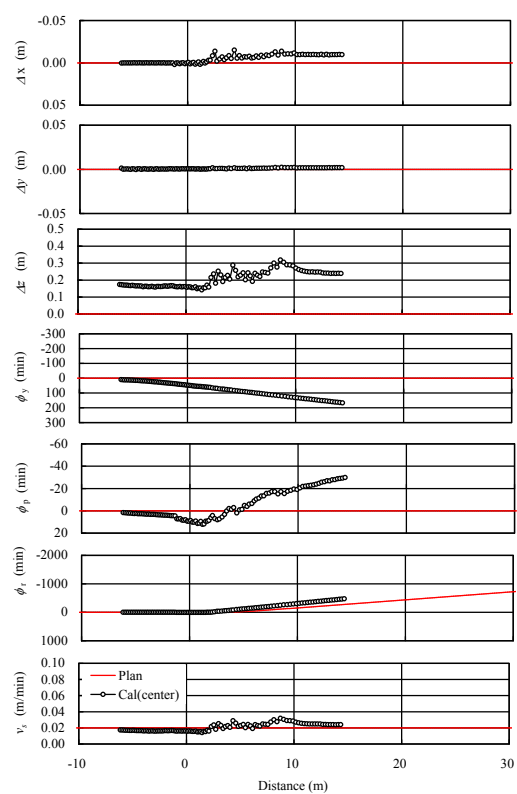
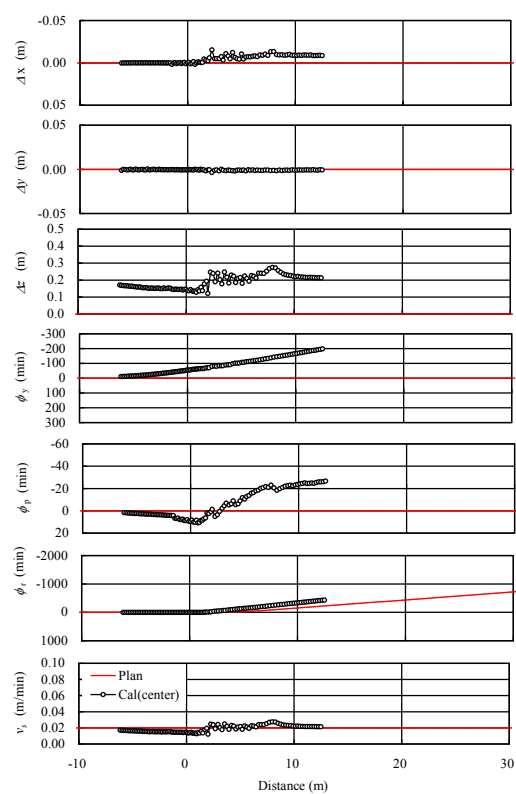
$$\text{Angle and Pitching Angle, } \phi_{\text{pRR}} = -\theta_{\text{CV}})$$



(c) Case 250203

Figure 3.16 Normal effective earth pressure on the shield periphery (Parameter 2: Crease

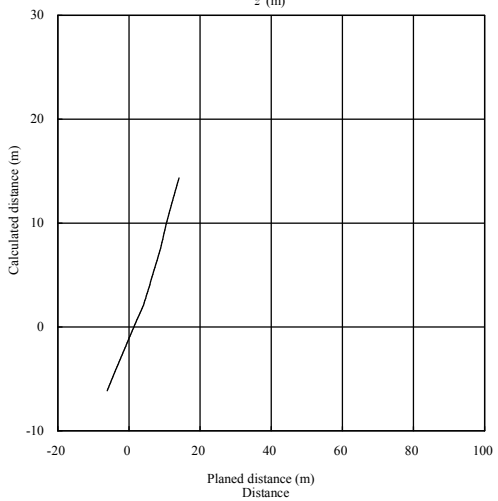
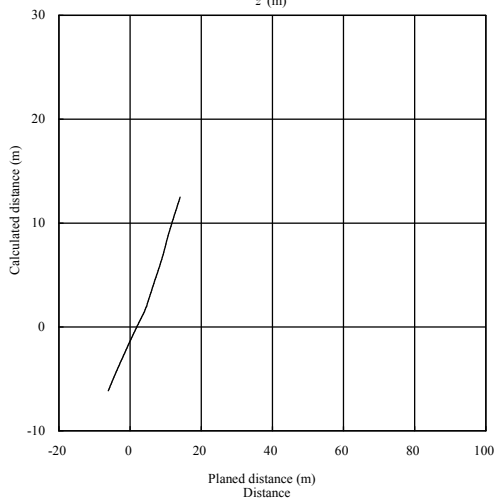
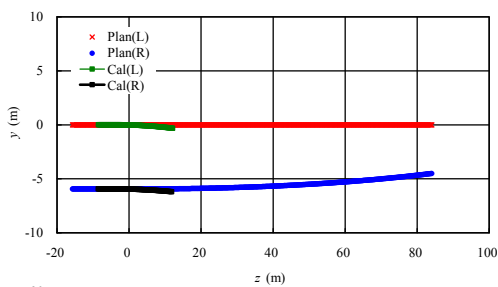
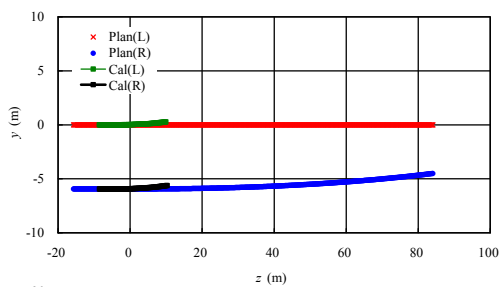
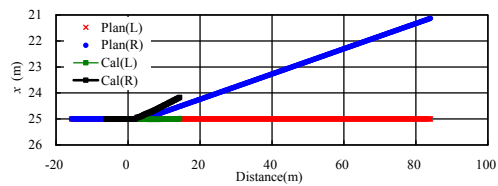
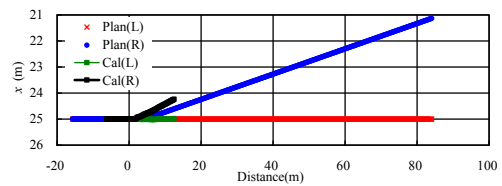
Angle and Pitching Angle,  $\phi_{pRR} = -\theta_{CV}$  )



(a) Case No. 350043

(b) Case No. 350063

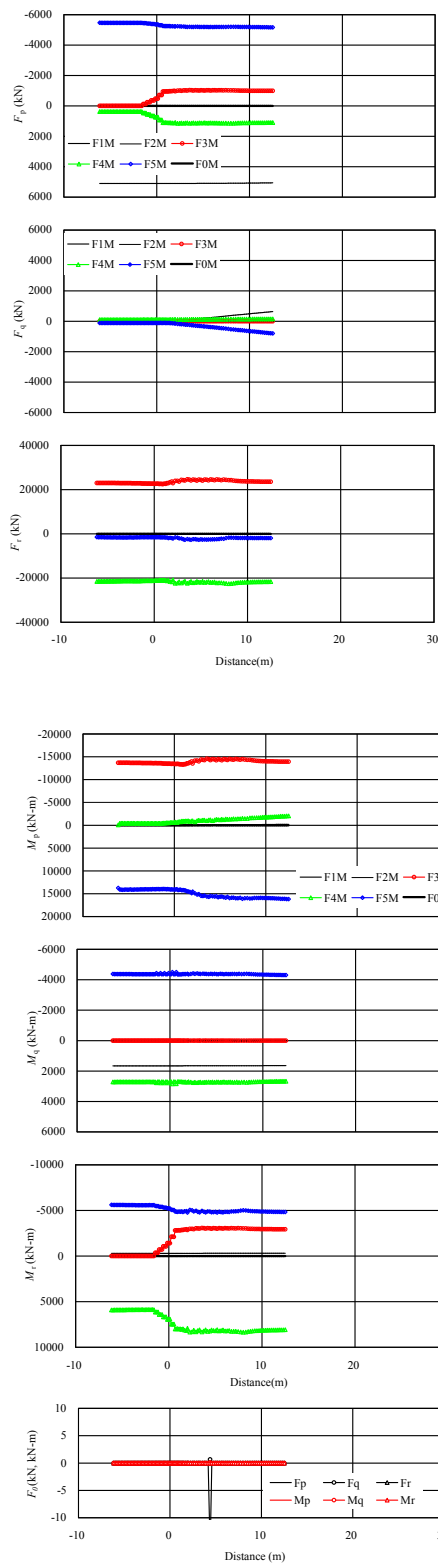
Figure 3.17 Shield Behavior (Parameter 3: Share of jack force for both bodies)



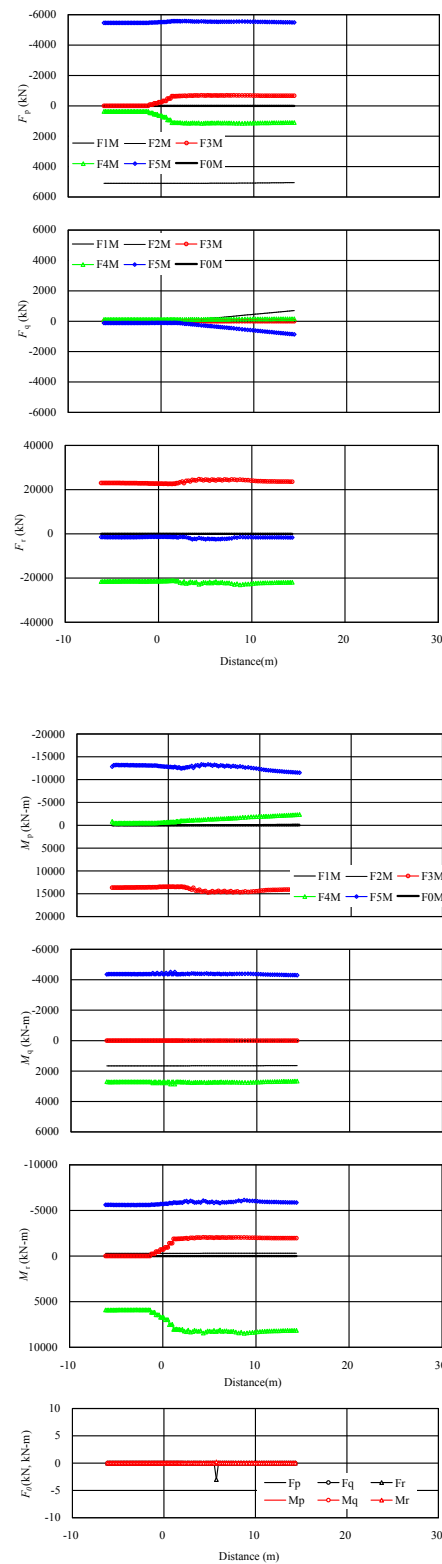
(a) Case No. 350043

(b) Case No. 350063

Figure 3.18 Trace of shield on the vertical and horizontal plane (Parameter 3: Share of jack force for both bodies)

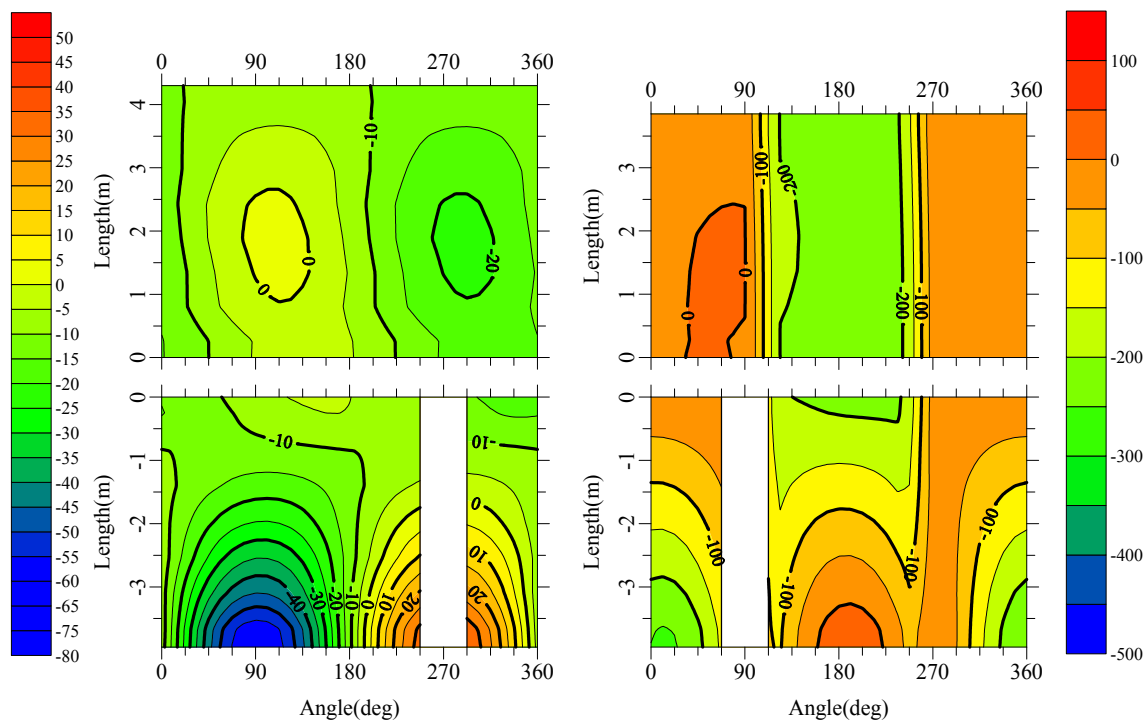


(a) Case No. 350043

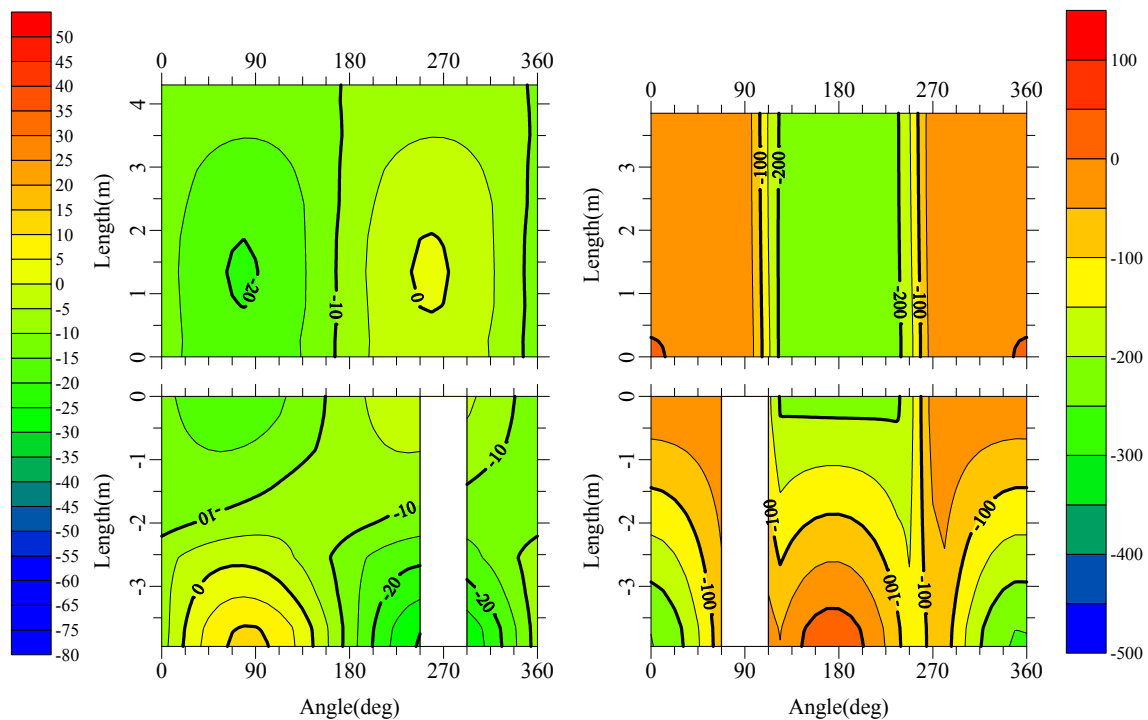


(b) Case No. 350063

Figure 3.19 Forces and moments against distance (Parameter 3: Share of jack force for both bodies)

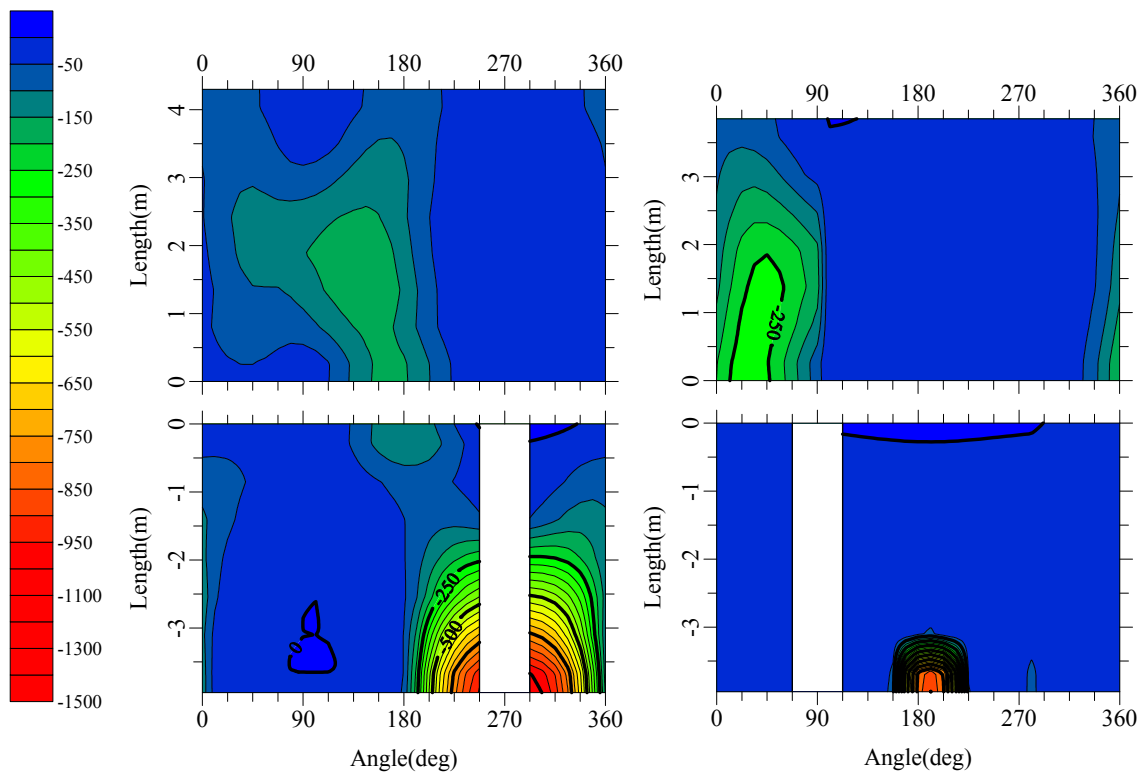


(a) Case 350043

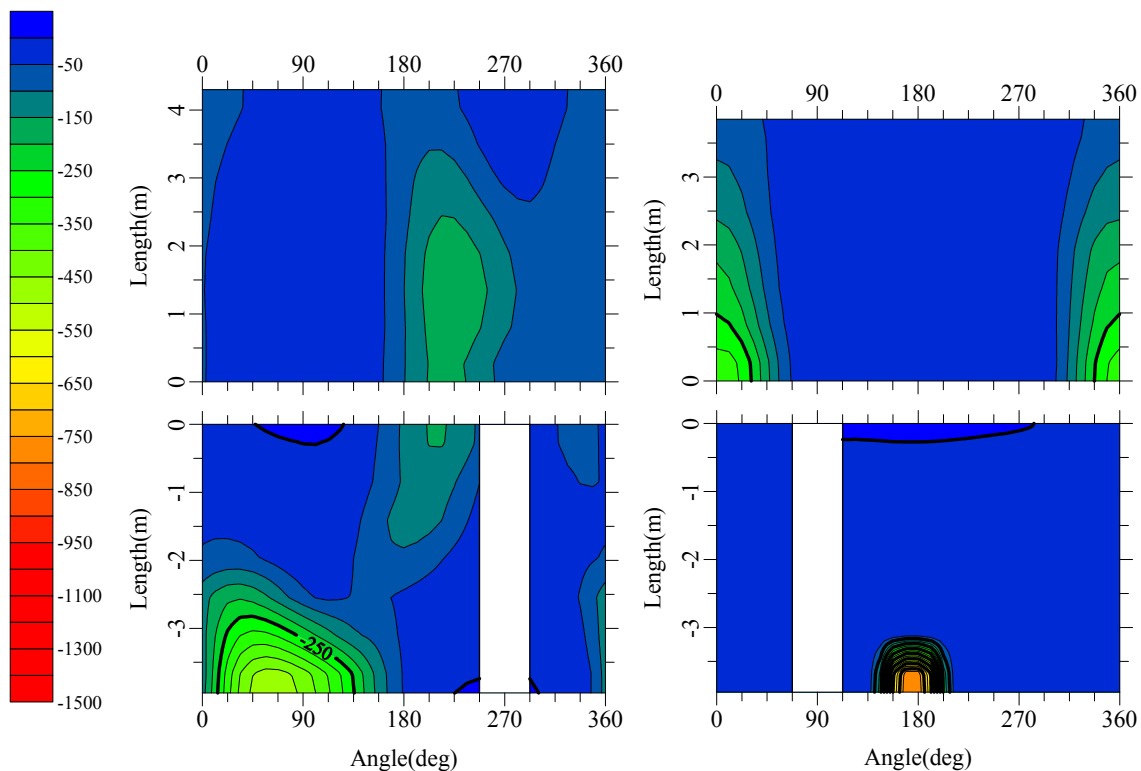


(b) Case 350063

Figure 3.20 Gap around the shield periphery (Parameter 3: Share of jack force for both bodies)

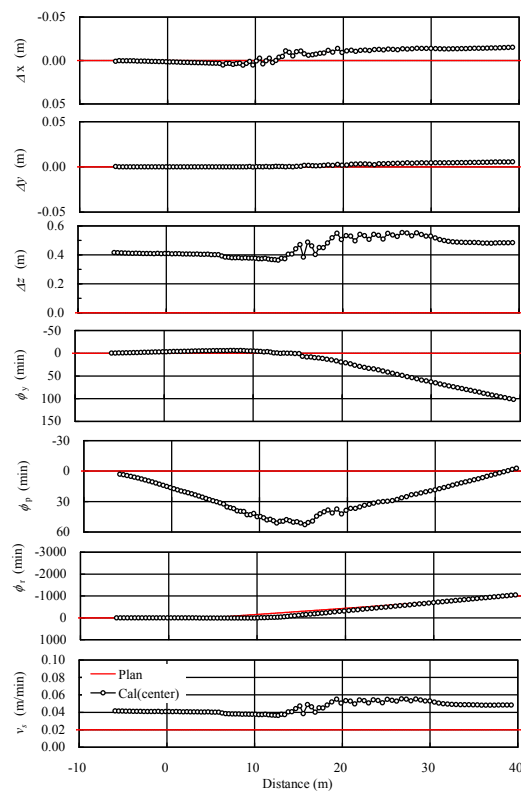
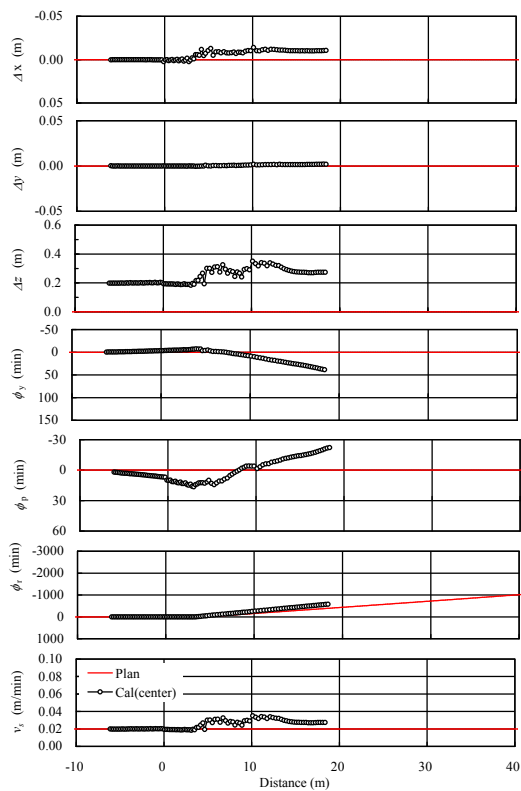


(a) Case 350043



(b) Case 350063

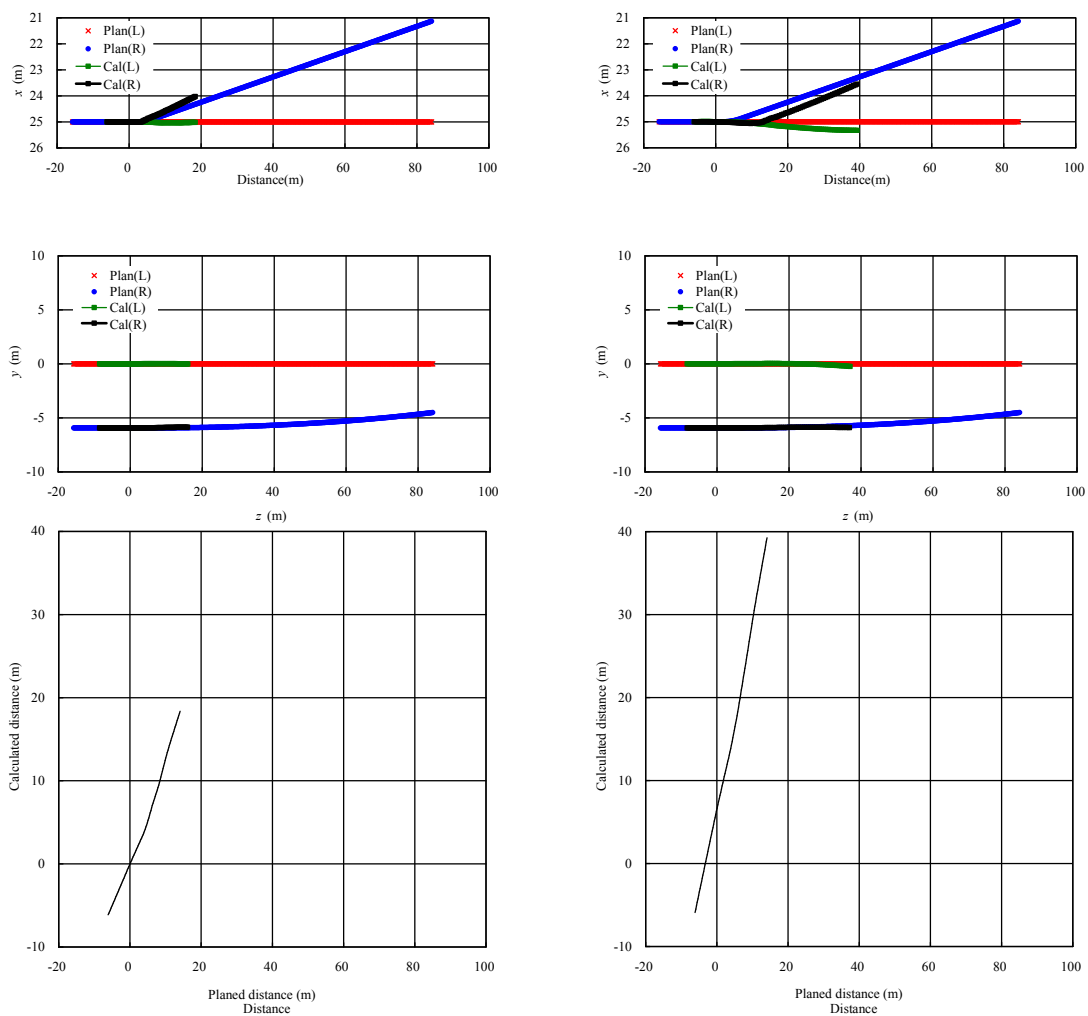
Figure 3.21 Normal effective earth pressure on the shield periphery (Parameter 3: Share of jack force for both bodies)



(a) Case No. 150003

(b) Case No. 450005

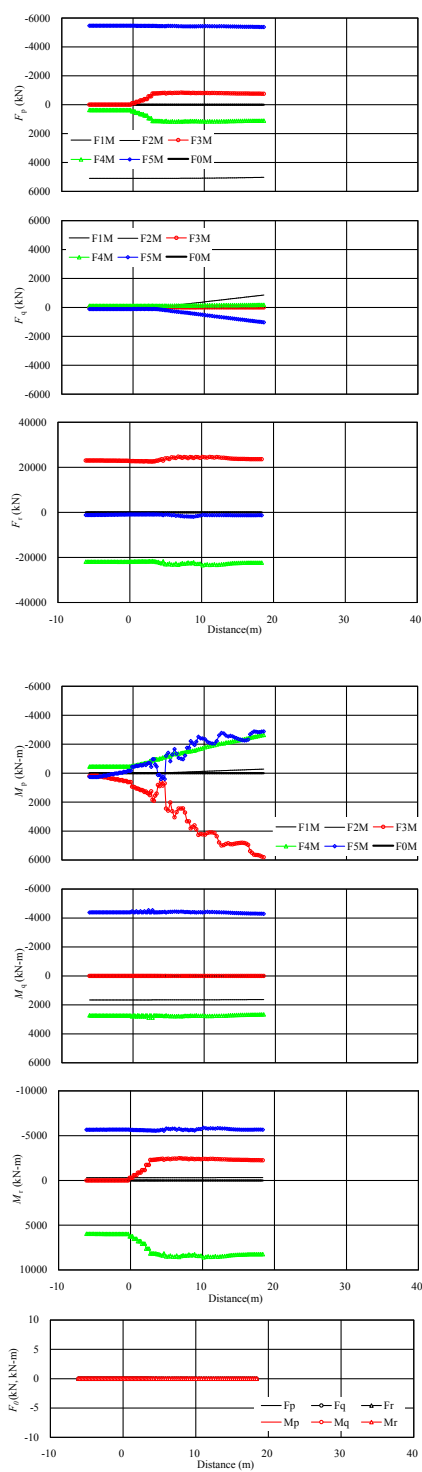
Figure 3.22 Shield behavior (Parameter 4: Ground stiffness)



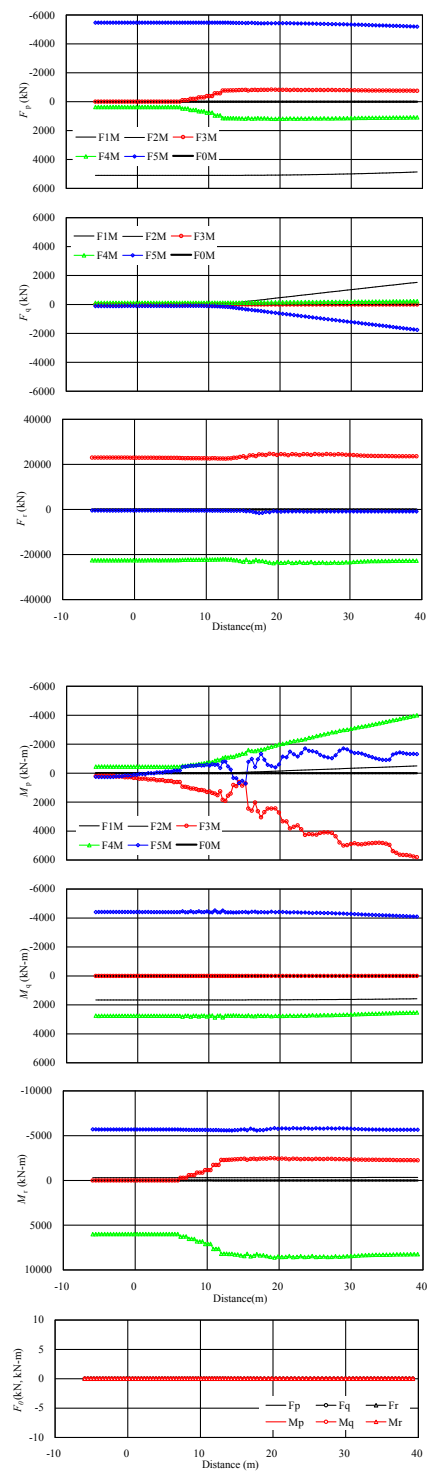
(a) Case No. 150003

(b) Case No. 450005

Figure 3.23 Trace of shield on the vertical and horizontal plane (Parameter 4: Ground stiffness)

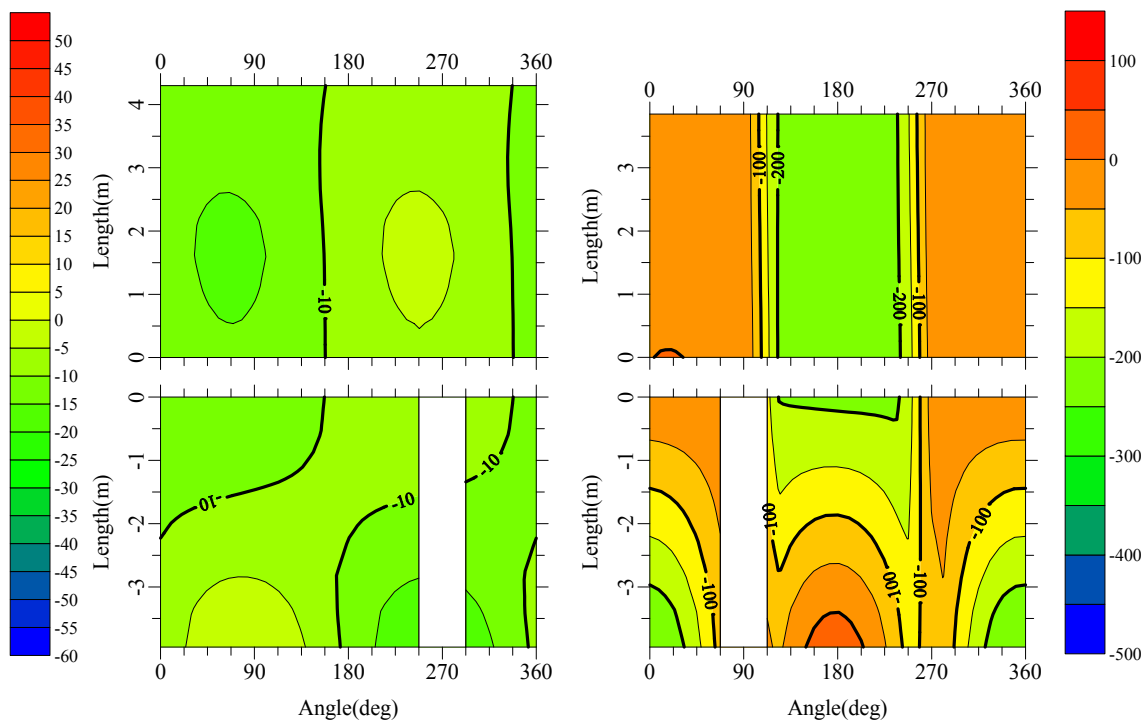


(a) Case No. 150003

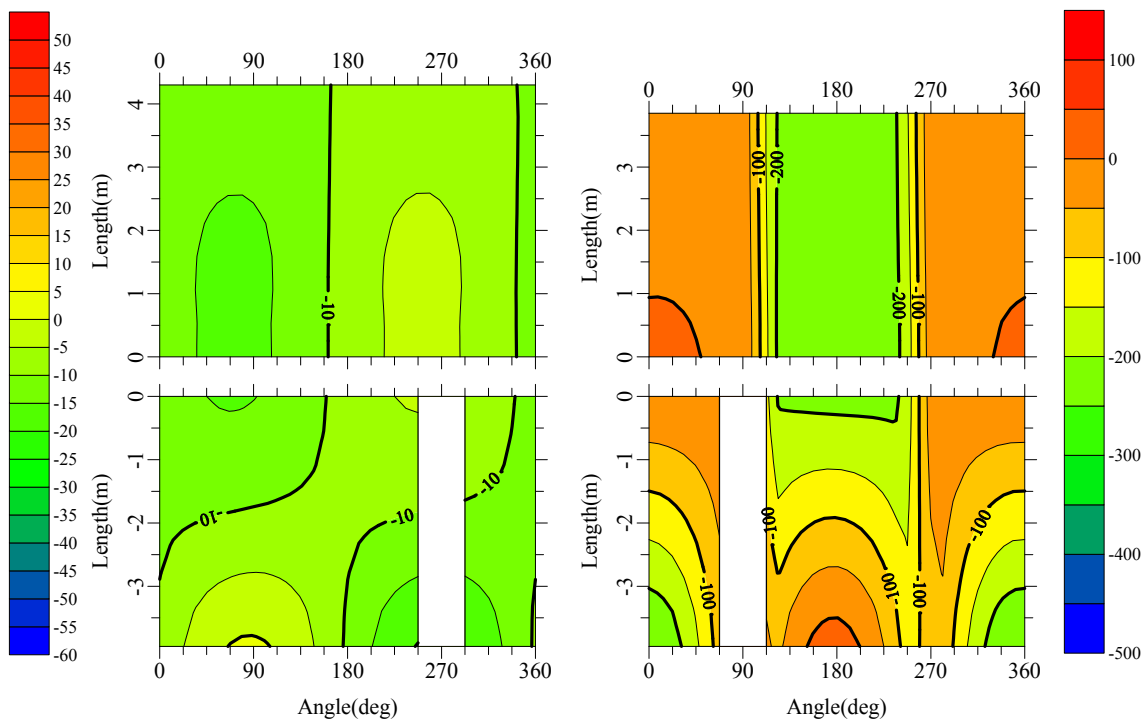


(b) Case No. 450005

Figure 3.24 Forces and moments against distance (Parameter 4: Ground stiffness)

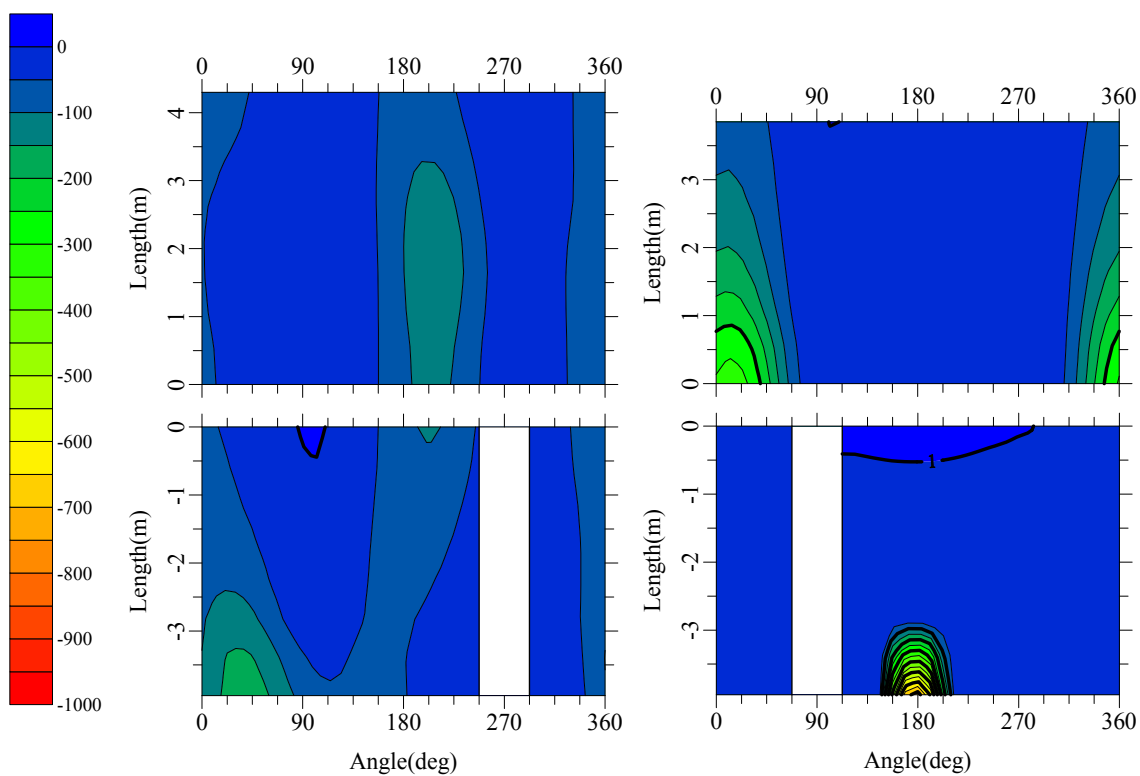


(a) Case 150003

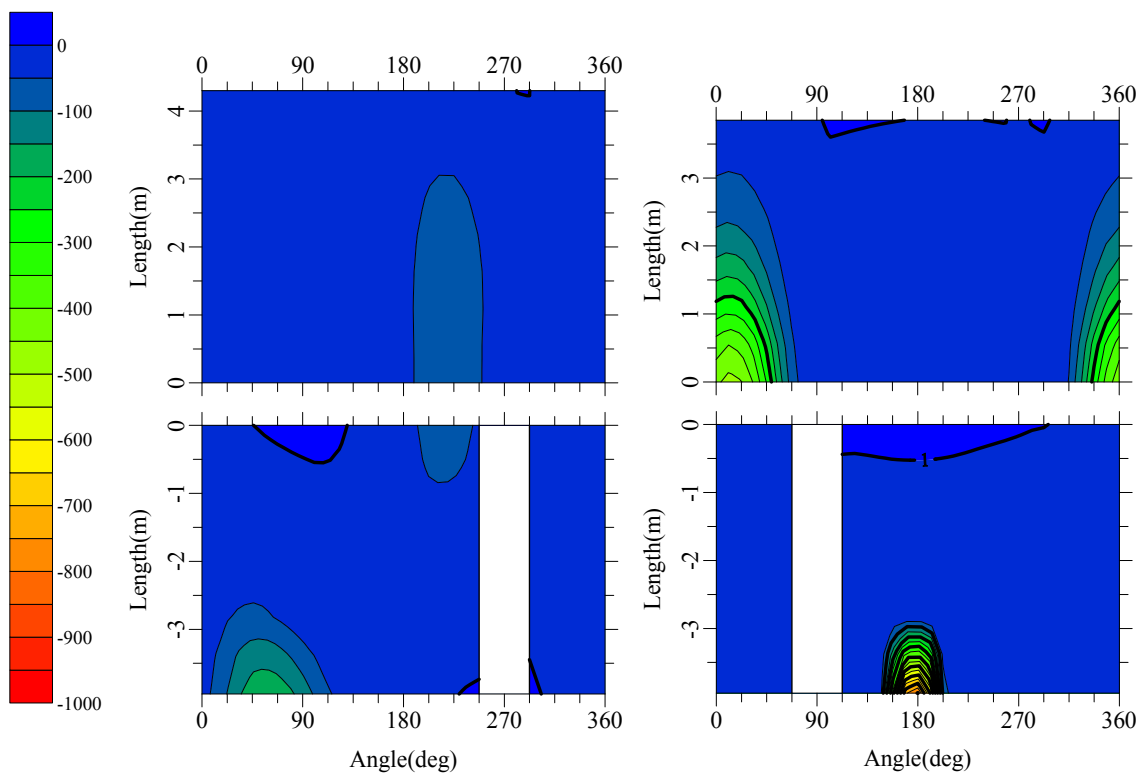


(b) Case 450005

Figure 3.25 Gap around shield periphery (Parameter 4: Ground stiffness)



(a) Case 150003



(b) Case 450005

Figure 3.26 Normal effective earth pressure on the shield periphery (Parameter 4: Ground stiffness)

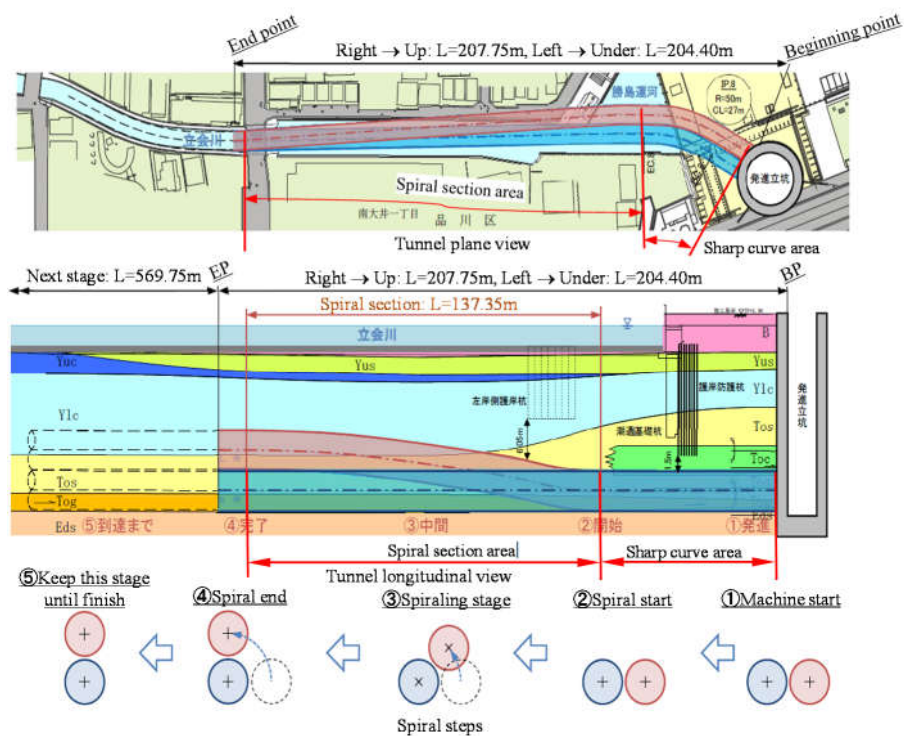


Figure 4.1 Site location and geological profile

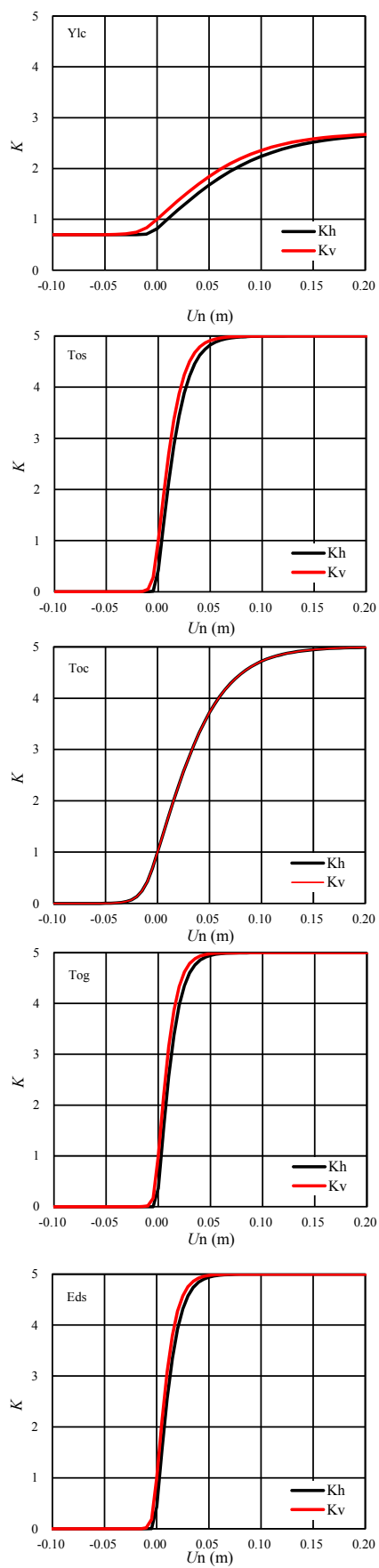


Figure 4.2 Ground reaction curve of the soil layers at the construction.

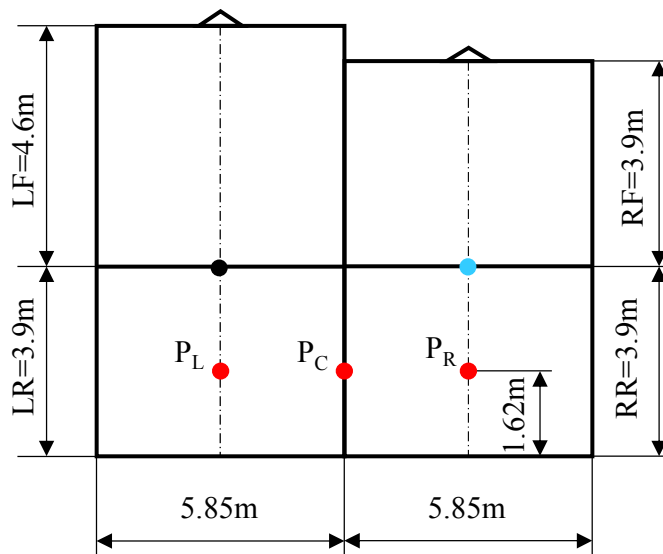


Figure 4.3 Dimension of H&V shield machine.

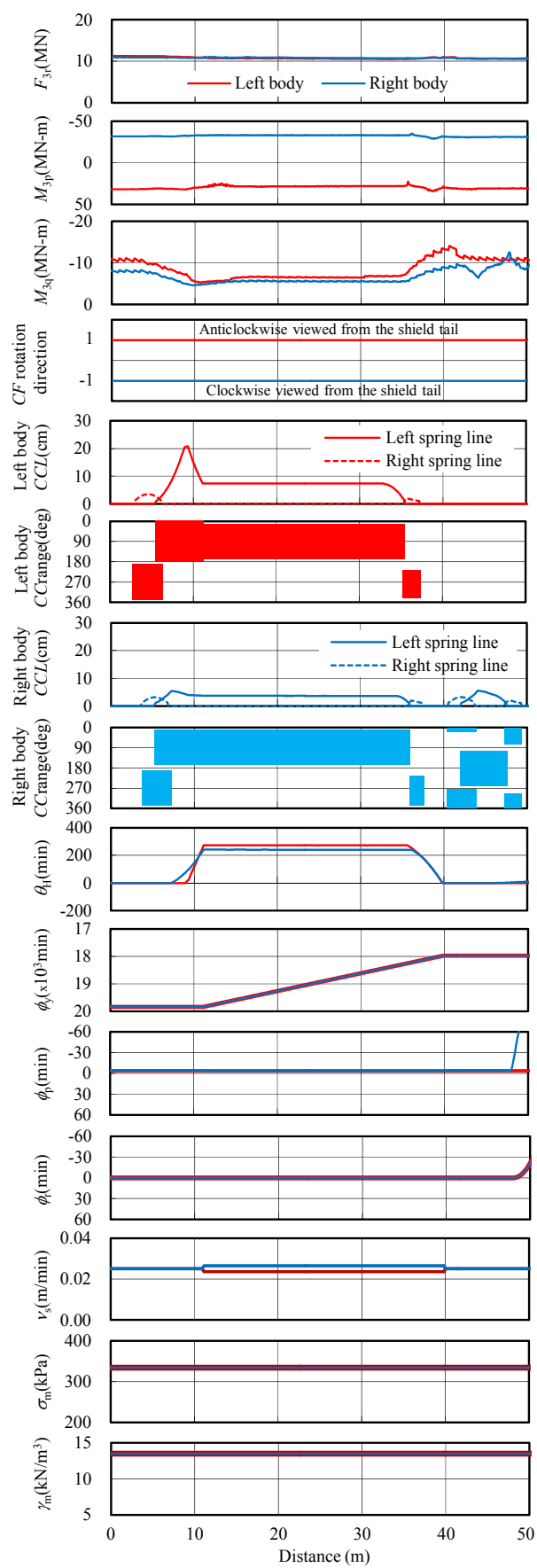


Figure 4.4 Shield tunneling input data at sharp curve

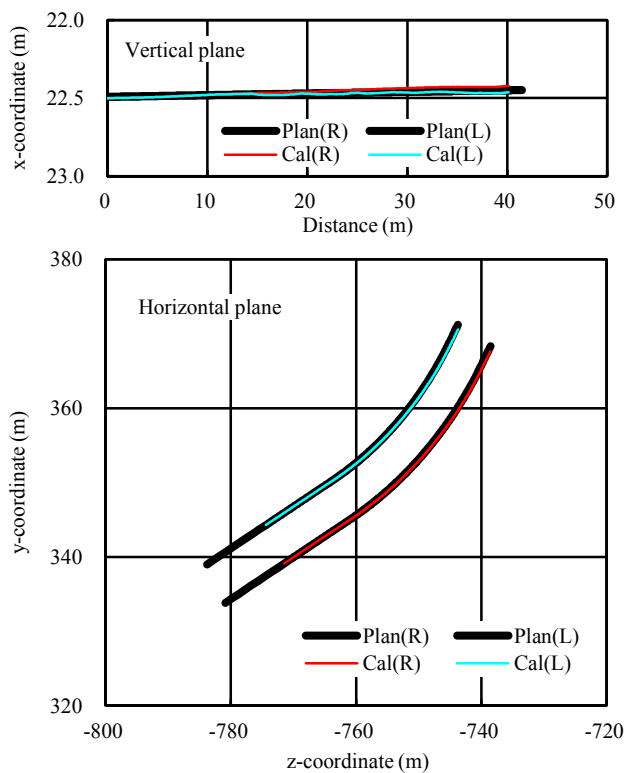


Figure 4.5 Calculated and planned shield traces at sharp curve

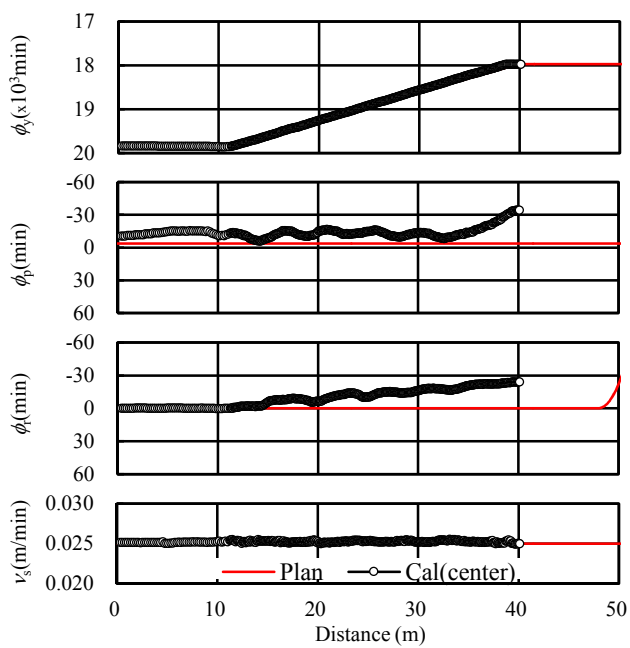


Figure 4.6 Calculated and planned shield behavior at sharp curve

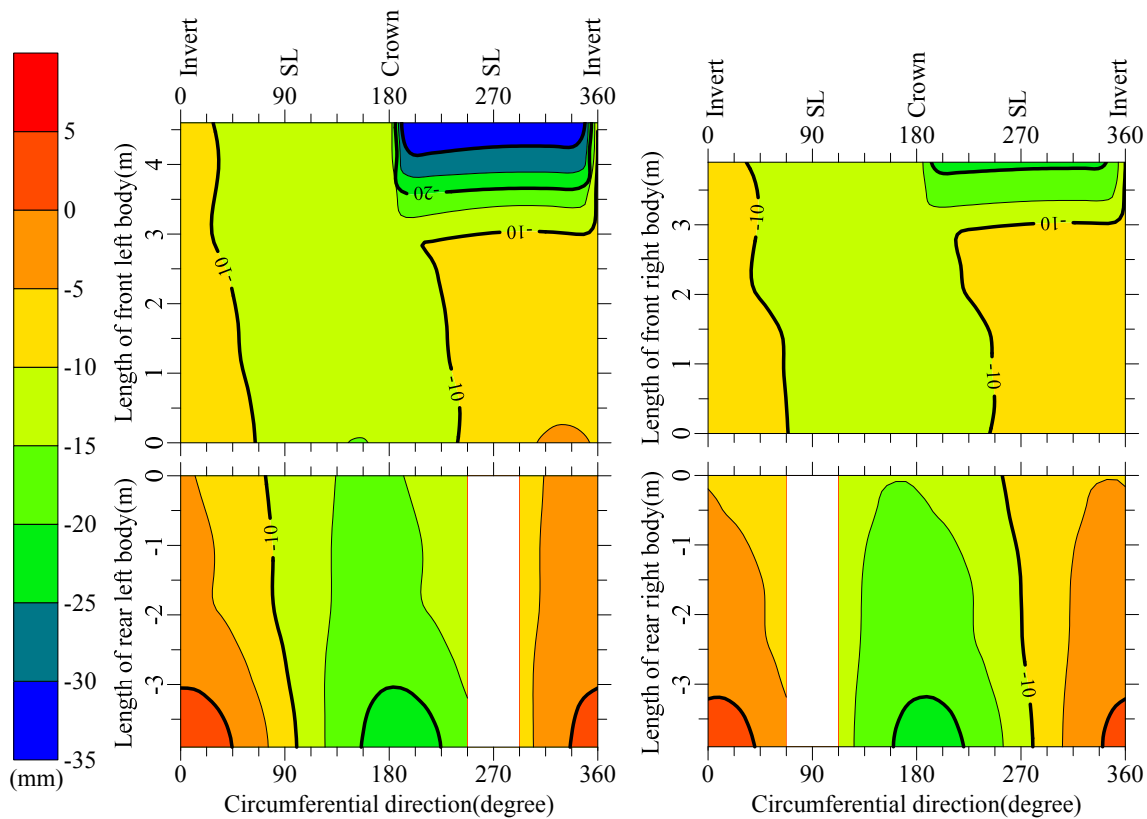


Figure 4.7  $U_n$  around shield on the straight line at 4.345 m.

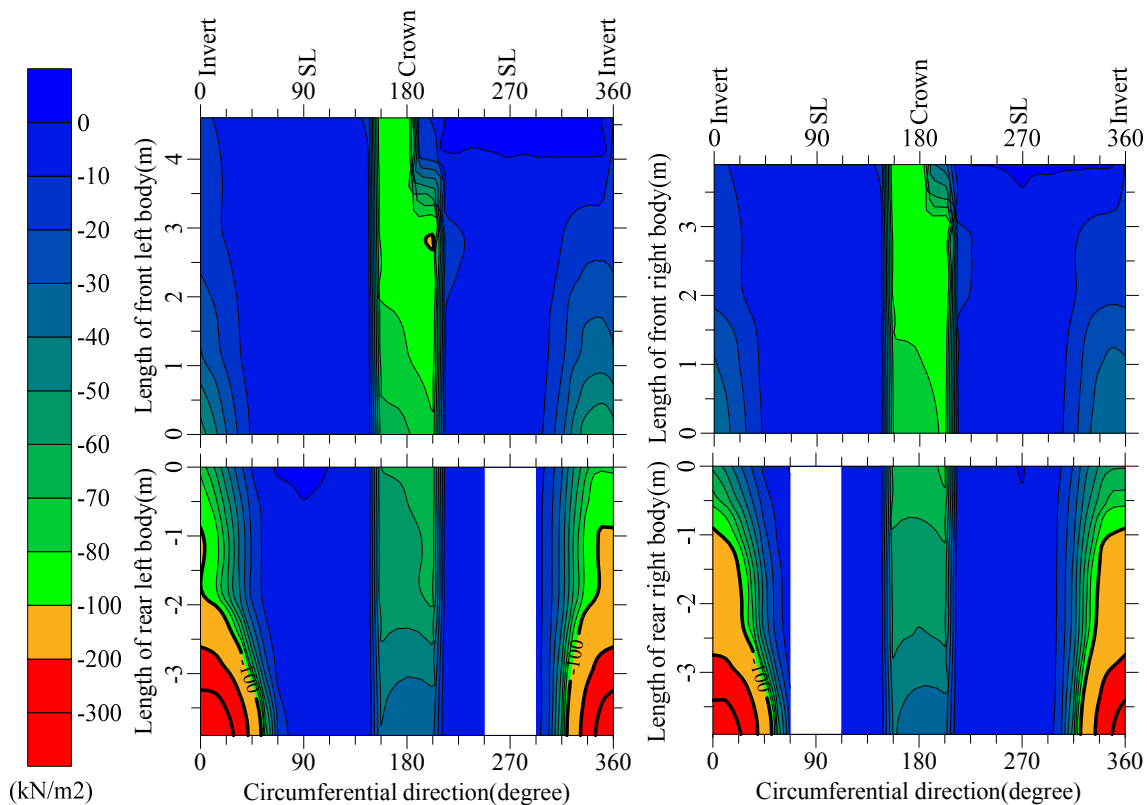


Figure 4.8  $\sigma'_n$  around shield on the straight line at 4.345m.

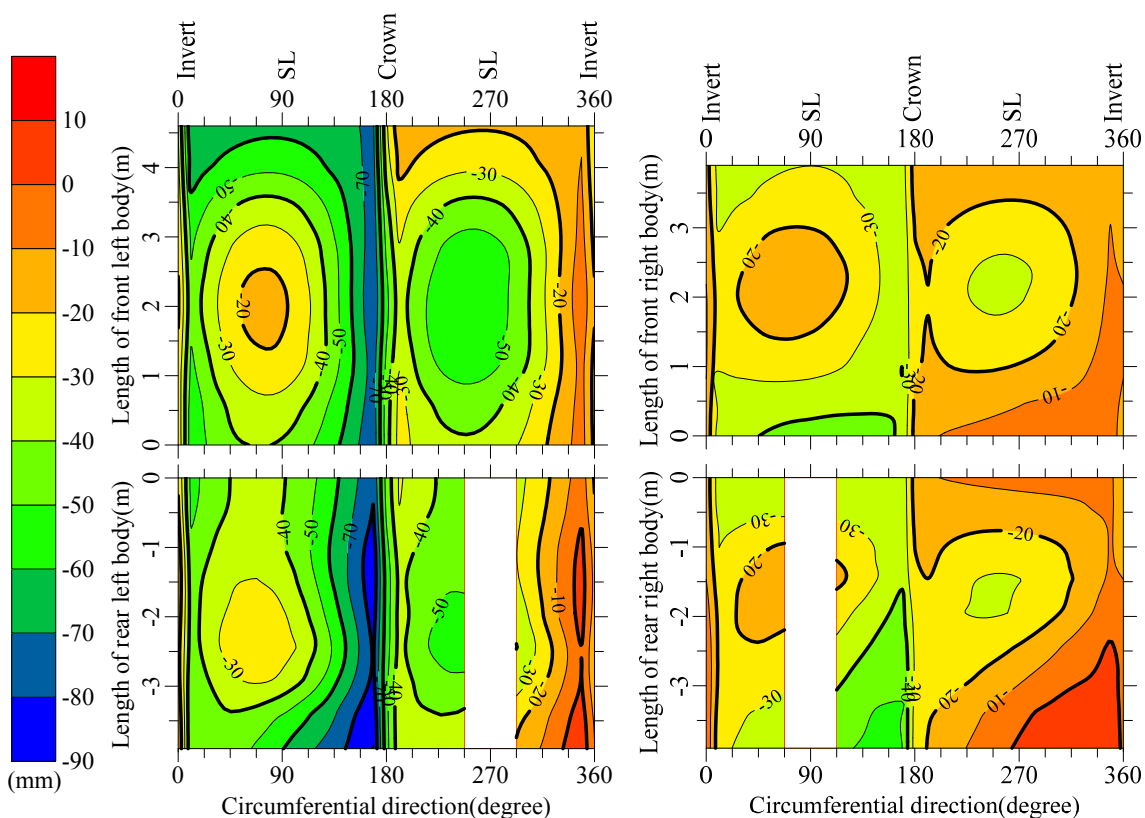


Figure 4.9  $U_n$  around shield on the sharp curve at 22.574m.

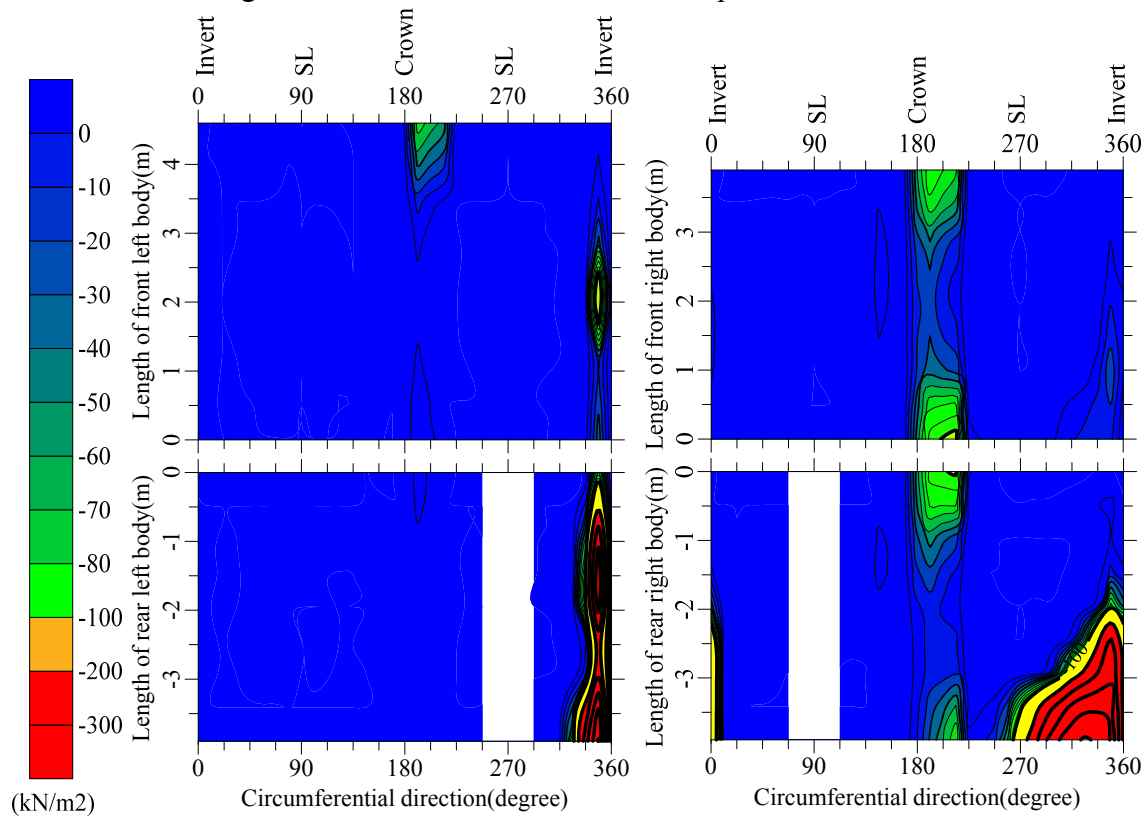


Figure 4.10  $\sigma_n'$  around shield on the sharp curve at 22.574m.

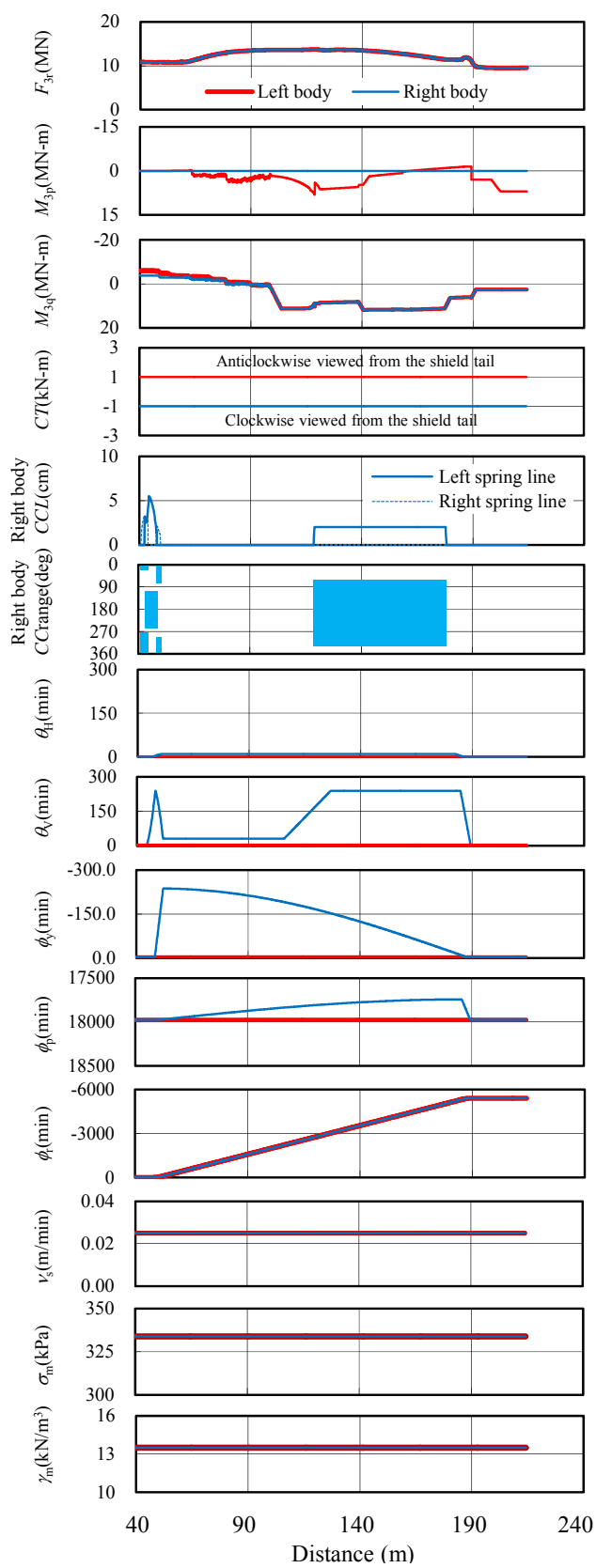


Figure 4.11 Shield tunnelling input data at spiral section

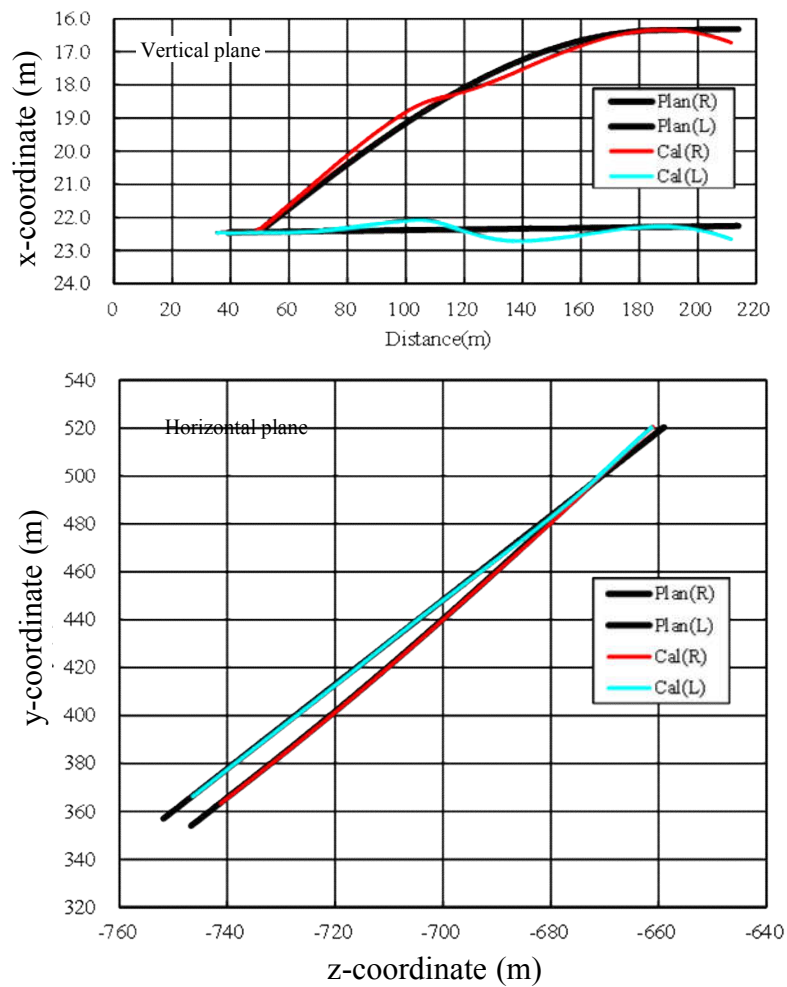


Figure 4.12 Calculated and planned shield traces at spiral section

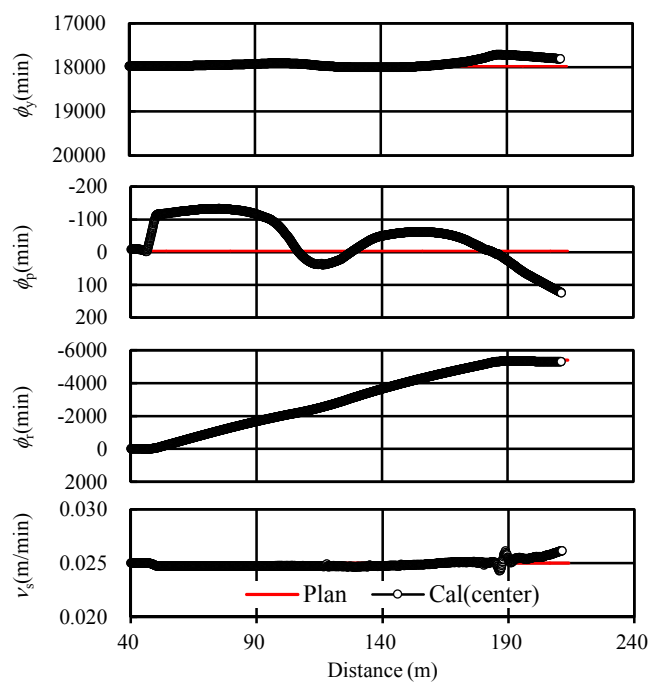


Figure 4.13 Calculated and planned shield behavior at spiral section

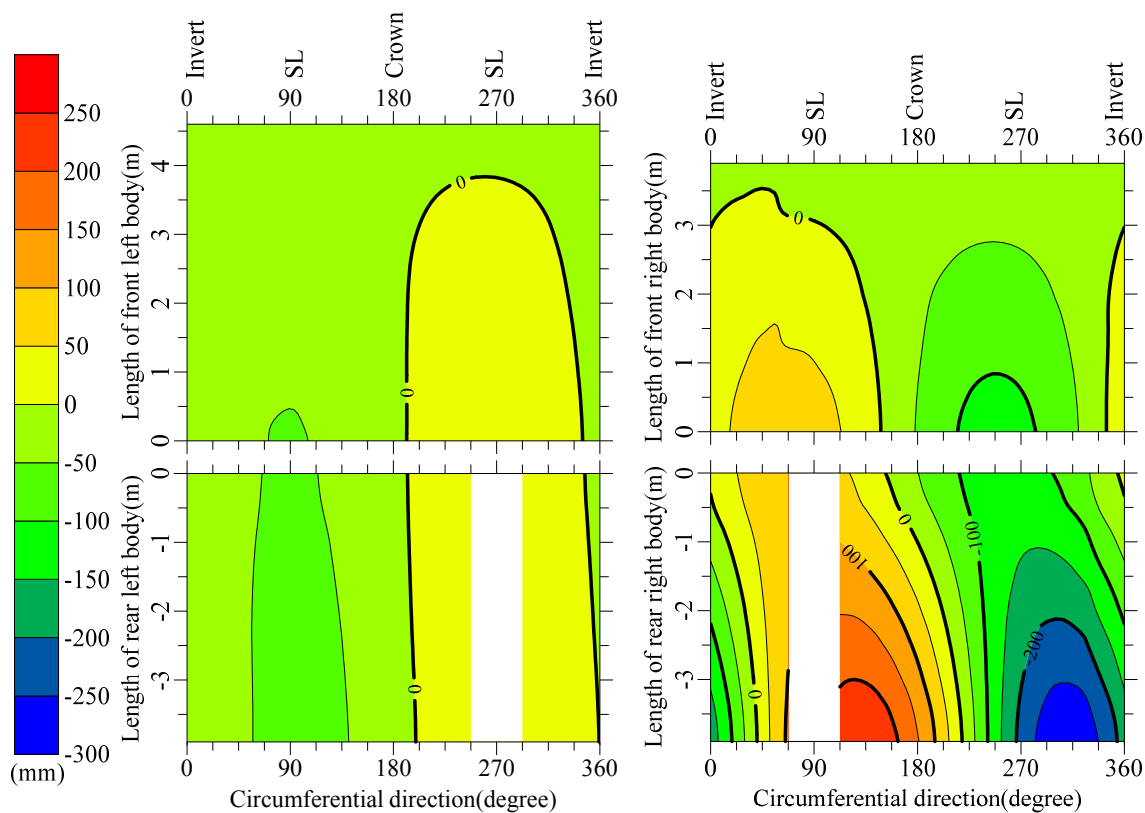


Figure 4.14  $U_n$  around shield on the spiral section at 125.5m.

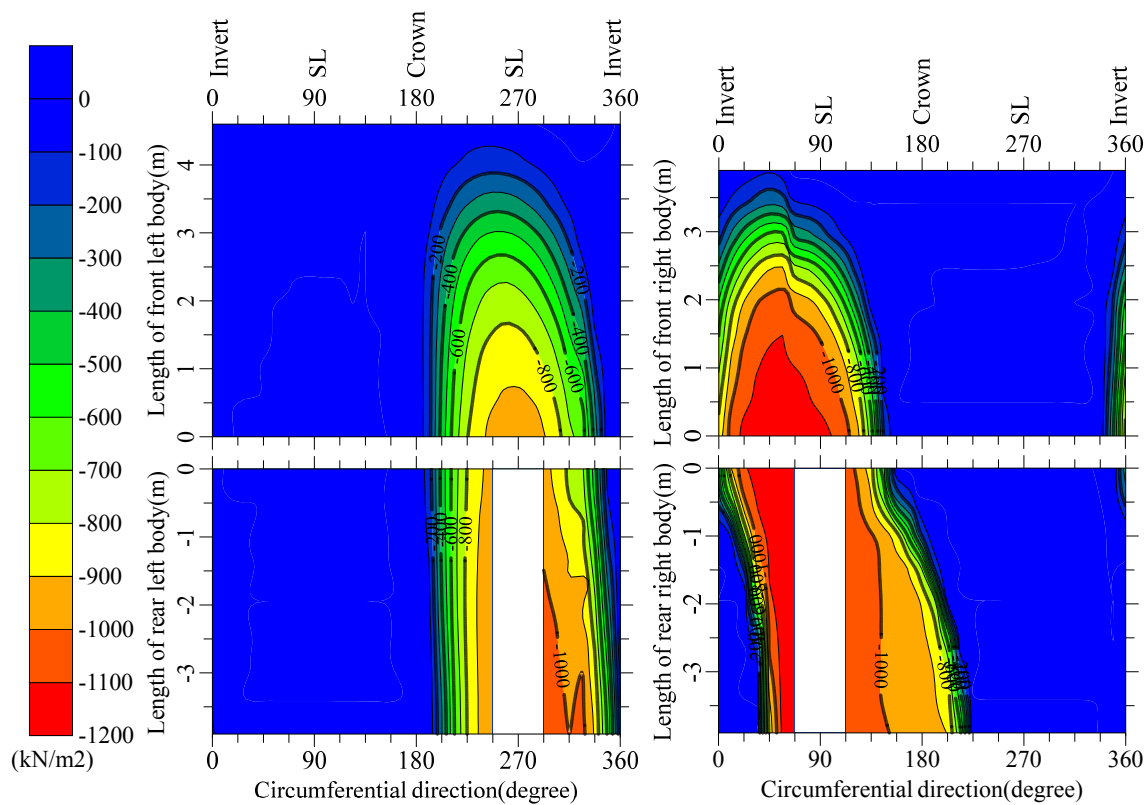


Figure 4.15  $\sigma_n$  ' around shield on the spiral section at 125.5m.